Explosive spalling and permeability of high performance concrete under fire – numerical and experimental investigations

Von der Fakultät Bau- und Umweltingenieurwissenschaften
der Universität Stuttgart zur Erlangung der Würde
eines Doktor-Ingenieurs (Dr.-Ing.)
genehmigte Abhandlung

Vorgelegt von
Josipa Bošnjak
aus Široki Brijeg, Bosnien und Herzegowina

Hauptberichter: Prof. Dr.-Ing. Joško Ožbolt
Mitberichter: Prof. Dr.-Ing. Christian Große
Mitberichter: Prof. Dr.-Ing. Jan Hofmann

Tag der mündlichen Prüfung: 23.05.2014

Institut für Werkstoffe im Bauwesen der Universität Stuttgart
2014

ACKNOWLEDGMENTS

First and foremost, I wish to express my deepest appreciation and gratitude to my guide Prof. Joško Ožbolt, for the great guidance, encouragement and advice he has provided throughout my time at IWB. I have always been impressed by his vast technical knowledge and incredible work enthusiasm. It inspired me to learn more and to expand my research interests. His insightful comments were of great help and his optimistic view on things always made me carry on with more confidence. I could not have imagined having a better guide.

The project on explosive spalling (in cooperation with TU Munich) was funded by the German Research Foundation DFG. Their support is greatly acknowledged.

I am very much indebted to the project partner Prof. Christian Große (TU Munich) for kindly accepting to be the co-reporter of the thesis. Many fruitful discussions with Prof. Große during our collaboration on the project significantly contributed to the progress of my work.

I would also like to thank to Prof. Jan Hofmann for accepting the co-report of the thesis. Professors Rolf Eligehausen, Jan Hofmann, Hans-Wolf Reinhardt and Harald Garrecht made it possible for me to work at IWB and encouraged me to take part in various approval projects, teaching activities and research. I am grateful for the given opportunity. Special thanks to Prof. Reinhardt for sharing his knowledge with me and advising me on many occasions.

Ronald Richter (TU Munich) was my partner on the explosive spalling project. Working with Ronald, particularly on fire experiments, was a very nice experience. Also, I appreciate the kind reception at TU Munich on several occasions, as well as his efforts to overcome the distance between Munich and Stuttgart.

Fire experiments were performed at FMPA Leipzig, under guidance of Prof. Frank Dehn and Michael Juknat. Their professional support and friendly reception at FMPA Leipzig is greatly acknowledged. It would have been impossible to develop the test setup for the permeability tests without the help of Rolf Hahn and David Haidle (MPA Stuttgart), who generously allowed me to use their equipment. I further wish to express my gratitude to company *baumhüter extrusion* for providing polypropylene fibres.

I am very grateful to the former head of applied research, Bernd M. Schlottke, for his great support and guidance during my first two years at IWB. To Dr. Werner Fuchs I am obliged for the support on several projects and all things administrative. Dr. Goran Periškić introduced me to working with MASA and Femap. I am thankful for the many versions of the code he prepared for me. The time spent with him and his family was very enjoyable for me.

I owe a very special thanks to Khalil Jebara, my first office colleague at IWB. Besides from helping me with all formalities which I faced upon moving abroad, he was also the most patient German language teacher one can possibly imagine. I cherish our

friendship very much. I enjoyed working with Dr. Akanshu Sharma very much. I have always been impressed by his knowledge and unique perspective of things. He motivated me to try out different things and encouraged me to carry on during tough times. Friendship with him and his family means a lot to me.

Filip Oršanić helped me immensely with everything I undertook during the past years, from experiments to numerical modelling and programming. His never-ending diligence, punctuality and patience have always inspired me. Filip is truly a great colleague and friend. It was really enjoyable to work with Marina Stipetić. Whenever I was not able to come to the office, I could always count on Marina to check on my experiments and replace me in the exam or lecture. It is great to have a cool and supportive friend like her.

I am very thankful to Sören Sippel and Dr. Alexander Assmann for their help with casting and for keeping my German readable. Thomas Rauscher always had time for a technical discussion over a cup of coffee. I appreciate his advice very much.

Martin Herzog and Christian Kontzi invested a lot of their time to teach me many things, from using lab equipment to basics of Swabian grammar and way of thinking. With the two of them I was never bored.

Working with Philipp and Christoph Mahrenholtz was a lot of fun, even more so during the initial month or two, when I was not able to differentiate between the two of them. It has been a pleasure to work with Natalija Bede, Daniela Ruta, Emiliano Sola, Kaipei Tian and Baris Irhan, who gave me so many laughs and crazy memories.

Kind help of IWB technicians Peter Scherf, Eugen Lindenmeier and Paul Geiger with experimental setup is greatly acknowledged. I would also like to thank the IWB staff (Silvia Choynacki, Simone Stumpp, Gisela Baur, Regina Jäger, Olga Weber) for their help on all things administrative and for many fun moments together. Monika Werner was extremely helpful with the literature review and she found every book and paper I needed. I am very much obliged to all my former and present colleagues at IWB for the time spend together and for many nice memories. It has been a great experience working with all of you!

My parents Vesna and Jozo have always supported me in all possible ways and for that I am forever grateful. My siblings Stjepan, Marko, Antonija, Marijana and Domagoj are my allies in all things important. I am so happy to have them.

Last, but not the least, I express my deepest gratitude to my amazing husband Mario. I would never have started or finished this PhD if it was not for his unconditional love, support and encouragement. There are no words good enough to describe what your support means to me. I love you with all my heart.

Stuttgart, Mai 2014

Josipa Bošnjak

ABSTRACT

Explosive spalling of high performance concrete under fire is one of the major concerns in front of the engineering community today. It is associated with violent failure of thin layers of concrete resulting in sudden reduction of load carrying capacity which may lead to complete collapse. High pore pressures due to low permeability and stresses due to thermal gradients are considered to be the governing causes of explosive spalling. However, the failure mechanisms and all influencing parameters are not yet fully understood.

The most popular method to prevent spalling is the addition of polypropylene (PP) fibres in concrete. It is generally accepted that the PP fibres leave a porous network after melting at around 160 °C, leading to an increase in permeability, thus allowing the water vapour to escape. However, it seems that there also might be other mechanisms which lead to relief of pore pressure.

This work is aimed at investigating the phenomenon of explosive spalling and understanding the causes behind the same. Technical difficulties in measuring during the experiments at high temperatures or fire limit the data that can be obtained. On the other hand, numerical analysis provides a better insight into the governing causes and a quantitative estimate of the relevant properties. Therefore, in this work, the experimental investigation is augmented by extensive numerical parametric studies.

Experiments under two typical fire scenarios are conducted on slabs made of plain and concrete with PP fibres to compare the performance of the two mixes as well as to investigate the effect of the heating rate on explosive spalling. Significant influence of PP fibres in mitigating explosive spalling is confirmed by these experiments.

In order to measure the permeability of concrete at elevated temperature, a new test setup is developed and validated. Permeability experiments on plain and concrete with addition of PP fibres are performed at temperatures up to 300 °C using the new test setup. The results show that permeability of concrete with PP fibres rises even before the fibres melt, thus indicating that the melting of fibres is not the only mechanism responsible for the permeability increase. To confirm this, microstructure of the specimens before and after heating is studied using a scanning electron microscope.

The existing thermo-hygro-mechanical model is validated against experiments and is used to investigate the influence of various parameters on explosive spalling. The parameters studied include: permeability, relative humidity, restraint, load, non-homogeneity, aggregate type, etc. The numerical parametric studies are performed at macro- and meso-scale. Due to the high influence of the local inhomogeneities, analysis at macro-scale could only partially capture the failure mode. It is found that all aspects of explosive spalling can be considered only while performing analysis at meso-scale.

KURZFASSUNG

Explosives Abplatzen von Hochleistungsbeton unter Brandeinwirkung stellt einen der wichtigsten Aspekte der Betondauerhaftigkeit dar. Unter explosiven Abplatzungen ist ein schlagartiges Versagen der dünnen Oberflächenschichten gemeint, das eine schnelle Abminderung der Tragfähigkeit zur Folge hat. Dies kann sogar zum Versagen des Bauwerkes führen. Die durch die niedrige Permeabilität hervorgerufenen Porendrücke und die Druckspannungen infolge thermischen Gradienten sind als Hauptursachen dieser Versagensart identifiziert. Allerdings sind der Versagensmechanismus und die Beiträge der wichtigsten Einflussparameter noch nicht ausreichend verstanden.

Die meistverwendete Methode zur Vermeidung der explosiven Abplatzungen ist die Zugabe von Polypropylenfasern in Beton. Nach dem Schmelzen bei ca. 160 °C hinterlassen die Fasern ein Netzwerk der miteinander verbundenen Poren. Dadurch wird die Permeabilität erhöht und der Wasserdampf kann einfacher entweichen. Dahingegen gibt es auch Hinweise, dass auch weitere Mechanismen für die Permeabilitätserhöhung verantwortlich sind.

In der vorliegenden Arbeit wurden die Hauptmechanismen der Abplatzungen sowie die wichtigsten Einflussparameter untersucht. Aufgrund der messtechnischen Einschränkungen konnten bei den Brandversuchen nur bedingt Informationen gewonnen werden. Andererseits bietet die numerische Analyse mehr Einblick in das Betonverhalten bei hohen Temperaturen. Aus diesem Grund wurden die experimentellen Ergebnisse mit umfangreichen numerischen Parameterstudien erweitert.

Brandversuche wurden für zwei Brandszenarien an Hochleistungsbeton ohne und mit Polypropylenfasern durchgeführt. Dies ermöglichte, das Verhalten des Betons unter verschiedenen Brandbelastungen sowie den Wirkungsgrad der Fasern zu untersuchen. Die Ergebnisse bestätigten die hohe Wirksamkeit der Fasern, trotz des relativ geringen Faseranteils in Beton (1 kg/m^3). Weiterhin wurde ein neuer Versuchsaufbau für Permeabilitätsmessungen bei hohen Temperaturen entwickelt und validiert. Die Permeabilitätsmessungen an zwei Betontypen zeigen, dass die Permeabilität des faserverstärkten Betons schon bei Temperaturen deutlich unterhalb der Schmelztemperatur einen ausgeprägten Sprung aufweist. Das Verhalten der Fasern wurde auch mittels SEM Aufnahmen untersucht.

Das bestehende thermo-hygro-mechanische Modell für Beton wurde anhand von Versuchsergebnissen validiert und für die numerische Untersuchung der explosiven Abplatzungen eingesetzt. Der Einfluss der wichtigsten Parameter (Erhitzungsrate, Brandszenario, relative Feuchtigkeit, Permeabilität, Belastung, Inhomogenität, Zuschlagtyp usw.) wurde untersucht. Dabei wurde Beton sowohl auf Makro- als auch auf Mesoebene untersucht, um den Einfluss des lokalen Charakters der Abplatzungen sowie der Betonheterogenität zu berücksichtigen. Es wurde gezeigt, dass alle Aspekte der explosiven Abplatzungen nur unter mesoskopischer Betrachtung vollständig erfasst werden können.

CONTENTS

1. INTRODUCTION 15

1.1 BACKGROUND, MOTIVATION AND CONTEXT OF RESEARCH 15
1.2 OBJECTIVES 19
1.3 SCOPE OF WORK 20

2. LITERATURE REVIEW 21

2.1 CONCRETE AT ELEVATED TEMPERATURES 21
2.2 PHYSICAL PROPERTIES OF CONCRETE AT ELEVATED TEMPERATURES 23
2.2.1 Density 23
2.2.2 Heat capacity 23
2.2.3 Thermal conductivity 24
2.2.4 Permeability 24
2.3 MECHANICAL PROPERTIES OF CONCRETE AT ELEVATED TEMPERATURES 25
2.3.1 Compressive strength 25
2.3.2 Young's modulus 26
2.3.3 Tensile strength 27
2.3.4 Fracture energy 28
2.4 THERMAL DILATATION OF CONCRETE 28
2.4.1 Free thermal strain 28
2.4.2 Load induced thermal strain 29
2.5 EXPLOSIVE SPALLING OF CONCRETE 31
2.5.1 General 31
2.5.2 Factors influencing explosive spalling 33
2.5.2.1 Heating rate 33
2.5.2.2 Moisture content – relative humidity 34
2.5.2.3 Permeability 35
2.5.2.4 Compressive stress and restraint 35
2.5.2.5 Aggregate size and type 37
2.5.2.6 Concrete strength and quality 37
2.5.2.7 Section size and shape 38
2.5.2.8 Polypropylene fibres and air entrainment 38
2.6 THEORIES TO EXPLAIN THE MECHANISM OF EXPLOSIVE SPALLING 39
2.6.1 Thermally induced explosive spalling 39
2.6.2 Pore pressure induced spalling 40
2.6.3 Combination of thermally induced stresses and pore pressures 40
2.7 NUMERICAL MODELLING OF CONCRETE AT ELEVATED TEMPERATURES 41
2.8 CONCLUSIONS 43

EXPERIMENTAL STUDY 45

3. EXPERIMENTAL INVESTIGATION OF HPC SLABS IN FIRE 46

3.1 MATERIALS AND SPECIMEN 46
3.2 HEATING SCENARIO AND TEST SETUP 48
3.3 RESULTS AND DISCUSSION 49
3.3.1 Temperature measurements 49
3.3.2 Behaviour of plain HPC in fire 51
3.3.3 Behaviour of HPC with PP fibres in fire 54
3.4 CONCLUSIONS 56

4. EXPERIMENTS ON CONCRETE CUBES 57

4.1 MATERIALS AND SPECIMENS 57
4.2 HEATING REGIME AND MECHANICAL LOADING 58
4.3 RESULTS AND DISCUSSION 59

5. PERMEABILITY OF HPC AT ROOM AND ELEVATED TEMPERATURE 63

5.1 GENERAL 63
5.2 THEORETICAL BACKGROUND 64
5.3 EXPERIMENTAL INVESTIGATIONS 67
5.3.1 Test setup 67
5.3.2 Material properties 70
5.3.2.1 Concrete 70
5.3.2.2 Polypropylene fibres 71
5.3.2.3 Sealant 71
5.4 RESULTS AND DISCUSSION 72
5.4.1 Validation against RILEM-CEMBUREAU method (permeability measurements at room temperature) 72
5.4.2 New test setup - permeability measurements at room and elevated temperatures 72
5.4.3 Influence of the compressive stress on permeability 74
5.4.4 Microscopic investigation of the concrete with polypropylene fibres 75
5.5 CONCLUSIONS 77

NUMERICAL STUDY 79

6. THE THERMO-MECHANICAL MODEL 80

6.1 TRANSIENT THERMAL ANALYSIS 80
6.2 MICROPLANE MODEL WITH RELAXED KINEMATIC CONSTRAINT 80
6.3 THERMO-MECHANICAL COUPLING 83
6.3.1 Young's modulus of concrete 83
6.3.2 Compressive strength of concrete 83
6.3.3 Tensile strength of concrete 84
6.3.4 Concrete fracture energy 84
6.3.5 Yield strength of steel 85
6.4 THERMAL STRAINS IN THE MICROPLANE MODEL 86
6.4.1 Decomposition of strain tensors 86
6.4.2 Free thermal strain 87
6.4.3 Load-induced thermal strain 87
6.5 VALIDATION OF THE THERMO-MECHANICAL MODEL AGAINST EXPERIMENTS ON PLAIN CONCRETE: MACRO SCALE 88
6.5.1 Material properties 89
6.5.2 Heating/cooling regime and subsequent loading 90
6.5.3 Results and discussion 90
6.6 VALIDATION OF THE THERMO-MECHANICAL MODEL AGAINST EXPERIMENTS ON REINFORCED CONCRETE: MACRO SCALE 92
6.6.1 Experiments – geometry and material properties 92
6.6.2 Spatial discretization and loading 93
6.6.3 Results and discussion 94
6.7 VALIDATION OF THE THERMO-MECHANICAL MODEL AGAINST EXPERIMENTS WITH RESPECT TO THERMAL STRAIN: MESO SCALE 99
6.7.1 Free thermal strains 99
6.7.1.1 Experimental data (Cruz & Gillen 1980) 100

6.7.1.2 Numerical approach ... 100
6.7.1.3 Results and discussion ... 101
6.7.2 Load induced thermal strains ... 102
6.7.2.1 Experimental data (Hager 2004) ... 102
6.7.2.2 Numerical model ... 103
6.7.2.3 Results and discussion ... 103
6.7.2.4 Experimental data (Anderberg & Thelandersson 1976) ... 106
6.7.3 Numerical model ... 106
6.7.3.1 Results and discussion ... 106
6.7.4 Conclusions ... 107

7. THE THERMO-HYGRO-MECHANICAL MODEL ... 108

7.1 COUPLED HEAT AND MOISTURE TRANSFER ... 108
7.2 STATE OF PORE WATER AND PERMEABILITY ... 109
7.3 THERMO-MECHANICAL COUPLING ... 112
7.4 THERMO-HYGRO-MECHANICAL COUPLING ... 113
7.5 NUMERICAL IMPLEMENTATION ... 114

8. MODELLING EXPLOSIVE SPALLING ... 115

8.1 INTRODUCTION ... 115
8.2 MODELLING APPROACH ... 116
8.2.1 Macro-scale model ... 116
8.2.2 Meso-scale model ... 118
8.3 VALIDATION OF THE MODELLING APPROACH AGAINST EXPERIMENTS ... 121
8.3.1 Standard fire ISO 834 (ETK) ... 121
8.3.1.1 ISO 834 fire analysed employing TM model ... 122
8.3.1.2 ISO 834 fire analysed employing THM model ... 125
8.3.1.3 Tunnel fire curve (ZTV-ING) analysed employing THM model ... 130
8.3.2 Conclusions ... 134
8.4 PARAMETRIC STUDY AT MACRO- AND MESO-SCALE ... 135
8.4.1 Comparison of 3D and 2D model ... 138
8.4.2 Heating rates and fire scenarios ... 140
8.4.3 ISO 834 fire ... 141
8.4.3.1 Geometric nonlinearity ... 141
8.4.3.2 Relative humidity ... 143
8.4.3.3 Permeability ... 146
8.4.3.4 Compressive load ... 148
8.4.3.5 The role of load induced thermal strain ... 151
8.4.3.6 Aggregate type ... 154
8.4.3.7 Aggregates distribution (meso-scale model) ... 157
8.4.4 ZTV-ING fire ... 159
8.4.4.1 Relative humidity ... 159
8.4.4.2 Permeability ... 160
8.4.4.3 Compressive load ... 161
8.4.5 Constant heating rate ... 162
8.5 CONCLUSIONS ... 164

9. CONCLUSIONS AND OUTLOOK ... 167

BIBLIOGRAPHY ... 170

LIST OF INDICES

Microplane model

σ	stress	[N/mm^2]
ε	strain	[-]
σ^V	volumetric stress	[N/mm^2]
ε^V	volumetric strain	[-]
K	bulk modulus	[N/mm^2]
ε_{ij}	total strain tensor for concrete	[-]
ε_{ij}^m	mechanical strain tensor	[-]
ε_{ij}^{fst}	free thermal strain tensor	[-]
ε_{ij}^{lits}	load induced strain vector	[-]
ε_N	normal component of the microplane strain	[-]
ε_D	deviatoric component of the microplane strain	[-]
ε_V	volumetric component of the microplane strain	[-]
ε_{Tr}	tangential component of the microplane strain	[-]
S	sphere surface area	[N/mm^2]
φ	discontinuity function in the microplane model	[-]
σ_N	normal component of the microplane stress	[N/mm^2]
σ_D	deviatoric component of the microplane stress	[N/mm^2]
σ_V	volumetric component of the microplane stress	[N/mm^2]
σ_{Tr}	tangential component of the microplane stress	[N/mm^2]
ν	Poisson's coefficient	[-]
E	macroscopic E modulus	[N/mm^2]
f_t	macroscopic tensile strength	[N/mm^2]
f_c	macroscopic compressive strength	[N/mm^2]
G_f	macroscopic fracture energy (tension)	[N/mm^2]
G_c	macroscopic fracture energy (compression)	[N/mm^2]

Heat and moisture transport, permeability measurements

a_{app}	apparent permeability	[m^2]
a_{int}	intrinsic permeability	[m^2]
b_K	Klinkenberg flow constant	[N/m^2]
μ	dynamic viscosity	[Ns/m^2]
Q	volumetric flow	[m^3/s]
Q_m	volumetric flow corresponding to the mean pressure p_m	[m^3/s]

r	radius	[m]
L	length of the specimen	[m]
r_1	inner radius of a ring specimen	[m]
r_2	outer radius of a ring specimen	[m]
H	height	[m]
V	volume	[m^3]
λ	thermal conductivity of concrete	[W/mK]
C	isobaric heat capacity of concrete	[J/kgK]
ρ	density of concrete	[kg/m^3]
$\boldsymbol{J}$	moisture flux	[kg/m^2s]
$\boldsymbol{q}$	heat flux	[J/m^2s]
w	water content	[kg/m^3]
T	temperature	[K]
p	pressure, pore pressure	[N/mm^2]
g	gravity constant	[kg/m^2s]
a_p	relative permeability	[m/s]
a_0	reference permeability at 20 °C and rH=100 %	[m/s]
t	time	[s]
w_d	mass of free water	[kg/m^3]
C_a	sorption heat of free water	[J/kg]
C_w	isobaric capacity of free water	[J/kgK]
p_0	pore pressure at the element surface	[N/mm^2]
p_1	inlet pressure	[N/mm^2]
p_2	outlet pressure	[N/mm^2]
p_m	mean pressure	[N/mm^2]
p_E	pore pressure of the surrounding environment	[N/mm^2]
T_0	temperature at the element surface	[K]
T_E	temperature of the surrounding environment	[K]
α_P	moisture transfer coefficient	[kg/Ns]
α_T	heat transfer coefficient	[W/m^2K]
p_s	saturation pressure	[N/mm^2]
c	cement content	[kg/m^3]
w_1	water content at saturation, for T=20 °C	[kg/m^3]
h	relative pore humidity ($h=p/p_s$)	[kg/m^3]
c	cement content	[kg/m^3]
ρ_0	initial water density	[kg/m^3]
w_{d0}	initial water content	[kg/m^3]

n	porosity	[-]
v	specific volume	[m^3/kg]
α_c	thermal expansion coefficient for concrete	[1/K]
α	model constant (α = 0.05)	[-]
h_c	transition humidity (h_c=*0.75*)	[kg/m^3]
Q'	activation energy for the migration of the water molecules through a layer of adsorbed water	[J]
R	universal gas constant	[J/K]
T	absolute reference temperature	[K]
n	the amount of substance	[mol]

Thermo-hygro-mechanical coupling

θ	relative temperature (model specific)	[-]
E^{20}	E module at 20 °C	[N/mm^2]
$\omega_{t,E}$	temperature dependent damage parameter, E module	[-]
f_t	uniaxial (direct) tensile strength of concrete	[N/mm^2]
f_{st}	splitting tensile strength of concrete	[N/mm^2]
f_{bt}	bending strength of concrete	[N/mm^2]
f_t^{20}	uniaxial tensile strength at 20 °C	[N/mm^2]
$\omega_{t,ft}$	temperature dependent damage parameter, tensile strength	[-]
f_c^{20}	uniaxial compressive strength at 20 °C	[N/mm^2]
$\omega_{t,fc}$	temperature dependent damage parameter, compressive strength	[-]
G_F^{20}	fracture energy at 20 °C	[N/mm]
$\omega_{t,GF}$	temperature dependent damage parameter, fracture energy	[-]
f_y^{20}	uniaxial tensile strength at 20 °C	[N/mm^2]
$\omega_{t,fy}$	temperature dependent damage parameter, yield stress	[-]
E_s^{20}	steel E module at 20 °C	[N/mm^2]
ω_{Es}	temperature dependent damage parameter, E module of steel	[-]
δ_{ij}	Kronecker delta (operator)	[-]
A, B, C	model constants for the definition of LITS	[N/mm^2]
T_{max}	maximal reached temperature	[K]
$\boldsymbol{D}$	tangential material stiffness tensor (microplane model)	[N/mm^2]
$\dot{\varepsilon}^m$	mechanical strain increment	[s^{-1}]

$\dot{\sigma}^p$	stress increment due to pore pressure	[N/mm^{2}s]
K	bulk modulus (total volume including pores)	[N/mm^2]
$\dot{p}$	increment of pore pressure	[N/mm^{2}s]
ε_{11}	principal tensile strain	[-]
w_c	critical crack width for plain concrete	[mm]
ε_c	critical tensile strain (corresponds to crack width w_c)	[-]
a_w	damage dependent relative permeability	[m/s]
$a_{w=0}$	relative permeability at $w = 0$	[m/s]
β	factor in the direct time integration (ranges from 0 to 1)	[s^{-1}]

1. INTRODUCTION

1.1 Background, motivation and context of research

High performance concrete (HPC) has gained more popularity in the past decades owing to its strength, high elastic modulus and durability (Aitcin 2011; Shah & Ahmad 1994). It finds its usage mostly in tunnels, bridges, high-rise buildings, etc. However, multiple tragic tunnel fire accidents (Channel tunnel fire in 1996, Mont-Blanc tunnel fire in 1999, etc.) have emphasized the vulnerability of HPC to explosive spalling. Compact structure and low porosity of HPC significantly reduce the porosity and permeability to gases and liquids. Under normal circumstances, low permeability is associated with high durability, since the ingress of harmful gases and chemicals is retarded. However, in the case of fire, the dense microstructure obstructs the transport of water vapour and promotes the development of high pore pressures.

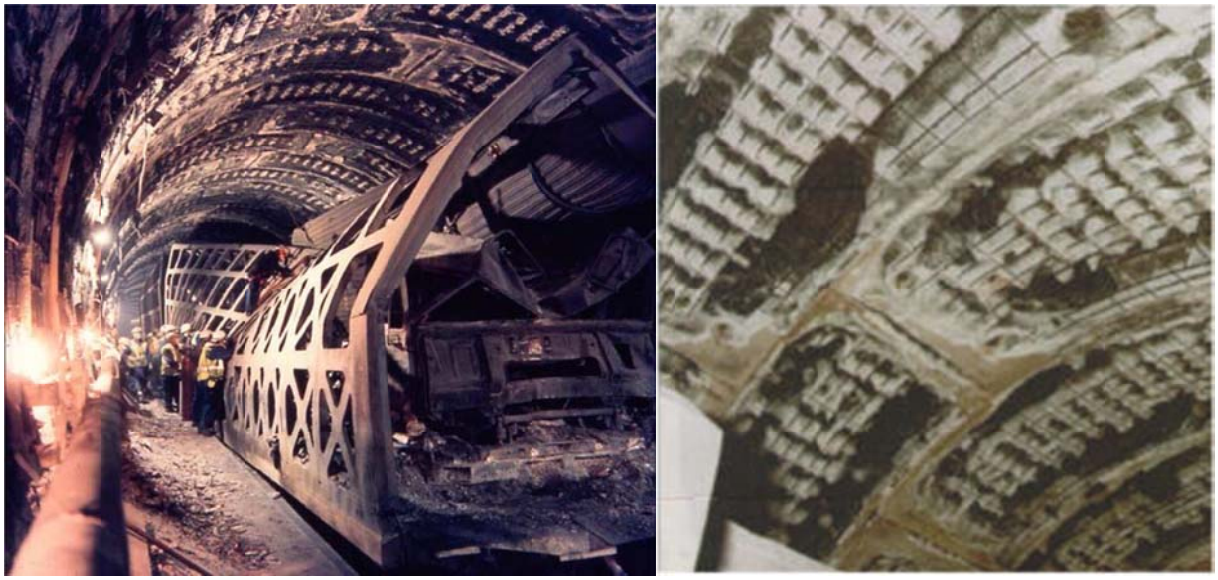

Figure 1.1. Channel fire (1999) resulting in explosive spalling

Non-combustible nature of concrete and its relatively low thermal conductivity render concrete desirable as a thermal barrier which prevents heat and fire spread. However, relatively low conductivity results in high thermal gradients, which invoke substantial compressive stresses close to the heated surface.

Combination of pore pressures and thermally induced stresses causes the concrete to fail abruptly with a sudden release of energy. This type of concrete failure, termed as explosive spalling, is characterized by bursting and forcible separation of thin layers of concrete, accompanied by a typically loud explosive noise. The failure is progressive in nature, which may lead exposure of reinforcement or prestressing cables to direct fire. Furthermore, it reduces concrete cross section and can thus lead to partial or complete collapse of the structure.

The main causes of explosive spalling are development of pore pressures and thermally induced stresses. Figure 1.2 depicts the mechanism of explosive spalling, which is now accepted by most of the researchers. When concrete is exposed to elevated temperature, capillary water vapour migrates towards the surface as well as into the core of the concrete element (Figure 1.2 a). Since the concrete core retains significantly lower temperatures compared to the surface, the water vapour migrating towards the core tends to condense (Figure 1.2 b), leading to the formation of impenetrable layer of condensate, so called "moisture clog" (Shorter & Harmathy 1965), as shown in Figure 1.2 c. Further transport of water vapour towards the core is prohibited by the impermeable layer, giving rise to high vapour pressures (Figure 1.2 d). Additionally, temperature gradients across the section and restraints result in development of thermal stresses in concrete layer close to the exposed surface (Figure 1.2 d). In this way a high amount of potential energy is accumulated in the near surface zone. Once the pore pressure reach a threshold value, this energy is violently released and concrete cover fails in an explosive manner (Figure 1.2 e).

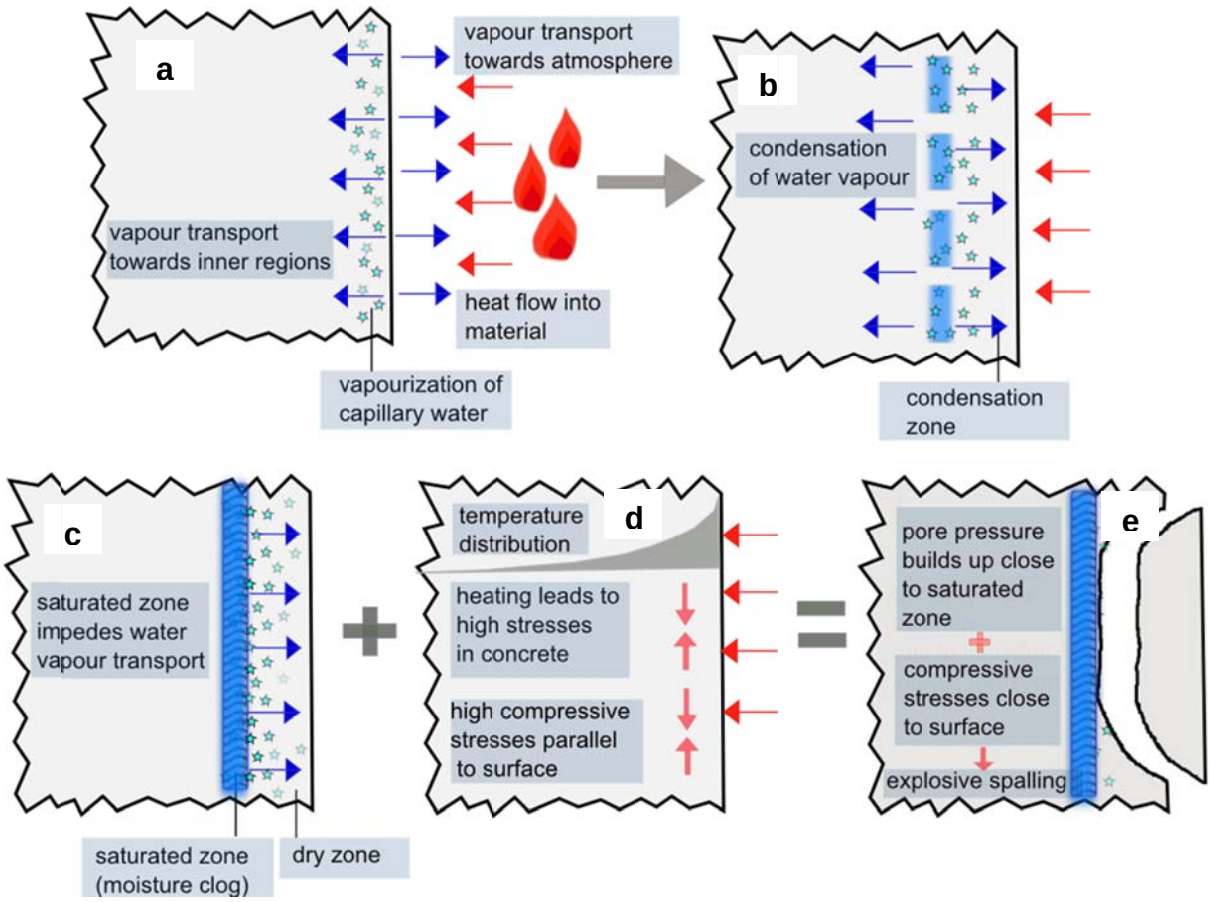

Figure 1.2. Mechanism of explosive spalling

Though the mechanisms behind explosive spalling are accepted by the vast majority of researchers, the influence of various parameters is not yet fully understood. The main reason for this lack of understanding comes from technical limitations in obtaining the experimental data at elevated temperatures.

The most efficient and popular method to mitigate explosive spalling is the addition of polypropylene (PP) fibres in concrete. According to experimental evidence, explosive spalling occurs typically at temperatures between 200 °C and 250 °C (Khoury & Anderberg 2000), while the PP fibres melt at approx. 160 °C to 170 °C. Empty or partially empty fibre beds together with the existing concrete capillary pores and microcracks form an interconnected porous network in concrete. The created network (i.e. increased permeability) provides free path for the water vapour to escape resulting in a relief of the pore pressure, and hence no or very limited spalling occurs. However, there are a few theories about the possible mechanism of the formation of porous network. Some researchers such as Kalifa et al. (2001) found that the melted PP fibres are absorbed by the cement matrix. On the other hand, Khoury (2008) suggests that the water vapour passes through the weakened interface between the fibre and concrete matrix. Furthermore, he postulates that the high viscosity of the PP fibres prevents their absorption into the concrete matrix. Considering the scarce experimental data for both theories, further experimental investigation is required to gain better insight into the mechanism of permeability increase due to presence of PP fibres.

In this work, an attempt is made to assess the performance of HPC without and with addition of PP fibres when subjected to fire loads, in general and the explosive spalling behaviour of the same in particular. It is well known from the literature that the permeability of concrete is the main physical property governing the explosive spalling. Most of the experiments on permeability measurements available in literature were performed either at room temperatures (virgin concrete) or in residual state, i.e. after cooling the specimens to room temperature. However, very limited information is available on the permeability of concrete at elevated temperature. It is, therefore, essential to perform the measurements and evaluate the permeability directly at elevated temperatures. In order to fill this gap, a new test setup for gas permeability measurements at elevated temperatures is developed and validated within the framework of this thesis. Using the test setup, the permeability measurements are carried out over a range of temperature and a special emphasis is placed on the temperature region in the proximity of the melting point of PP fibres (160 °C). The variation of permeability with temperature is reported for HPC without and with PP fibres (PP content 1 kg/m^3).

In order to gain more insight into the processes at microscopic level at the interface between concrete matrix and PP fibres at room temperatures and 200 °C, scanning electron microscope observations are made. Concrete samples are exposed to 200 °C for different periods of duration in order to evaluate the importance of time variable on melting of fibres.

Experiments under fire loads are performed on HPC slabs cast from the same batches of concrete used for permeability measurements (without and with PP fibres). Spalling behaviour of concrete without and with PP is investigated for two typical fire

scenarios (ISO 834 fire curve and modified tunnel curve ZTV-ING). Temperature profiles, extent and location of spalling as well as thermal cracking induced in the slabs are reported and discussed. The influence of PP fibres on mitigation of explosive spalling is clearly observed for both fire scenarios.

The whole experimental program resulted in a better understanding of the mechanisms behind explosive spalling and influence of PP fibres on the same. However, the extent of data that can be obtained experimentally is often very limited, owing to the technical difficulties in measurements at elevated temperatures. An experimental parametric study to understand the influence of various parameters is not economically and technically viable. The complete mechanisms of explosive spalling with specific influence of chosen parameters can only be obtained employing numerical methods.

In the past few decades, various researchers have undertaken significant effort to model and understand the phenomenon of explosive spalling numerically. The main advantage of this approach is that the influence of individual parameters can be studied and extensive parametric studies can be performed. However, it is essential that the model is general, reliable, robust and verified against experiments.

The numerical investigations performed so far were mainly based on thermo-hygro-mechanical models, these ranging from simple single phase models to very complex multiple phase models. The vast majority of the researchers followed the macroscopic modelling approach, i.e. concrete was modelled as a homogeneous material. Even though each of the aforementioned models was able to predict and clarify the mechanism of explosive spalling up to certain extent, neither of the existing models could fully capture the phenomenon of explosive spalling. For example, Periskic (2009) found a good agreement of the numerical results (single phase model) with experiments in terms of influence of relative humidity, permeability and humidity on explosive spalling. Similarly, the prediction of pore pressures obtained by Gawin et al. (2006) exhibited a very good agreement with the experimental measurements.

Large scatter observed in the experiments suggests that the macroscopic modelling approach is possibly inappropriate to model the complex phenomenon of explosive spalling, which is highly influenced by the local inhomogeneities. Based on this argument, in this work both macro- and meso-scale modelling approaches are followed and thoroughly investigated and compared. The numerical model used in this study is a single phase thermo-hygro-mechanical continuum model developed in the framework of irreversible thermodynamics (Periskic 2009). This model is an extension of the previously developed thermo-mechanical model that uses temperature dependent microplane model as the constitutive law for concrete, see Ozbolt et al. (2005). The transport of moisture and heat is adopted from Bazant & Kaplan (1996).

First, the thermo-mechanical model is validated against a number of experiments on plain and reinforced concrete with different geometries. The degradation of concrete properties with temperature (20 °C to 800 °C) is validated against experiments performed by Yaragal (2010) on plain concrete specimens such as beams and cylinders. Further, the load-displacement behaviour of reinforced concrete is analysed simulating the experiments on beams under three sided exposure to ISO 834 fire with subsequent loading till failure, as obtained from A. Kumar & V. Kumar (2003).

In the next phase, thermo-hygro-mechanical model is employed to investigate explosive spalling phenomenon. Two different modelling approaches were followed: (i) concrete modelled as a homogeneous macroscopic material and (ii) concrete modelled as a three-phase material at meso-scale level. The influence of permeability, relative humidity, external compressive load, heating rate, aggregate type is investigated at both macro- and meso-scale. Additionally, the influence of inhomogeneities such as different distribution of aggregates is considered at meso-scale.

In the numerical study of explosive spalling, it is attempted to principally simulate the majority of experimental aspects in terms of material properties, boundary conditions, loading conditions and fire scenarios. However, the inherent complexity of concrete as highly heterogeneous material as well as the complex nature of the experiment under fire load itself prohibits a one-to-one correspondence between experiment and numerical model. Nevertheless, the major aspects of explosive spalling such as time of spalling, pore and volumetric pressures, thermal stresses, temperature profiles, humidity distribution and local damage are successfully simulated and the results are found to be in good agreement with the performed experiments as well as the experiments available in the literature.

It is observed from the numerical study that the macroscopic modelling approach is suitable for the thermo-mechanical considerations such as structural response of a structural member or structure in fire. However, in order to successfully simulate the complex phenomenon of explosive spalling, meso-scale approach is essential. The results of simulations following meso-scale approach display high correspondence with experiments. Furthermore, with this approach various parameters and their influence on the overall behaviour of concrete could be investigated, thus overcoming the limitations of the experimental studies. A detailed parametric study following this approach is performed and the same has been reported herewith.

1.2 Objectives

The objectives of work presented in this thesis are to:

1. Validate the existing thermo-mechanical and thermo-hygro-mechanical model against the experiments

2. Numerically investigate the phenomenon of explosive spalling employing the thermo-hygro-mechanical model through series of parametric studies

3. Compare the macro-scale and meso-scale modelling approach

4. Provide more insight into the mechanism behind explosive spalling as well as to investigate the effect of PP fibres on explosive spalling

5. Perform experimental investigation on high performance concrete without and with PP fibres

6. Develop and validate a new test setup to estimate intrinsic permeability of concrete at elevated temperatures

7. Investigate the effect of elevated temperatures on the intrinsic permeability of high performance concrete without and with PP fibres

8. Suggest provisions for a better durability performance of concrete, with accent on high performance concrete

1.3 Scope of work

The scope of this work mainly revolves around the phenomenon of explosive spalling employing numerical methods augmented by experiments. The study is aimed at understanding and numerical modelling of all the aspects related to explosive spalling. Experimental part of the work is divided in fire experiments, permeability measurements at elevated temperatures and compression tests on heated concrete specimens, all aimed at providing a better insight into the mechanism of explosive spalling of high performance and high strength concrete. The numerical analyses are performed to validate the applicability of the existing thermo-hygro-mechanical model for concrete at high temperatures as well as to complete the existing experimental data. The research is aimed neither at experimental optimization of the concrete mix with respect to fibre properties nor content, since this topic has been widely investigated in the literature, see for example Hager & Tracz (2010) and Suhaendi & Horiguchi (2006). Reproduction of experiments widely available in literature is also excluded from this work and only essential experiments are performed.

2. LITERATURE REVIEW

2.1 Concrete at elevated temperatures

Concrete is the most widely used building material, with 90 % of total world structures built using it. Even though the performance of concrete in fire is relatively favourable in comparison with other building materials, exposure to elevated temperatures results in degradation of concrete with respect to its mechanical and physical properties. Concrete is a composite comprising cement mortar, aggregates and interfacial transition zone, each of them exhibiting different properties and response to thermal exposure. High thermal gradients give rise to high stresses across the concrete cross section due to the restraining effect. Relaxation and creep can, under certain circumstances, become important factors in the behaviour of concrete at elevated temperatures.

Concrete mechanical and transport properties are very dependent on moisture content and porosity. The presence of water, especially free, evaporable water stored in the capillary pores, influences behaviour due to the phase change from liquid (water) to gas (vapour) at 105 °C. Furthermore, concrete possesses a very complex porous system which is subject to change when concrete is heated. The weight loss of a normal and a high strength concrete with increasing temperature obtained by Noumowe et al. (1996b) is shown in Figure 2.1 (left). Between 120 °C and 350 °C the mass loss is associated with the dehydration of the C-S-H gel. Cement gel itself undergoes a phase change when portlandite decomposes (450-550 °C) and when C-S-H phase decomposes at around 600-700 °C. Overall increase in porosity due to exposure to high temperature is reported by Noumowe et al. (1996b), see Figure 2.1 (right). A typical distribution of pore sizes of high strength concrete is shown in Figure 2.2. The porous system changes as early as only 70 °C, whereby the total porosity, as well as the average pore radius, increases.

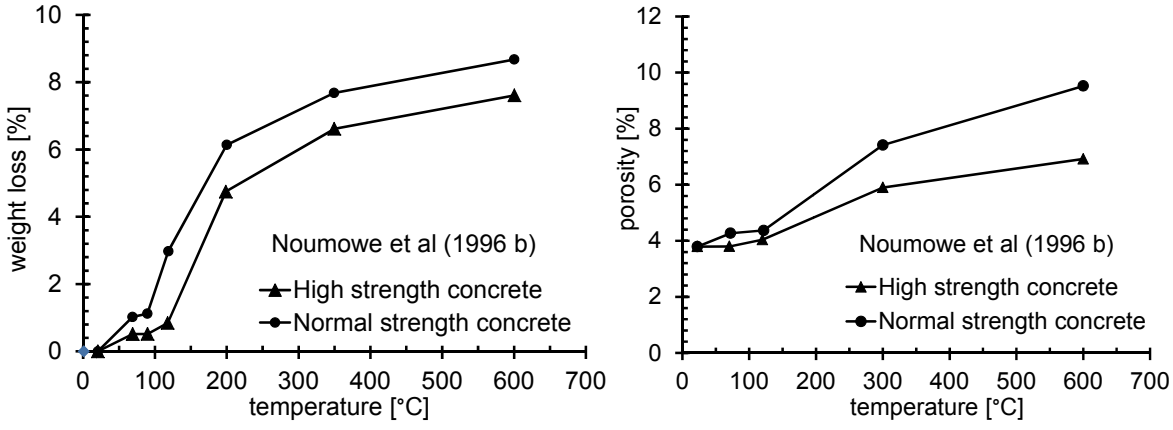

Figure 2.1. Weight loss (left) and porosity increase (right) with increasing temperature

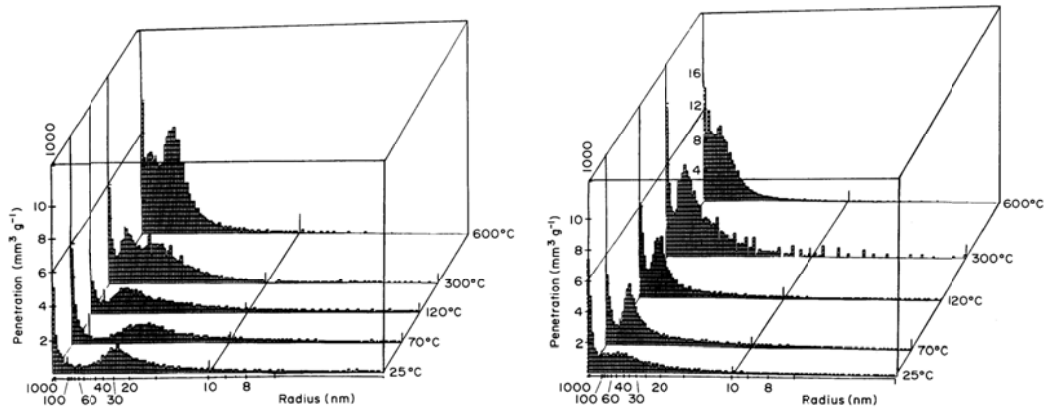

Figure 2.2. Pore radius distribution for normal strength concrete (left) and high strength concrete (right) – Noumowe et al (1996 b)

The mismatch in the thermal dilatation of the concrete constituents at elevated temperatures leads to incompatibility and, consequently, damage. An overview of thermal strains for cement gel and different aggregates is provided in Figure 2.3 (left). Rock materials (aggregates) expand when heated, whereas cement gel starts to contract at temperatures beyond 150 °C. Furthermore, some of the aggregates used in concrete are highly unstable when heated (such as flint), others change phase at a certain temperature (phase change of quartz at 573 °C). The influence of different aggregate types on thermal strain of concrete as composite is provided in Figure 2.3 (right).

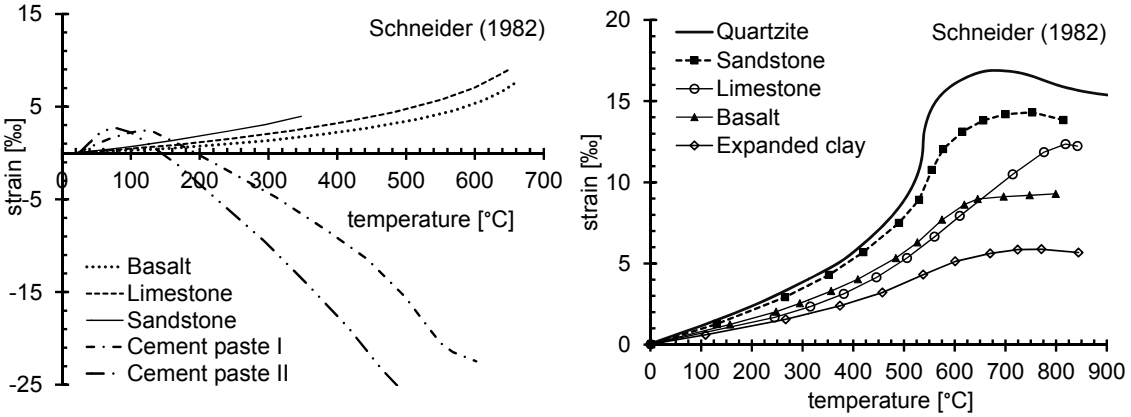

Figure 2.3. Thermal expansion: concrete constituents (left), concrete made of different aggregates

The combination of the mentioned processes and phase changes result in degradation of both mechanical and physical properties of concrete upon exposure to elevated temperatures. An overview of the effect of elevated temperature on relevant concrete properties is presented in the following sections.

2.2 Physical properties of concrete at elevated temperatures

2.2.1 Density

Among others, Schneider (1982), Harmathy & Allen (1973) and Hildenbrand & Peehs (1978) investigated the effect of temperature on density of calcareous and siliceous concrete. Experimentally obtained data are plotted in Figure 2.4 (left). Due to the evaporation of water, the density is a function of moisture content for temperatures up to 150 °C. In the region between 150 °C and 600 °C there is only a minor reduction in density for calcareous concrete. Limestone decarbonation (between 600 °C and 900 °C) governs the sudden decrease in density in this region. At 800 °C calcareous concrete retains only 60 % of the initial density. After the sintering process and subsequent melting of concrete, the density is expected to increase (Schneider 1982).

Siliceous concrete experienced somewhat higher loss of density in the region up to 700 °C as compared to calcareous concrete. Schneider (1982) attributed this to the high thermal dilatation of the quartzite aggregates. In general, the nature of aggregates defines the thermal expansion of concrete and thus controls the density, i.e. aggregates with low thermal expansion (such as basalt) retain higher density than aggregates with high thermal expansion.

2.2.2 Heat capacity

Heat capacity is defined as the heat required to raise the temperature of a material by a unit temperature. Moisture content in concrete influences heat capacity for temperatures below 200 °C, due to the increased energy required for the phase change from liquid to gas. The results of the heat capacity measurements are presented in Figure 2.4 (right). Aggregate type does not seem to have any significant impact on specific heat of concrete. DIN EN 1-2 (2004) provision for heat capacity at different temperatures is also plotted in Figure 2.4 (right) for comparison.

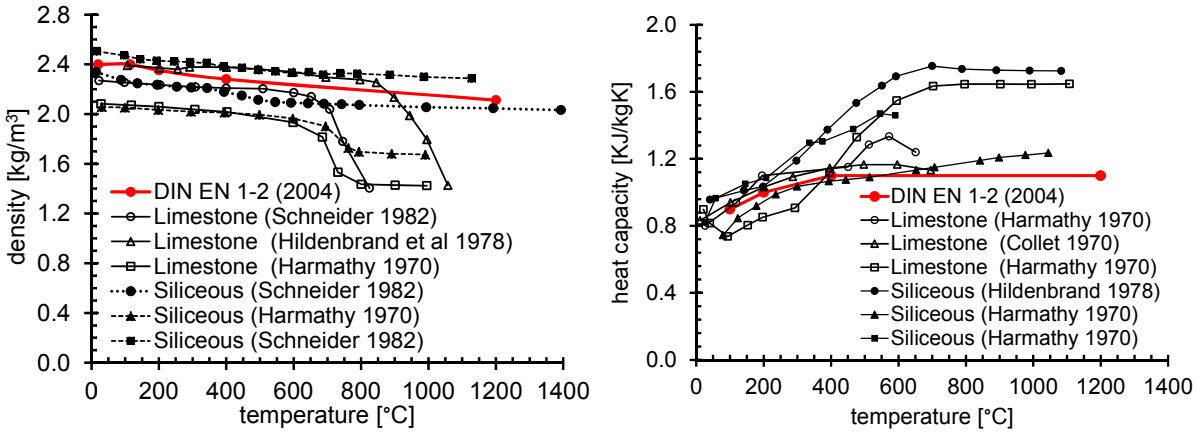

Figure 2.4. Influence of temperature on density of concrete (left) and on specific heat of concrete (right)

2.2.3 Thermal conductivity

Given two surfaces on either side of a material with a temperature difference between them, the thermal conductivity is defined as the heat energy transferred per unit time and per unit surface area, divided by the temperature difference. Thermal conductivity of concrete reduces significantly with temperature, as can be observed in Figure 2.5. It is mainly influenced by the moisture content and aggregate type, as observed by Schneider (1982). DIN EN 1-2 (2004) recommendations for thermal conductivity at different temperatures are also plotted in Figure 2.5 for comparison.

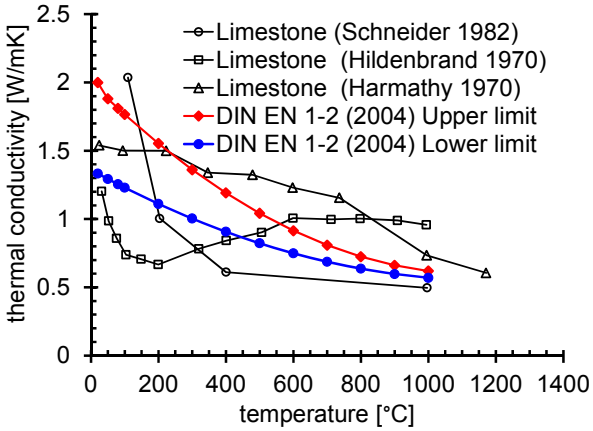

Figure 2.5. Influence of temperature on thermal conductivity of concrete

2.2.4 Permeability

Permeability is defined as the ability of a material to resist ingress of gases and liquids. It depends on the porosity of the material as well as on the connectivity of the pores. Permeability can be expressed in two different units, namely m^2 and m/s, whereby the latter is sometimes referred to as hydraulic conductivity. The conversion of units is as follows (Hilsdorf & Kropp 1995):

$$a[\mathrm{m}^2] = \frac{\rho g}{\mu} a[\mathrm{m/s}] \qquad (2.1)$$

where a = permeability, g = gravitational constant, ρ = density and μ = dynamic viscosity of the fluid.

An overview of some of the data from the literature is provided in Figure 2.6. The results obtained by Schneider (2010) on high performance concrete (compressive strength 95 N/mm^2) at elevated temperatures were performed on concrete without prior drying, which is visible in the sudden permeability increase close to the boiling point of water. The evaporation of free water leaves empty pores behind, thus increasing permeability. Beyond this point, the change of porous system is considered to govern the behaviour, as observed by Gallé & Sercombe (2001).

Kalifa et al. (2001), Zeiml et al. (2008) and Gallé & Sercombe (2001) measured permeability of high strength concrete specimens previously dried at 105 °C. Unlike Schneider, who performed measurements directly at elevated temperatures, most of the researchers measured residual permeability, i.e. after reaching the target temperature the specimens were cooled to room temperature before permeability measurement. Kalifa et al. (2001) concluded that the permeability increase up to temperatures of approx. 300 °C is driven by loss of evaporable water and changes in the porous system. Beyond this point the micro-cracking due to incompatibility of concrete phases is considered to govern the permeability increase.

In general, experimental data on permeability exhibit certain scatter, partially due to the differences in measurement methods and the choice of permeating fluid (Loosveldt et al. 2002). This is evident by comparing absolute values for permeability (Figure 2.6 right). However, all data point out the trend of increasing permeability with rising temperature.

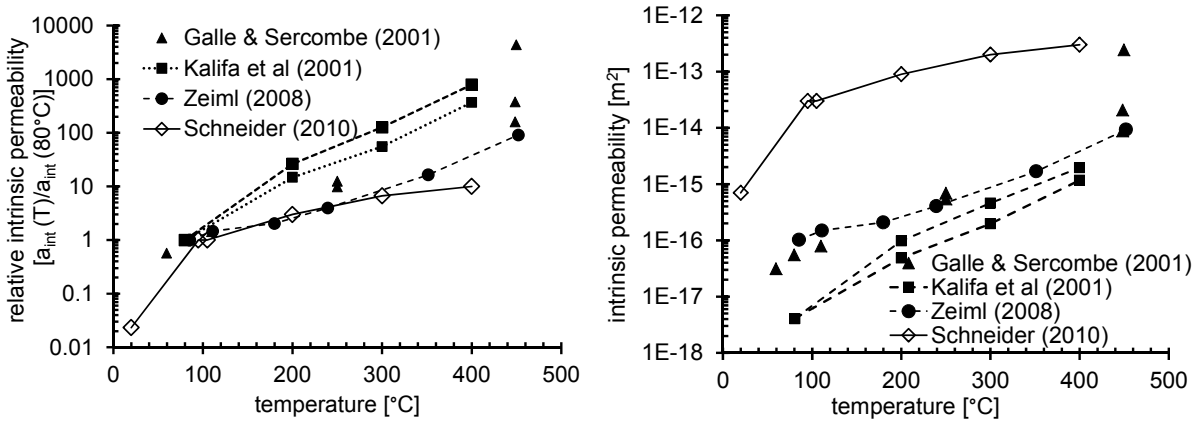

Figure 2.6. Influence of temperature on permeability of concrete

2.3 Mechanical properties of concrete at elevated temperatures

2.3.1 Compressive strength

Schneider (1982) investigated degradation of compressive strength of normal strength concrete with different aggregate types, see Figure 2.7 (left). Up to 300 °C compressive strength of normal strength concrete appears unaffected by temperature, mainly owing to the increased hydration of cement. Furthermore, due to the thermal strain the frictional and aggregate locking phenomena are more pronounced than for the concrete at normal temperature. At higher temperatures micro-cracks, vaporization and decomposition of cement paste and aggregate result in an almost linear reduction of compressive strength.

Phan & Carino (2003) summarized results of a number of researchers on compressive strength measurements after exposure to elevated temperatures, see Figure 2.7

(right). In spite of the obvious scatter in case of high strength concrete, the experimental data indicate that high strength concrete is more sensitive to temperatures up to 300 °C than normal strength concrete. At temperatures beyond 1000 °C both normal and high strength concrete completely lose compressive strength.

Hager & Pimienta (2004a) performed compression tests on concrete with different water-cement ratios (0.3, 0.4 and 0.5) and concluded that the degradation of compressive strength is almost insensitive to water-cement ratio. The same authors further investigated the effect of polypropylene fibres on compressive strength of high performance concrete. The results indicate that the presence of fibres in quantities 0.9 and 1.75 kg/m^3 does not significantly influence the behaviour of concrete in compression, except for the somewhat higher strength of concrete with PP fibres at 250 °C. This is attributed to the increased permeability due to presence of fibres, which facilitates the evaporation of water.

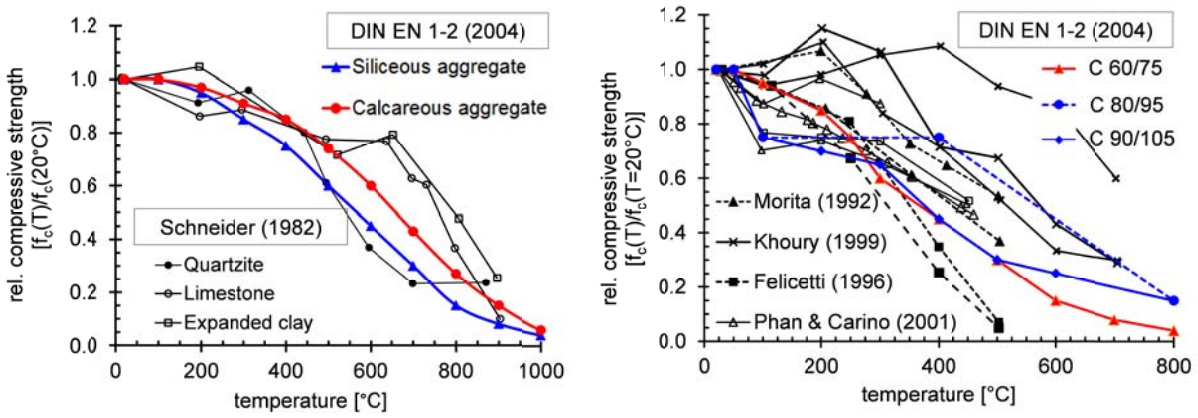

Figure 2.7. Influence of temperature on compressive strength of concrete: normal strength concrete (left) and high strength concrete (right)

2.3.2 Young's modulus

Experiments performed by Schneider (1982) are presented in Figure 2.8 (left). The results show a degradation of Young's modulus with increasing temperature with a pronounced influence of aggregate type.

Zhang & Bicanic (2002) stated that the degradation of Young's modulus up to 300 °C can mainly be attributed to the loss of evaporable water, whereas further degradation is caused by the decomposition of the individual concrete constituents.

Hager & Pimienta (2004b) investigated the effect of polypropylene fibres on Young's modulus of high performance concrete. The results shown in Figure 2.8 (right) indicate that the presence of fibres in quantities 0.9 and 1.75 kg/m³ systematically reduces Young's modulus, maximum reduction was 17 %.

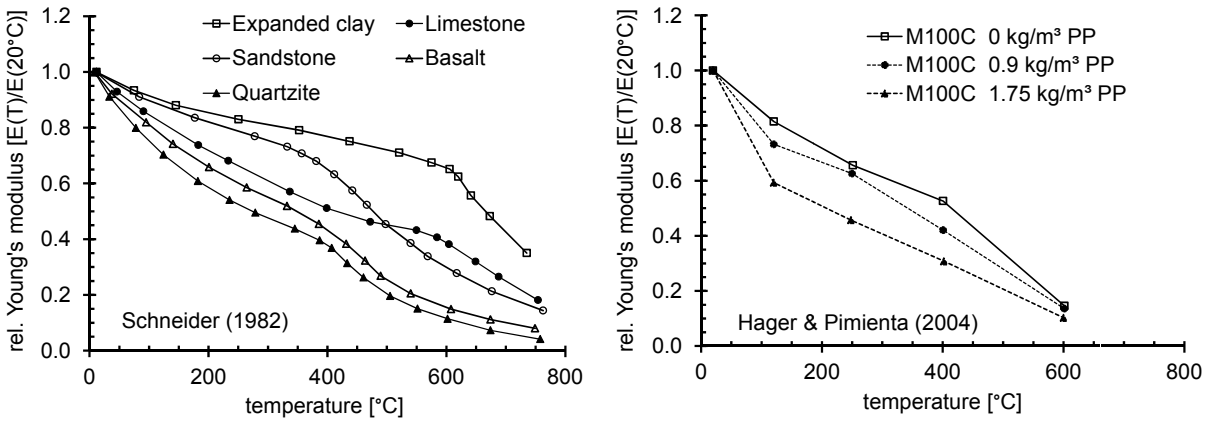

Figure 2.8. Influence of temperature on Young's modulus of normal strength concrete (left) and of high strength concrete without and with PP fibres (right)

2.3.3 Tensile strength

Bazant & Kaplan (1996) performed splitting tests on normal strength concrete at elevated temperatures, and Noumowe et al. (1996a) investigated uniaxial tensile strength of high strength concrete (compressive strength 61 N/mm^2). Relative reduction of tensile strength with increasing temperature is plotted in Figure 2.9. In comparison with other mechanical properties, tensile strength degrades much faster with increasing temperature. The limited experimental data indicate that tensile strength of normal strength concrete is strongly influenced by the aggregate type. The degradation of tensile strength is enhanced by a pronounced mismatch of aggregates and concrete matrix, and at 400 °C concrete exhibits only ca. 30 % of the initial tensile strength. At temperatures above 600 °C both normal and high strength concrete exhibit almost no tensile strength. Felicetti et al. (2000) performed direct tension tests on high strength concrete (compressive strength 90 N/mm^2) in hot state as well as after subsequent cooling to room temperature (residual strength), and observed that cooling does not influence tensile strength, i.e. hot and residual tensile strength are almost the same.

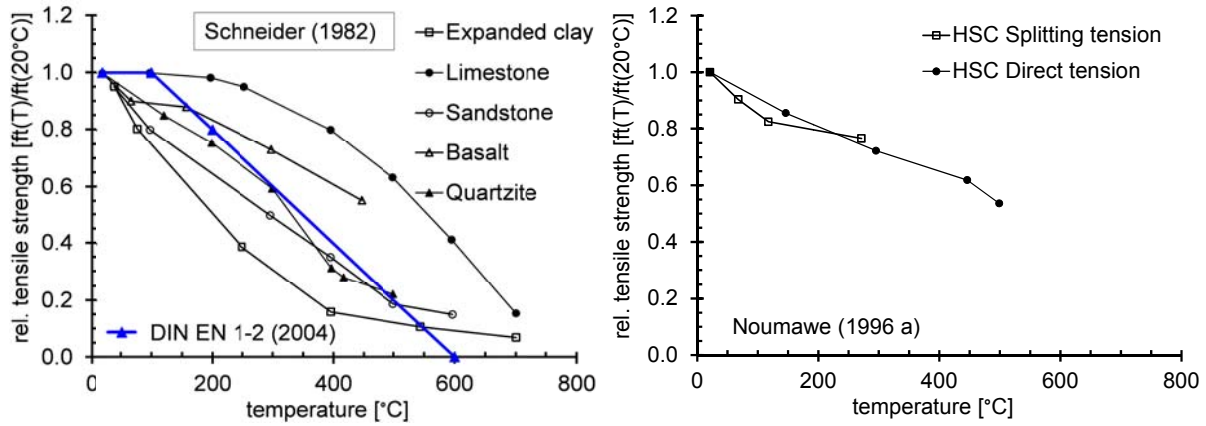

Figure 2.9. Influence of temperature on tensile strength of normal (left) and high strength concrete (right)

2.3.4 Fracture energy

Schneider (1982) measured stress-strain curves for concrete in compression at room and elevated temperatures. The results are presented in Figure 2.10 (left). With increasing temperature, both strength and Young's modulus decrease. However, concrete becomes more ductile at higher temperatures, i.e. fracture energy does not follow the degradation of other mechanical properties.

Zhang & Bicanic (2002) measured fracture energy of concrete at elevated temperature (Figure 2.10 right). Increase in fracture energy for temperatures up to 300 °C is attributed to the rehydration of cement as well as to the increased friction between coarse aggregates and concrete matrix. Beyond this temperature, micro-cracking mainly governs the behaviour, thus causing fracture energy to decrease to the initial value at 600 °C.

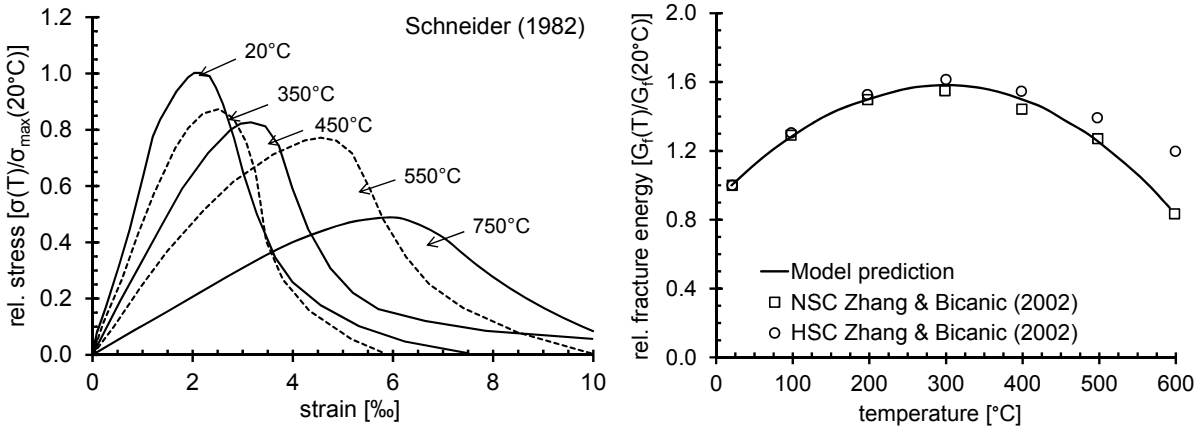

Figure 2.10. Stress-strain curves for concrete at different temperatures (left) and influence of temperature on fracture energy of concrete (right)

2.4 Thermal dilatation of concrete

2.4.1 Free thermal strain

It is shown earlier that concrete expands when exposed to elevated temperatures in non-loaded state. These strains are denoted as free thermal strains. Measurements performed by Schneider (1982) are shown in Figure 2.11 (left). The type of aggregates has the governing influence on thermal dilatation of non-loaded concrete due to its high volumetric ratio in concrete.

Hager (2004) investigated the behaviour of high strength concrete upon cooling from 400 °C and from 600 °C back to room temperature. The results are shown in Figure 2.11 (right). It can be observed that most of the thermal strains are recovered if the maximum exposure temperature is relatively low. However, when cooling after exposure to 600 °C, the largest part of thermal strain cannot be recovered. This is at-

tributed to the high level of thermal damage caused by the mismatch of concrete matrix and aggregates which increases for higher temperatures.

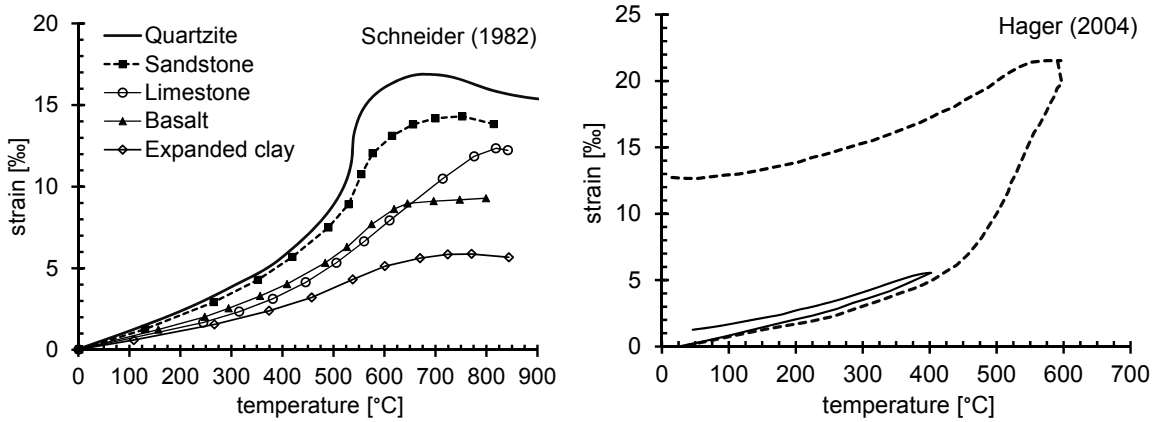

Figure 2.11. Free thermal strain of concrete containing different aggregate types (left); free thermal strain and residual strain of high strength concrete (right)

2.4.2 Load induced thermal strain

When concrete is loaded in compression and subsequently heated, the thermal dilatation significantly changes depending on the load (stress) level. This effect was termed load induced thermal strain and it was first observed by Anderberg & Thelandersson (1976). The results of their measurements performed on concrete cylinders (diameter = 75 mm, height = 150 mm) are presented in Figure 2.12 (left).

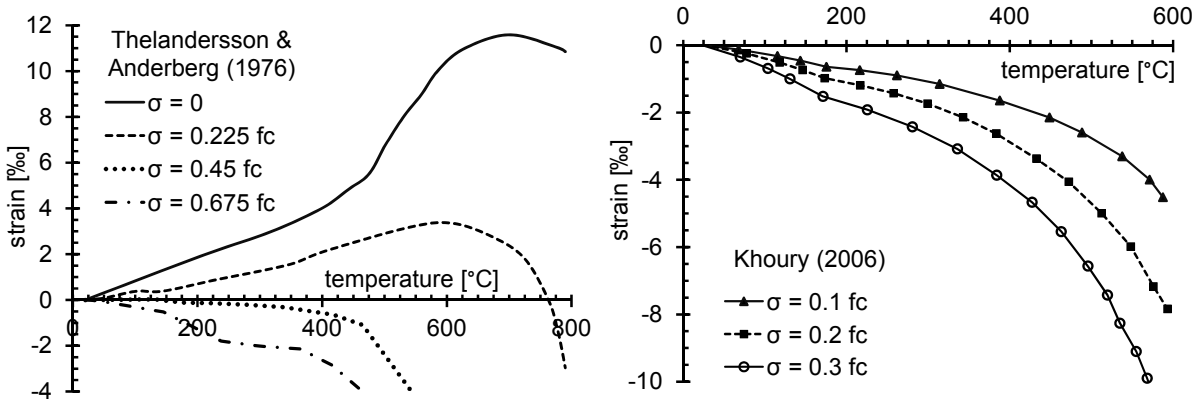

Figure 2.12. Thermal strain of concrete without and with prestressing (left); master LITS curve (right)

At low load levels (below 20 % f_c) concrete expands, however, the level of expansion is significantly reduced as compared to the free thermal strain. At higher load levels (above 40 % f_c), concrete does not expand at all, rather it contracts, and fails at temperature of only 500 °C. Khoury (2006) observed that LITS occurs only during first heating, it is irreversible upon cooling. Furthermore, he found that LITS is independent of the aggregate type and cement type and postulated that this effect is mainly

due to the CSH phase change in the cement gel. Up to loads of approx. σ = 0.30 f_c the strains are almost proportional to the load applied. By plotting the difference between free thermal strain and strain under different load levels, he obtained a “master LITS curve”, as shown in Figure 2.12 (right). He also reported that the effect of LITS is observed for both normal and high strength concrete.

Hager (2004) investigated the effect of heating rate on thermal strain of high strength concrete, see Figure 2.13 (left). Heating of 1 °C/min and 5 °C/min produced significant differences for all three investigated loading scenarios. When heating rate increases, thermal gradients become more pronounced. Surface heats very fast, whereas inner regions of the specimen retain lower temperatures. Consequently, the thermal strains are not fully developed at higher heating rate.

Results published by Hager (2004) and more recently by Mindeguia et al. (2013) suggest that LITS effect can be divided in two main parts: (i) up to temperature of approximately 400 °C LITS seems to originate from the drying and dehydration of heated concrete and (ii) beyond 400 °C LITS is mainly driven by the micro-cracking resulting from incompatibility of the concrete constituents.

Furthermore, the same authors investigated the behaviour of cement paste without and with preloading. The results (Figure 2.13 right) demonstrate the contribution of cement paste drying to the load induced thermal strain. Up to approximately 200 °C cement paste loaded to σ = 0.20 f_c exhibits significantly lower strain than cement paste without prior loading. At these temperatures, LITS can mainly be attributed to the processes in cement paste itself. However, beyond 170 °C load induced thermal strain of cement paste is almost parallel to free thermal strain.

Mindeguia et al. (2013) performed similar experiments under tensile load, however, they did not observe any load induced strain, and concluded that the effect is limited to compressive behaviour.

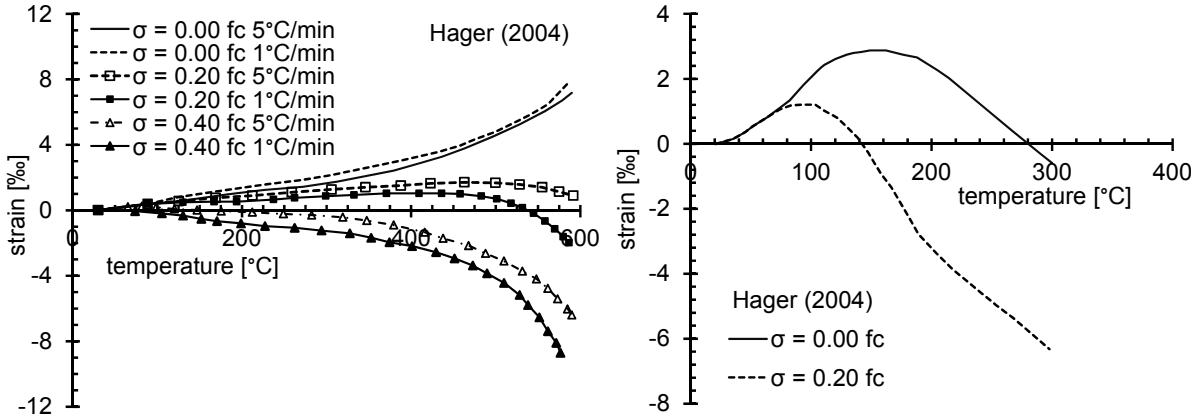

Figure 2.13. Effect of heating rate on free thermal strain and LITS (left); thermal strain of cement paste without and with prestressing (right)

2.5 Explosive spalling of concrete

2.5.1 General

When exposed to elevated temperatures or fire, concrete can become vulnerable to explosive spalling. It is characterized by forcible separation of concrete pieces and it can lead to an extensive reduction of concrete cross section and direct exposure of the reinforcement to fire. Since it generally occurs in early stages of fire, approximately in the first 30 minutes, the load-carrying capacity and the stability of the concrete or reinforced concrete structure can be endangered even before any fire regulation and extinguishing measures are undertaken.

Explosive spalling is observed in different kinds of structures, ranging from buildings to tunnels. Many tragic tunnel accidents such as Great belt fire (1994), Channel fire (1996) and Mont-Blanc fire (1999) emphasized the importance of understanding and preventing this phenomenon.

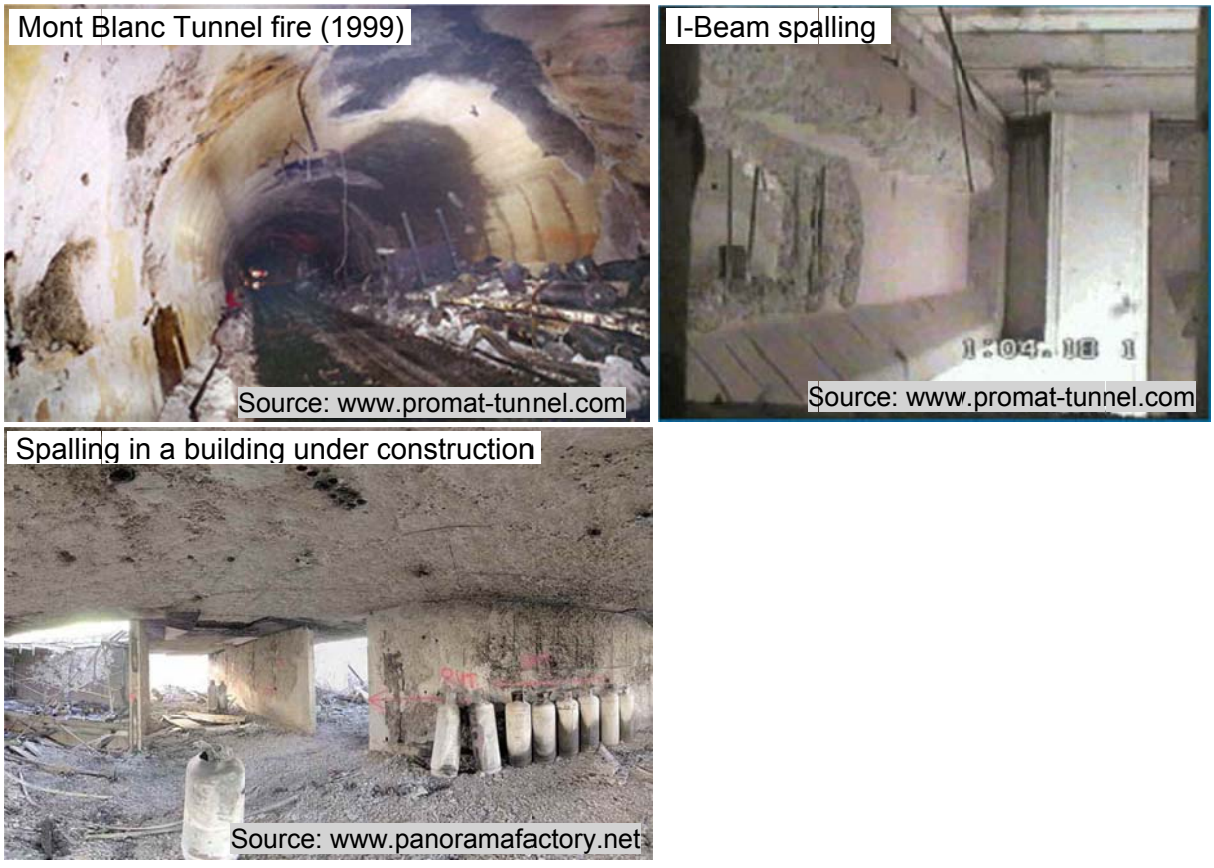

Figure 2.14. Damage caused by explosive spalling

High strength concrete (HSC) and high performance concrete (HPC) have become increasingly popular in the past decades. Even though their high strength and durability are highy desirable when considering mechanical properties and resistance against ingress of harmful fluids, these exact properties render them more suscepti-

ble to explosive spalling. The dense structure of these concretes cannot accommodate the water vapour created upon heating. Consequently, pore pressure rises and the probability of explosive spalling increases. Since the future of concrete is directed towards higher performance and durability, it is essential to deal with the problem of explosive spalling.

In the past decades a lot of research work has been undertaken to provide more insight into the processes preceding spalling and the main influencing parameters. Many codes and design guides worldwide such as CEB-FIP-bulletin-46 (2008) have recognized the need to provide protection against spalling. These provisions are, however, mainly oriented towards passive protection. Typical measures are thermal insulation, which reduces surface temperatures, and limitation of moisture content (typically maximum moisture content is defined as 3 % mass content). The most popular passive measure of prevention is addition of polypropylene (PP) fibres which facilitate the transport of water and water vapour by creating additional channels upon melting.

Spalling in general involves different kinds of forcible separation of concrete pieces and can be categorized in four types, according to Gary (1916):

a) aggregate spalling (popping sound)
b) corner spalling (not violent)
c) surface spalling (violent - cracking sound)
d) explosive spalling (violent - loud bang)

Aggregate spalling is associated with bursting or splitting of aggregates at the concrete surface. (Gary 1916) attributed it to mineralogical characteristics of the aggregates, whereas Austin et al. (1992) considered it to be a type of thermal shock. Typical aggregate spalling is shown in Figure 2.15 and it is evident that, due to its limited size, it does not compromise the structural function of the concrete element.

Corner spalling is non-violent mode of spalling and it is characterized by separation of concrete corners. Typically it occurs in the later stages of fire, unlike other types of spalling. It is mainly attributed to loss of tensile strength due to a prolonged exposure to elevated temperatures (Connolly 1995). An effective preventive measure is provision of supplementary reinforcing mesh within the depth of concrete cover.

Surface spalling is a violent failure of smaller surface pieces accompanied by a typical cracking sound. Due to its progressive nature it can influence the resistance of concrete to fire.

Explosive spalling is the most dangerous form of spalling. Gary (1916) reported concrete pieces of various sizes (up to 1 m^2) to be forcibly separated from the concrete element, whereby a very high amount of energy is released. According to him, the

main difference to surface spalling is its magnitude (intensity); he reported pieces being expelled up to 12 m from the heated surface. In its nature explosive spalling is completely stochastic and can be categorized as a local failure mode. This type of spalling has mostly been the topic of investigation regarding spalling, since it is the most dangerous form which can lead to a complete collapse of the structure. This work is also mainly directed towards investigation of explosive spalling.

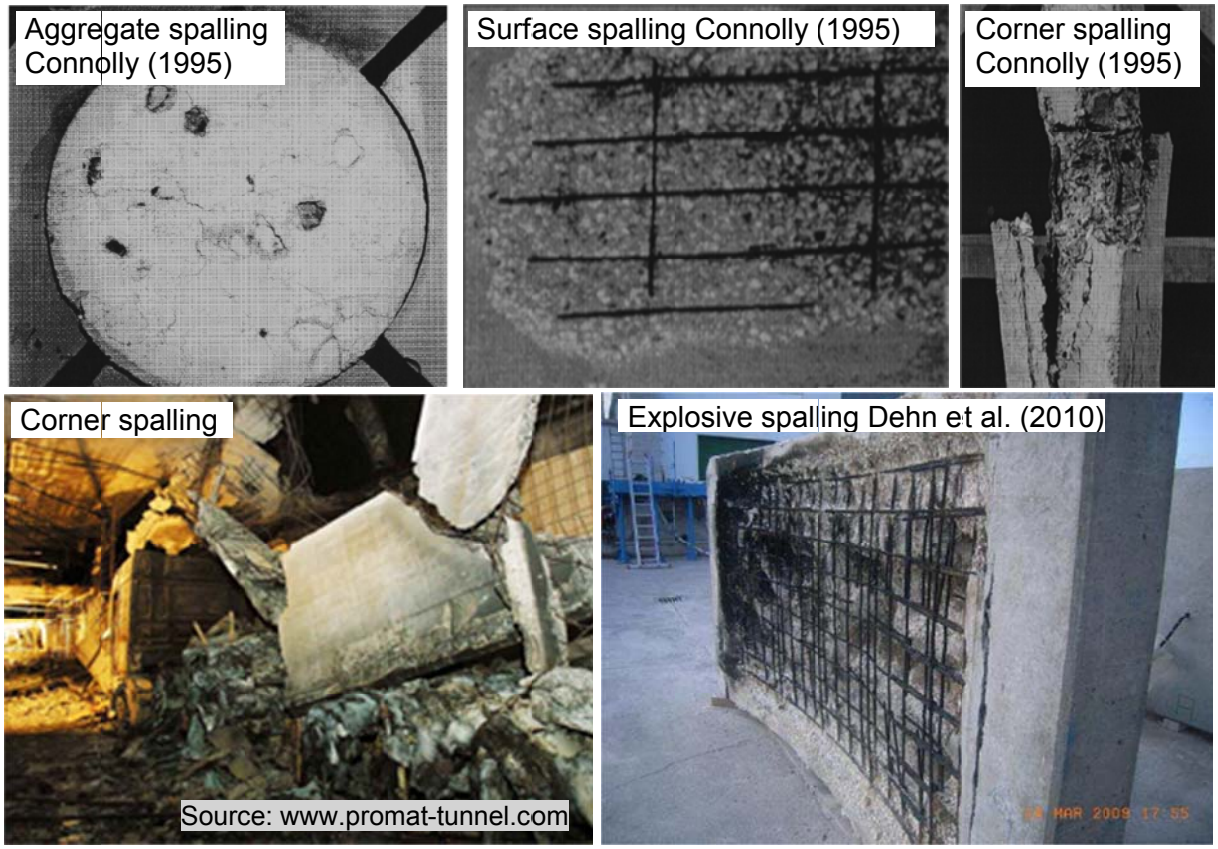

Figure 2.15. Different forms of spalling

2.5.2 Factors influencing explosive spalling

Many experimental studies were aimed towards investigation of different influencing factors on the sensitivity of concrete to explosive spalling. Due to the complexity of the phenomenon and its random and local character, a variety of influences have been tested. The data available up to date are summarized in following sections.

2.5.2.1 Heating rate

The rate of heating governs the thermal gradients and maximum temperature reached in concrete. Furthermore, the rate at which water evaporates is also controlled by heating rate. Since thermally induced stresses and pore pressures are considered to be the main driving forces behind spalling, it is reasonable to expect a pronounced effect of heating rate on explosive spalling. Most of the experimental data available in the literature confirm this. Some authors did not observe spalling even

at very high heating rates, such as Shirley et al. (1988); however, this is attributed to the small thickness (900 x 900 x 104 mm) of the concrete specimens used in these studies. Ali et al. (2011) compared the performance of normal strength concrete slabs (compressive strength 42 N/mm^2) under ISO 834 and ZTV-ING fire and observed explosive spalling after 16 min and 2.5 min, respectively. Jumppanen (1989) heated high strength concrete slabs (compressive strength ranged from 50 to 110 N/mm^2) with dimensions 100 x 100 x 400 mm at 20 °C/min and 32 °C/min under load and observed extensive spalling. Connolly (1995) also observed that the likelihood of spalling increases for higher heating rate. Tests were performed on concrete cylinders (diameter = 100 mm, height = 150 mm) with compressive strength of ca. 45 N/mm^2. In his tests heating rate ranged from 80 kW/m^2 to 140 kW/m^2.

Experimental data lead to the conclusion that heating rate plays a very important role with respect to explosive spalling of concrete. It controls the development of the two most important quantities, thermally induced stresses and pore pressure.

2.5.2.2 Moisture content – relative humidity

Moisture content is usually expressed as the mass percentage of water with respect to the mass of dry specimen. It can also be expressed in terms of relative humidity, which is defined as the ratio of pore pressure to saturation pressure. In case of concrete without admixtures and additives the relation between the two can be found in the literature depending mainly on the water-cement ratio of the concrete, see for example Hansen (1986) and Nielsen (2007). However, in case of concretes with fine particle admixtures this ratio can vary substantially, depending on the amount and type of admixtures and additives, as is observed comparing the available experimental data, e.g. Norling Mjörnell (1997), Baroghel-Bouny (2007), Canut & Geiker (2011). This effect is caused by the changes in porous system, i.e. reduced porosity and permeability associated with the use of fine particle admixtures. It is, therefore, more suitable to express moisture content in terms of pore saturation (relative humidity).

Moisture content defines the amount of evaporable water and is therefore expected to have a significant influence on the generation of pore pressure, provided sufficient thickness of the section. Meyer-Ottens (1972) investigated a wide range of moisture content and concluded that explosive spalling does not occur for moisture mass content less than 3 %. These findings mainly influenced the code provision of maximum recommendable moisture content. Copier (1979) found that moisture content is the most important material parameter governing the likelihood of explosive spalling. Connolly (1995) investigated concrete pre-dried at 105 °C and found that it does not spall at all, whereas concretes with moisture content 4-9 % experienced explosive spalling. This finding is of special importance, since it highlights the contribution of pore pressures to explosive spalling and excludes thermally induced stresses as the only source of explosive spalling.

Even though the provision of 3 % moisture mass content is applicable to traditional concrete, it was shown by Jumppanen (1989) that this limit is not applicable to dense ultra-high strength concrete, which can spall explosively at even much lower moisture content (2.3-3.0 %). For this reason, the limitation of water content is better expressed in terms of relative humidity, i.e. pore saturation.

Experimental data lead to the conclusion that the increased moisture content enhances explosive spalling of concrete, whereas dry concrete does not experience explosive spalling at all.

2.5.2.3 Permeability

Permeability governs the ability of concrete to resist ingress of liquids and gases. Analogously, it also governs the rate at which water and water vapour can be transported thought concrete, and directly influences the generation of pore pressures. Low permeability impedes transport of water vapour and result in a faster build-up of pore pressures. Jumppanen (1989) and Sanjayan & Stocks (1993) observed that normal strength concrete is less susceptible to explosive spalling than high strength concrete. With increased use of high performance concrete the contribution of permeability gained more attention, since such concrete generally exhibits low permeability.

Furthermore, the beneficial effect of PP fibres, which are found to mitigate spalling, is attributed to their ability to increase the permeability of concrete at elevated temperature. Hence, permeability is considered to be the most important material property governing the likelihood of explosive spalling.

2.5.2.4 Compressive stress and restraint

Meyer-Ottens (1972) performed experiments on concrete specimens with compressive strength of 45 N/mm^2, and found that presence of additional compressive stresses enhances spalling. Furthermore, he related the effect of stresses with section size, as can be seen in Figure 2.16 (left). The diagram does not account for spalling of very thin specimens in which case moisture can evaporate through the side opposite to heated side of the specimen. Furthermore, he investigated the effect of load on concretes with different moisture contents and concluded that load higher than 2 N/mm^2 and moisture mass content higher than 3.3 % increase the probability of explosive spalling. Similar trends are obtained by Sertmehmetoglu (1977) and Christiaanse et al. (1972), see Figure 2.16 (left) and (right), respectively.

Connolly (1995) confirmed that increased level of compressive load, either by imposed loads or restraints, enhances explosive spalling of concrete. The detrimental effect of load and restraint is explained primarily by the increase in compressive stress level in concrete and hence, likelihood of spalling. A secondary effect of load is that of increasing pore pressures by restraining the thermal cracking of the specimen.

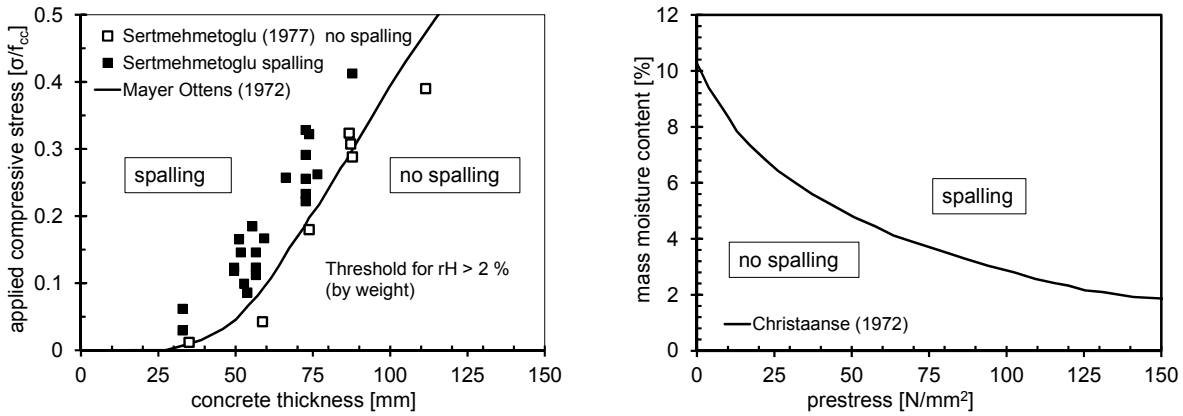

Figure 2.16. Explosive spalling diagrams: effect of applied stress and thickness (left), effect of applied stress and moisture content (right)

Khoury & Anderberg (2000) reported results from Morris obtained through personal correspondence. He investigated the behaviour of concrete columns under different load levels and found that increased load results in an earlier occurrence of explosive spalling, as illustrated in Figure 2.17. This behaviour Morris explained by the restraining effect of the load with respect to thermal expansion of column.

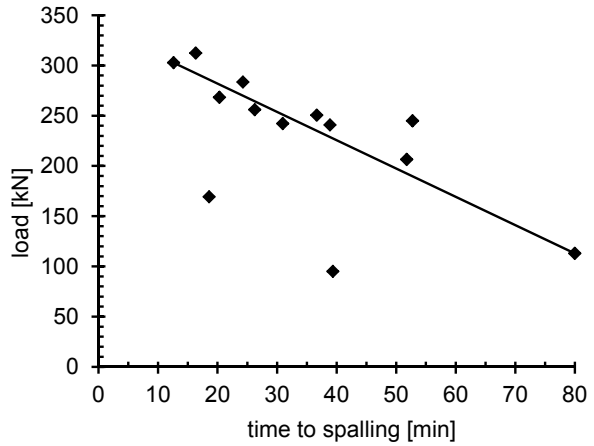

Figure 2.17. Effect of applied load on spalling of concrete columns, reproduced from Khoury & Anderberg (2000)

Ali (2002) investigated the susceptibility of normal and high strength concrete columns without and with restraint to explosive spalling. The main conclusion of this study is that presence of restraint or load promotes explosive spalling for both normal and high strength concrete.

Boström et al. (2007) investigated prestressed slabs made of high strength concrete (compressive strength ranged from 72.9 to 106.9 N/mm^2) and self-compacting concrete (compressive strength ranged from 37 to 78.3 N/mm^2). The moisture content ranged from 3.7 % to 4.5 % for high strength concrete and 4.8 % to 5.18 % for self-compacting concrete. They found that presence of compressive stress increases the

probability and amount of explosive spalling for all the investigated cases, thus confirming the findings of previous researchers. Zheng et al. (2010) also reported that imposed compressive stresses enhance explosive spalling of prestressed concrete slabs (compressive strength ranged from 22.8 to 56.9 N/mm^2).

Overall conclusion is that imposed compressive loads and/or restraint promote explosive spalling. Current guidelines, e.g. CEB-FIP-bulletin-46 (2008) recommend a limitation of loads in order to prevent spalling.

2.5.2.5 Aggregate size and type

Experiments performed by Connolly (1995) indicate that the use of larger aggregate promotes explosive spalling.

As to the aggregate type, it can in general be expected that lower thermal dilatation of aggregates leads to a less pronounced mismatch between cement mortar and aggregates, thus decreasing the probability of explosive spalling. Connolly (1995) tested three different aggregate types (gravel, limestone and Lytag) and observed that gravel is more susceptible to spalling than limestone. Malhotra (1984) found that explosive spalling is present for a range of aggregate types, with siliceous aggregate concrete having the highest susceptibility to explosive spalling.

2.5.2.6 Concrete strength and quality

As mentioned earlier, many experimental studies have demonstrated the increased susceptibility of high strength and high performance concretes to explosive spalling, e.g. Jumppanen (1989) and Sanjayan & Stocks (1993). High performance concrete is required to fulfil durability requirements, such as low permeability to potentially harmful gases and liquids. This exact property is responsible for reduced performance in case of fire, since low permeability inhibits the transport of water and water vapour through concrete. It should be noted, however, that explosive spalling directly depends on humidity of concrete, external loading and that an unfavourable combination of these factors can adversely influence the behaviour of concrete.

Sanjayan & Stocks (1993) compared the performance of normal strength (compressive strength 27 = N/mm^2 and mass moisture content = 4 %) and high strength concrete T-beams (compressive strength = 105 N/mm^2 and mass moisture content = 4.6 %) exposed to ISO 834 fire curve. Normal strength concrete did not spall, whereas high strength concrete experienced extensive explosive spalling.

Contrary to these results, Ali (2002) found that both normal and high strength concrete are susceptible to explosive spalling when heated according to BS 476 fire (corresponds to ISO 834). Moisture mass content for all the tested specimens ranged from 5.2 % to 6.0 %.

Hertz (2003) found that significant spalling cannot be expected if concrete does not contain small particle grains, such as silica fume, and if moisture mass content is less than 3 %.

2.5.2.7 Section size and shape

Section size and shape can influence the behaviour of concrete with respect to explosive spalling. Corners are found to be more susceptible to spalling, which is mainly attributed to high stresses and high heat influx, see Meyer-Ottens (1974). Connolly (1995) and Meyer-Ottens (1974) found that thicker specimens are less likely to spall. If the specimen thickness is too small, moisture can escape through the rear side of the specimen, thus alleviating explosive spalling.

2.5.2.8 Polypropylene fibres and air entrainment

Connolly (1995) found that air entrainment of 0.125 % by weight prevents explosive spalling for different heating scenarios. On the other hand, it lowers compressive strength thus decreasing concrete durability.

The most popular measure of spalling prevention is the addition of polypropylene fibres of different geometries and melting properties. The effectiveness of PP fibres on mitigation of spalling is demonstrated in a multitude of experimental studies, e.g. Bentz (2000), Connolly (1995), Jansson (2008) and Dehn et al. (2010). The dosage of PP fibres used in different studies varied from only 0.5 kg/m^3 to 4 kg/m^3 concrete. High dosages are not desirable, due to the adverse effect on compressive strength. Furthermore, the dosage depends on the geometry of fibres, as well as on the viscosity of fibres upon melting, as shown by Knack (2011). He further demonstrated the importance of flow viscosity of fibres on the mode of action by testing various fibres with different flow properties. By producing special fibres with very high viscosity and comparative fire tests he found that the fibres with high viscosity can even enhance explosive spalling. Stepwise reducing the viscosity of fibres resulted in increasing resistance of the corresponding concretes to explosive spalling.

Experimental permeability measurements have shown that concrete with PP fibres exhibits much higher permeability than plain concrete at temperatures above melting point of fibres, see for example Kalifa et al. (2001), Zeiml et al. (2008). Some of the results available on the effect of PP fibres on permeability of heated concrete are summarized in Figure 2.18. From these results it is apparent that the PP fibres introduce a significant permeability increase at temperatures close to the melting point of fibres.

The exact mechanism of the permeability increase in concrete containing PP fibres is still a matter of discussion. One theory is that the melted fibres are absorbed by the surrounding cement matrix thus providing additional channels for transport of liquids and gases, as advocated by Kalifa et al. (2001) and Zeiml et al. (2008). Khoury

(2008), on the other hand, suggests that the molecule size of the melted polypropylene and its connectivity to other molecules is too high in order for it to be absorbed by the matrix. Furthermore, he introduced the concept of PITS (pressure induced tangential space), in which the steam squeezes between the fibre and concrete matrix and passes along the fibre length, hence resulting in increased permeability. The influence of micro-cracking observed around the fibres is also considered to enhance the steam transport.

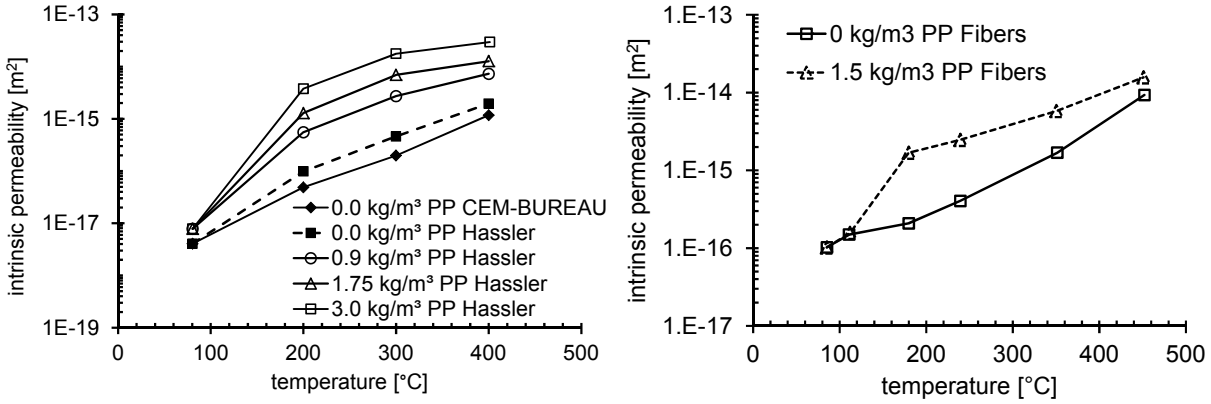

Figure 2.18. Influence of temperature on permeability of concrete containing PP fibres: left - Kalifa et al. (2001), right Zeiml et al. (2008)

2.6 Theories to explain the mechanism of explosive spalling

Due to the complexity of the phenomenon and inherent difficulties at measurements, multiple theories were developed to explain the mechanism of explosive spalling.

2.6.1 Thermally induced explosive spalling

When concrete is heated, high thermal gradients are present in the cross section. Surface region is heated, whereas inner portions of the specimen retain low temperatures, and are thus acting as a restraint to the thermal deformation. Consequently, compressive stresses are generated close to the heated surface, and tensile stresses in the inner cool region. Saito (1965) calculated thermally induced stresses and obtained a result that the thermally induced compressive stresses lead to explosive spalling when they exceed the compressive strength of the material. He explained the lack of spalling in later stages of fire by reduced thermal gradients.

Dougill (1972) considered the stress distribution in heated concrete to be similar to that observed in the splitting test. He explained the violent nature of explosive spalling by the strain softening region in the stress-strain curve in concrete. This theory can account for several aspects of explosive spalling, such as heating rate, specimen thickness, concrete strength and the fact that spalling takes place in the early stage of fire, but it cannot explain the effect of moisture on spalling.

2.6.2 Pore pressure induced spalling

Shorter & Harmathy (1965) proposed that spalling originates from what they termed as “moisture clog”. When concrete is heated, the surface layer starts to dry and the moisture present within concrete evaporates towards the exposed surface. However, a large part of the moisture is transported towards the inside region of concrete, and condensates upon reaching cooler region. In time, a fully saturated layer of concrete (moisture clog) is created. With further heating the moisture clog can be shifted, since the evaporation in the direction of the heated surface continues. However, the saturated zone inhibits further vapour transport in the direction opposite to heated surface. Therefore, steam can only evaporate towards the heated surface. This results in a build-up of pore pressure, and the time required for this depends on the heating rate and permeability of concrete. If heating rate is high and concrete exhibits low permeability, pore pressures will increase at a faster rate. Explosive spalling occurs when pore pressures overcome the tensile strength of concrete. More recent research has confirmed the existence of moisture clog due to vapour condensation by means of NMR analysis (van der Heijden et al. 2007) and by measuring permeability of heated concrete without prior drying (Chen et al. 2009).

2.6.3 Combination of thermally induced stresses and pore pressures

Zhukov (1970) first recognized the possibility that explosive spalling originates from the superposed action of thermally induced stresses and pore pressure. The total stress can then be compared to concrete strength, and this represents the failure criteria. Figure 2.19 gives an overview of the stresses acting close to the heated surface. Later he extended his model (Zhukov 1994) to incorporate fundamental cracking theory, and, based mainly on experimental data, developed a model to calculate the susceptibility to spalling.

Sertmehmetoglu (1977) suggested that thermally induced stresses at the heated end introduce weak planes parallel to the heated surface. His pore pressure measurements resulted in peak pore pressure of approx. 2.1 N/mm^2, which is lower than concrete tensile strength. However, he performed additional experiments where he artificially introduced weak planes and showed that relatively low pore pressure is required to cause explosive spalling on these planes.

Most of the researches today acknowledge the contribution of both thermally induced stresses and pore pressure on explosive spalling of concrete, but the exact mechanism of explosive spalling and the effects of different parameters are not yet sufficiently understood.

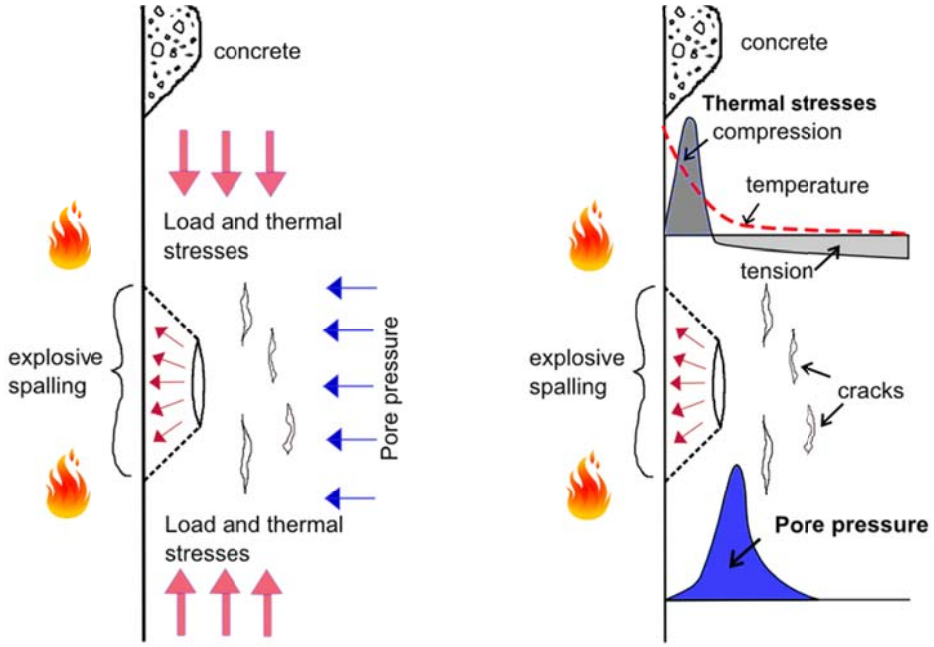

Figure 2.19. Stresses close to the heated surface after Zhukov (1970)

2.7 Numerical modelling of concrete at elevated temperatures

Numerical modelling of concrete at elevated temperatures has been based on two types of models, namely thermo-mechanical and thermo-hygro-mechanicals models. The former consider the coupling of thermal strain and material degradation with mechanical damage, and are in principle suitable for analysis of structural behaviour of concrete in fire. The latter are generally very complex models which account not only for the mechanical damage and heat transfer, but also for the contribution of moisture transport to the overall behaviour.

Some of the existing thermo-mechanical models are introduced by de Borst & Peeters (1989), Luccioni et al. (2003), Ozbolt et al. (2005) and Kodur et al. (2009). Even though their applicability for structural analysis gives good results, such models cannot account for explosive spalling. At maximum, thermo-mechanical models can predict corner spalling that takes place later in the fire. However, this kind of damage is not of the same origin as explosive spalling.

Thermo-hygro-mechanical models or even more complex chemo-thermo-hygro-mechanical modes are developed by Bazant & Thonguthai (1979), Gawin et al. (2003), Ichikawa & England (2004), Tenchev & Purnell (2005), Periskic (2009), Kukla (2010) and Zhao (2012). The list is not exhaustive. Such models can be used to investigate complex phenomena such as explosive spalling, which require coupling of thermal, hygral and mechanical processes in heated concrete.

Bazant & Thonguthai (1979) and Bazant & Kaplan (1996) analysed the distribution of pore pressures in rapidly heated concrete. They described the state and transport of pore water using a “one-phase model” which was verified and calibrated using experimental data. The model considers the dependency of permeability on relative humidity and temperature. It has served as basis for many successive models; the model used in the present study (Periskic 2009) is no exception.

Gawin et al. (2003) developed a coupled thermo-hygro-mechanical model which they later extended to a thermo-hygro-chemo-mechanical model (Gawin et al. 2006). In this model gas pressure, capillary pressure, temperature and mechanical damage are coupled together. Different spalling criteria are introduced depending on the failure mode: shear failure, buckling failure, simplified fracture failure and integral failure.

Ichikawa & England (2004) developed a model for one-dimensional heat and moisture transfer. Model calculates tensile stress using pore volume and vapour pressure. These are then compared to tensile strength to obtain a failure criterion.

Tenchev & Purnell (2005) separated liquid and gas pore water phase and incorporated the thermo-hygro-mechanical model into the damage model developed by Ortiz (1985). The effect of pore pressure on the damage evolution is modelled by applying a body force in the stress analysis module proportional to the pressure gradient. In a numerical example the authors varied permeability and relative humidity of concrete and observed that explosive spalling is alleviated for certain limiting value of permeability (approx. 10^{-16} m^2). They predicted explosive spalling even for extremely low relative humidity of 20 %. The model is not yet tested for other influencing factors.

Dwaikat & Kodur (2009) suggested a one-dimensional thermo-hygral model. Spalling criteria is temperature dependent tensile strength. When pore pressure overcomes tensile strength, failure occurs. However, this model does not account for thermal damage and stresses.

Zhao (2012) used steam tables to calculate pore pressures. The damage due to thermally induced stresses and pore pressure caused damage are considered separately. Therefore, no further information could be obtained about the combined effect of the two on explosive spalling. An important development is introduction of mesoscale model to account for the inhomogeneity of concrete.

Even though some of these models can predict the susceptibility of concrete to explosive spalling, a few limiting factors inhibited further investigation: (i) high computational and time demand of such complex models, (ii) lack of experimental measurements of relevant material properties and parameters and (iii) assumption of concrete homogeneity, i.e. use of macroscopic models for concrete.

2.8 Conclusions

Upon exposure to elevated temperatures, concrete degrades and most of the material properties are adversely affected. The presence of water in concrete influences its properties at temperatures in the proximity of the boiling point of water. Further degradation is governed by the phase changes of concrete constituents and the incompatibility of the aggregates and cement matrix. Tensile strength and Young's modulus exhibit almost linear decrease with rising temperature. Compressive strength reduces only from 300 °C onwards for normal strength concrete, whereas high strength concrete exhibits linear degradation of compressive strength from the beginning of heating. Even though relevant mechanical properties reduce, ductility of concrete increases for higher temperature. This is reflected in fracture energy, which retains its initial value even at 600 °C. Increase in porosity, change of pore size distribution and micro-cracking present at high temperatures adversely affect permeability of concrete. Consequently, permeability increases for higher temperatures. Exposure to high temperatures results in a decrease of thermal conductivity and increase of heat capacity. Concrete expands when heated in unrestrained state; the rate of expansion is mainly controlled by the aggregate type due to their high volumetric ration in concrete. When it is loaded in compression prior to heating, the expansion of concrete reduces and can, depending on the initial load level, go into the shrinkage and lead to premature failure of specimen.

Explosive spalling of concrete in fire is identified as one of the weakest performance characteristics of high performance concrete. Vast amount of experimental research has been undertaken to explain the mechanism of spalling and to identify the key parameters and material properties that govern the failure. Heating rate is observed to be the most important parameter with respect to spalling, since it influences the development of both thermally induced stresses and pore pressures. Permeability of concrete is found to be the most important material property influencing the behaviour, since lower permeability leads to a faster development of pore pressures in concrete. Experiments have demonstrated that the susceptibility of concrete to spalling increases for higher relative humidity (water content), as well as for higher level of compressive stresses and restraint. Furthermore, sections with complex and rapidly changing cross section are more prone to explosive spalling. Thermal stability of aggregates can also influence the susceptibility to spalling, since aggregates with high thermal dilatation promote explosive spalling. Numerical analysis has so far mainly been limited to macro-scale modelling approach, and even though a number of thermo-hygro-mechanical models have been developed, none of the models could capture all of the aspects of explosive spalling.

EXPERIMENTAL STUDY

3. EXPERIMENTAL INVESTIGATION OF HPC SLABS IN FIRE

Even though many researchers performed fire test on different types of concrete, employing various fire scenarios, very few data are available for concrete with the new type of PP fibres with very high flow melt ratio (Knack 2011). Furthermore, most of the experimental studies available in the literature encompassed very few additional measurements, such as permeability on concrete without and with PP fibres. It was therefore deemed essential to perform a more comprehensive study of the material behaviour under elevated temperatures, the accent being on the comparison of concrete without and with PP fibres.

In the framework of this project, high performance concrete without and with addition of PP fibres is exposed to one sided heating for two different heating scenarios, namely ISO 834 and ZTV-ING fires. The objectives of the fire tests are as follows:

(i) Compare the performance of high performance concrete with respect to explosive spalling exposed to standard fire (ISO 834) and to tunnel fire (ZTV-ING)

(ii) Investigate the efficacy of PP fibres with very high flow melt ratio at very low dosages (1 kg/m^3) for the two fire curves

(iii) Provide relevant input data for the numerical study of explosive spalling and allow the validation of the numerical model against the experiment

(iv) Investigate the suitability of acoustic emission measurement methods to capture the explosive spalling events. The research on this topic is performed by project partners from TU Munich, Prof. C. Grosse and Dipl. Ing. R. Richter. More details on this part of the study can be found in their publications (Grosse et al. 2010; Grosse et al. 2013).

3.1 Materials and specimen

High performance concrete is used to cast the slab specimens. Concrete mixes used for the two fire scenarios differ somewhat in strength and microstructure, as is evident from the mixtures and material properties summarized in Table 3.1 and Table 3.2. The first two batches (without and with PP fibres) are used for the ISO 834 fire experiments, and this concrete exhibited poor workability. Hardened concrete had a very inhomogeneous structure with pronounced air lumps mainly owing to the high viscosity of the mixture. This should be accounted for when evaluating the performance of this concrete.

The mixtures 3 and 4 used for ZTV-ING fire experiments are somewhat changed as compared to the first two in order to assure better workability of concrete. This concrete exhibited somewhat lower strength and better workability than the previous batch. The structure of the hardened concrete was more uniform and without extensive air voids.

Table 3.1. Concrete mixtures

	Cement		Aggregates			w/c	Silica fume [1]	Plasticizer [2]	Fibres [4]
	type	kg/m^3	sand 0-4 mm	basalt 2-8 mm	-	-	kg/m^3	kg/m^3	kg/m^3
1	CEM I 42,5 R-HS	450	1077	798		0.26	60	15.3	-
2	CEM I 42,5 R-HS	450	1077	798		0.26	60	15.3	1
	Cement		Aggregates			w/c	Silica fume [1]	Plasticizer [3]	Fibres [4]
	type	kg/m^3	sand 0-2 mm	basalt 2-5 mm	basalt 5-8 mm	-	kg/m^3	kg/m^3	kg/m^3
3	CEM I 42,5R-HS	500	814	182	727	0.34	45	5	-
4	CEM I 42,5R-HS	500	814	181	727	0.34	45	6	1

Notes: [1] Silica fume Silicol P (doral fused materials)
[2] ViscoCrete Gold
[3] Woerment FM 787 (BASF)
[4] PB Eurofibre HPR 1.7 d_{tex} / 15.4 / 6mm Polypropylene fibres (baumhüter)

Table 3.2. Properties of the hardened concretes

No.	Density	7 days f_c	14 days f_c	28 days f_c	water content	permeability
-	kg/m^3	N/mm^2	N/mm^2	N/mm^2	% of mass	m^2
1	2563	91.6	-	125,9	3.0	1.5×10^{-15}
2	2547	77.1	-	121,6	3.0	1.5×10^{-15}
3	2490	74.4	85.6	93.5	2.5	3×10^{-15}
4	2460	66.8	82.0	90.7	2.5	3×10^{-15}

Concrete compressive strength is reported as the mean value of at least 6 tested specimens. PP fibres can cause significant reduction in compressive strength of concrete, owing to their low strength. Since the amount of PP fibres used in this study is relatively low, it is found that the presence of PP fibres has a relatively small effect on the compressive strength of concrete. The difference between the compressive strength of the two concrete types is around 5 %. Water content was measured by drying concrete prisms at 105 °C up to the constant mass and is given as a mass ratio of water to dry concrete. It should be noted here that the moisture content lies at or below the typical limit for spalling (3 %), as provided by current codes. Specimens used in the fire experiments were 700 x 700 x 350 mm slabs for the ISO 834 fire and

750 x 750 x 350 mm slabs for the ZTV-ING fire test. For both fire curves, three slabs without and with PP fibres each were tested. Concrete specimens were kept at 20 °C and 100 % relative humidity during the first 28 days after casting.

3.2 Heating scenario and test setup

The fire tests were performed for two fire scenarios: standard ISO 834 fire according to DIN EN 1-2 (2004) shown in Figure 3.3 and modified ZTV-ING car tunnel (Zusätzliche technische Vertragsbedingungen und Richtlinien für Ingenieurbauten 2003), see Figure 3.4. The latter is modified (retention at 1200 °C is 10 minutes instead of 20 minutes) for following reasons: (i) to avoid damage of the temperature sensitive acoustic emission sensors positioned on the lateral sides of the slabs as well as to calibrate/validate the sensors, (ii) to avoid complete collapse of the specimen and possible damage to the complete monitoring devices, and (iii) to investigate the effect of cooling phase on explosive spalling. For simplicity, the modified ZTV-ING curve is in the present work referred to as ZTV-ING curve.

The ISO 834 fire test is performed in an indoor oven and the ZTV-ING fire test in an outdoor oven. The test setup used for the two fire scenarios is presented in Figure 3.1 and Figure 3.2. As can be seen, this setup allowed testing of three specimens simultaneously. All three specimens were placed on top of the oven to provide one sided heating of the specimens. The burners were located laterally in the oven, the total number of burners being 2 and for the ISO 834 and 4 for the ZTV-ING fire. Other than this, the oven setup for the two fire curves was the same. In order to avoid complete collapse of the specimens without PP fibres, the test was stopped after 30 minutes in the case of ISO 834 fire scenario. The ZTV-ING fire was stopped after 60 minutes of fire.

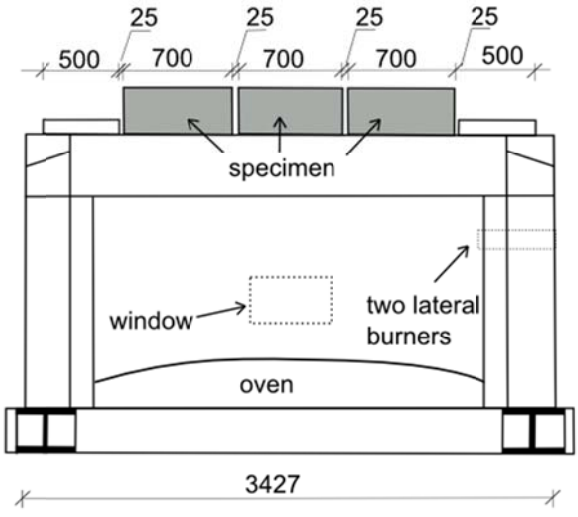

Figure 3.1. Test setup for the ISO 834 fire test (indoor oven)

Figure 3.2. Test setup for the ZTV-ING fire test (left), thermocouples to measure air temperature in the oven (right)

Thermocouples placed in the specimens before casting were used to measure temperature along the specimen depth. The measurements were performed at distances 20 mm, 40 mm, 60 mm, 80 mm and 150 mm from the heated surface. The air temperature in the oven was measured at 6 locations using thermocouples located 10 cm from the heated surface of the specimen, see Figure 3.2 (right).

Throughout the experiment (ISO 834), the behaviour of the concrete surface was recorded using a video camera placed in front of the oven window. Significantly higher temperatures in the experiment under ZTV-ING fire inhibited the monitoring with a camera. In this case, the experiment was only visually observed, and the time and progress of spalling was documented. The temperature of the unexposed side of the specimens was monitored using a thermo camera, in order to prevent any temperature induced damage of the acoustic sensors placed on this surface. The depth of the spalling was measured one day after the fire testing. The measurements were performed using Tachymeter type Leica TCRP 1202+R400. The cracking of the specimen on the lateral sides was also documented at the same time.

3.3 Results and discussion

3.3.1 Temperature measurements

Temperature distribution along specimen depth for the ISO 834 and ZTV-ING fire curves are shown in Figure 3.3 and Figure 3.4, respectively. The measurements are taken from the specimens with PP fibres which did not experience explosive spalling. In the specimens which underwent spalling the thermocouples were damaged and partially exposed to direct fire. It is, however, found that the presence of PP fibres has almost no influence on the temperature profiles within the specimen. The furnace temperatures were obtained as average values from 6 measurements. The target fire temperature and the measured air temperature in the oven are plotted along with the temperature profiles for both curves. As can be observed, the oven could not exactly

simulate the two curves, which is especially pronounced in the higher initial heating rate, and subsequent reduction of the same in case of tunnel fire curve (ZTV-ING). These deviations are, however, within acceptable limits.

Very steep temperature can be observed in the surface layers of the concrete specimens (measurement at 20 mm from the surface). These thermal gradients can invoke very high thermal stresses which, in combination with high pore pressures, can lead to explosive spalling.

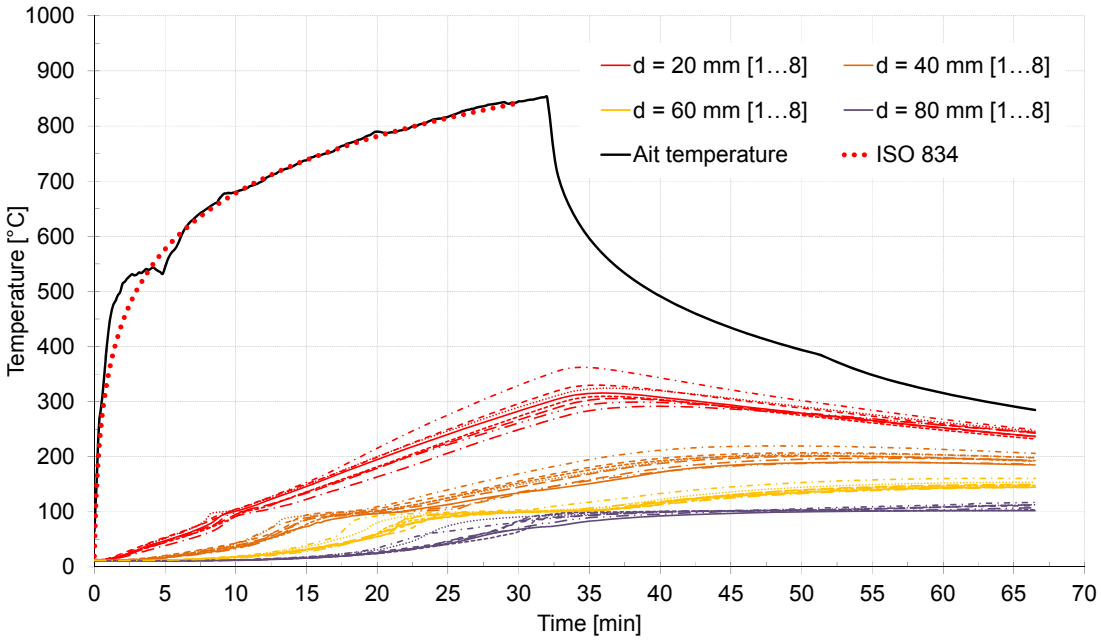

Figure 3.3. Temperature measurement under ISO 834 fire

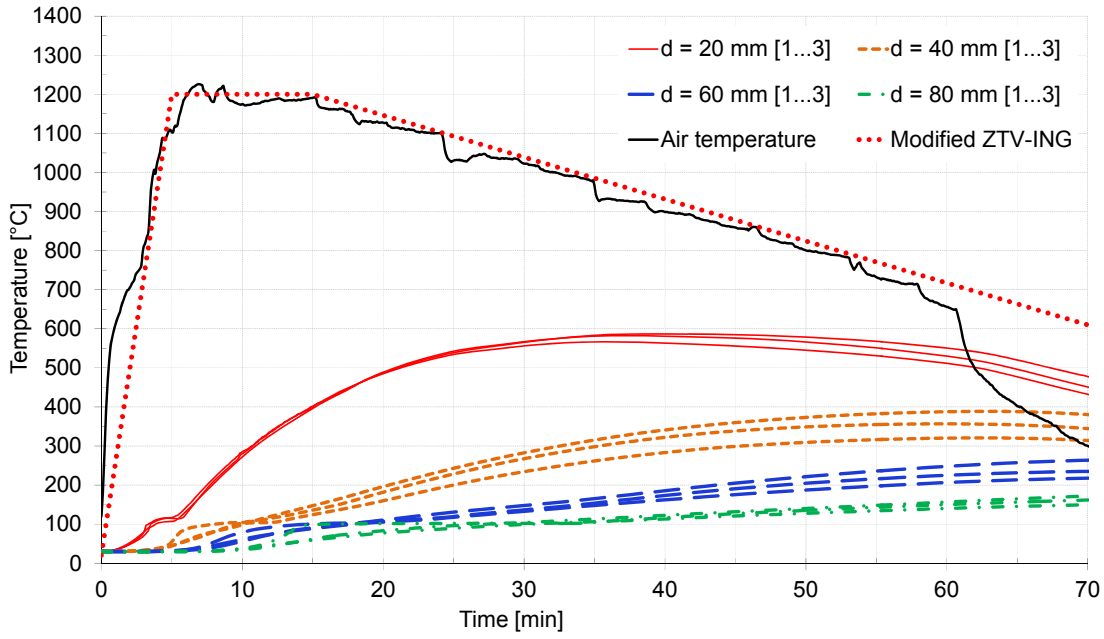

Figure 3.4. Temperature measurements under ZTV-ING fire

3.3.2 Behaviour of plain HPC in fire

In the case of ISO 834 fire, concrete without PP fibres exhibited extensive explosive spalling. Isolated spalling events started after approximately 8 minutes of fire, whereby only two out of total three specimens were affected. Successive explosive spalling of all three specimens started after about 9.5 minutes of fire.

Explosive spalling was observed as a sudden failure of very thin concrete layers accompanied by very loud bursting sounds. No pattern whatsoever in terms of the position of explosive spalling or the size of the surface portion that failed could be observed. The size of the concrete parts that spalled varied from very small of 1-2 cm to much larger pieces of more than 10 cm in diameter. The depth of the individual spalling events could not be measured directly due to obvious technical difficulties. The oven temperature at the onset of spalling was between 600 °C and 650 °C, whereas temperature of only 80-90 °C was measured at the depth of 20 mm (Figure 3.3).

After approx. 14 minutes of fire, cracking of the slabs in the vertical direction was observed. After the test was completed, the position, length (L) and width (W) of the cracks were documented. These are presented in Figure 3.5. These cracks are attributed to high thermal stresses present due to thermal gradients in the vertical direction (height). The heated surface tends to expand in all directions whereas the inner parts of the concrete slab maintain very low temperature, and do not expand. The cracking is further enhanced by cooling after the test. Even though extensive cracking is documented, it is not considered to be very beneficial in terms of explosive spalling. Overall porosity of concrete does indeed increase as cracks form and widen, and also a certain amount of water is observed to leave the specimen through the cracks, as shown in Figure 3.6. However, these cracks in concrete are not sufficiently interconnected and cannot significantly contribute to the relief of pore pressures in concrete. They only introduce a very localized relief of pressures at the location of cracks, but have little effect on the surrounding concrete.

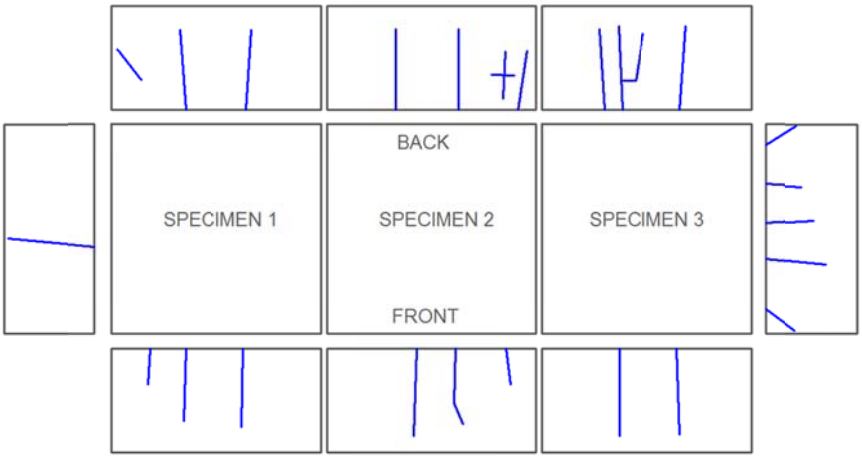

Figure 3.5. Cracking of the specimens after the test (ISO 834 fire)

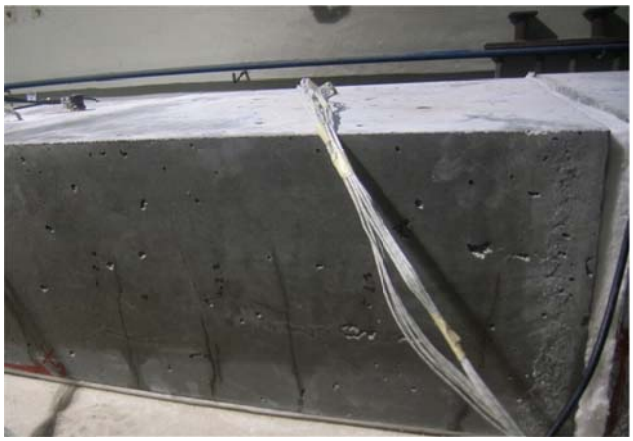

Figure 3.6. Cracking of the specimens as observed after the test (ISO 834 fire)

After 30 minutes of fire, the test was stopped by turning off the oven in order to prevent total collapse of the specimens. The oven reached room temperature 2 hours after the beginning of the test. No spalling was observed after the oven was turned off. Measurements of the spalling depth performed for all three specimens and the results are presented in Figure 3.7.

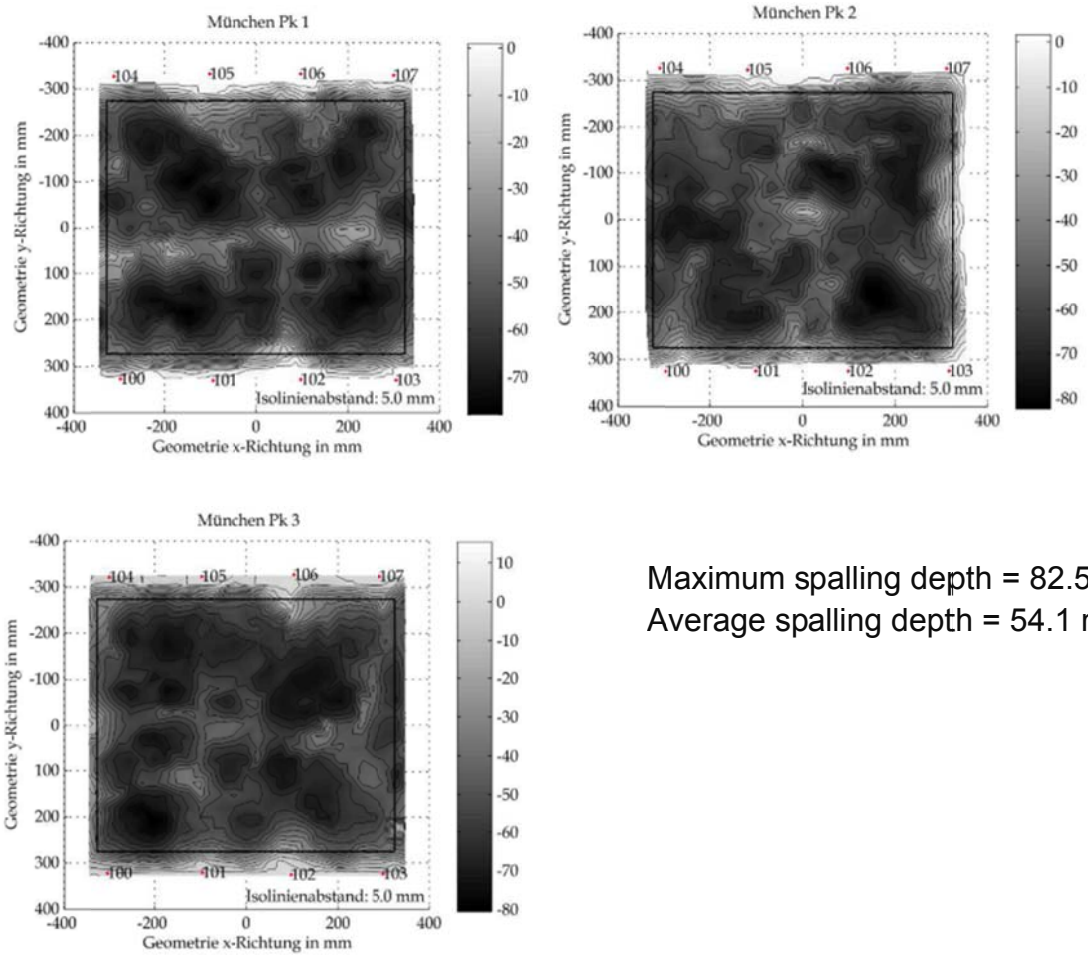

Maximum spalling depth = 82.5 mm
Average spalling depth = 54.1 mm

Figure 3.7. Spalling depth measured after 30 min of ISO 834 fire experiment (concrete without PP fibres)

Similar behaviour was observed in case of plain concrete exposed to the tunnel ZTV-ING fire. Isolated spalling events started at 2.3 minutes of fire and successive explosive spalling of all three investigated specimens initiated at approx. 3 minutes. Extensive explosive spalling occurred during heating phase and constant temperature phase (1200 °C). During the descending branch of the ZTV-ING fire curve, spalling activity tended to reduce accordingly and after a few minutes almost completely ceased. The depth of explosive spalling ranged from almost no spalling up to 80 mm spalling depth, with an average depth of 30 mm. Explosive spalling occurred at oven temperatures of 700-750 °C, whereas concrete at depth of 20 mm experienced temperatures of only 80-90 °C.

The same stochastic nature of the spalling location as in the previous case was observed. The final spalling depth after 60 minutes of fire exposure was documented and the visual results are presented in Figure 3.8. Spalling depth ranged from 0 to 133 mm, with an average of 40 mm.

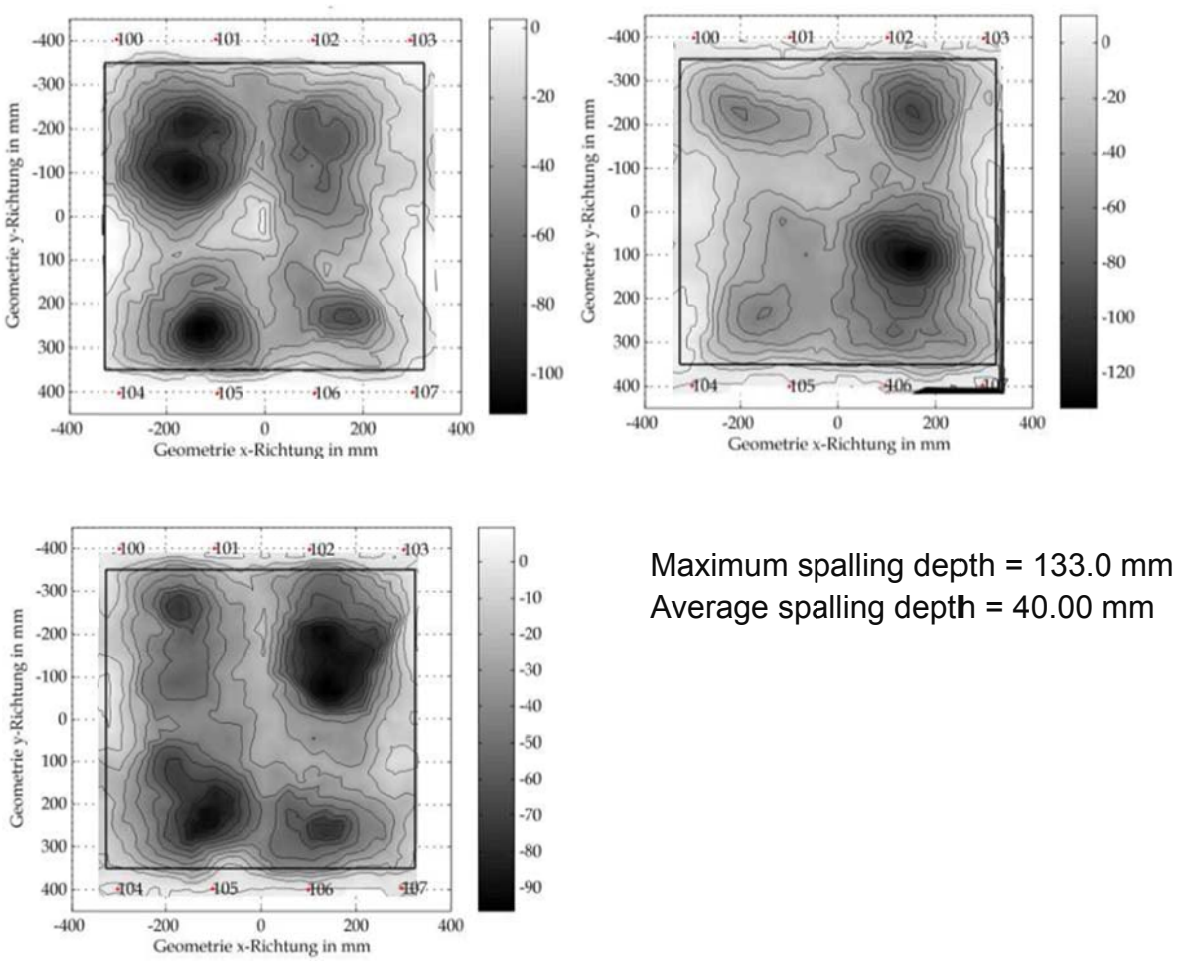

Figure 3.8. Spalling depth measured after 60 min of ZTV-ING fire experiment

Comparing these results with those obtained for the more moderate heating regime of ISO 834 fire, it can be concluded that the heating rate plays a very important role in the severity of explosive spalling. After 30 minutes of ISO 834 fire the spalling

depth was 50 mm, whereas the specimens exposed to 15 minutes of ZTV-ING fire experienced severe damage with maximum depth of 133 mm. Higher heating rates lead to high thermal stresses but also higher pore pressures. Hence, it is expected that the severity of explosive spalling increases in case of higher heating rates.

Figure 3.9. Plain concrete specimen after ISO 834 fire (left) and after ZTV-ING fire (middle), cracking of specimens during fire (right)

3.3.3 Behaviour of HPC with PP fibres in fire

Concrete with 1 kg/m^3 PP fibres exhibited very high efficacy in mitigating explosive spalling. In case of ISO 834 fire only a very limited spalling was observed on one of three tested specimens. The initial spalling event was followed by a few smaller events of spalling with overall depth of max. 15.6 mm. This isolated spalling is most likely caused by the very dense mixture of the first concrete batch, which might easily have resulted in somewhat uneven distribution of polypropylene fibres. In general, higher inhomogeneity of concrete structure can be expected to result in increased variation of local transport properties, i.e. permeability and porosity. Since only minor isolated spalling events occurred without subsequent further explosive damage, it can be concluded that the addition of PP fibres successfully mitigated explosive spalling. In the case of tunnel fire curve, the addition of fibres to concrete resulted in complete mitigation of explosive spalling. All six tested slabs experienced severe surface cracking, as can be seen in Figure 3.11.

The main mechanism behind the beneficial effect of PP fibres is the permeability increase, which starts at temperatures below the critical point of explosive spalling. As the temperature increases, fibres soften and eventually melt thus causing an increased connectivity of existing capillary pores. This topic is further discussed in Section 5, where the results of permeability measurements at elevated temperatures are presented.

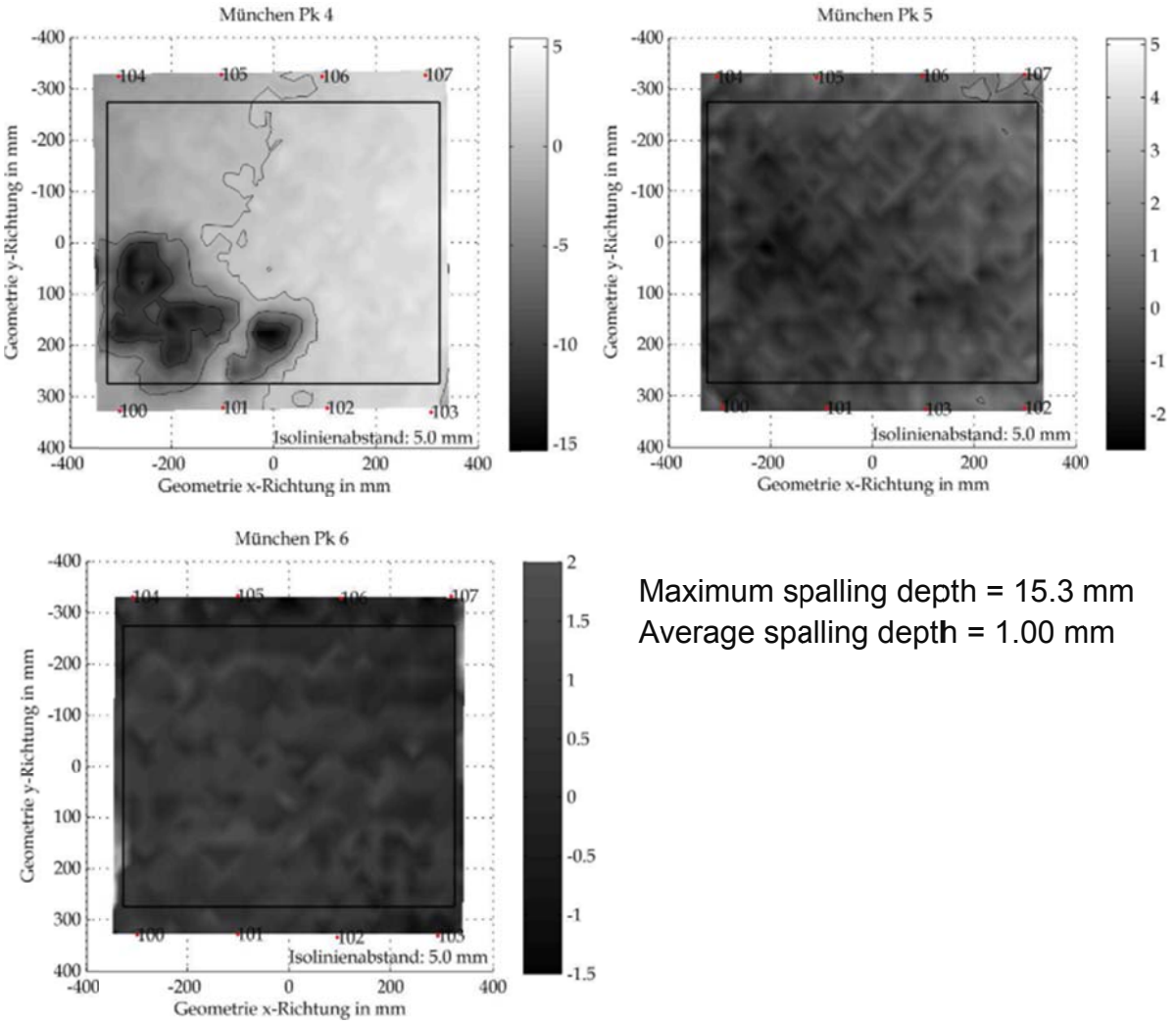

Figure 3.10. Spalling depth measured after 30 min of ISO 834 fire experiment (concrete with PP fibres)

Figure 3.11. Cracking of the heated surface of concrete with PP fibres after ISO 834 fire (left), cracking of the heated surface of concrete with PP fibres after ZTV-ING fire (right)

3.4 Conclusions

The effect of two different fire scenarios, namely ISO 834 and modified ZTV-ING, on the explosive spalling of high performance concrete without and with addition of PP fibres is experimentally investigated. Even though the two concretes differed in the mixture and mechanical properties (concrete strength differed by 30 %), a comparison of the performance provides more insight into the effect of heating rate on behaviour of concrete with respect to explosive spalling.

Plain HPC exposed to ISO 834 fire underwent explosive spalling after approximately 8-10 minutes of fire. Explosive spalling of thin concrete layers with varying dimensions was observed on all three tested specimens made of plain HPC. Similar concrete underwent spalling after only 2.5 - 3 minutes when exposed to a much more severe ZTV-ING fire. Heating rate governs two most important factors that influence explosive spalling, namely thermally induced stresses and pore pressures. It is, therefore, expected to obtain higher susceptibility of concrete to explosive spalling when it is exposed to faster heating and higher temperatures.

On the other hand, HPC with addition of PP fibres (1 kg/m^3) exhibited no spalling to very limited spalling for both fire scenarios. The specimens underwent severe surface cracking, but almost no explosive spalling. The addition of fibres results in a very high increase in concrete permeability (Kalifa et al. 2001). More permeable concrete can allow the water vapour to pass deep into the concrete specimen without creating a moisture (saturated) zone. If the water / water vapour transport is enabled, moisture clog is not generated, i.e. pore pressures remain at relatively low level.

4. EXPERIMENTS ON CONCRETE CUBES

Fire experiments demonstrated the beneficial effect of fibres the explosive spalling of concrete, and the permeability experiments (Section 5) confirmed that the permeability is the material property which governs the susceptibility of concrete to explosive spalling. However, due to inherent difficulties in fire experiments it is very difficult to gain data which could clarify the mechanism of spalling, such as distribution of thermal stresses and pore pressures.

Experimental results available in the literature, such as those obtained by Mindeguia et al. (2010), Phan (2002), Consolazio et al. (1998) and Jansson & Boström (2010), offer some insight into the development of pore pressures in concrete. However, the measurement itself has a few drawbacks. The scatter of results is relatively high, the measurement equipment itself introduces a change in the concrete micro- and meso-structure and it is almost impossible to predict the location of spalling and measure the pore pressure at the exact location. As heating rate increases, the introduction of pore pressure gauges leads to cracking in concrete, and thus pore pressures are relieved. In spite of these difficulties, pore pressure measurements have been a useful tool to better understand the moisture transport in concrete. Different authors have confirmed that certain amount of pore pressure is required for spalling to take place, and that dry concrete or concrete with very low moisture content is very unlikely to undergo explosive spalling (Connolly 1995).

On the other hand, no experiments on the contribution of thermal stresses on the explosive spalling can be found in the literature. Since the measurements of thermal stresses during standard fire experiments are highly demanding, an attempt is made in this work to indirectly evaluate the effect of thermally induced compressive stresses on the explosive behaviour of high strength concrete.

The specimens were heated to temperatures up to 230 °C with relatively moderate heating rate and were subsequently (without prior cooling) loaded in compression. When employing such a heating regime, one can expect moderate pore pressures, but very low thermal stresses. The purpose of subsequent compressive loading is to account for the compressive stresses induced by the high gradients in fire / fire experiments, and hence investigate the combined effect of pore pressure and compressive stress on behaviour of concrete.

4.1 Materials and specimens

Specimens used in these experiments were cubes with 150 mm side length. Different concrete batches with slightly different mixture were used, all of them within the limits of concrete class C 50/60. The mixtures and compressive strength for each batch are

provided in Table 4.1. After initial curing (7 days in water, 21 day at room temperature), all specimens were kept at room temperature and at humidity of approximately 60 %.

4.2 Heating regime and mechanical loading

The first loading phase consisted of heating the specimens. In order to invoke higher pore pressures, an electrical oven was first heated to 120 °C and the specimens are subsequently placed in it. The oven was then heated up to 230 °C and left at this temperature for different duration times, ranging from 60 min to 180 min. It was not possible to control the heating rate due to limitations of the very simple electrical oven. The maximum temperature of 230 °C was reached within 15 minutes from the moment of placing the specimens in the oven, what corresponds to an approximate heating rate of (230 °C -120 °C) /15 min = 7.5 °C/min. The readings of the temperature were taken from the oven thermometer. Specimens were taken out of the oven after the targeted exposure times and immediately loaded in compression using a universal testing machine. The load was applied in such manner to reach peak within 1.5-2 minutes.

Three specimens were not loaded in compression immediately upon finishing the heating; these are allowed to cool down at room temperature. The objective was to check if the explosive spalling will occur upon cooling. After the specimens reached room temperature, they were loaded in compression up to failure.

Reference specimens were loaded in compression without prior heating to obtain a reference compressive strength. In every test the peak compressive stress and the failure mode (occurrence of explosive spalling) were recorded.

Table 4.1. Concrete mixture and mechanical properties

Batch	Cement		Aggregates			w/c	Plasticizer	Retardant	f_c	Density
-	type	kg/m^3	0-2 mm	2-8 mm	8-16 mm	-	kg/m^3	kg/m^3	N/mm^2	kg/m^3
1	CEM I 42.5R	375	700	478	662	0.46	0.002	0	60.4	2.35
2	CEM I 42.5R	375	719	458	683	0.48	0.003	0.002	59.0	2.32
3	CEM I 42.5R	375	715	461	680	0.46	0.003	0.002	63.1	2.39
4	CEM I 42.5R	375	724	460	674	0.45	0.003	0.002	60.0	2.34

4.3 Results and discussion

Table 4.2 gives an overview the investigated cases, corresponding peak compressive loads and descriptions of the failure mode. After 60-minutes exposure to elevated temperature (specimen 1-1) peak compressive stress decreased by 17 % as compared to compressive strength. The failure mode was typical concrete cracking in compression and concrete exhibited no explosive spalling. Even though the compressive stress was very high, the level of pore pressure was most probably too low to induce explosive spalling. When the specimen failed in compression, it was observed that some water vapour condensed on the steel loading plates.

Table 4.2. Overview of the measured peak stresses and observed failure modes

No.	Exposure duration	Peak load	σ_{max}	σ_{max} / f_c	Failure mode
-	min	kN	N/mm^2	-	-
Ref 1	0	1271	56.5	1.00	no explosive spalling
Ref 2	0	1338	59.5	1.00	no explosive spalling
Ref 3	0	1429	63.5	1.00	no explosive spalling
Ref 4	0	1416	62.9	1.00	no explosive spalling
1-1	60	1051	46.7	0.83	no explosive spalling
1-2	110	980	43.6	0.77	no explosive spalling, release of water vapour when concrete cracked
4-1	125	1020	45.3	0.72	explosive spalling
2-1	145	985	43.8	0.74	explosive spalling
2-2	160	970	43.1	0.72	explosive spalling
4-3	160	1080	48.0	0.76	explosive spalling
3-1	180	1042	46.3	0.73	explosive spalling
3-2	185	1023	45.5	0.72	no explosive spalling
4-2	145	1120	49.8	0.79	no explosive spalling
3-3	185 + cooling at 20 °C	1000	44.4	0.71	no explosive spalling
4-4	125 + cooling at 20 °C	1130	45.0	0.72	no explosive spalling
4-5	125+ cooling at 20 °C	1118	47.5	0.76	no explosive spalling

After 110-minutes exposure (specimen 1-2) the peak stress reduced to 77 % of the compressive strength and no change in failure mode was observed. However, after the initial cracking of concrete, a large amount of water vapour escaped from the specimen. The vapour partially condensed on the both steel loading plates, see Fig-

ure 4.1. Specimen 4-1 kept in the oven for 125 minutes exhibited very sudden explosive spalling at the peak stress of 77 % of the concrete compressive strength. Shortly before spalling occurred a substantial amount of water vapour escaped from the specimen.

Similar results were obtained for specimens heated for 140-180 minutes (specimens 2-1, 2-2, 3-1, 4-3). The progress of failure for specimen exposed to heating for 180 minutes (specimen 3-1) is depicted in Figure 4.2. Shortly before explosive spalling took place, some water vapour left the specimen due to cracking, but the pressure relief was not fast enough to avoid explosive spalling.

For all investigated scenarios the peak stress at failure remained between 70 and 80 % of compressive strength. Explosive spalling was more violent and more energy was released with increased exposure duration, which can be attributed to the increased pore pressure inside the specimen. The pore pressures in the specimens were not measured, however, it can be assumed that the maximum pore pressures within the specimen increased with the time of exposure to elevated temperature. Hence, the severity of explosive spalling increased with increasing heating duration. On the other hand, the peak compressive stress in all tests on heated specimens ranged from 70 to 80 % of the compressive strength, depending mainly on the concrete batch. Only a very slight decrease in peak compressive stress with increased duration of heating was observed.

Figure 4.1. Water vapour condensed on the steel loading plates

Two specimens (4-2 and 3-2) were loaded almost up to peak and immediately unloaded. In this case concrete was allowed to crack, which lead to a relief of the pressure. A very big amount of water vapour was observed to escape from the specimen. Upon subsequent repeated loading, the two specimens failed without explosive bursting. The progress of damage during the repeated loading for specimen 3-2 is depicted in Figure 4.3. It is visible that a very big amount of water vapour escaped the specimen once the cracks opened. Further loading resulted in typical compressive failure mode, but no explosive spalling took place.

The specimens 3-3, 4-4 and 4-5 did not experience any spalling during cooling, most probably because the level of compressive stresses was not high enough to cause spalling. After cooling to room temperature and loading in compression, also no spalling was observed, since the pore pressures were relieved during cooling phase. These results clearly point out the importance of both pore pressure and compressive stress for explosive spalling.

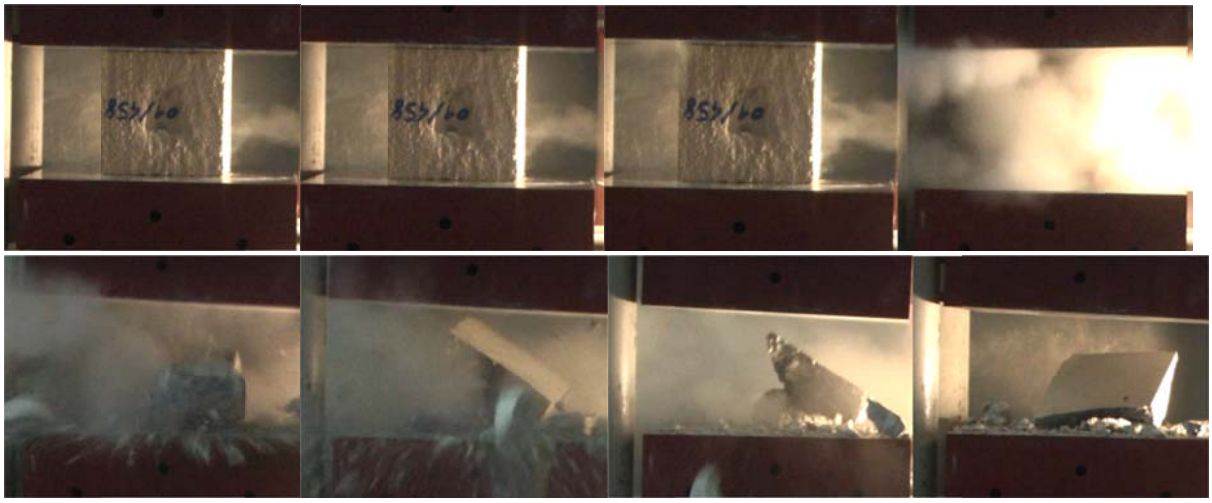

Figure 4.2. The progress of damage during compressive loading (specimen 3-1 – 180 min exposure duration)

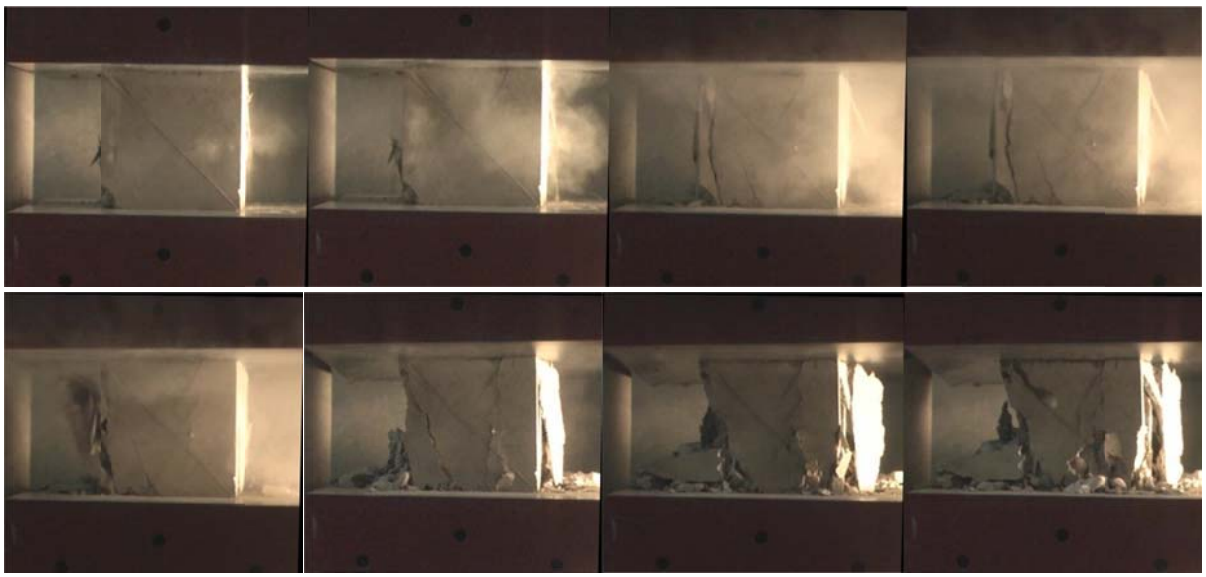

Figure 4.3. The progress of damage during compressive loading (specimen 3-2, exposure duration of 180 minutes)

In this work, the specimens were put in an already preheated oven and heated relatively fast. The thermally induced stresses lead to cracking and material degradation which finally results in a lower compressive strength. The behaviour of specimens 4-4 and 4-5 demonstrates the effect of thermally induced damage on the compressive strength. These specimens were kept in the oven for 125 minutes and were then al-

lowed to cool down slowly. The residual compressive strength of these two specimens is approx. 20 % lower than that of the reference specimens.

These results indicate that very high levels of compressive stresses in combination with sufficiently high pore pressures can lead to explosive spalling. The pore pressures and the thermal stresses present in the specimen during heating did not result in explosive spalling, until the level of compressive stress was increased by mechanical loading. Even though the level of pore pressures most probably increased from 60-minutes to 180-minutes exposure duration, almost constant peak compressive stresses was recorded. There is no critical pore pressure that leads to explosive spalling, but there seems to be a critical combination of compressive stress and pore pressure that results in explosive spalling. Concrete failure in compression changed from non-explosive to explosive due to presence of pore pressures. In this case, pore pressures can be considered as the trigger to explosive release of energy accumulated due to high compressive stresses.

It is important to note here that these experiments cannot account for all the aspects of explosive spalling. However, they prove to be useful in providing better understanding of the combined action of pore pressure and thermally induced stresses.

5. PERMEABILITY OF HPC AT ROOM AND ELEVATED TEMPERATURE

5.1 General

Available pore space and the connectivity of pores govern the ingress and transport of gases and liquids into porous materials and, consequently, the durability of these materials. The pore volume is characterized by porosity and connectivity of pores by permeability. These two properties together govern durability of porous materials such as concrete. Low permeability of high performance concrete (HPC) typically makes it more sensitive to explosive spalling.

Various experimental and numerical studies have demonstrated the influence of permeability on explosive spalling, see Schneider et al. (1985), Ozbolt et al. (2008), Kalifa et al. (2001). Experimental studies of permeability are performed by employing different permeating media (gases and liquids) as well as different measurement methods, since currently there is no generally accepted testing method. Some of the laboratory measurement methods that using liquids (water) as medium are constant head experiment (Bamforth 1987) and falling head experiment (Loosveldt et al. 2002). The methods using gases (oxygen, nitrogen, helium) as medium are the RILEM-CEMBUREAU method (Kollek 1989) and the Hassler method (Kalifa et al. 2001). In general, permeability to an inert gas yields more realistic values than permeability to water, since water addition in concrete can result in rehydration of unhydrated cement.

The vast majority of the experimental studies on the influence of temperature on permeability were performed in residual state, i.e. after cooling the specimens to room temperature. Only very limited studies aimed at measuring permeability on heated specimens can be found in the literature, see for example Schneider et al. (1985), Choinska et al. (2007), X. Chen et al. (2009) and Lion et al. (2005). This is mainly due to the technical difficulties involving measurements of permeability at elevated temperatures. Nevertheless, it is important to measure the material properties directly at elevated temperatures to understand the phenomenon occurring at high temperature. It is also interesting to compare them with their residual counterparts.

Another very important aspect from the viewpoint of explosive spalling is the influence of PP fibres. According to experimental evidence (Khoury & Anderberg 2000), explosive spalling occurs typically at temperatures between 200 °C and 250 °C, while PP fibres melt at approx. 160 °C to 170 °C. Therefore, it is reasonable to assume that the melted fibre leaves free path for the water vapour to escape. Thus, the pore pressure is relieved and hence no or very limited spalling occurs. However, it is still not clear what happens with the fibres after melting. Kalifa et al. (2001) suggest that

the melted polypropylene is absorbed by the cement matrix and thus empty fibre beds are available for pressure relief. Khoury (2008), on the other hand, considers diffusion of polypropylene into cement matrix impossible because of the large molecule size, i.e. high viscosity of the fibre melt. He suggests that prior to melting of fibres, the contact between the fibres and matrix becomes permeable to water vapour. This topic requires further experimental investigation of the concrete microstructure.

Here, a new test setup for permeability measurement of concrete at high temperature is presented. The setup is relatively simple and easy to operate while being reasonably accurate at the same time. It is validated against the widely used RILEM-CEMBUREAU method (Kollek 1989) for permeability measurements at room temperature. Using the new test setup, experiments are performed on concrete without and with PP fibres subjected to thermal loads ranging from 20ºC to 300ºC. Permeability to nitrogen is calculated by employing the pressure decay method. In order to provide more insight into the concrete microstructure after exposure to elevated temperature, microscopic investigations are performed on concrete containing fibres before and after exposure to elevated temperature. In the following sections the theoretical background, test methodology, material properties and results are presented and discussed.

5.2 Theoretical background

One-dimensional laminar flow in a porous material is described by Darcy's law:

$$Q = -a \frac{A}{\mu} \frac{dp}{dx} \tag{5.1}$$

where Q = the volumetric flow, a = the permeability, A = the area of the specimen perpendicular to the flow direction, dp/dx = the pressure gradient and μ = the dynamic viscosity of the permeating fluid. Intrinsic permeability describes the ability of a porous material to resist fluid ingress. It depends only on the geometry and connectivity of the porous network, and not on the pressure of the permeating fluid. For incompressible fluids the permeability a as given in Eq. (5.1) corresponds to the intrinsic permeability. However, the same is not true for compressible fluids, since the permeability obtained from Eq. (5.1) is a function of pressure. Therefore it is denoted as apparent permeability a_{pp} for gases, and it is valid for the specific pressure at which the permeability is measured.

When gases are transported through porous media, the flow consists of viscous flow as well as slip flow. The slip flow phenomenon is present in the case when the pore size is of the same order of magnitude as the mean path of the gas molecules, in which case the molecules slide on the pore walls. The mean free path describes the average distance covered by a moving particle (atom, molecule) between successive

impacts and is inversely proportional to pressure. Klinkenberg (1941) suggested a method to correct the apparent permeability in order to obtain intrinsic permeability. The formulation reads:

$$a_{app} = a_{\text{int}}\left(1+\frac{b_K}{p_m}\right) \tag{5.2}$$

where a_{app} = the apparent permeability, a_{int} = the intrinsic permeability, b_K = the Klinkenberg "slip flow constant", and p_m = mean of the pressures between the inner and outer face of the specimen, thus one of them always being atmospheric pressure, i.e. $p_m = (p_1+p_2)/2$, where p_1 corresponds to the inlet pressure and p_2 to the outlet pressure (atmospheric pressure). The slip flow constant b_K is a function of gas and porous system. It is inversely proportional to the average diameter of the capillaries.

The following is valid for compressible fluids:

$$Q\,p = const = Q_m p_m \tag{5.3}$$

where p_m = the mean pressure and Q_m = the volumetric flux corresponding to the mean pressure.

The specimens used in the experiments are hollow cylinders with inner radius r_1, outer radius r_2 and height H (see Figure 5.4). Multiplying Eq. (5.1) with p and integrating from r_1 to r_2, following can be obtained:

$$Q_1 p_1 \int_{r_1}^{r_2} dr = -a_{\text{int}} \frac{A}{h} \int_{p_1}^{p_2} (b_K + p)\,dp \tag{5.4}$$

After integration and solving the equation for a_{app}:

$$a_{app} = \frac{\eta \ln\left(r_2/r_1\right)}{\pi H} \frac{Q_1 p_1}{\left(p_1^2 - p_2^2\right)} \tag{5.5}$$

Under the assumption of ideal gas, Clapeyron's law can be applied:

$$n\,R\,T = p_1 V \tag{5.6}$$

where n = the amount of substance, R = the ideal gas constant, T = the temperature and V = the volume occupied by gas. Thereby, isothermal conditions are assumed,

i.e. temperature is constant during measurement at each of the target temperatures. Since the volume of the pressurized gas is also constant, the following is valid:

$$\frac{dn}{dt}RT = \frac{dV\,p_1}{dt} = Q_1\,p_1 = const \tag{5.7}$$

For a certain time interval Δ*t*, Clapeyron's law can be rewritten as:

$$\frac{\Delta n}{\Delta t} = \frac{\Delta p_1 V}{RT} \;\Rightarrow\; \frac{\Delta n}{\Delta t} \approx Q_1\,p_1\frac{1}{RT} \tag{5.8}$$

and

$$Q_1\,p_1 = \frac{\Delta p_1}{\Delta t}V \tag{5.9}$$

Using Eq. (9) in Eq. (5) the following relation is obtained:

$$a_{app} = \frac{\eta \ln\left(r_2/r_1\right)}{\pi H}\frac{\frac{\Delta p_1}{\Delta t}V}{\left(p_1^2 - p_2^2\right)} \tag{5.10}$$

In each time interval Δ*t,* the apparent permeability a_{app} is calculated according to Eq. (5.10). Pressure decay history is obtained from the experiment. The dynamic viscosity of gases is a function of temperature. This is accounted for when calculating the permeability. In order to obtain the intrinsic permeability, the apparent gas permeability is extrapolated to the infinite mean pressure ($1 / p_m = 0$), as shown in Figure 5.1.

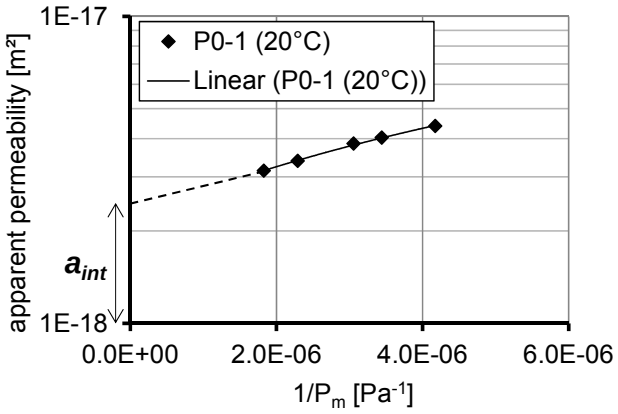

Figure 5.1. Evaluation of intrinsic permeability according to Klinkenberg method

5.3 Experimental investigations

5.3.1 Test setup

In the experimental investigations two different test setups are used. Namely, in order to verify the new experimental setup for measurement of permeability of concrete at high temperature, the experiments are first carried out at room temperature. The results of the measurement are then compared with the results which are obtained using relatively simple and widely used RILEM-CEMBUREAU method.

The test setup according to the RILEM-CEMBUREAU method is shown in Figure 5.2.

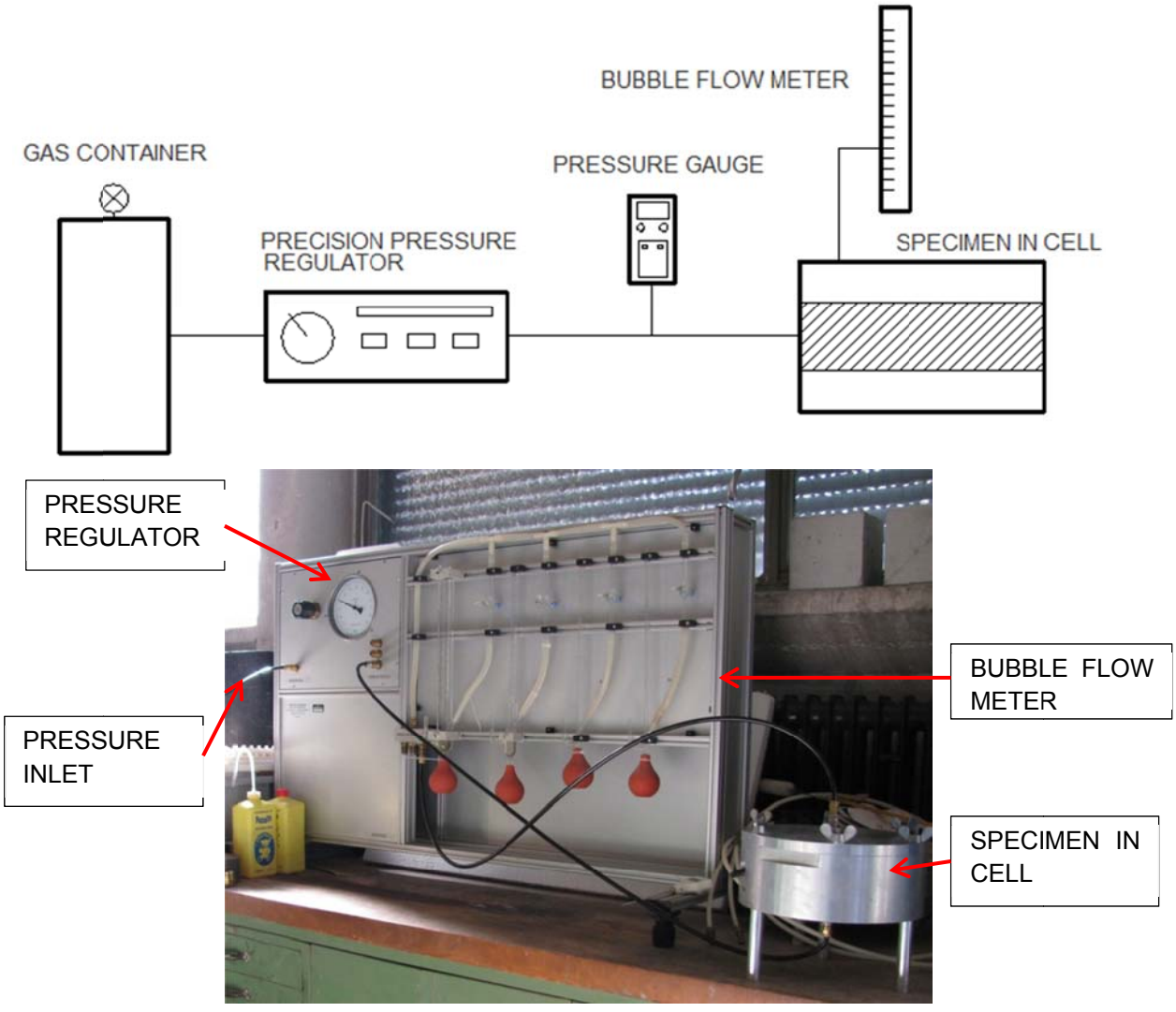

Figure 5.2. Test setup according the RILEM-CEMBUREAU method

The cylindrical specimen (diameter d = 100 mm, height H = 50 mm) is placed in the steel frame and the gas (nitrogen) is flowing from the top to the bottom of the specimen. Pressurized rubber ring (1.2 MPa air pressure in the ring) around the specimen ensures the tightness of the setup. Volumetric flow is measured using the bubble flow

meter. Permeability coefficient is calculated according to the Hagen-Poiseuille relation for the laminar flow of fluids through a porous body (Gallé & Sercombe 2001):

$$a = \frac{2Q p_1 L \eta}{A\left(p_1^2 - p_2^2\right)} \tag{5.11}$$

where L = the length of the specimen in the flow direction. The measurements are performed at room temperature for pressures ranging from 0.1 to 0.3 MPa. The Klinkenberg method described above is used to evaluate the intrinsic permeability.

The new test setup developed for measurement of permeability at elevated temperatures is shown in Figure 5.3. The hollow cylindrical specimen is placed between two steel plates. The top and the bottom steel plates are provided with 2 mm wide holes for the gas inlet and outlet, respectively. Between the steel plates and the specimen the graphite sealant with an outer diameter of 125 mm and inner diameter of 30 mm is placed. The thickness of the sealant is chosen as 1.0 mm. Both below the top steel plate and under the bottom steel plate one cooling and one insulating plate is placed. The cooling is achieved by letting the cool water flow through the cooling plates. A 500 kN loading cell for the load measurement is placed above the top cooling plate. The steel frame consisting of two T-plates and four steel rods is used to apply the load. Four hydraulic jacks are placed on the four steel rods, the required load is subsequently applied and the nuts are fastened. The load is monitored throughout the experiment using data acquisition software.

The specimen is heated using a spiral heating collar fastened to the four rods. Around the heating collar a heat resistant insulation is applied (not visible in Figure 5.3) in order to minimize the heat loss to the environment. Temperature is measured and controlled during the whole experiment in both steel plates using thermocouples connected to the thermo regulator. A rather slow heating a rate of 0.5 °C/min is selected to reduce possible cracking due to thermal gradients. The gas container is connected to the gas inlet, and the gas outlet is connected to the pressure gauge. The precision of the pressure gauge is +/- 10^{-4} MPa. Nitrogen is used as permeating gas due to its inert behaviour with respect to concrete and since it does not enhance combustion. Once the load corresponding to a pressure of 20 MPa is applied, the first permeability measurement is performed at the room temperature. The hollow portion of the specimen is pressurized using nitrogen and the pressure is measured. Maximum applied pressure is 1.1 MPa, while the minimum is 0.2 MPa (both gauge, i.e. relative pressure). The pressure history is obtained and using Eq. (5.10) apparent permeability for every time step is calculated. The slip flow effect is accounted for, and intrinsic permeability is evaluated.

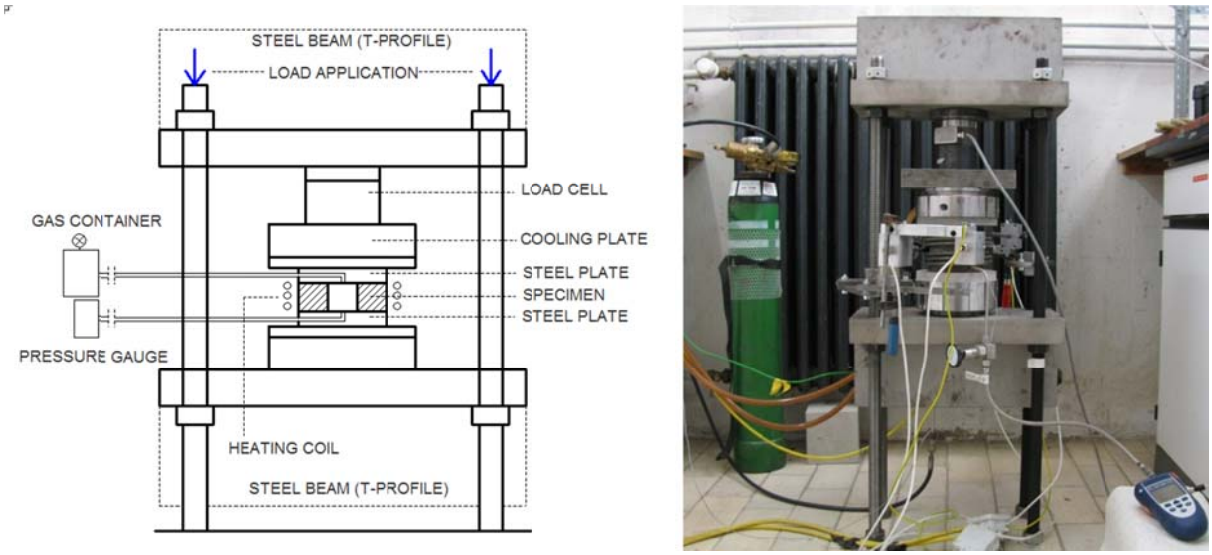

Figure 5.3. New test setup for the permeability measurements at elevated temperatures

In case of specimens tested at elevated temperature, once the desired temperature level is attained, the same is kept constant for 24 to 72 hours to allow uniform heating of specimen. Prior to performing permeability experiments, temperature measurements are performed on samples containing thermocouples in the concrete specimen itself. These measurements are used to calibrate the retention time such that the whole concrete specimen reaches desired temperature. Upon the end of the retention time, at least three permeability tests are performed following the above-described procedure and the specimen is heated to the next target temperature. Temperature levels used for permeability measurements in case of specimens without PP fibres are 20 °C, 80 °C, 150 °C, 200 °C and 300 °C. A few more measurements are made in case of specimens with fibres to capture the region around the melting point of fibres, i.e. measurements are also performed at 130 °C and at 170 °C. Measurements beyond 200 °C are not performed since the permeability already reached the limit of the test setup. However, using a similar setup, the temperature range can be increased if desired. Upon finishing the test at last target temperature, the specimen is cooled to the room temperature with a cooling rate of 0.5 °C/min in order to avoid high temperature gradients. Residual permeability measurements are performed after the specimen is kept at room temperature for at least 12 hours.

It should be noted that the current test setup does not allow measurement in case of very high permeability, since the volume of the pressurized gas is not sufficiently large. In order to increase the range of permeability which can be measured using this setup as well as to increase the accuracy of the measurements, it is required to increase the pressurized volume in the future tests, i.e. the size of the test specimen should be increased.

5.3.2 Material properties

5.3.2.1 Concrete

For validation of the test setup against the RILEM-CEMBUREAU method, high strength concrete (grade C 50/60) with maximum aggregate size of 16 mm is used. For the measurements at elevated temperatures, high performance concrete (grade C 80/95) without and with PP fibres with maximum aggregate size of 8 mm is used. The concrete composition is provided in Table 3.1. Concrete with polypropylene fibres required higher amount of plasticizer to assure better workability. The cube compressive strength of C 50/60 at the time of testing was 55 MPa, whereas C 80/95 exhibited a compressive strength of 94 and 90 MPa for concrete without and with PP fibres, respectively. It is found that relatively small amount of fibres (1.0 kg/m^3) does not have any significant effect on the compressive strength of concrete.

Concrete is water cured for the first seven days after casting and afterwards it is stored at 20 °C and approx. 60 % relative humidity. The age of concrete at the time of testing is approximately two years for grade C 50/60, and between 7 and 9 months for grade C 80/95 without and with PP fibres. Specimens are prepared by core cutting from the slab. For the tests according to RILEM-CEMBUREAU method solid cylindrical specimens with diameter of 100 mm and height of 50 mm are prepared, while for the tests at elevated temperatures hollow cylinders with inner radius, r_1 of 40 mm and outer radius, r_2 of 120 mm are used (Figure 5.4). In both cases the specimens are drilled from slabs (500 x 500 x 200 mm) and cut into pieces of required height. Top and bottom surface of the specimens are then polished to ensure that the surfaces are smooth and parallel.

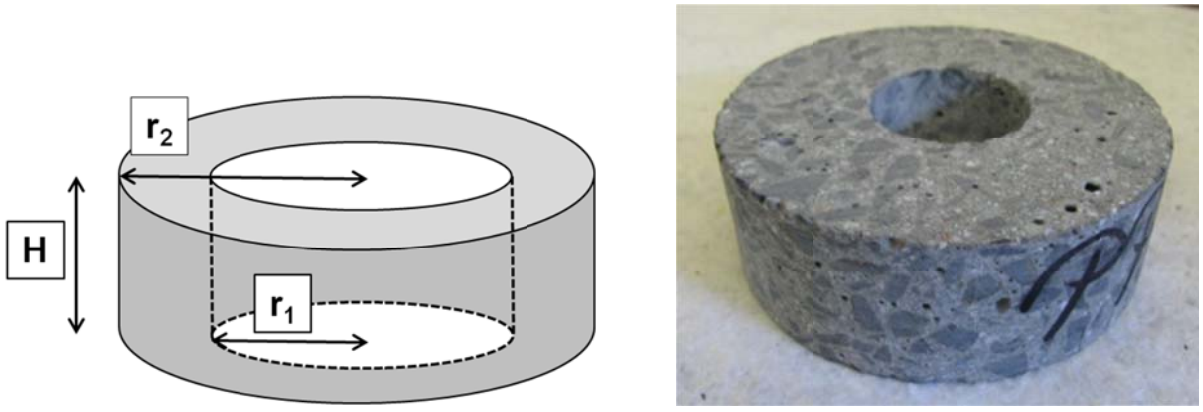

Figure 5.4. Specimen geometry for tests at high temperatures

Since the objective of the measurements is to evaluate the intrinsic permeability of concrete, the effect of humidity on the same is not accounted for. Therefore, prior testing, all specimens are subjected to thermal preconditioning. Different preconditioning methods can be found in the literature with drying temperatures ranging from

60 °C to 105 °C. In the present study, all specimens are dried in oven at 60 °C until constant mass is reached, i.e. less than 0.5 % variation of mass during 24 hours. Concrete C 50/60 is dried for at least 4 weeks, and C 80/95 for at least 6 weeks. Very moderate drying temperature is used in order to minimize the risk against cracking that might influence permeability of concrete.

5.3.2.2 Polypropylene fibres

In this study, polypropylene fibres with a diameter of 15.4 μm and a length of 6 mm are used. Relatively high length to diameter ratio combined with small diameter helps in achieving an interconnected network of fibres and capillaries. The fibres are extruded from pure polypropylene with following material properties: mass density 910 kg/m^3, tensile strength 241 MPa, Young's modulus 573 MPa, maximum (limit) strain 250 %. Fibres lose the thermal stability at 120 °C, melt at approximately 160 °C and burn at 320 °C. The viscosity of the fibres is very low with a melt flow rate (MFR) greater than 1000 g / 10 min, which makes them more effective as compared to the standard fibres (MFR = 30 g / 10min).

Concrete with addition of PP fibres contained 1.0 kg of fibres per m^3 of concrete. The fibres are mixed with aggregates and cement before the water is added to ensure good distribution of fibres throughout the specimen. The microscopic investigations confirmed that the fibres were evenly distributed.

5.3.2.3 Sealant

Graphite sealant is used to seal the specimen and prevent leakage. Graphite is very resistant to high temperatures, but it is susceptible to oxidation. For this reason, the inert nitrogen gas is employed as permeating media. In order to reach desired permeability of graphite (few orders of magnitude lower than the lowest concrete permeability), it is required to apply a pressure of at least 15 MPa. In the experiments the pressure applied prior to measurement and heating was at least 20 MPa. Figure 5.5 presents the specimen and the sealant after the experiment. It can be seen that the graphite deformation reflects the surface texture of the concrete specimen.

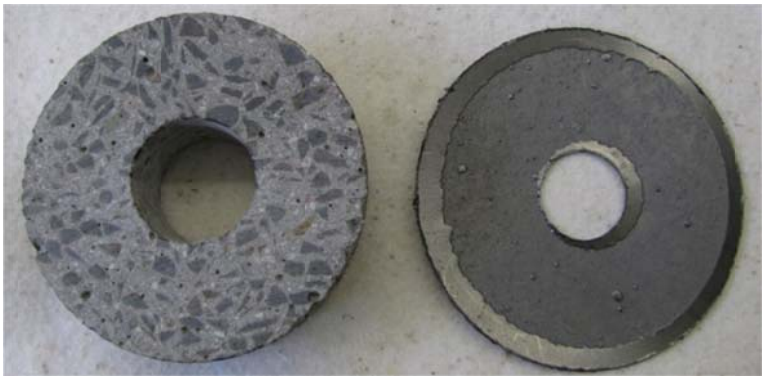

Figure 5.5. Specimen (left) and graphite sealant (right) after the test

5.4 Results and discussion

5.4.1 Validation against RILEM-CEMBUREAU method (permeability measurements at room temperature)

Total of three specimens are tested using RILEM-CEMBUREAU method. The permeability obtained for concrete C 50/60 ranged from 2.16 x 10^{-17} m^2 to 2.95 x 10^{-17} m^2. The permeability for the same concrete obtained using the new test setup ranged from 1.5 x 10^{-17} m^2 to 2.5 x 10^{-17} m^2 for the two tested specimens. Considering the inherent scatter in the permeability values, these results confirm that the new test setup yields realistic permeability values that are comparable to the values obtained following the RILEM-CEMBUREAU method.

5.4.2 New test setup - permeability measurements at room and elevated temperatures

Permeability measurements at elevated temperatures using the new test setup are performed on HPC without and with PP fibres. The relation between measured permeability and temperature is plotted in Figure 5.6. It can be observed that concrete without addition of PP fibres displays a steady rise in permeability with increasing temperature. The average permeability for plain concrete at 20 °C is obtained as 2.6 x 10^{-18} m^2. It is observed that up to 80 °C there is no significant increase in permeability and the change in initial permeability is less than 10 %. Only one specimen exhibited an increase in permeability of approximately 20 %. From 80 °C onwards, there is almost a linear increase in permeability with rise in temperature (semi-log scale). After reaching a temperature of 200 °C, permeability increases by approximately 20 to 30 times, whereas at 300 °C there is an increase in permeability of two orders of magnitude as compared to the value at room temperature. Since no visible surface cracking is observed upon finishing the heat treatment, it can be concluded that the increase of permeability is primarily due to the change in the internal porous system of concrete, i.e. the percentage of larger pores is increased as well as total porosity, as observed by Gallé & Sercombe (2001).

Residual values obtained after cooling the specimens to room temperature are approx. 10-25 % higher than the values obtained at the elevated temperatures. This difference between permeability at hot state and residual permeability is attributed to the damage (micro-cracking) of concrete due to inevitable thermal gradients present at cooling.

In case of concrete with PP fibres, at 20 °C the permeability is found to be very similar to that of concrete without fibres. Therefore, it can be stated that the addition of PP fibres does not significantly influence the transport properties of concrete at room temperatures. Up to 80 °C the behaviour of the concrete with fibres remains similar to that of the concrete without fibres. However, between 80 °C and 130 °C concrete

with fibres exhibits a sudden progressive increase in permeability of approximately two orders of magnitude (Figure 5.6). The trend continues up to the temperatures of around the melting point (160 °C) of PP fibres. At 150 °C, the difference between the two concrete mixtures is almost two orders of magnitude. Beyond 130 °C the rate of increase in permeability reduces and it roughly corresponds to that of the concrete without fibres. Same as in the case of concrete without fibres, the residual permeability values of concrete with fibres are found to be somewhat higher than the permeability values at elevated temperatures.

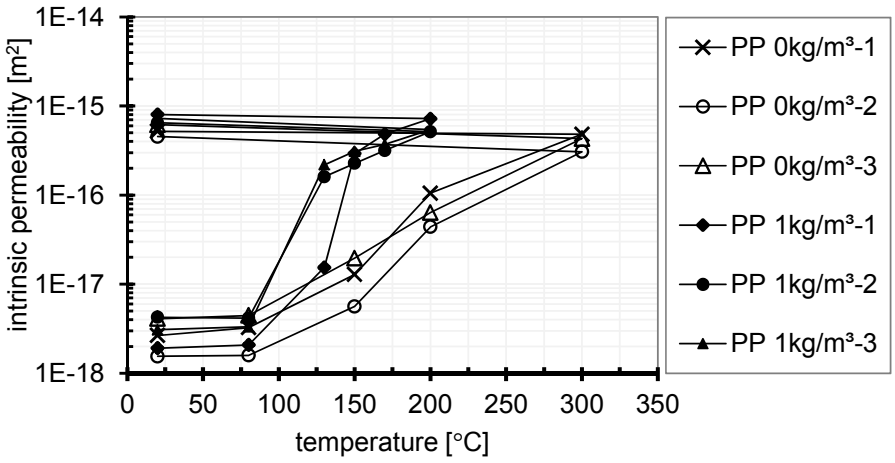

Figure 5.6. Intrinsic permeability of concrete as a function of temperature

The increase in permeability at temperature in the vicinity of the melting temperature is generally considered to be a consequence of flow of polypropylene into the surrounding material (micro-cracks). However, it is important to note that the experiments clearly demonstrate that the permeability increases already at a much earlier stage, and this behaviour cannot be attributed solely to the flow (melting) of polypropylene. Moreover, it can be noticed that this rate is much higher than that around the melting point of fibres. It is obvious that sudden permeability increase of the concrete with PP fibres prevents explosive spalling. Moreover, since vapour pressure is controlled by permeability the experimental results indirectly confirm that vapour pressure is responsible for explosive spalling.

The polypropylene fibres melt at approximately 160 °C, however, the thermal stability is lost already at approximately 120 °C. Measurements of the elastic modulus up to approximately 100 °C performed by Zhou & Mallick (2002) show that the elastic modulus of polypropylene decreases progressively with increasing temperature. Upon reaching 120 °C the fibres soften and are susceptible to change of shape. Fibres with higher melt flow index will most likely exhibit faster decrease of the elastic modulus. When heated, fibres expand with a total expansion of approximately 7 %, see for example Albizzati & Moore (1996). Even though pure polypropylene expands equally in all directions, extruded fibres expand in the width direction, but shorten in the length direction. This is a consequence of the polypropylene extrusion, the method

which is used to manufacture the fibres. The change of shape during heating weakens the link between concrete and fibres.

Because of the hydrophobic nature of polypropylene, the fibre-concrete interface is not very strong even in the virgin concrete. Combination of these effects can result in compressed gas pushing the weakened fibres away from the concrete thus creating a path for the gas. This is assumed to be the main driving force influencing the sudden increase in permeability at temperatures below the melting point of the fibres. As fibres start to melt at 160 °C, permeability further increases (Figure 5.6). It is not completely clear what happens to fibres after melting. Therefore, a preliminary microscopic investigation of the microstructure using scanning electron microscope is performed with the main objective of providing a better understanding of the processes at the microscopic level. The results of microscopic investigation are discussed later.

5.4.3 Influence of the compressive stress on permeability

In the new test setup proposed here, compressive load is applied on the specimen before measuring permeability. Due to thermal expansion and restraints on the specimen, the compressive load applied before the first measurement increased during the heating. The measured increase in pressure due to temperature is plotted in Figure 5.7 (left). It can be seen that the initial compressive stress of approximately 20 MPa increases due to heating to approximately 26 MPa.

Since the permeability measurements are performed on loaded concrete, it is important to evaluate the influence of compressive stress on permeability. This investigation is performed at room temperatures. The maximum temperature reached during the experiments is 300 °C. At this temperature there is a maximum reduction of compressive strength of 20 % for high strength concrete (Phan & Carino 2003). It is therefore acceptable to perform these experiments at room temperatures. The prestressing in the experiments is varied from 18.5 MPa to 33 MPa.

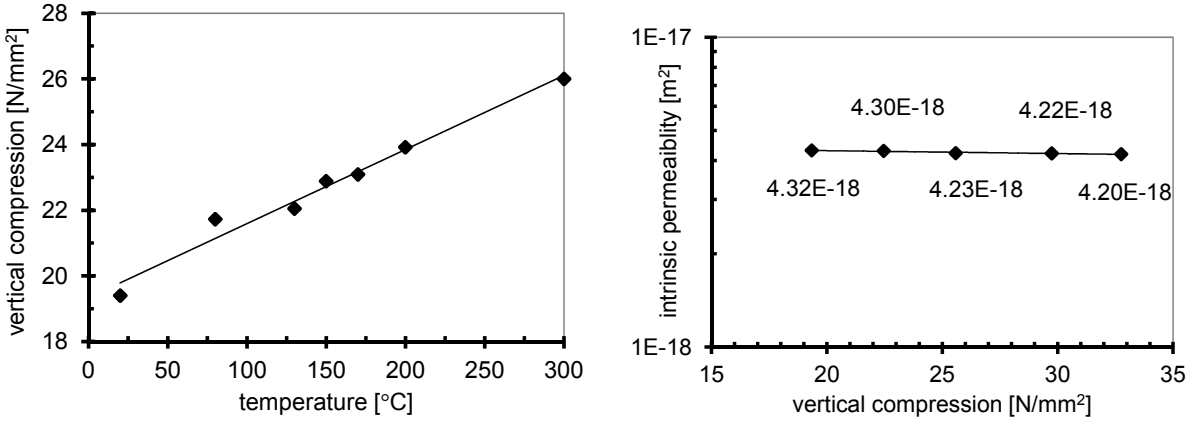

Figure 5.7. The relation between temperature and compressive stress (left) and the relation between compressive stress and permeability at room temperature (right)

The results of the permeability measurements at different load levels are shown in Figure 5.7 (right). It can be seen that the change of permeability with increasing pressure is not pronounced for pressures up to 33 MPa (approximately 40 % of the average compressive strength at room temperature). With increasing pressure, permeability slightly decreases, such that the permeability measured for pressure 18.5 MPa and 33 MPa differ by approximately 3 %. Since there is no additional connectivity of pores created, this slight decrease in permeability can be attributed to the effect of the applied stress on concrete specimen, i.e. the volumetric behaviour at low load levels is strictly contracting (Choinska et al. 2007). After the application of the highest load level, the specimen is inspected for any visible cracks and no cracks could be observed. These findings are consistent with the results of other researchers, such as Choinska et al. (2007) and Hoseini et al. (2009), who stated that the mechanical compressive stress adversely effects permeability only at very high stress levels (75-80 % of the compressive strength). Therefore, it can be concluded that the compressive load applied in the new test setup has no significant effect on the measured permeability of concrete.

5.4.4 Microscopic investigation of the concrete with polypropylene fibres

As already mentioned, fibres melt and thereby leave free pores for the water vapour to escape. It is, however, not completely clear how exactly do fibres increase the available pore space. Kalifa et al. (2001) suggest that the polypropylene fibres melt (at 160-170 °C) and are then absorbed by the cement mortar matrix. However, permeability measurements clearly show that the permeability increases progressively already at temperatures between 80 °C and 130 °C. In order to throw more light on the possible reasons, microscopic investigation using electron microscope is performed.

The specimens of sizes 20 x 20 x10 mm are cut out from concrete rings (concrete containing 1.0 kg/m^3 PP of fibres). The rings were previously stored for 9 months at relative humidity of 60 %. The surface of the specimens is polished to assure good visibility of the microstructure. The specimen without prior exposure to high temperature is observed under a scanning electron microscope (SEM) and the result is shown in Figure 5.8 (left). Black round particles in the figure represent the PP fibres in cross section. At larger scale it could be observed that the fibres are nicely dispersed in the concrete specimen. The same specimen is then heated up to 200 °C at a very moderate temperature rate of 5 °C/min. Specimen is kept at this temperature for 20 minutes, 6 hours and 2 days, respectively, and cooled to the room temperatures after each of these exposures. Due to technical difficulties, the cooling after the first exposure is performed at a very fast rate.

Upon the completion of each temperature step, the microstructure of the specimen is observed using SEM. For the exposure duration of 20 minutes, no changes of the PP fibres could be noticed, whereas the cement matrix suffered extensive micro-

cracking. The latter is partially due to the very fast cooling. However, a closer examination of the microstructure in Figure 5.8 (left) reveals that the contact fibre-cement matrix is not perfectly round, but there are certain flaws (notches) as well as some initial micro-cracks. During heating the notches lead to initiation of micro-cracking and existing micro-cracks propagate. Therefore, possibly, even if the cooling rate is much slower, the difference in the thermal dilatation of cement matrix and polypropylene combined with the initial micro flaws would cause micro-cracking at the contact of the two materials.

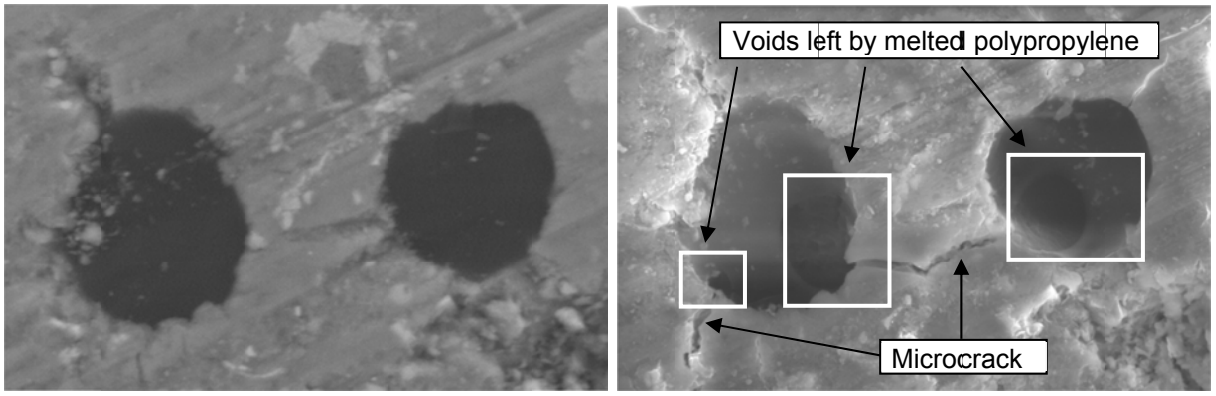

Figure 5.8. Scanning electron microscope photos of the virgin concrete with addition of PP fibres (left) and the same concrete exposed to 200 °C for 2 days (right)

Even though the temperature was well above the melting point of the fibres, exposure duration of 20 minutes was insufficient for the polypropylene to flow either into the mortar matrix or into the micro-cracks. The photos of the exposure duration of 20 minutes and 6 hours are not shown for brevity reasons. Figure 5.8 (right) shows the specimen after 2 days of exposure to 200 °C. As can be seen, the volume of the polypropylene in the pore is reduced, since part of the polypropylene is transported into the micro-cracks in the cement matrix. Small dark portions (marked rectangles in Figure 5.8 right) represent the voids created by melting of polypropylene. However, no such change could be observed in the parts of the fibre not surrounded by micro-cracks. This implies that the cement matrix is not capable of absorbing the fluid polypropylene. Specimen after 6 hours of exposure is similar to the one shown in Figure 5.8 (right), the only difference is that the amount of the polypropylene that went into the micro-crack is substantially smaller. If we compare the three exposure durations, it is obvious that even though the fibres melt rather fast, it takes much more time for them to flow into the micro-cracks. For given boundary conditions (e.g. temperature and confinement) the transport of fluid polypropylene is obviously time dependent, and this should be taken into consideration.

It should be noted that PP fibres with different properties are available in the market. Recent studies reported by Knack (2011) have shown that the effectiveness of fibres in mitigation of spalling depends greatly on their viscosity in fluid state. The decrease in viscosity is achieved by decreasing the molecular size of the fibres. Concrete con-

taining fibres with low viscosity exhibited no spalling, whereas concrete containing fibres with high viscosity suffered severe spalling even at very high dosages. Thin fluids are more fluent and will be absorbed much faster than thick fluids. PP fibres used in this study exhibit very low viscosity (melt flow rate index indicates that the ease of flow is 40 to 50 times greater than for the standard PP fibres). Concrete containing these fibres proved to be effective in mitigating spalling at a very low dosage of 1.0 kg/m^3. However, in spite of very low viscosity, the microscopic investigation suggests that no polypropylene could be absorbed by the cement matrix. Finally, it is important to note that only micro-cracks, which exist also in concrete without polypropylene fibres, are not capable of increasing permeability at the critical temperature level (spalling temperature). This is because they do not form an interconnected porous network, as it is case with polypropylene fibres.

5.5 Conclusions

A new experimental setup for measuring permeability of concrete at high temperature is presented. The new setup is first verified and then employed in the measurements of permeability of high strength concrete without and with polypropylene fibres at elevated temperature. Based on the presented results the following can be concluded:

(i) The new test setup is validated against the widely used RILEM-CEMBUREAU method. It is shown that the results obtained at room temperature exhibit very good agreement;

(ii) Even though the new test setup yields acceptable results, the improvements are needed in order to enhance the applicability of the test setup and to increase the accuracy of the measurements;

(iii) It is shown that permeability of concrete without PP fibres increases almost linearly (semi-log scale) during heating, whereas concrete with PP fibres exhibits a sudden rise in permeability at temperature between 80 °C and 130 °C, i.e. before the melting temperature of fibres;

(iv) The results clearly point out the role of permeability on explosive spalling and indirectly confirm that vapour pressure is responsible for the explosive spalling of concrete;

(v) Softening of fibres and weak concrete-fibre interface are considered to be the main driving force of the permeability increase below the fibre melting point;

(vi) The effect of compressive load on permeability is investigated and it is shown that the moderate compressive stresses do not influence permeability of concrete;

(vii) Scanning electron microscope observations suggest that the melted fibres flow into the surrounding micro-cracks (generated by the thermally induced stresses), and provide additional path for the gas transport in concrete, which results in permeability increase. There is a clear indication that the fluid polypropylene does not diffuse into the cement paste.

NUMERICAL STUDY

6. THE THERMO-MECHANICAL MODEL

The thermo-mechanical (TM) model used in this work employs the temperature dependent microplane model as constitutive law for concrete. The model is developed by Ozbolt et al. (2005) and Periskic (2009). The numerical analysis is based on (i) evaluating the temperature profile accounting for convection, conduction and radiation, and (ii) evaluating the mechanical behaviour of the structural element considering degradation of the material properties due to elevated temperatures. In this section the model is presented in detail and the validation of the same against the available experimental results is reported. More details on the TM model can be found in Ozbolt et al. (2005) and Periskic (2009).

6.1 Transient thermal analysis

First step of the transient analysis is to obtain the temperature distribution over a solid structure of volume Ω at time t. In each point of continuum, which is defined in Cartesian coordinate system (x,y,z), the conservation of energy has to be fulfilled. This can be expressed by the following equation:

$$\lambda \Delta T(x,y,z,t) - c\rho \frac{\partial T}{\partial t}(x,y,z,t) = 0 \tag{6.1}$$

where T = temperature, λ = conductivity, c = heat capacity, ρ = mass density and Δ = Laplace-Operator. The surface boundary condition that has to be satisfied reads:

$$\lambda \frac{\partial T}{\partial \boldsymbol{n}} = \alpha (T_M - T) \tag{6.2}$$

where $\boldsymbol{n}$ = normal to the boundary surface Γ, α = transfer or radiation coefficient and T_M = temperature of the media in which surface Γ of the solid Ω is exposed to. To solve the problem by the finite element method the equations (6.1) and (6.2) have to be written in weak (integral) form. For more detail see Ozbolt et al. (2005), Ozbolt et al. (2008) and Periskic (2009).

6.2 Microplane model with relaxed kinematic constraint

The constitutive law employed for concrete in this work is temperature dependent microplane, which is an extension of the microplane model with relaxed kinematic constraint (Ozbolt et al. 2001). The model utilizes the strength of both macroscopic and microscopic models and therefore is known to provide results in very good agreement with the experiments, see for example Ozbolt et al. (1999). The model is

able to realistically describe micro-structural phenomena such as cohesion, friction and aggregate interlock.

Contrary to classical macroscopic type of constitutive laws, which are based on tensorial invariants of stresses and strains, in the microplane model the material response is calculated based on the monitoring of stresses and strains in a number of predefined directions. Integrating microplane stresses in a thermodynamically consistent way, it is possible to calculate macroscopic stress tensor from a known macroscopic strain tensor. The constitutive framework is similar to discrete type of the models (e.g. random particle model) with the difference that the model is formulated in the framework of continuum. The physical concept behind the microplane model was already discussed at the beginning of last century by Mohr (1900) and Taylor (1938). The microplanes may be imagined to represent damage planes or weak planes in the microstructure, such as those that exist at the contact between aggregate and the cement matrix or slip planes in the theory of plasticity as shown in Figure 6.1 (Ozbolt et al. 2001).

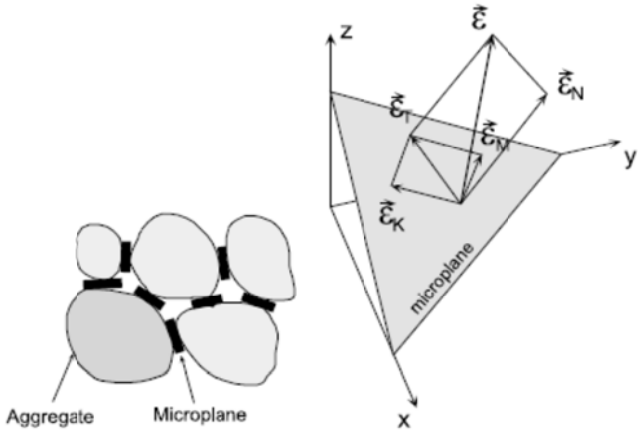

Figure 6.1. Microplane model: Idealized contact planes (left) and decomposition of the total macroscopic strain tensor on the microplane (Ozbolt et al. 2001) (right)

Generally, in macroscopic models, the macroscopic strain tensor is related to a macroscopic stress tensor through a constitutive relationship valid at macro level. In the microplane model the macroscopic strain tensor at each integration point is projected into a number of microplanes in normal and shear directions, which characterize the material behaviour.

In the model each microplane is defined by its unit normal vector components n_i. Microplane strains are assumed to be the projections of macroscopic strain tensor ε_{ij} (kinematic constraint). Normal (σ_N, ε_N) and two shear stress-strain components (σ_K, σ_M, ε_K, ε_M) are considered on the microplane. To realistically model concrete, the normal microplane stress and strain components have to be decomposed into volumetric and deviatoric parts ($\sigma_N = \sigma_V + \sigma_D$, $\varepsilon_N = \varepsilon_V + \varepsilon_D$). Unlike the most microplane formu-

lations for concrete, which are based on the kinematic constraint approach, to prevent unrealistic model response for dominant tensile load, in this model kinematic constraint is relaxed (Ozbolt et al. 2001).

Figure 6.2 shows the implementation of the model at the 3D FE level. As shown, for a 3D solid finite element having eight integration points, the macroscopic strain tensor is for each integration point first projected to the microplane and then decomposed into normal and shear microplane directions. Uniaxial stress-strain relations on each microplane are then employed to determine the respective microplane stress components. Finally, using the principle of virtual work, a numerical integration over all microplanes is performed to determine the macroscopic stress tensor.

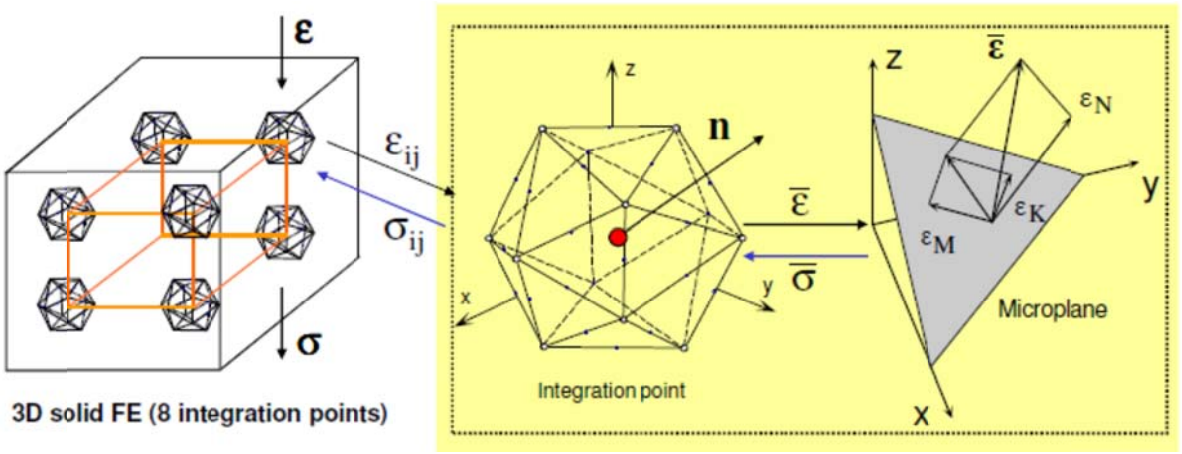

Figure 6.2. Concept of microplane model (Ozbolt et al. 2001)

At the integration point, the number of microplanes considered can have any natural number as a value. Obviously, larger number of microplanes will produce more accurate results but at the same time will need much higher computational effort. A good balance between the computational time and accuracy can be obtained by considering 21 microplanes for the symmetric part of the unit radius sphere, as shown in Figure 6.2. The major advantage of the model is that, since microplanes with different spatial orientations have been considered, the tensorial invariant restrictions are automatically fulfilled and they need not be directly enforced.

Based on the micro-macro work conjugancy of volumetric-deviatoric split and using in advance defined microplane stress-strain constitutive laws, the macroscopic stress tensor is calculated as an integral over all possible predefined microplane orientations:

$$\sigma_{ij} = \sigma_V \delta_{ij} + \frac{3}{2\pi}\int_S \left[\sigma_D \left(n_i n_j - \frac{\delta_{ij}}{3} \right) + \frac{\sigma_K}{2}\left(k_i n_j + k_j n_i \right) + \frac{\sigma_M}{2}\left(m_i n_j + m_j n_i \right) \right] dS \qquad (6.3)$$

where S = the surface of the unit radius sphere, δ_{ij} = Kronecker delta and k_i and m_i = directions of shear microplane components.

To account for large strains and large displacements, Green-Lagrange finite strain tensor is used. Furthermore, to account for the loading history of concrete, the co-rotational Cauchy stress tensor is employed. For more detail see Bazant et al. (2000) and Ozbolt et al. (2001).

6.3 Thermo-mechanical coupling

To account for the effect of temperature the macroscopic mechanical properties of concrete need to be temperature dependent. The nonlinear finite element analysis is incremental and the load increment is defined by the time step Δt in which the load, boundary conditions, temperature, etc. change. In the present model temperature is constant during the load increment. Consequently, in each load step, the material parameters (that are temperature dependent) are constant as well, Ozbolt et al. (2005) and Periskic (2009).

6.3.1 Young's modulus of concrete

Experiments show that with the temperature increase Young's modulus E decreases (Schneider 1982). In the present model, temperature dependent Young's modulus follows the proposal of Stabler (2000), i.e. E is assumed to be a scalar function of temperature that reads:

$$\begin{aligned} &E(T) = \left(1 - \max\left(\omega_{t,E}\right)\right) E^{20} \\ &\omega_{t,E} = 0.2\theta - 0.01\theta^2 \qquad \text{for } 0 \le \theta \le 10 \\ &\omega_{t,E} = 1.0 \qquad\qquad\qquad\quad \text{for } \theta > 10 \end{aligned} \tag{6.4}$$

where E^{20} = Young's modulus at temperature T_0 = 20 °C and θ = $(T\text{-}T_0)$ / 100 $^{\circ}C$ is the relative temperature. The dependency (6.4) is plotted in Figure 6.3 (left). As can be seen it shows good agreement with the experimental evidence.

6.3.2 Compressive strength of concrete

According to the experimental evidence (see Section 2.3.1) at temperatures up to 300 °C concrete compressive strength remains almost constant and decreases linearly thereafter. In the present model it is assumed that up to T = 300 °C cylinder compressive strength f_c is temperature independent and for higher temperature it decreases as a linear function of temperature (Periskic 2009):

$$
\begin{aligned}
&f_c(T) = \max\left(\omega_{t,f_c}\right) f_c^{20} \\
&\omega_{t,f_c} = 1.0 \qquad \text{for } 0 \le \theta \le 2.80 \\
&\omega_{t,f_c} = 1.43 - 0.153\theta \qquad \text{for } \theta > 2.80
\end{aligned}
\tag{6.5}
$$

where f_c^{20} = uniaxial compressive strength at T = 20 °C. The adopted dependency is plotted in Figure 6.3 (right) and compared with experimental results. As can be seen the comparison shows good agreement.

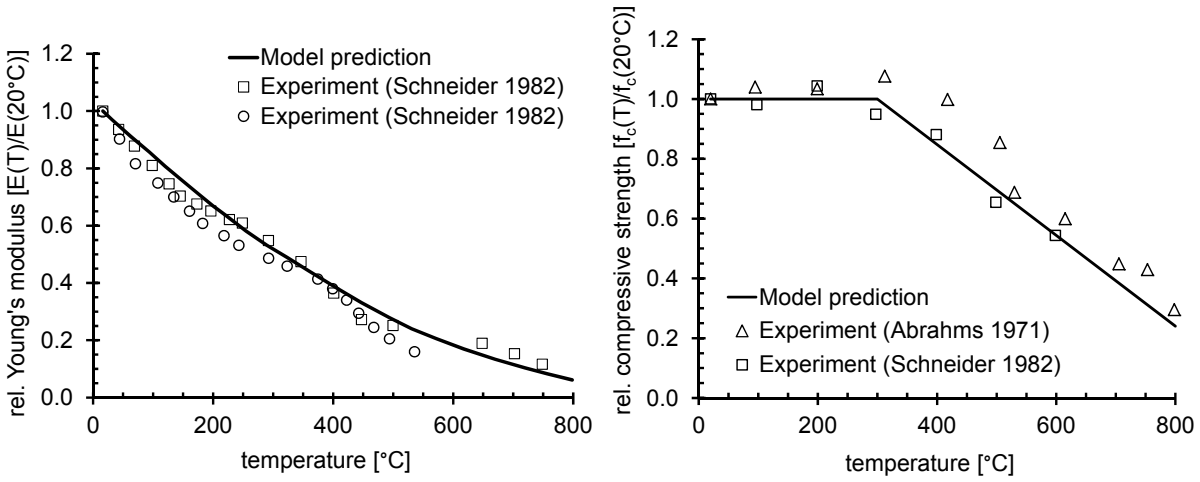

Figure 6.3. The dependency of the Young's modulus of concrete (left) and concrete compressive strength (right) on temperature

6.3.3 Tensile strength of concrete

Experimental evidence indicates that the tensile strength of concrete decreases almost linearly with increase of temperature, as discussed in Section 2.3.3. In the present model the following dependency of tensile strength on temperature is adopted as (Periskic 2009):

$$
\begin{aligned}
&f_t(T) = \max\left(\omega_{t,f_t}\right) f_t^{20} \\
&\omega_{t,f_t} = 1.0 - 0.13\theta
\end{aligned}
\tag{6.6}
$$

where f_t^{20} = uniaxial compressive strength at T = 20 °C. The plot of Eq. (6.6) is shown in Figure 6.4 (left) along with the experimental data.

6.3.4 Concrete fracture energy

The experimental data presented in Section 2.3.4 (Zhang et al. 2002) show that fracture energy increases by 60 % up to 300 °C and decreases to approximately 90 % of its initial value at 600 °C. In the present model, the dependency of concrete fracture

energy G_F on the temperature is obtained by fitting of test data of Zhang & Bicanic (2002). The adopted dependency reads (Periskic 2009):

$$
\begin{aligned}
&G_F(T) = \max\left(\omega_{t,G_f}\right) G_F^{20} \\
&\omega_{t,G_F} = 1.0 + 0.407\,\theta - 0.0727\,\theta^2 \qquad \text{for } 0 \le \theta \le 2.80 \\
&\omega_{t,G_F} = 0.917 + 0.467\,\theta - 0.0833\,\theta^2 \qquad \text{for } \theta > 2.80
\end{aligned}
\tag{6.7}
$$

where $G_F{}^{20}$ = concrete fracture energy at T = 20 °C. The dependency is plotted in Figure 6.4 (right) and compared with experimental results. As can be seen, the comparison shows good agreement.

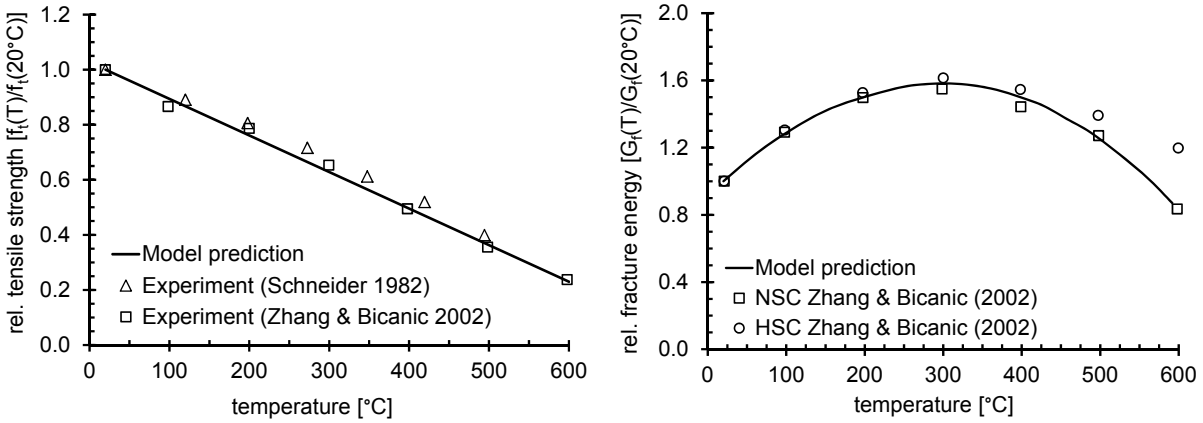

Figure 6.4. Relative tensile strength of concrete as a function of temperature (left) and relative concrete fracture energy of concrete as a function of temperature (residual conditions) (right)

6.3.5 Yield strength of steel

The experiments show that the mechanical properties of steel exposed to elevated temperature degrade (Kordina & Meyer-Ottens 1999). In the model this has been accounted for through reduction of the yield stress and Young's modulus, as shown in Figure 6.5.

Even though there is a reduction of these two properties due to high temperatures, experiments have shown that, unlike concrete, steel can recover its yield stress (Takeuchi et al. 1993; Neves et al. 1996). Furthermore, the residual Young's modulus of steel is equal to the value of virgin steel, i.e. residual Young's modulus is not temperature dependent. The recovery of the yield stress of steel as implemented in the model is plotted in Figure 6.6.

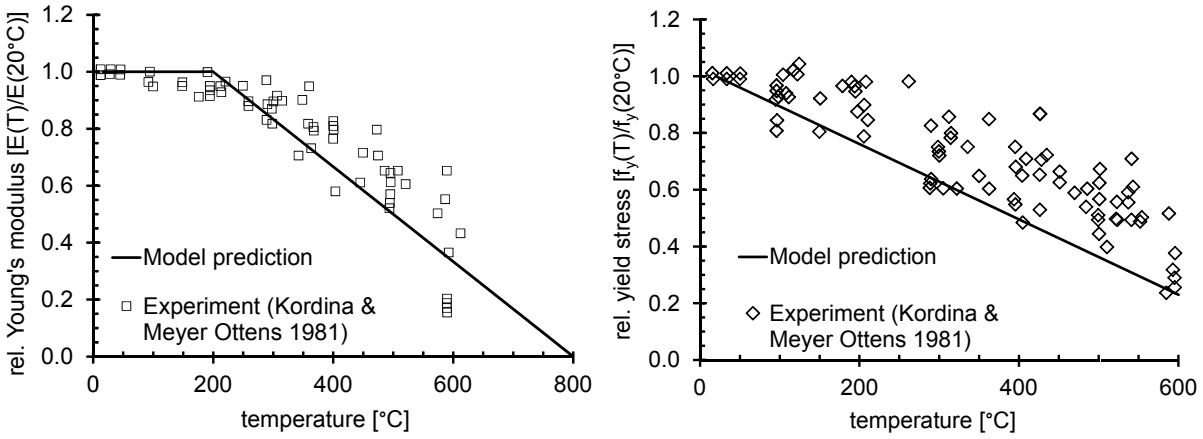

Figure 6.5. Relative steel Young's modulus (left) and relative steel yield stress (right) as a function of temperature (hot conditions)

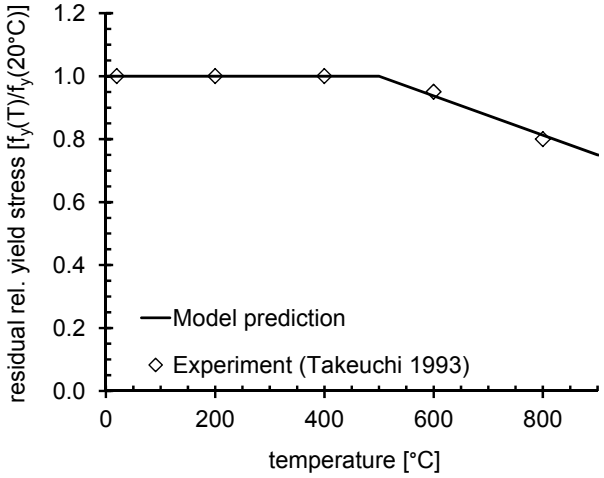

Figure 6.6. Relative steel yield stress as a function of maximum exposure temperature (residual conditions)

6.4 Thermal strains in the microplane model

6.4.1 Decomposition of strain tensors

In the present model the total strain tensor ε_{ij} (indicial notation) for stressed concrete exposed to high temperature is decomposed as (Ozbolt et al. 2005):

$$\varepsilon_{ij} = \varepsilon_{ij}^{m}(T,\sigma) + \varepsilon_{ij}^{fts}(T) + \varepsilon_{ij}^{lits}(T,\sigma) \tag{6.8}$$

where ε_{ij}^{m} = mechanical strain tensor, ε_{ij}^{fts} = free thermal strain tensor, ε_{ij}^{lits} = load-induced thermal strain tensor. Note that it is assumed here that strains are small such that the addition and not multiplication decomposition is used. In general, the mechanical strain component can be decomposed into elastic, plastic and damage part. In the present model these strain components are obtained from the constitutive

law. The free thermal strain is stress independent and is experimentally obtained by measurements on non-loaded specimen. In such experiments it is not possible to isolate shrinkage of cement paste, therefore the temperature dependent shrinkage is contained in the free thermal strain. As discussed in Section 2.4.2, the load-induced thermal strain is stress and temperature dependent. This strain is also modelled using a single tensor.

6.4.2 Free thermal strain

Although the experiments indicate that the free thermal strain depends on the heating rate (see Section 2.4.1), in the present model it is assumed that this strain depends only on temperature. Moreover, it is assumed that in the case of a non-loaded specimen, the thermal strains are equal in all three mutually perpendicular directions (isotropic thermal strains). The temperature dependency of the free thermal strain, as adopted in the present model, reads (Periskic 2009):

$$\dot{\varepsilon}_{ij}^{fts}\left(T\right)=\alpha\,\dot{T}\,\delta_{ij}$$
$$\alpha=\begin{cases}6.0\cdot10^{-5} & \text{for } 0\le\theta\le 6.0\\ 0 & \text{for } \theta>6.0\end{cases} \tag{6.9}$$

$$\text{with } \theta=\left(T-T_0\right)/100°C \tag{6.10}$$

This temperature dependency approximately corresponds to experimental data obtained for sandstone aggregates. However, it is also possible to input a desired temperature dependent path for free thermal strain in order to account for the effect of different aggregates or to model the thermal strain of different concrete constituents.

6.4.3 Load-induced thermal strain

As discussed in Section 2.4.2, when concrete is loaded before heating, the resulting thermal strain is different from that occurring in a non-loaded specimen (Khoury 2006). The difference can be obtained if the free thermal strain is subtracted from the resulting thermal strain, which results in the so called load-induced thermal strain. Due to its similarity for different concrete types, a common “master” LITS curve is taken to exist up to temperatures of about 450 °C Khoury (2006) In the present model (Periskic 2009) the bi-parabolic function is used for representing load induced thermal strain (Pearce et al. 2004) at macro-scale, which reads:

$$\dot{\varepsilon}^{lits}\left(T,\sigma\right)=\frac{\sigma}{f_c^{20}}\beta\dot{T}$$
$$\beta=0.01\begin{cases}2A\theta+B & \text{for } 0\le\theta\le\theta^*=4.5\\ 2C\left(\theta-\theta^*\right)+2A\theta^*+B & \text{for } \theta>\theta^*\end{cases} \tag{6.11}$$

where θ^* = dimensionless transition temperature between the two expressions (470 °C) and θ according to Eq. (6.10). The above two expressions are introduced to account for abrupt change in behaviour detected in the experiments. Constants *A*, *B* and *C* are experimentally obtained constants and in the present model are set as: *A* = 0.0005, *B* = 0.00125 and *C* = 0.0085.

The presented implementation of load induced thermal strain is valid for the macro-scale modelling approach, when concrete is idealized as a homogeneous material. However, when modelling concrete at meso-scale, load induced thermal strains are not explicitly defined in the model, since the largest part of these strain comes automatically from the meso-scale model. The validity of this hypothesis is investigated by modelling experiments available in the literature and the results are presented in the following section.

The strong form of the governing differential equations (6.1) and (6.2) is rewritten into the integral form and together with the temperature dependent microplane model for concrete implemented into 3D FE code (Periskic 2009). Damage and cracking are modelled in the framework of smeared crack continuum. To assure objectivity of the analysis with respect to the size of the finite elements crack band method is used (Bazant & Oh 1983). The non-mechanical part of the model is obtained using direct integration scheme of implicate type, whereas the equilibrium between external and internal forces is obtained iteratively employing Newton-Raphson method. For more detail see Ozbolt et al. (2001), Ozbolt et al. (2008) and Periskic (2009).

6.5 Validation of the thermo-mechanical model against experiments on plain concrete: macro scale

The above described numerical model was implemented into a three-dimensional FE code, see Ozbolt et al. (2005) and Periskic (2009). In order to demonstrate that this code is able to realistically predict the behaviour of concrete exposed to high temperatures (fire), the same is used to simulate the temperature dependent flexural and splitting strength of concrete after exposure to elevated temperatures. The numerical results are then compared to the experiments performed by Yaragal (2010). Concrete used in these tests ranged from grade M20 to M40. In the experiment the specimens were heated in an electrical oven with a rate of 2 °C/min up to 800 °C in steps of 100 °C. Before performing residual strength test the specimens were cooled down to room temperature with a rate of 2 °C/min. Residual flexural tensile strength was measured on beam specimens with dimensions 500 x 100 x 100 mm according to IS516 (1959). In the second example the cylinders with a diameter of 150 mm and height of 300 mm were used to test the residual splitting tensile strength. Both test setups are shown in Figure 6.7.

The geometry and boundary conditions for both test types are same as in the experiment. Figure 6.8 depicts the 3D finite element mesh and boundary conditions for the flexural and splitting test specimens. In both cases concrete is discretized with hexahedral solid finite elements. Platens at the supports and in the loading points are introduced to prevent localization of damage in these points. These are also modelled as hexahedral finite elements. The mechanical loading in both cases is performed in displacement control regime.

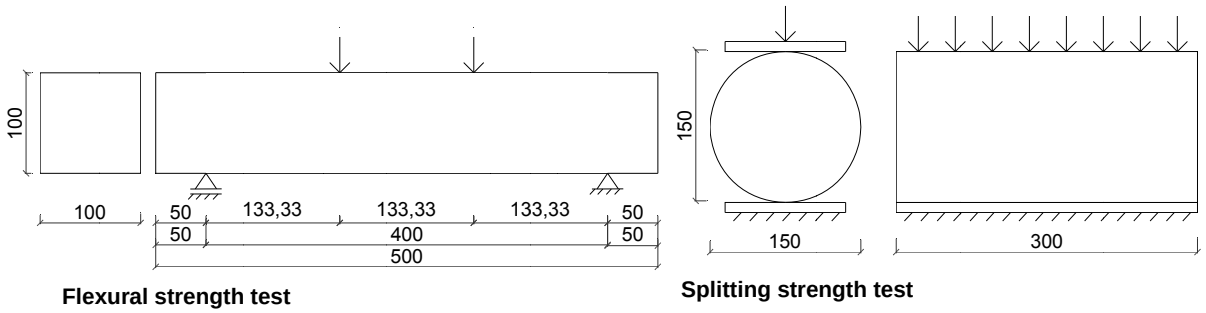

Figure 6.7. Experimental setup: four point bending test (left) and splitting test (right)

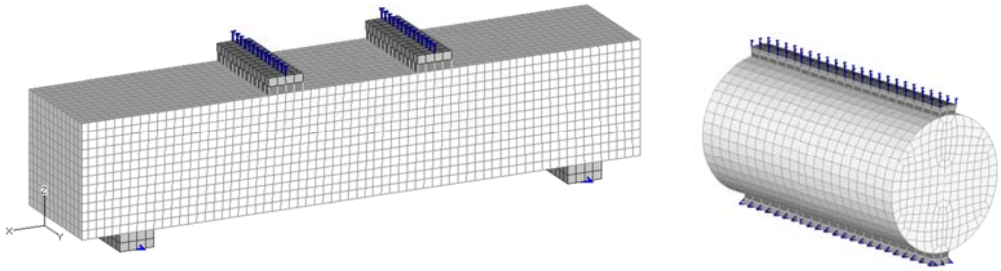

Figure 6.8. 3D finite element mesh: beam (left) and cylinder model (right)

6.5.1 Material properties

The retention of flexural and splitting strength is analysed for concrete grades M20, M30 and M40. The summary of all concrete properties used in the finite element study is given in the Table 6.1. Tensile and compressive strength are obtained from the experiments and other material properties are estimated from literature (Karihaloo 1995).

The material used for the loading and supporting plates is assumed to be linear elastic in order to avoid unrealistic local damage. The contact between the loading platens and concrete is assumed to be extremely weak during the heating phase. This allowed concrete to expand freely when heated as in the experiment. Otherwise the concrete would be constrained and unrealistic cracking of these contact areas would occur. After the heating phase the analysis is stopped, and the material of the contact interface is replaced with initial linear elastic, relatively stiff elements. The analysis is then restarted and four point bending and splitting tests are performed.

Table 6.1. Concrete properties used in the finite element analysis

Concrete	M20	M30	M40
$f_{c,cube}$	32.96	31.93	50.60
$f_{c,cyl}$	26.37	25.54	40.48
G_F	0.07	0.07	0.09
E	24391	24007	30220
f_{st}	2.78	3.25	4.38
f_t	2.50	2.93	3.94

6.5.2 Heating/cooling regime and subsequent loading

The specimens are heated up to 800 °C with the temperature steps of 100 °C. Heating rate is 2 °C/min. After each step temperature is retained for 2 hours. Flexural and splitting strength are investigated on both heated (“hot strength”) and specimens cooled down to room temperature (“residual strength”). To investigate the hot strength the specimen is mechanically loaded upon end of the retention time at each of the target temperatures. Residual strength tests are performed on cooled specimens. After retention time of 2 hours at each temperature level the specimens are cooled down to 20 °C at a cooling rate of 2 °C/min.

6.5.3 Results and discussion

Figure 6.9 shows the results of numerical simulation along with their experimental counterparts. The experimental results represent residual flexural strength, as the loading is performed on specimens cooled down to room temperature. It can be seen that for all concrete qualities there is an almost linear decrease of flexural strength with increasing temperature. Flexural strength reduces to zero at temperatures between 500 °C and 600 °C. The decrease of the hot strength is also given in Figure 6.9. It has no experimental counterparts as experiments on hot specimens are demanding and were not performed. It is noticeable that the hot strength is in general somewhat higher than the residual strength. This can be explained by the additional cracking (damage), which concrete suffers during cooling. As the cooling rate is relatively slow (2 °C/min), the cracking due to the cooling is not very severe. If, however, cooling rate would be somewhat higher most probably the difference between residual and hot strength would also increase. This can be a significant effect since the decrease of temperature in real fires can be quite fast. It can be concluded that the numerical prediction of residual strength is in good agreement with the experimental results.

Figure 6.9 (bottom right) shows the load-displacement curves obtained for concrete grade M30 for different temperature levels. The data given are numerically obtained residual flexural strengths. No experimental counterparts were provided in the literature. It is apparent that flexural strength drops with increasing temperature. The stiff-

ness of the beams decreases whereas ductility increases with increasing temperature.

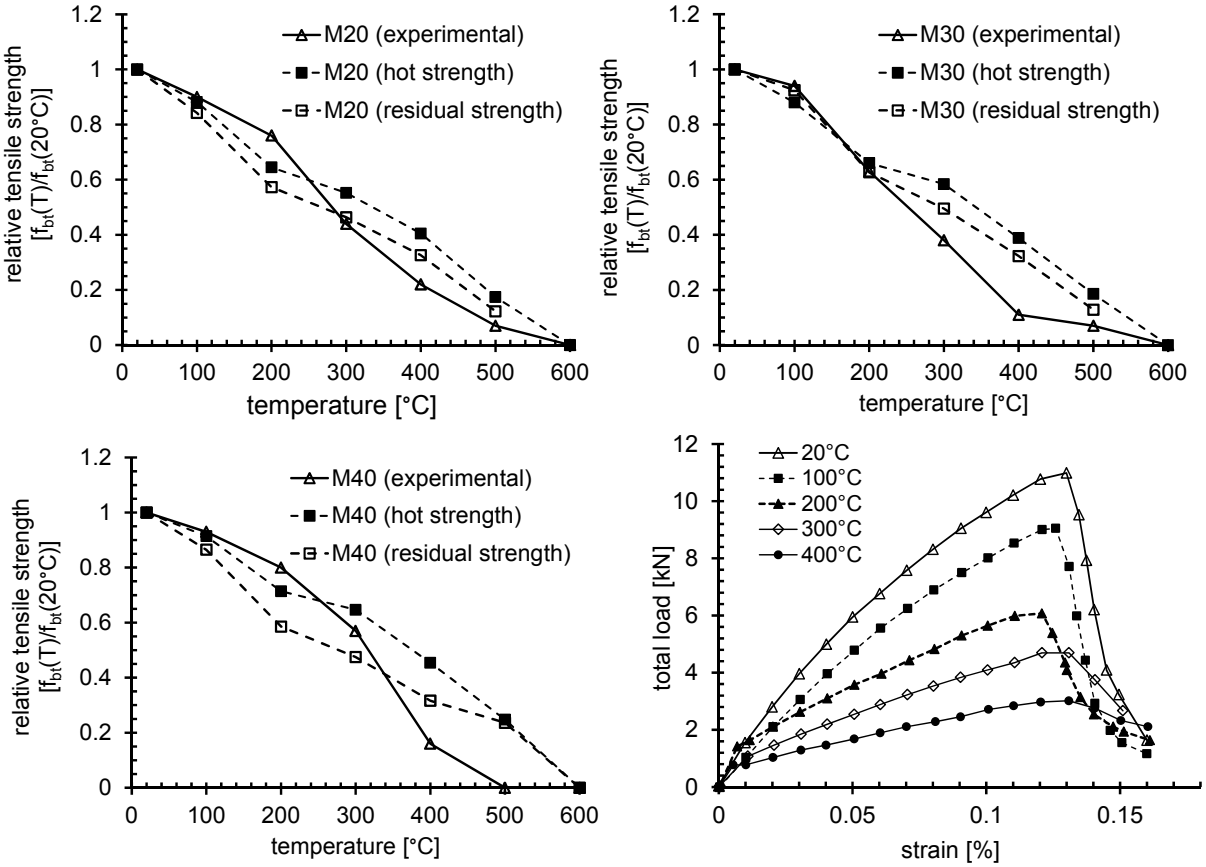

Figure 6.9. Decrease of flexural strength as a function of temperature for different concrete grades and load displacement curves for different temperatures (concrete M30)

The comparison of the numerical and experimental results for splitting strength of concrete at high temperature is shown in Figure 6.10. The experimental results represent residual splitting strength. The loss of splitting strength is almost a linear function of temperature. Beyond 700 °C residual strength drops almost to zero, thus demonstrating the ability of the model to reproduce experimental data. In this case the difference between residual and hot strength is not as obvious as in the case of four point bending. Only at temperatures above 600 °C hot strength exceeds the residual values. These findings are in good agreement with results reported by Felicetti et al. (2000). He obtained very similar values for hot and residual tensile strength (direct tensile strength).

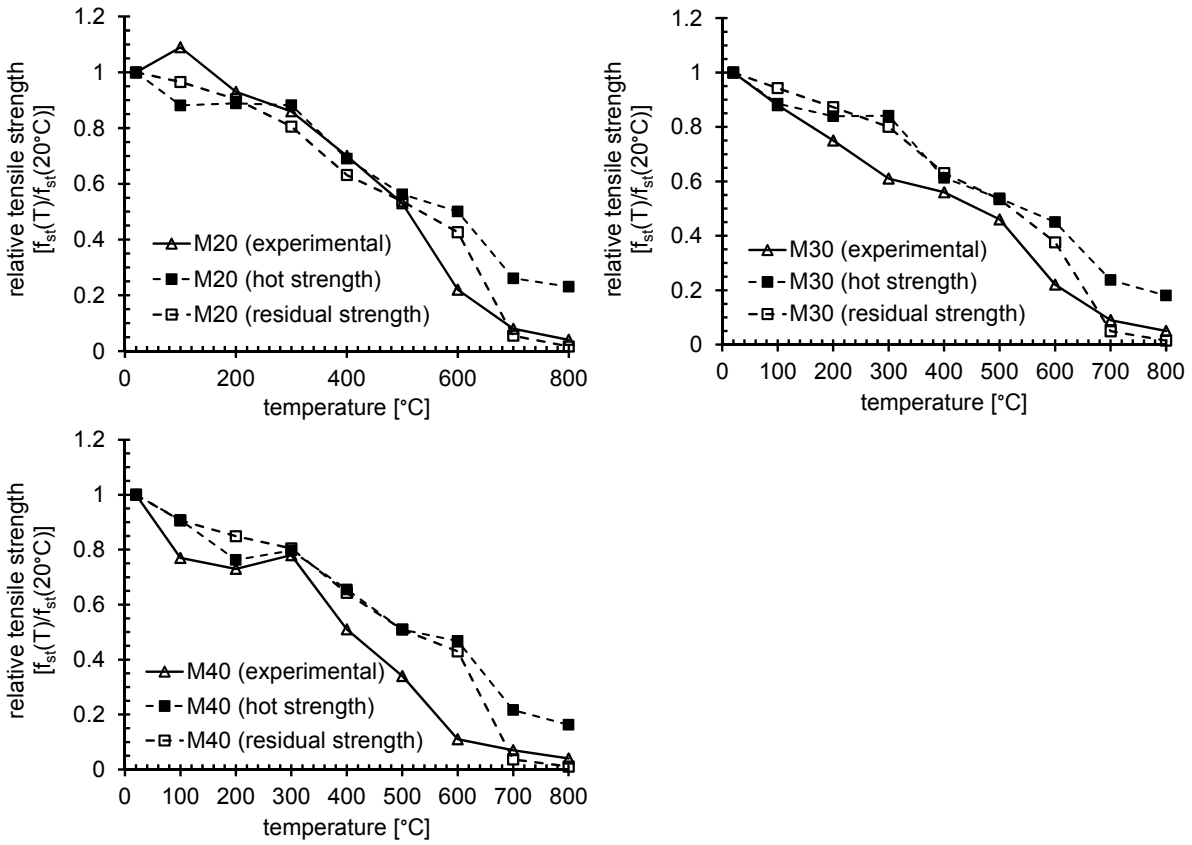

Figure 6.10. Decrease of splitting strength as a function of temperature for different concrete grades

6.6 Validation of the thermo-mechanical model against experiments on reinforced concrete: Macro scale

The 3D thermo-mechanical model discussed above is employed in the transient numerical study of RC beam exposed to elevated temperature.

6.6.1 Experiments – geometry and material properties

The experiments performed by A. Kumar & V. Kumar (2003) on simply supported RC beams are numerically simulated. The test setup of the investigated beams is shown in Figure 6.11. The concrete used for the experimental investigation was normal strength concrete with average cube strength of 20.89 N/mm^2 (28 days). Crushed stone aggregates with 20 mm maximum size were used. The reinforcement used was Fe 415 grade high strength deformed steel bars according to IS516 (1959). All beams were designed according to IS456 (2000). The reinforcement details are given in Figure 6.11.

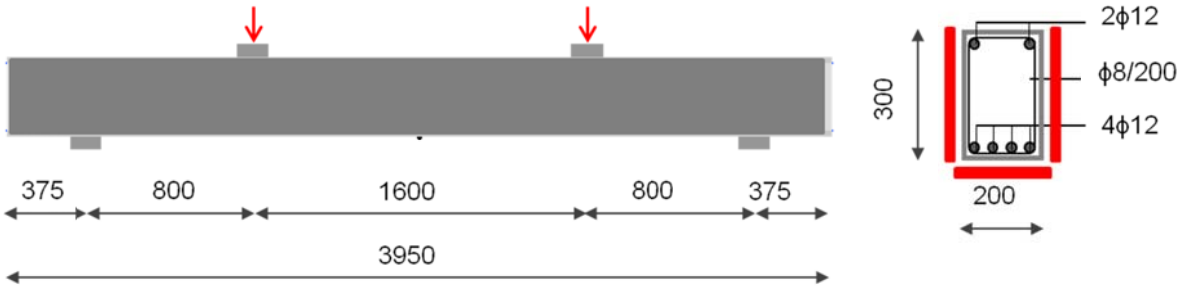

Figure 6.11. Geometry of the four-point bending reinforced concrete beam

Fire tests were performed on the beams by heating them from three sides according to ISO 834 curve (see Figure 3.3). The upper face of the beam was not exposed to the heat. To investigate the behaviour of the beams after different fire exposures, companion specimens were tested after 1 hour, 1.5 hours and 2 hours of heating, respectively. To have reference values, one specimen was loaded without imposing temperature. The heated specimens were cooled down to the room temperature and subsequently static four point bending tests up to failure (load control) were performed (Figure 6.11).

6.6.2 Spatial discretization and loading

Because of the symmetry of the test setup, only one half of the specimen is modelled. Concrete is discretized with eight node solid hexahedral elements (linear strain field), whereas the longitudinal and transversal reinforcement is modelled using 1D bar elements. To avoid unrealistic local damage, loading and supporting platens are modelled as linear elastic hexahedral elements. Figure 6.12 shows FE mesh of the beam and reinforcement. As in the experiments, the beams are exposed to three-sided thermal loading. Boundary conditions are the same as in the experimental tests.

At room temperature the following concrete properties are used in the analysis: cylinder compressive strength of 17.10 N/mm^2, tensile strength of 2.00 N/mm^2, concrete fracture energy of 0.08 N/mm and Young's modulus of 19600 N/mm^2. Thermal material properties of concrete used for the analysis are assumed to be temperature dependent according to DIN EN 1-2 (2004). Steel reinforcement with yield stress of 480 N/mm^2 and ultimate strength of 550 N/mm^2 is used.

The analysis is performed in two steps. In the first step non-stationary thermal analysis is carried out where the beams are heated and then cooled down to the room temperature. The heating is performed according to the ISO 834 curve where the air temperature is given as:

$$T_{Air}(t) - T_{Air}(t_0) = 345\log(8t - 1) \qquad (6.12)$$

where $T_{Air}(t_0)$ = initial air temperature (20 °C) and t = time [min]. The cooling is performed by linear decrease of air temperature over two hours. After cooling the air temperature is kept constant until the whole cross-section of the beam reached the room temperature. The heating is performed according to ISO 834 fire curve, same as in the experiments.

Four cases are analysed: (1) no heating (reference specimen); (2) 1 hour of exposure; (3) 1.5 hours of exposure and (4) 2 hours of exposure. In order to calculate residual resistance of previously damaged RC beams, in the second step of the analysis the four-point bending is applied up to failure. The analysis is carried out by controlling deflection of two loading platens.

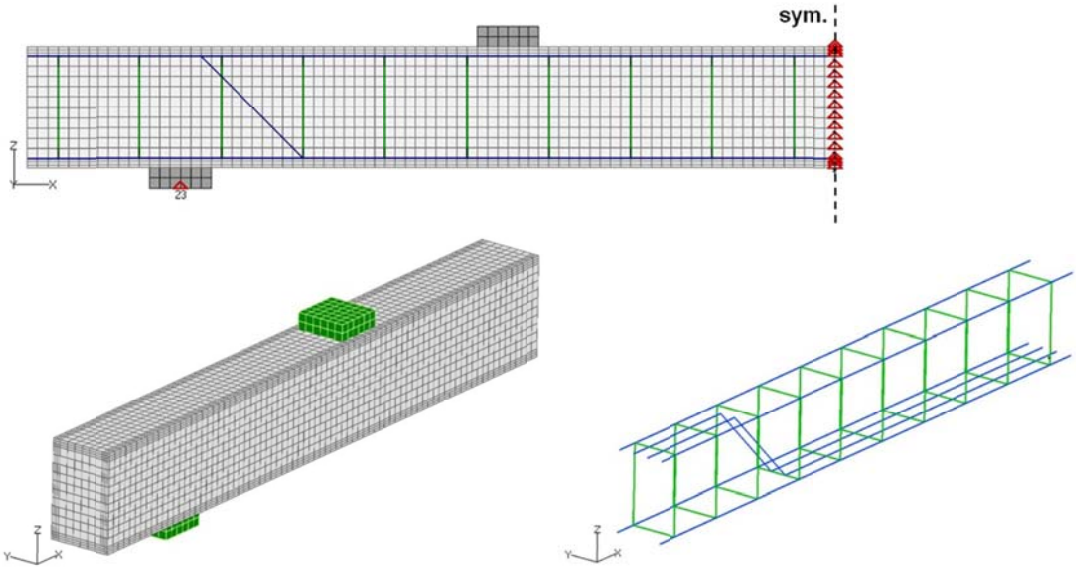

Figure 6.12. Finite element discretization of concrete and reinforcement

6.6.3 Results and discussion

The comparison of experimentally and numerically obtained load-deflection curves for reference beam (no heating) is shown in Figure 6.13. The total load is plotted as a function of deflection measured during static four point bending. Due to the fact that the load control was used in the experiment, it was not possible to obtain the post-peak response. In the analysis the post-peak response shows sudden drop of load what indicates brittle type of failure (diagonal shear), see Figure 6.16. Figure 6.13 shows that for the reference beam measured and calculated load-deflection curves exhibit good agreement.

Temperature distribution over the beam cross-section after 1 hour, 1.5 hours and 2 hours of fire exposure is shown in Figure 6.14. These temperature contours are found to be in very good agreement with corresponding contours provided in the literature (Kordina & Meyer-Ottens 1999).

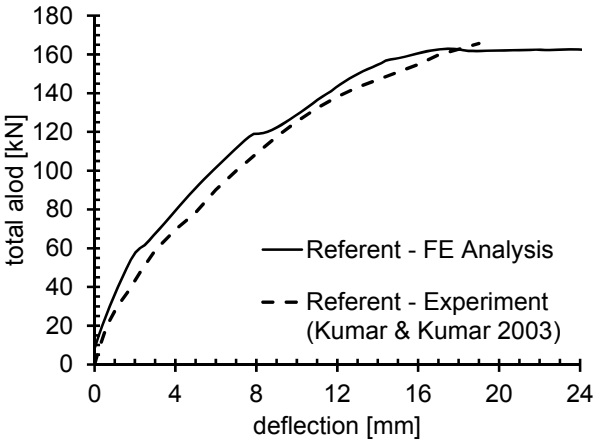

Figure 6.13. Experimentally measured and numerically predicted load-deflection curves for the reference (not heated) beam

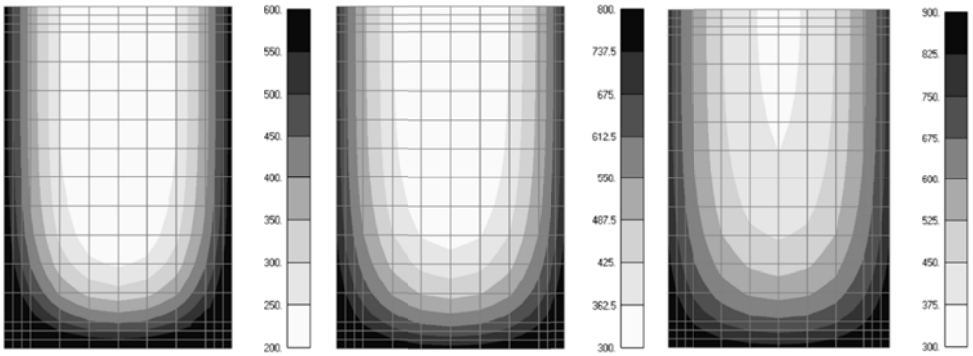

Figure 6.14. Temperature distribution over the beam cross section after heating exposure of: (a) 1 hour, (2) 1.5 hours and (c) 2 hours

Figure 6.15 shows the comparison of the load-deflection curves for the reference beam and beam subjected to loading after 1, 1.5 and 2 hours of heating, respectively.

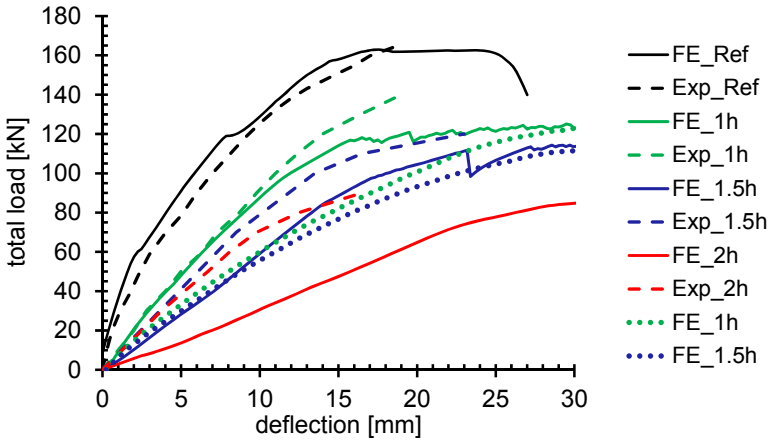

Figure 6.15. Complete experimentally measured and calculated load-deflection curves (residual conditions)

As can be seen, the numerical results are in very good agreement with their experimental counterparts for all the cases. To have a better overview, the deflection is plotted only up to 30 mm. In Figure 6.16 complete load-deflection curves for all the cases are shown. The reduction of the beam resistance as a function of fire duration is plotted in Figure 6.17 (left). As can be seen there is again very good agreement between predicted and measured data. The analysis and experiment show that after two hours of fire exposure the beam resistance is reduced by approximately 50 %.

Figure 6.17 (right) shows the initial (k_1) and secant (k_2) relative beam stiffness plotted as a function of fire duration. The relative stiffness is calculated as the ratio between temperature dependent stiffness and corresponding stiffness of reference beam. The initial and secant stiffnesses are calculated at 25 % and 75 % of the ultimate load, respectively.

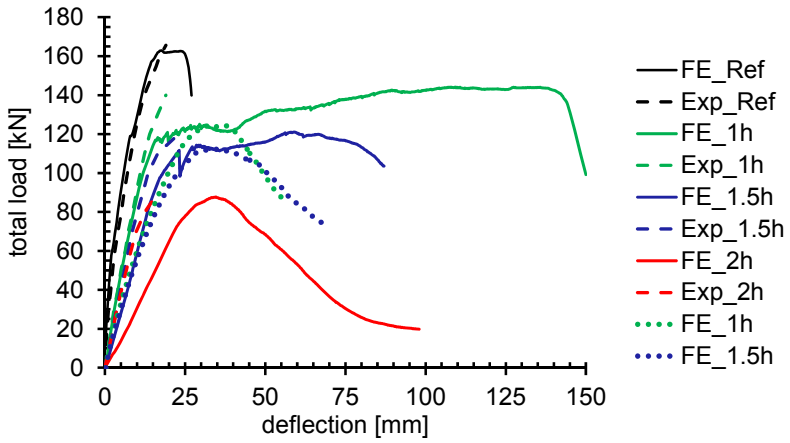

Figure 6.16. Complete experimentally measured and calculated load-deflection curves (residual conditions)

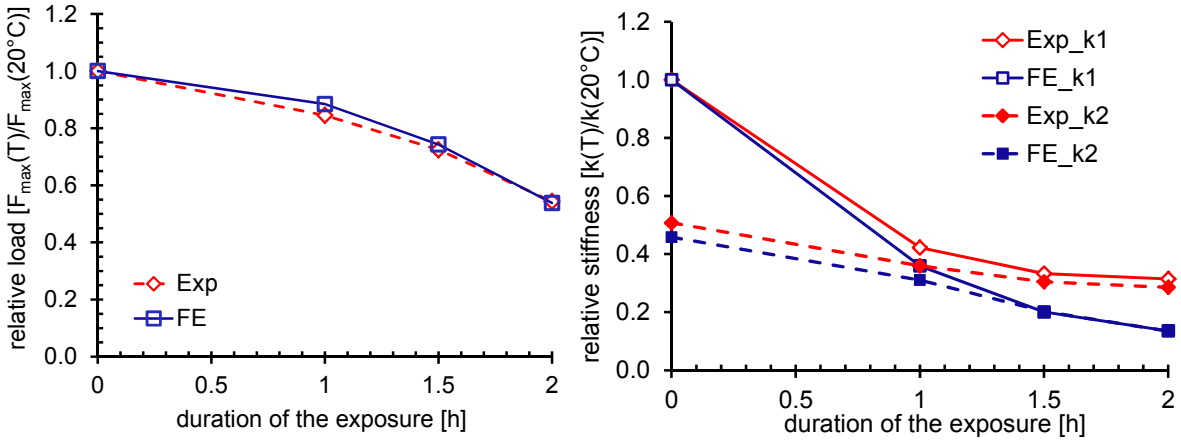

Figure 6.17. Ultimate load reduction (left) and stiffness (k_1 and k_2) reduction (right) due to fire exposure (residual conditions)

As expected, with increase in duration of heating both stiffnesses decrease significantly. This is especially the case for the first hour of heating. Moreover, it can be seen that for the case of the reference beam, experimental and numerical results show that the ratio between k_1 and k_2 is approximately 2, whereas the same ratio for the beam heated more than one hour is close to 1. This is attributed to the fact that the initial stiffness of the reference beam corresponds to the non-cracked stiffness, which is significantly higher than the stiffness of the beams already damaged due to thermal loads. Consequently, the initial and secant stiffness of the beams heated over one hour and cooled down to the room temperature are approximately the same. Figure 6.17 shows good agreement between experimental and numerical results. The peak load values together with the initial and secant stiffness (analytical and experimental) are given in Table 6.2. The results are in good agreement with the results known from the literature (CEB-FIP-bulletin-46 2008).

Table 6.2. Overview of the numerical and experimental results

Duration of heating [h]	Stiffness k_1 [kN/mm]		Stiffness k_2 [kN/mm]		Ultimate load [kN]	
	Analysis	Experiment	Analysis	Experiment	Analysis	Experiment
0	28.75	25.00	13.18	12.69	163.00	168.00
1	10.33	10.56	8.93	9.00	144.12	140.00
1.5	5.77	8.33	5.83	7.62	121.08	120.00
2	3.90	7.86	3.88	7.14	87.70	90.00

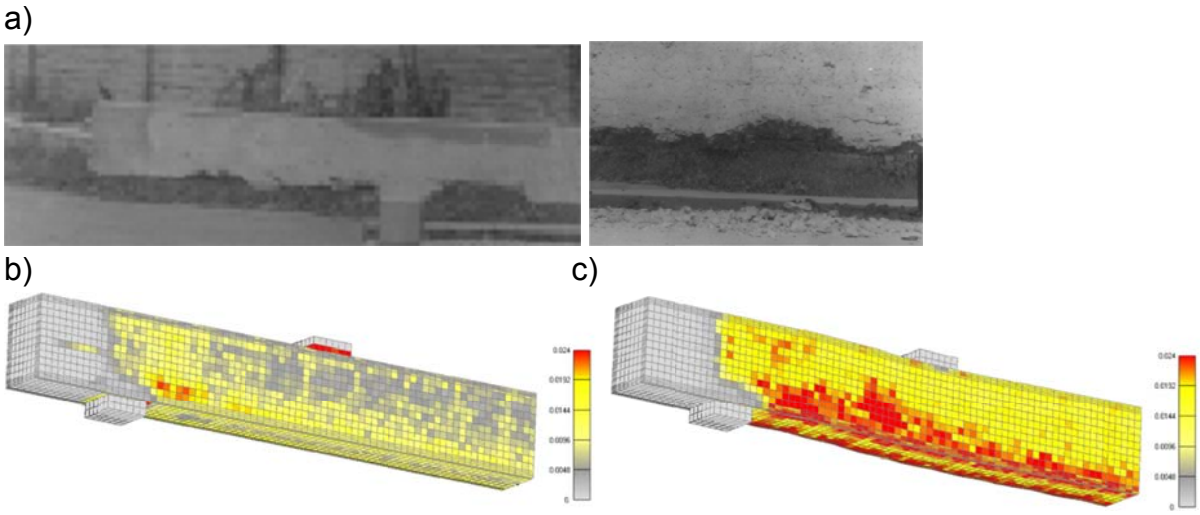

Figure 6.18. Crack patterns after heating, and after heating and cooling: experiment: between 1.5 and 2 hours of heating (top), FE analysis: 2 hours of heating (bottom left), and 2 hours of heating and subsequent cooling (bottom right)

Figure 6.18 shows the experimentally and numerically observed damage of the surface layer of concrete due to 2-hour heating and cooling, before performing the load test. Severe spalling of the concrete cover was observed (red colour of the elements corresponds to crack width of at least 0.1 mm). The time of occurrence of spalling in experiments was reported to be 1.5 to 2 hours after begin of heating. This is a nice

example of corner spalling, which is not explosive and takes place quite late in the fire. The numerical results indicate that the concrete damage due to heating is further enhanced by cooling. It is also found that longer the fire exposure, more severe is the concrete damage. The damage due to thermally induced stresses of concrete cover combined with the reduction in mechanical properties results in the severe reduction of ultimate load carrying capacity.

The principal tensile strains (cracks) at the peak residual load for all four cases are shown in Figure 6.19. The strain of 0.012 corresponds to the crack width of 0.30 mm which is approximately the critical crack width of concrete. In all the cases brittle failure occurs in the flexural-shear mode irrespective of the heating scenario. In the experimental investigations the same type of brittle shear failure mode was observed. Both experiments and analysis indicate severe damage of the concrete cover.

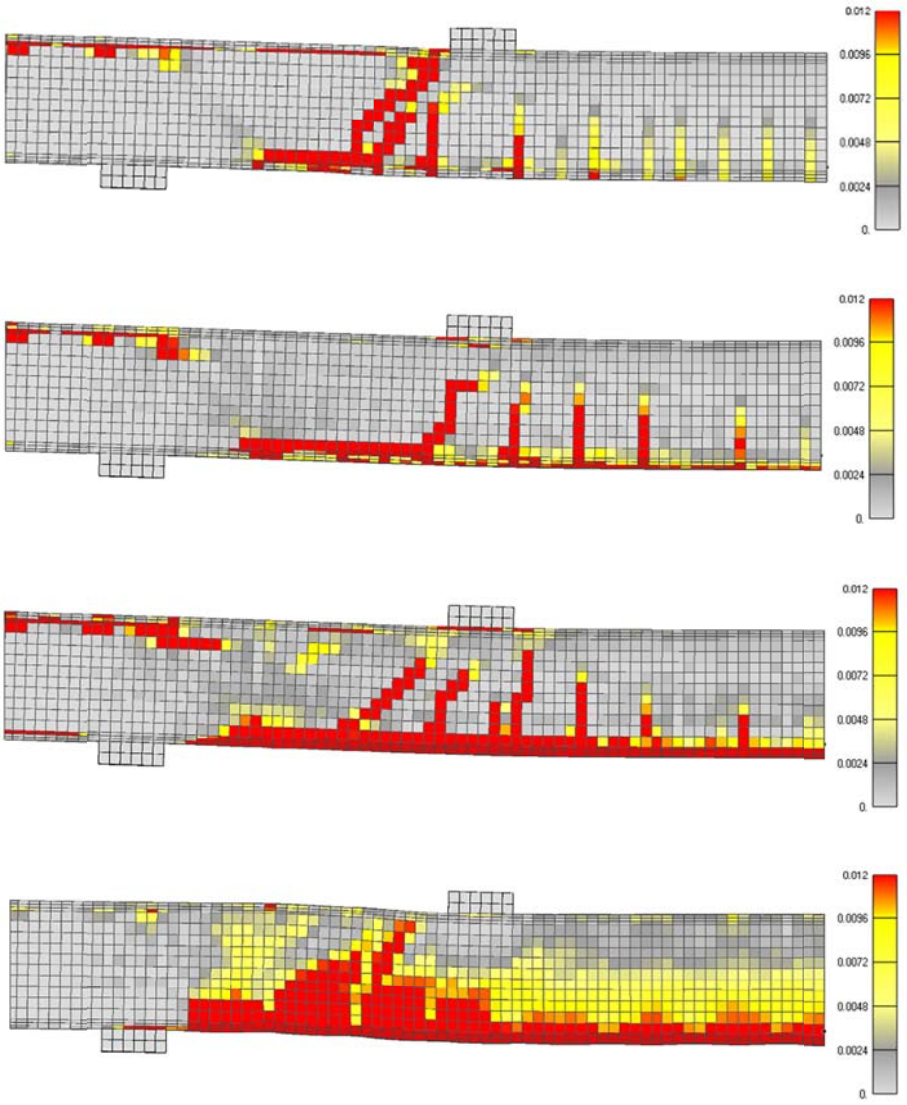

Figure 6.19. Crack pattern (max. principal strains) at the peak load for the four scenarios: (a) no heating; (b) after 1 hour of heating, (c) after 1.5 hours of heating and (d) after 2 hours of heating

Even though experimentally only limited information from the tests were available, much more information could be deduced from the numerical analysis. The following are the major conclusions that could be drawn out from the study:

(i) In general, the employed 3D thermo-mechanical numerical model is capable of reproducing the experimental results very well.

(ii) The temperature distributions across the beam cross section after 1 hour, 1.5 hours and 2 hours of fire exposure are found to be in good agreement with corresponding results provided in the literature (Kordina & Meyer-Ottens 1999).

(iii) The numerically obtained load-deflection curves, for all the cases, are found to be in good agreement with their experimental counterparts.

(iv) The load-carrying capacity as well as the initial stiffness of the beams reduces with the increase in duration of fire exposure.

(v) The ratio of the initial stiffness to the stiffness at 75 % of the peak load is found to be high for the reference specimen; however, this is not the case for the specimens exposed to fire longer than approximately one hour. This is attributed to the concrete damage due to the thermally induced damage of concrete.

(vi) Cooling down the beams to room temperature cause additional damage that is due to the thermally induced strains.

(vii) Numerically obtained crack patterns and failure modes correspond very well with the experimental observations. In all the cases, flexural shear failure is observed with cover spalling occurring after 1.5 - 2.0 hours of fire exposure.

(viii) Besides predicting the overall response of the beams, the model promises to be an effective tool to numerically investigate several phenomena that are difficult to observe experimentally such as spalling of the concrete cover.

6.7 Validation of the thermo-mechanical model against experiments with respect to thermal strain: Meso scale

6.7.1 Free thermal strains

Free thermal strains (see Section 2.4.1) are strains occurring in non-loaded concrete during heating and are mainly influenced by the type of aggregates. When using

macro-scale approach in numerical modelling, the total free thermal strains (obtained from experiments) are directly defined as input data for concrete. In case of meso-scale approach the concrete constituents (mortar and aggregates) are assigned different free thermal strains and the total free thermal strain is obtained as a combination of aggregates and mortar. Experiments performed by Cruz & Gillen (1980) are simulated in order to investigate the suitability of the meso-scale model to capture the effect of aggregates, cement gel and mortar on thermal dilatation of concrete and mortar as composite materials.

6.7.1.1 Experimental data (Cruz & Gillen 1980)

Cruz & Gillen (1980) performed measurements of thermal dilatation on several types of aggregate, cement paste, mortar and concrete. Cylindrical specimens with a diameter of 13 mm and height of 76 mm were used. The heating treatment included heating from room temperature up to ca. 870 °C at a rate of approx. 5 °C/min.

6.7.1.2 Numerical approach

In the finite element model concrete is discretized as a two-phase material comprising cement mortar and coarse aggregates. The interfacial transition zone is omitted due to its relatively small impact on the expansion behaviour of concrete, because of its negligible size.

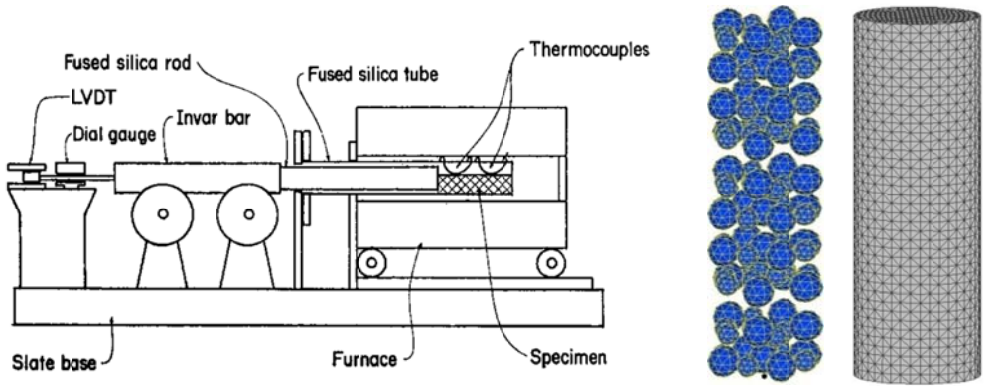

Figure 6.20. Experimental setup, Cruz & Gillen (1980) (left) and finite element model (right)

Additionally, analyses are performed on cement mortar which is also discretized as a two-phase material consisting of cement paste and sand. It should be noted that the model of cement mortar is only a rough approximation of the real mortar structure. Basically, the same finite element mesh used for concrete is employed for cement mortar, only the free thermal strains for different constituents and scale of the model are changed.

The material properties were not provided in the publication by Cruz & Gillen (1980). These are therefore assumed according to DIN EN 1-2 (2004) to correspond to con-

crete class C25/30. The list of material data is provided in Table 6.3. The thermal dilatation of the individual constituents is taken from the experiment, and the total resulting dilatation / thermal strain of the composite is predicted numerically.

Table 6.3. Material properties used in the experiment and numerical analysis

Material property	Mortar	Aggregates (Dolomite)	Cement paste	Sand
$f_{c,cyl}$	37.0	90.00	37.00	90.00
G_f	0.08	0.09	0.08	0.09
E	30000	50000	30000	50000
f_t	3.00	6.00	3.00	6.00

6.7.1.3 Results and discussion

The comparison of experimental and numerical results is depicted in Figure 6.21. As can be observed, the meso-scale concrete and cement mortar model are both capable of capturing the thermal expansion observed in the experiments. Concrete mortar and aggregates both exhibit expansion during heating, so the concrete as a composite lies between the two.

Unlike aggregates and concrete, cement paste exhibits expansion only up to 100 °C, thereafter it shrinks. Shrinkage reaches its lower bound at approximately 600 °C. Cement mortar expands during the whole heating range, indicating the governing influence of aggregates on thermal dilatation of cementitious materials. A very good agreement of the numerical results with the experimental counterparts can be observed in Figure 6.21 (right). Even though the numerical model for cement mortar is relatively simple, it can still realistically reproduce the experimentally observed behaviour of mortar. Numerical analysis of the heated specimens has confirmed the governing role of the aggregate type on the thermal behaviour of both concrete and cement mortar, as observed in experiments (Schneider 1982).

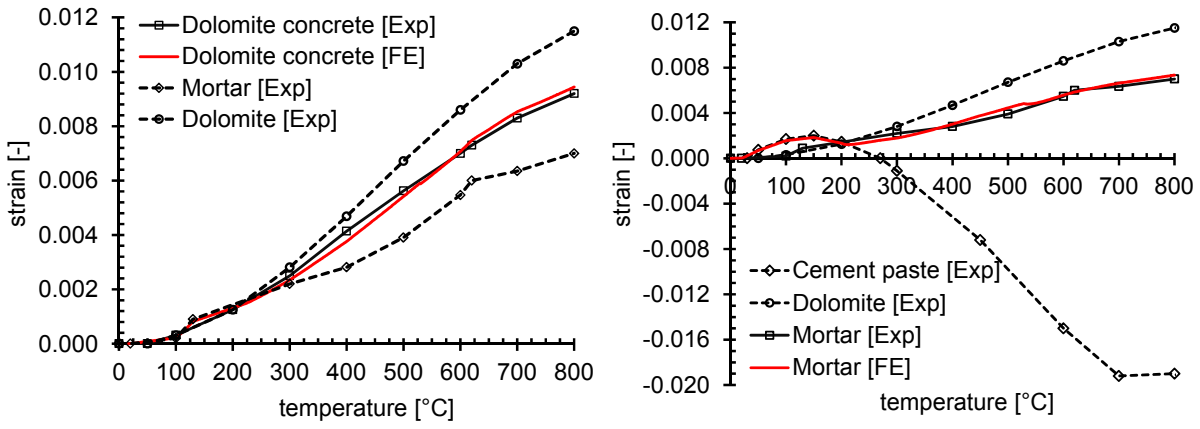

Figure 6.21. Thermal strain of concrete as a composite (left) and of cement mortar as a composite of sand and cement gel (right)

6.7.2 Load induced thermal strains

As discussed in Section 2.4.2, concrete loaded in compression and subsequently heated exhibits load induced thermal strain (LITS) during the first heating cycle. This phenomenon is very well documented in the literature, e.g. Anderberg & Thelandersson (1976), Khoury (1995) and Hager (2004). Most of the present concrete models account for the LITS at macro-scale in a fashion to predefine the relaxation of the stresses directly in the model. This approach is justified when concrete is assumed to be a homogeneous material (macro-scale). It was previously shown by Periskic (2009) that the macro-scale model with predefined LITS is capable of reproducing experimentally observed behaviour.

However, when the interaction of different concrete phases is accounted for (meso-scale model), it is assumed that the incompatibility of thermal dilatations, the degradation of the mechanical properties and the heterogeneity can account for LITS automatically. Therefore, when the analysis is performed at meso-scale, LITS are not predefined. In order to confirm the validity of this hypothesis, numerical analyses employing thermo-mechanical model are performed at meso-scale to simulate the experiments performed by Hager (2004). In the following sections, the experimental setup and corresponding models are presented, and the results of the analyses are discussed. Moreover, experiments on restrained specimens reported by Anderberg & Thelandersson (1976) are simulated and the results are reported.

6.7.2.1 Experimental data (Hager 2004)

Some of the experiments performed by Hager (2004) included:

a) Heating of concrete specimens up to 600 °C (heating rate of 1 °C/min)

b) Compressive loading to 20 % of the compressive strength, subsequent heating to 600 °C (heating rate of 1 °C/min)

c) Compressive loading to 40 % of the compressive strength, subsequent heating to 600 °C (heating rate of 1 °C/min)

The experiments were performed on several types of concrete ranging from ordinary to high performance concrete. In the present work, only concrete class M30 is considered (compressive strength = 37.20 N/mm^2, tensile strength = 3.0 N/mm^2, Young's modulus = 32000 N/mm^2). Concrete cylinders with a diameter of 104 mm and height

of 300 mm were used as specimens. Temperature profiles and axial thermal strain were monitored throughout the tests.

6.7.2.2 Numerical model

Geometry with the test setup and finite element mesh with loading conditions of the meso-scale model are shown in Figure 6.22. Concrete is discretized as a composite of cement mortar and coarse aggregates. For simplicity, only aggregates sizes 10, 14 and 24 mm are considered, whereby the volumetric ratio of coarse aggregates to concrete is kept same as in the experiments.

The thermal load is applied along the cylinder mantle. The material properties are obtained from the experiments. Free thermal strains for the concrete constituents are not provided by Hager (2004), so these are assumed such to obtain best fit with free thermal strain for concrete in the experiment. The three loading cases (a, b and c) experimentally investigated by Hager (2004) are simulated.

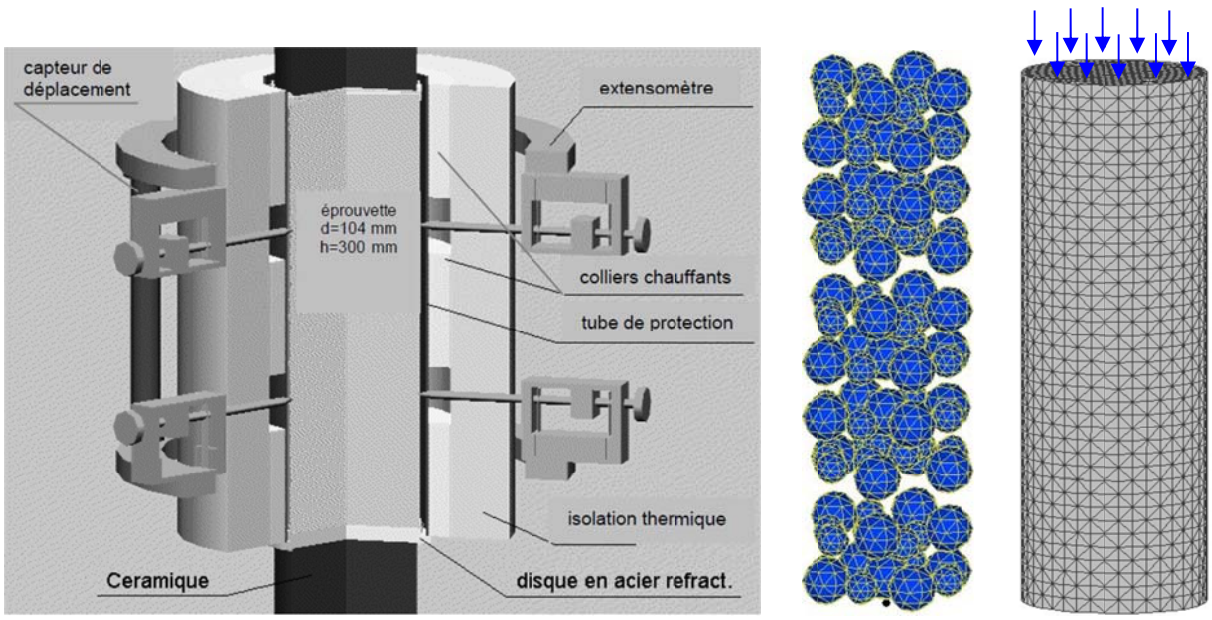

Figure 6.22. Experimental setup, Hager (2004) (left) and finite element model: aggregates and mortar (right)

6.7.2.3 Results and discussion

All three tested loading scenarios together with the experimental results obtained by Hager (2004) are shown in Figure 6.23 in terms of axial strain versus temperature. Non-loaded concrete exhibits only expansion during heating (free thermal strain), whereas preloaded concrete exhibits reduction in longitudinal strain, i.e. instead of expanding, it contracts.

Overall results indicate that the thermo-mechanical model at meso-scale can automatically capture the behaviour of loaded and subsequently heated concrete without explicit definition of load induced thermal strain. However, the numerical model cannot fully capture the load induced thermal strains up to temperatures of approximately 140 °C. In this region there is no difference between the three curves. In this temperature range (20 °C - 140 °C) LITS are assumed to originate from the drying and structural changes in the cement paste. These effects are only partially accounted for in the thermo-mechanical model by means of reduction of material properties with temperature. However, the level of strain is relatively low in this temperature region.

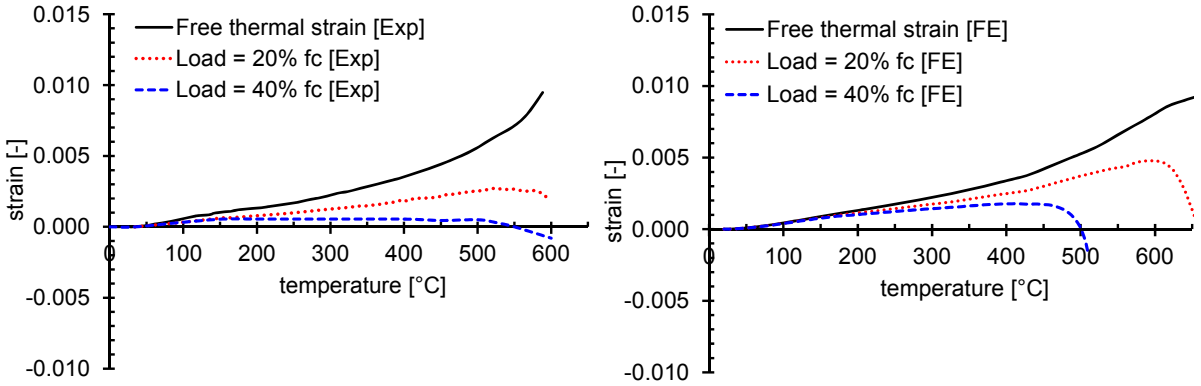

Figure 6.23. Experimentally (left) and numerically (right) obtained development of longitudinal strains with increasing temperature

From 140 °C onwards the experimental and numerical curves for loaded specimens are approximately parallel thus indicating that the model can realistically capture the behaviour. Somewhat more pronounced deviation of the numerical prediction from the experimental data is observed for σ = 20 % f_c at temperatures between 500 °C and 600 °C. Even though the total free thermal strain of concrete as a composite is almost the same as observed in the experiment, in the analysis the behaviour of concrete phases (mortar and aggregates) is assumed and therefore, most probably deviates from the experimental data.

For temperatures above 140 °C load induced thermal strains are a combination of: (i) the damage of cement mortar due to presence of load and elevated temperature, (ii) the damage of mortar caused by different thermal dilatations of mortar and aggregates and (iii) the damage of mortar due to the difference in the mechanical properties of the mortar and aggregates.

When concrete is axially loaded in compression and the load is kept constant throughout the heating phase, the material tends to expand more in lateral than in axial direction. The damage due to mechanical loading is further aggravated by heating. Since aggregates and cement mortar have different mechanical and thermal properties, the incompatibility of the two materials leads to thermo-mechanical damage. Lateral strains increase and the longitudinal strains decrease with temperature.

Increased lateral strain result in longitudinal cracks, finally leading to complete failure of the specimen. Higher the initial load level, higher is the mechanical damage before heating and sooner the failure occurs. The development of lateral strain with temperature is shown in Figure 6.24. The evaluation is performed for specimen at the mid height. In Figure 6.24 (right) can be observed that the meso-scale model predicts LITS only from ca. 140 °C onwards, due to the reasons discussed above.

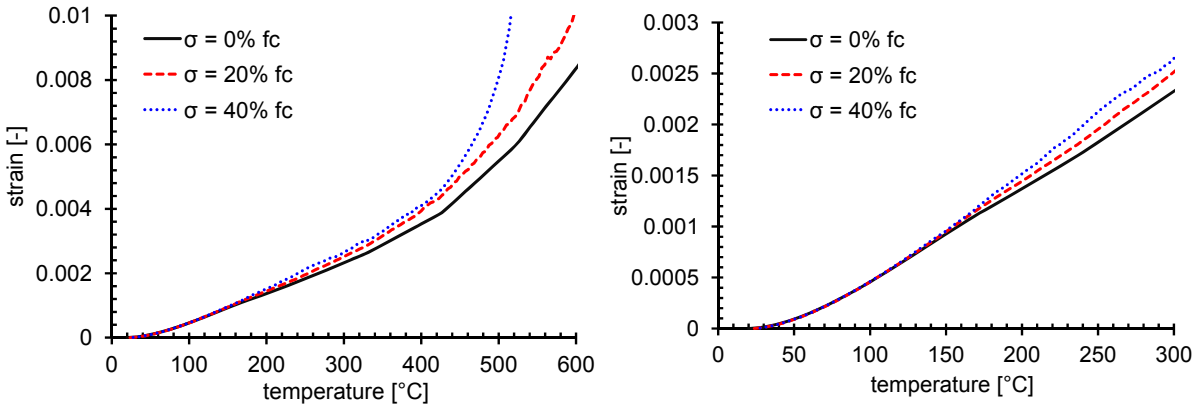

Figure 6.24. Numerically obtained development of lateral strains with increasing temperature (left) and detail of the initial part of the diagram (right)

Typical failure mode for non-loaded concrete heated up to 600 °C and concrete loaded up to 20 % of f_c and then heated to 600 °C are shown in Figure 6.25. Experimental failure modes are compared to the numerical results. In the case of not loaded concrete the cracking takes place randomly over the cylinder surface, since concrete undergoes equal expansion in all directions.

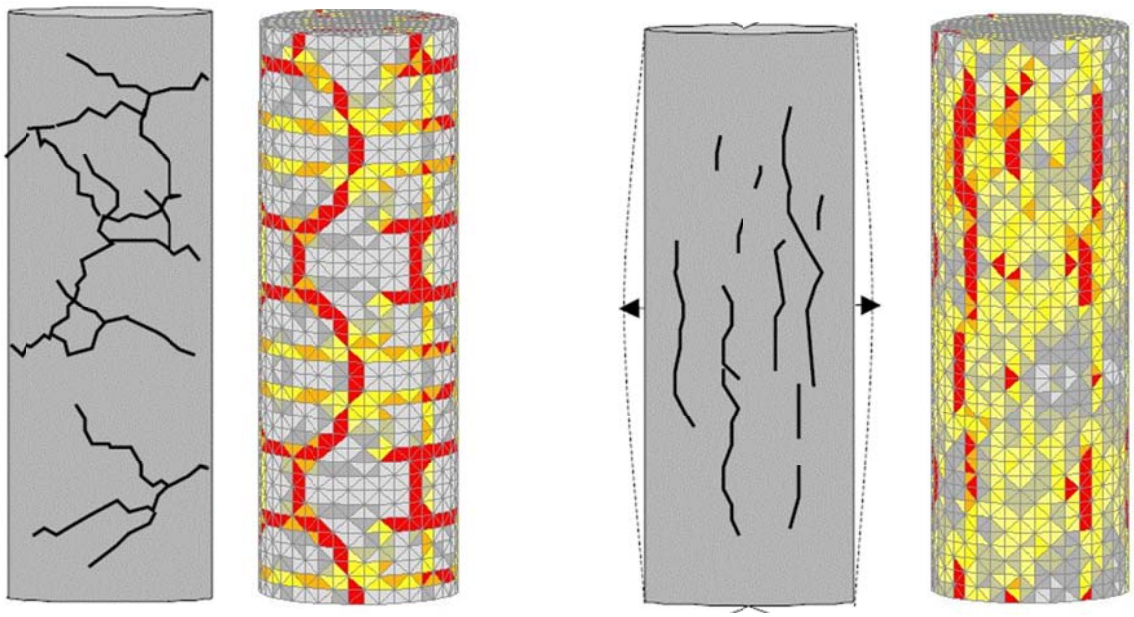

Figure 6.25. Experimentally and numerically obtained failure modes: concrete heated to 600 °C (left) and concrete loaded to 20 % f_c and subsequently heated to 600 °C (right)

Random pattern of the surface cracks is nicely captured using the meso-scale model. Loaded specimen, on the other hand, exhibits different kind of failure mode with cracks running parallel to the loading direction, indicating the effect of preloading.

It is evident that the thermo-mechanical model at meso-scale can realistically capture the failure mode of concrete under thermal and mechanical loading as well the combined effect of load and temperature. Keeping in mind the relative simplicity of the meso-scale model and the fact that the free thermal strain of the concrete constituents are assumed, it can be stated that the meso-scale model captures the behaviour with reasonable accuracy.

6.7.2.4 Experimental data (Anderberg & Thelandersson 1976)

Anderberg & Thelandersson (1976) performed experiments on concrete cylinders with diameter of 75 mm and height of 150 mm. The axial strain was restrained and the specimens were heated with two heating rates, namely 1 °C/min and 5 °C/min. Concrete compressive strength was 47.6 N/mm^2.

6.7.3 Numerical model

Similarly as in previous case, concrete is modelled as a two-phase material comprising coarse aggregates and mortar matrix, whereby only two aggregate sizes are considered (14 mm and 20 mm). Meso-scale model with boundary conditions is shown in Figure 6.26. The material properties and thermal strains are chosen such to give best fit with the experimental data. Vertical displacements of the specimen are restrained on both top and bottom surface of the cylinder.

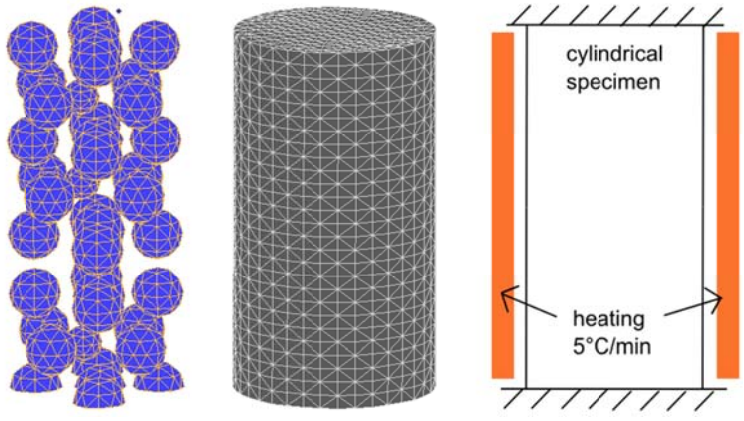

Figure 6.26. Finite element model – meso-scale approach (left), experimental setup (right)

6.7.3.1 Results and discussion

During the heating phase, restrained axial stresses are monitored, as in the experiment. Comparison of the experimental and numerical results is presented in Figure

6.27. As can be observed, meso-scale model can capture the general behaviour of restrained concrete exposed to relatively slow heating rate.

With increasing temperature, axial stresses in concrete initially rise, with the peak at about 40 % of the compressive strength at room temperature. Beyond approximately 320 °C the stresses start to relax. This effect is a result of damage due to incompatibility of the concrete mortar and coarse aggregates. Restrained stresses relax gradually, and at approximately 800 °C the specimen fails completely. The damage (cracking) is not reported in the experimental work. The cracking of the meso-scale model is presented in Figure 6.27 (right). Lateral expansion of the heated specimen leads to damage and subsequently, failure.

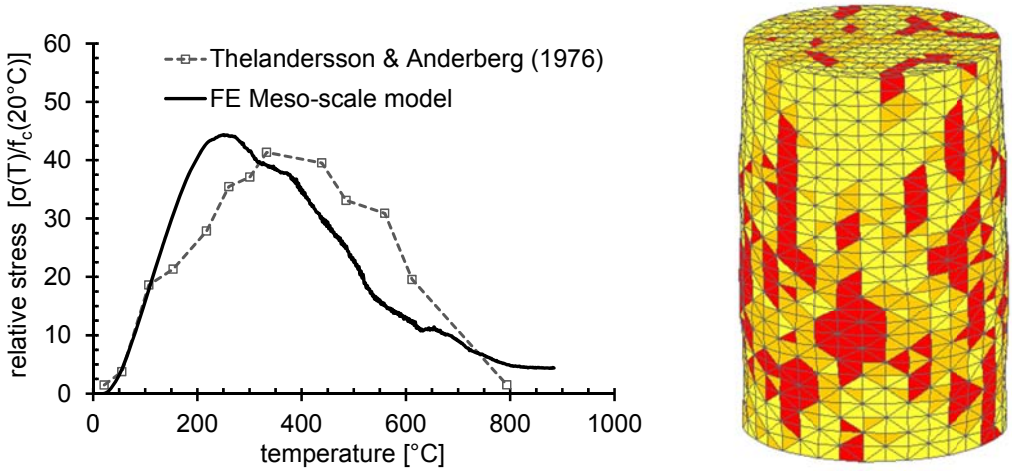

Figure 6.27. Restrained axial stresses in heated concrete cylinder (left) and numerically observed failure mode (right)

6.7.4 Conclusions

In this section, the thermo-mechanical model is employed to investigate the thermal dilatation of non-loaded and loaded concrete. The analysis is performed on meso-scale model for concrete, whereby the load-induced thermal strains are not explicitly accounted for in the thermo-mechanical model. It is found that the model is capable of capturing both, total free thermal strain of a composite material as well as thermal strain of previously loaded concrete. Furthermore, the model can realistically capture the stress development in restrained concrete specimens when exposed to heating. Load induced thermal strain are for the largest part composed of thermo-mechanical damage of concrete due to loading, as well as mechanical and thermal incompatibility of the concrete constituents. Even though a part of these strains is due to the changes within cement gel (Mindeguia et al. 2010), considering the overall small value of these strains, it can be concluded that the model realistically accounts for the effect of preloading on the behaviour of concrete (LITS). Consequently, as far as meso-scale analysis is concerned, in the following sections LITS are not explicitly accounted for in the thermo-mechanical model.

7. THE THERMO-HYGRO-MECHANICAL MODEL

The employed thermo-hygro-mechanical model is developed by Ozbolt et al. (2008) and Periskic (2009). It is a phenomenological model, formulated in the framework of continuum mechanics under the assumption of validity of irreversible thermodynamics. The response of the model is controlled by the following variables: temperature, pore pressure (moisture), stresses and strains. The model is coupled, i.e. the distribution of transport parameters and temperature depends on damage of concrete. Same as in the thermo-mechanical model, the relevant macroscopic mechanical properties are temperature dependent.

7.1 Coupled heat and moisture transfer

Even though the general approach for the coupled heat and mass transfer problem is known, the complexity of the problem requires certain simplifications (Bazant & Thonguthai 1978). Under assumption that the moisture flux ($\boldsymbol{J}$) and heat flux ($\boldsymbol{q}$) in concrete are stress and strain independent, the following is valid (Bazant & Thonguthai 1978):

$$\boldsymbol{J} = -a_{ww}\,\mathrm{grad}\,w - a_{wT}\,\mathrm{grad}\,T \tag{7.1}$$

$$\boldsymbol{q} = -a_{Tw}\,\mathrm{grad}\,w - a_{TT}\,\mathrm{grad}\,T \tag{7.2}$$

where a_{ww}, a_{TT}, a_{wT} and a_{Tw} = functions of evaporable water content w and temperature T. Water content w is a function of T and pore pressure p. Neglecting the influence of a_{wT} and a_{Tw} and replacing w with pore pressure p, Eq. (7.1) and (7.2) can be rewritten as:

$$\boldsymbol{J} = -\frac{a_p}{g}\,\mathrm{grad}\,p \tag{7.3}$$

$$\boldsymbol{q} = -\lambda\,\mathrm{grad}\,T \tag{7.4}$$

in which λ = thermal conductivity, a_p = relative permeability and g = gravity constant. Note that a_p is denoted as relative permeability, meaning that it depends not only on porosity, but also on temperature, pore pressure and saturation of concrete. It is obtained from sorption isotherms.

Applying the mass conservation law and Eq. (7.3), following is valid:

$$\frac{\partial w}{\partial t} = -\operatorname{div} \boldsymbol{J} + \frac{\partial w_d}{\partial t} \tag{7.5}$$

where t = time and w_d = total mass of water released into the pore by dehydration. In the present model dehydration is not accounted for. The energy conservation law together with Eq. (7.4) can be written as:

$$C\rho \frac{\partial T}{\partial t} - C_a \frac{\partial w}{\partial t} - C_w \frac{\partial T}{\partial t} \boldsymbol{J} \operatorname{grad} T = -\operatorname{div} \boldsymbol{q} \tag{7.6}$$

where ρ = mass density and C = isobaric heat capacity of concrete, C_a = heat sorption of free water and C_w = heat capacity of water, which is neglected in the present model. The first member of the left hand side of Eq (7.6) is the contribution of the temperature change to heat, the second one is the contribution of free water to heat in concrete and the third member is due to heat convection of moving water in concrete, which is usually important at high heating rates.

Boundary conditions at concrete surface are defined as:

$$\boldsymbol{n} \cdot \boldsymbol{J} = \alpha_P \left(p_0 - p_E \right) \tag{7.7}$$

$$\boldsymbol{n} \cdot \boldsymbol{q} = \alpha_T \left(T_0 - T_E \right) \tag{7.8}$$

where α_P = moisture transfer coefficient, α_T = heat transfer coefficient, T_0 and p_0 = temperature and pore pressure at concrete surface, respectively, and T_E and p_E = temperature and pore pressure of environment, respectively.

7.2 State of pore water and permeability

It is assumed that the constitutive laws for p, w and T follow simplified suggestions proposed by Bazant & Thonguthai (1978). To describe the state of pore water in concrete, for temperatures below the critical point of water (374.15 °C), one has to distinguish three different states: (i) non-saturated concrete – relative pore pressure $h \leq 0.96$, h=p/ps, ps = saturation pressure, (ii) saturated concrete – relative pore pressure $h \geq 1.04$, and (iii) transition from non-saturated to saturated concrete ($0.96 < h < 1.04$). Due to the complexity of the problem, controlling parameters had to be fitted by the available test data (Bazant & Thonguthai 1978).

Theoretical solution (Bazant & Thonguthai 1978) is based on simplified assumption that the porous system of concrete is not subject to change and that the amount of pore water is negligible. In order to assure realistic results, the model is augmented

with experimental data. According to Bazant & Thonguthai (1978) the state of pore water for non-saturated concrete ($p \le p_s$, where p_s = saturation pressure) reads:

$$\frac{w}{c} = \left(\frac{w_1}{c} h \right)^{1/m(T)} \qquad \text{with } h = \frac{p}{p_s(T)};\ h \le 0.96 \qquad (7.9)$$

$$m(T) = 1.04 - \frac{T'}{22.34 + T'} \qquad \text{with } T' = \left(\frac{T + 10}{T_0 + 10} \right)^2 \qquad (7.10)$$

where T_0 = 25 °C, c = mass of cement per m^3 of concrete and w_1 = saturation water content at 25 °C, h = relative pore pressure and p_s = water saturation pressure.

Porosity of concrete n at higher temperatures increases because of dehydration and chemical changes of cement paste (Noumowe et al. 1996b). Therefore, the initial porosity of concrete n_0 has to be corrected by an empirical correction function (Bazant & Thonguthai 1978):

$$n = \left(n_0 + \frac{w_d(T) - w_{d0}}{\rho_0} \right) P(h) \qquad \text{for } h \ge 1.04 \qquad (7.11)$$

$$P(h) = 1.0 + 0.12(h - 1.04) \qquad \text{for } h = \frac{p}{p_s(T)} \qquad (7.12)$$

Function $P(h)$ is obtained by fitting the test data and $w_d(T)$ is taken from the measurements of weight loss of heated concrete specimens (Harmathy & Allen 1973). Using Eq. (7.11) and (7.12), and accounting for the change of thermodynamic properties of water in terms of specific water volume v as a function of pressure and temperature (Wagner & Kruse 1998), water content in saturated concrete can be obtained from:

$$w = (1 + 3\varepsilon^v)\frac{n}{v}, \qquad \text{with } d\varepsilon^v = \frac{d\sigma^v}{3K} + \alpha\, dT, \sigma^v = n\, p \qquad (7.13)$$

in which ε^V = volumetric strain due to the resulting volumetric stress σ^v caused by pore pressure, v = specific volume of water, K = bulk modulus and α = coefficient of linear thermal expansion of concrete.

The transition from non-saturated to saturated concrete cannot be abrupt, since the size of the pores in concrete is not uniform. Furthermore, an abrupt transition would cause numerical difficulties. Therefore, for relative vapour pressure h between 0.96 and 1.04 and for a given temperature T, linear increase of free water content from non-saturated state (h =0.96) to saturated state (h =1.04) is assumed (Bazant &

Thonguthai 1978). The permeability function for concrete also follows suggestions proposed by Bazant & Thonguthai (1978). Due to the fact that permeability of concrete above 100 °C significantly rises, the function which controls permeability consists of two parts:

$$a_p = a_0 f_1(h) f_2(T) \quad \text{for } T \le 95°C \tag{7.14}$$

$$a_p = a_0^* f_3(T) \quad \text{for } T > 95°C \text{ with } a_0^* = a_0 f_2(95°C) \tag{7.15}$$

in which a_0 = the reference permeability at 25°C and relative humidity of 100 %. Function $f_1(h)$ describes the moisture transfer within the adsorbed water layers in the necks that connect pores of cement gel, and, according to Bazant & Thonguthai (1978), it is estimated as follows:

$$f_1(h) = \alpha + \frac{1-\alpha}{1+\left(\frac{1-h}{1-h_c}\right)^4} \quad \text{for } h \le 1.0$$
$$f_1(h) = 1.0 \quad \text{for } h > 1.0 \tag{7.16}$$

where h_c = 0.75 = transition humidity and α = 0.05 at 25 °C. The temperature dependence of permeability below 95 °C can be expressed as:

$$f_2(T) = \exp\left[\frac{Q'}{R}\left(\frac{1}{T_0'} - \frac{1}{T'}\right)\right] \quad T \le 95°C \tag{7.17}$$

in which absolute temperature, Q' = activation energy for water migration along the adsorption layers in the necks and R = gas constant.

Function $f_3(T)$ accounts for the fact that between 95 °C and 105 °C there is a transition from the moisture transfer mechanism that is governed by the activation energy of adsorption to a mechanism that is governed by viscosity of a mixture of liquid water and steam. This effect can be described by (Bazant & Thonguthai 1978):

$$f_3(T) = \exp\left(\frac{T-95}{0.881+0.214(T-95)}\right) \quad T > 95°C \tag{7.18}$$

where T is in °C. For more details related to the physical background of Eq. (7.16) to (7.18) see Bazant & Thonguthai (1978).

The effect of temperature and humidity on permeability of concrete (Bazant & Thonguthai 1978) is depicted in Figure 7.1 (left). Below 95 °C there is a significant influence of relative humidity, whereby permeability increases for higher relative hu-

midity. This assumption is not realistic for water and water vapour transport in concrete. Bazant & Thonguthai (1978) based their models on experimental measurements of diffusivity, which indeed increases for higher water content. Diffusivity and permeability are, however, of different physical meaning. Experimental studies performed by Kalifa et al. (1998) and Abbas et al. (1999) have demonstrated that permeability decreases for higher humidity levels. The reasoning for this effect is that with increased humidity, pores are partially or fully filled with water and ingress of gases and liquids is impeded. Even though the approach used in this model deviates from experimental data, it is shown numerically that this region (T < 95 °C) plays only a very minor role in the development of pore pressure. Considering the subsequent rise in permeability due to evaporation of water (T > 95 °C) it becomes evident that the effect of humidity on permeability is not as significant. For this reason, the dependency of permeability on temperature is not further changed.

Figure 7.1 (right) shows the experimentally obtained permeability of HPC at different temperatures, see Section 5. Overall increase in permeability from room temperature to 300 °C as predicted in the THM model corresponds well with the experimental data. Even though the model prediction for permeability exhibits certain deviations from the measurements, it is found numerically that these differences play only a minor role in the development of pore pressure.

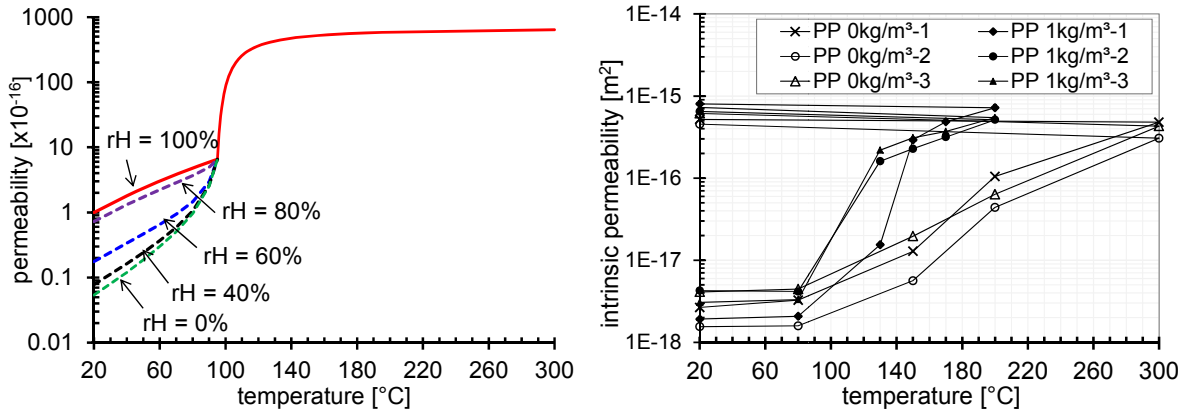

Figure 7.1. Permeability as a function of a temperature for a range of relative humidity levels (Bazant & Thonguthai 1978) (left); experimentally obtained permeability of HPC (right)

7.3 Thermo-mechanical coupling

In the mechanical part of the model the total strain tensor for non-loaded concrete exposed to high temperature is same as in the thermo-mechanical model. The mechanical strains are used to calculate the effective stresses increments (stress in solid phase - concrete matrix) and macroscopic stresses increments from the microplane constitutive law as (Periskic 2009):

$$\dot{\sigma}\left(\varepsilon,T,t\right)=\boldsymbol{D}\left(\varepsilon,T,t\right):\dot{\varepsilon}^{m}+\dot{\sigma}^{p}\left(\varepsilon,T,t\right) \tag{7.19}$$

in which $\boldsymbol{D}$ = tangent stiffness tensor obtained from the microplane model, $\dot{\varepsilon}^{m}$ = increment of the mechanical strain tensor and $\dot{\sigma}^{p}$ = stress increment due to pore pressure, which is calculated from the increment of volumetric pore pressure $\dot{\sigma}^{p}=n\,\dot{p}$, with $\dot{p}$ = increment of pore pressure. Note that according to definition pore pressure p is negative. The source of mechanical strain is external load, thermal strain induced stress and pore pressure in concrete.

7.4 Thermo-hygro-mechanical coupling

Thermo-hygro processes are coupled with mechanical properties of concrete in both directions. Porosity and permeability of concrete change (increase) for higher level of damage in concrete. In order to account for this, permeability and porosity of concrete are assumed to be damage dependent. Following suggestions from Wang et al. (1997), the relations plotted Figure 7.2 are adopted in the present model (Periskic 2009). Damage (crack opening) is calculated using temperature dependent microplane model (Ozbolt et al. 2008; Periskic 2009).

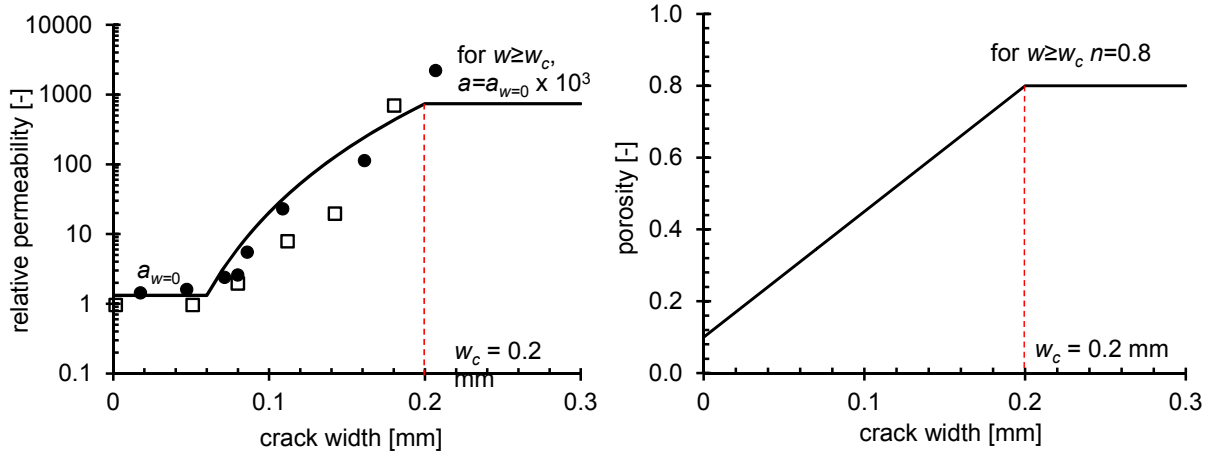

Figure 7.2. Permeability (left) and porosity as function of crack width (right)

From Figure 7.2 (left) it can be seen that after the crack opening reaches the threshold value (critical crack width), permeability of concrete increases up to its maximal value (1000 $a_{w=0}$). For further increase of the crack width (open crack), permeability is assumed to be constant, because of numerical reasons (continuum modelling). Furthermore, after the crack fully opens, pore pressure drops significantly, and permeability is no longer relevant parameter. The same reasoning is valid in case of porosity (Figure 7.2 right).

7.5 Numerical implementation

The numerical analysis is incremental (Ozbolt et al. 2008; Periskic 2009). In each time step Δt partial differential equations, which control heat and moisture transfer in concrete, and equation of equilibrium are solved simultaneously. It is assumed that damage is constant in each time step, i.e. thermo-hygro properties of concrete are controlled by damage from the end of the previous time step. To solve the problem by the finite element method the above differential equations, which govern heat and moisture transfer in concrete, are written in the weak (integral) form. The system of equations is then solved using direct integration method. In the obtained equations the controlling parameters are coupled, therefore, for each time step the set of linear equations is solved iteratively. As mentioned before, during iteration process damage is assumed to be constant, i.e. the equations are linearized. More details can be obtained from Ozbolt et al. (2008) and Periskic (2009).

8. MODELLING EXPLOSIVE SPALLING

8.1 Introduction

Macro-scale modelling is based on the assumption that concrete is a homogeneous material and that the macroscopic properties are sufficient to model the overall behaviour of concrete. Within the framework of finite element methods, structural element is discretized with tetrahedral, hexahedral or other type of finite elements, which are assigned the macroscopic properties of concrete such as elasticity modulus, compressive strength, tensile strength, fracture energy, etc. Certain rules are associated to simulate the failure and fracture of concrete at macro scale. Material properties are considered as average properties obtained for the concrete as a composite of the phases assuming material homogeneity in all points of the continuum. In most of the engineering applications, especially the ones involving mechanical behaviour of concrete structural elements, this assumption of concrete homogenization is commonly accepted. Examples of macro-scale modelling approach provided in Sections 6.5 and 6.6 demonstrate the applicability of this approach in case of modelling the effect of mechanical load as well as the effect of fire on structural performance.

However, in case of problems where local inhomogeneities of the concrete matrix govern the behaviour of concrete elements, the use of macro-scale models might not fully capture the phenomenon of interest. In these cases meso-scale modelling approach is required. Typically, such problems are characterized by severe spatial and temporal variations of stresses and strains in the material. An example of the influence of local properties and inhomogeneities is the phenomenon of explosive spalling of concrete. The large scatter in results from various experiments indicates that the local properties of concrete, which can vary significantly, strongly influence the behaviour.

Typically at meso-scale, concrete is modelled as a three phase material consisting of cement mortar, aggregates and an interfacial transition zone (ITZ) connecting the two. Each component of the concrete matrix is assigned different mechanical and thermal properties and the variation in their individual behaviour under loading is also modelled differently, which is closer to reality than the assumption of homogeneous behaviour.

Variation in strength and stiffness of the individual components governs the global fracture and stiffness of the material as a whole. Under temperature loading, internal stresses are generated in the material due to different thermal properties such as thermal expansion coefficient, thermal conductivity, etc. and this can be adequately accounted for.

Further, properties governing mass transport such as permeability and porosity are also different for different components. These properties influence the thermal and hygral dilation of concrete. From the above discussion, it is evident that the meso-scale modelling approach is not only desirable but also essential if simulation of complex phenomena sensitive to the local material structure, such as explosive spalling, is required.

Here, the numerical modelling of explosive spalling of concrete is studied at (i) macro-scale level and (ii) meso-scale level. Thermo-hygro-mechanical model presented in Section 7 is employed to simulate the coupling of thermal effects, transport process and resulting fracture behaviour of concrete. Temperature dependent microplane model is used as constitutive law for concrete. It has already been shown that the thermo-mechanical model within the same framework is capable of reproducing the experimental results on specimens and structural components subjected to elevated temperature and mechanical loading. The results of numerical analysis are compared with the experimentally obtained results presented in Section 3. A detailed parametric study employing the numerical procedure presented here is performed to assess the influence of various parameters and concrete properties on explosive spalling of concrete.

8.2 Modelling approach

The numerical investigation is performed for a concrete slab exposed to one-sided heating with boundary conditions corresponding to those in experimentally tested slabs (see Section 3). Simple 2D models under assumption of plane strain conditions are used in parametric studies in order to minimize the computation time. Moreover, selected cases are investigated by employing a 3D model, to check the suitability of the 2D model to capture the behaviour of concrete under fire. The results of the numerical meso- and macro-scale analysis on both 2D and 3D models are then compared with the experimentally obtained data.

8.2.1 Macro-scale model

The geometry and the boundary conditions for 2D model are shown in Figure 8.1. In order to minimize the analysis time, only a symmetric slice of the slab is simulated, under the assumption of plane strain conditions. In the case where the effect of the load prior to heating is investigated, the corresponding horizontal compressive load is applied by displacement control (Figure 8.1 right). The specimen is subsequently heated while keeping the applied displacement constant.

The thermal load is applied on the part of the top surface (Figure 8.1). The discretization is performed using hexahedral (eight-node) elements assuming linear strain field (Figure 8.1). The discretization is chosen very fine in the relevant area of concrete cover and quite coarse in the regions away from the heated surface.

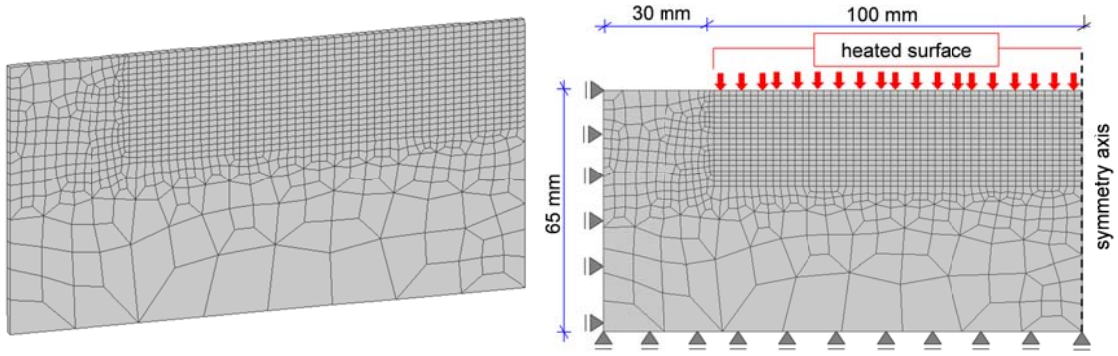

Figure 8.1. Geometry and boundary conditions for the 2D macro model

Similarly, in the case of the 3D model a 50 x 50 x 50 mm piece of the slab is modelled (Figure 8.2). The side surfaces of the specimens are constrained in the direction of the normal to the corresponding surface, in order to account for the restraining effect, which is also present in the real scale concrete structures. The material is discretized using tetrahedral (four-node) elements (Figure 8.3).

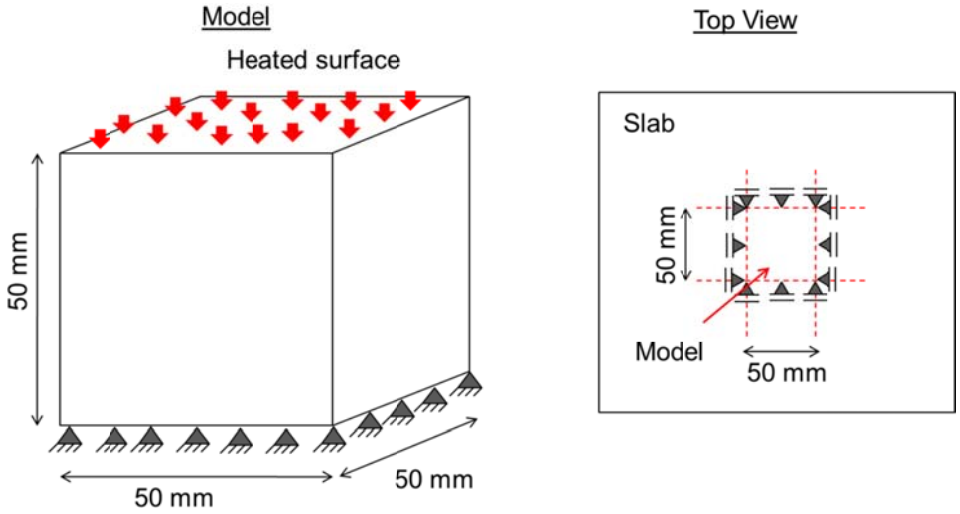

Figure 8.2. Geometry and boundary conditions for the 3D macro-scale model

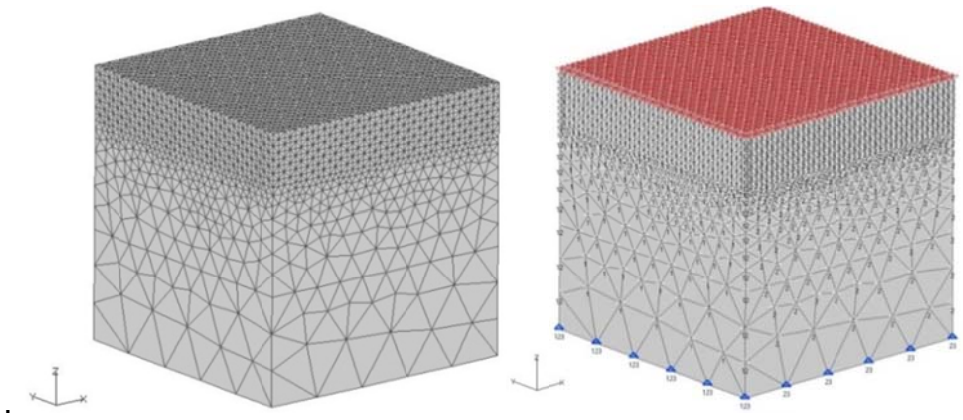

Figure 8.3. Finite element discretization for the 3D macro-scale model

Macro-scale modelling approach assumes homogeneity of concrete, i.e. material properties are the same in every point of the continuum. The material properties used in this study correspond to those obtained for experimentally investigated concrete, for the validation part, and to concrete class C 80/95, for the parametric study.

Table 8.1 Overview of the material properties used in the numerical analysis (macro-scale modelling approach)

Material	Compressive strength	Tensile strength	Fracture energy	Young's modulus	Porosity	Thermal conductivity	Heat capacity
	MPa	MPa	N/m	MPa	%	W/mK	J/kgK
Experiment ISO 834							
concrete	120	5.0	100	48000	10	1.9	750
Experiment ZTV-ING, Parametric study							
concrete	90	3.8	80	43000	10	1.7	850

The properties that are not measured in the experimental work are estimated according to guidelines from the literature (Karihaloo 1995). The material properties are summarized in Table 8.1. The values for thermal conductivity and heat capacity provided in the table are the initial values at room temperature. The influence of temperature on thermal properties of concrete (thermal conductivity and specific heat) is adopted according to DIN EN 1-2 (2004).

8.2.2 Meso-scale model

The geometry, boundary and loading conditions are the same as used for the macro-scale analysis. As mentioned earlier, at meso-scale concrete is typically modelled as a three-phase material consisting of coarse aggregate, mortar matrix and interface between the first two.

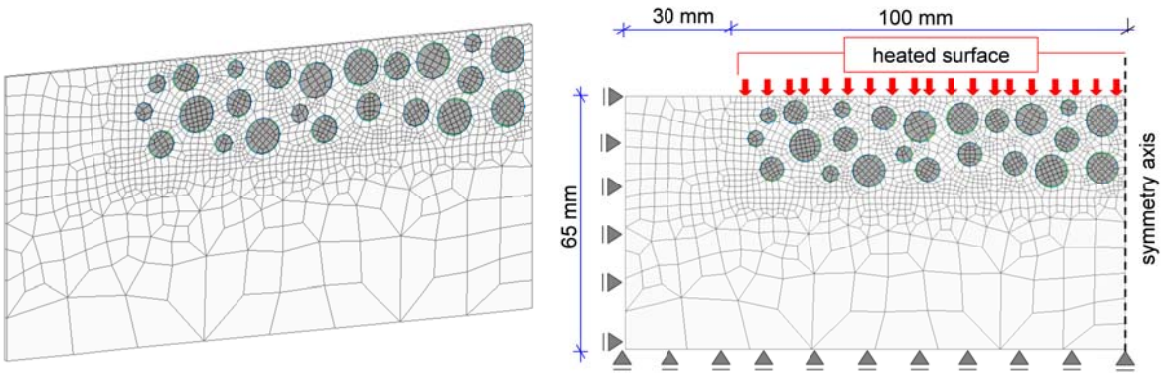

Figure 8.4. Finite element mesh of the meso-scale 2D model

For simplicity reasons, only the relevant portion of the concrete element (concrete cover) is modelled as a mesoscopic material, the rest is modelled the same as in the macro-scale model, assuming the mortar properties. Coarse aggregates are idealized as round (spherical) particles and the range of aggregates sizes as well as their mutual ratio is taken from the mixture used in the experiments. The volumetric ratio of coarse aggregates to concrete is also chosen as in the experiment. Interfacial transition zone is discretized as a thin layer around the aggregates with thickness of 0.2 mm. The finite element mesh is shown in Figure 8.4. Same as in the macro-scale model, the full three-dimensional model at meso-scale is modelled as a 50 x 50 x 50 mm piece of the slab. The finite element mesh of the model and the aggregates are shown in Figure 8.5. The mechanical and thermal properties of all three constituents are provided in Table 8.2.

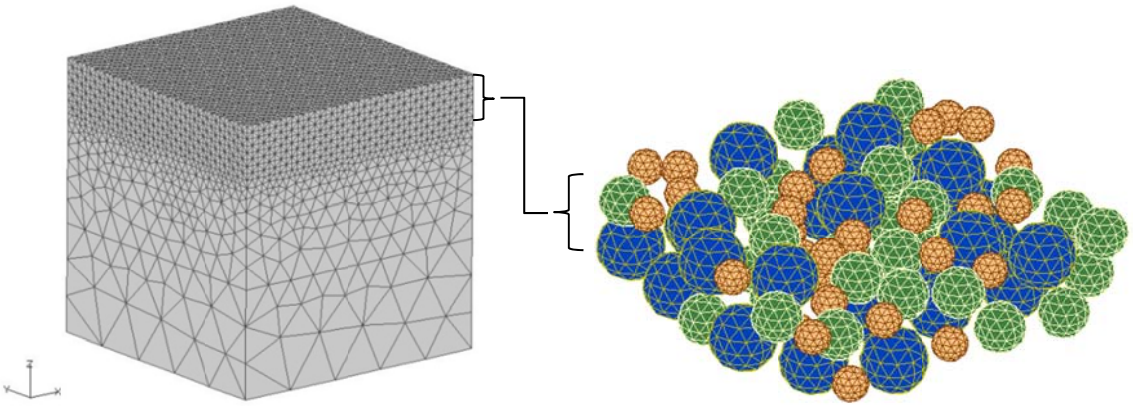

Figure 8.5. Finite element mesh of the meso-scale 3D model: full model (left) and aggregates in the concrete cover (right)

Table 8.2. Overview of the material properties used in the numerical analysis (meso-scale modelling approach)

Material	Compressive strength	Tensile strength	Fracture energy	Young's modulus	Porosity	Thermal conductivity	Heat capacity
	MPa	MPa	N/m	MPa	%	W/mK	J/kgK
Experiment ISO 834							
mortar	120	4.8	80	47000	10	1.7	850
(basalt) aggregates	150	15.0	100	60000	5	1.9	750
interface	120	1.6	30	47000	10	1.7	850
Experiment ZTV-ING, Parametric study							
mortar	90	3.8	70	43200	10	1.7	850
(basalt) aggregates	150	15.0	100	60000	5	1.9	750
interface	90	1.3	30	43200	10	1.7	850

The properties of coarse aggregates are taken from the literature (Jian Zhao 2012), since the measurements of the aggregate properties (basalt) were not performed in the experimental part of the project.

The mechanical and transport properties of the interfacial transition zone (ITZ) are difficult to investigate experimentally. In this study it is assumed that the compressive strength of ITZ corresponds to that of mortar matrix, whereas the tensile strength corresponds to one third of the matrix tensile strength. Permeability and porosity of the ITZ are in reality different from the mortar properties, namely both are higher than that of concrete mortar. However, in this work the ITZ is modelled as layer with thickness of 0.2 mm. This is an overestimation of the size of the ITZ and if the corresponding transport properties are assumed to be higher than that of mortar, this could result in an unrealistic relief of pore pressures in the ITZ.

8.3 Validation of the modelling approach against experiments

In this section, the results of the numerical analyses are compared with the respective experimental counterparts, for both macro- and meso-scale modelling approach. ISO 834 fire curve is analysed employing the thermo-mechanical (TM) and thermo-hygro-mechanical (THM) model, in order to verify the suitability of the two models for the analysis of explosive spalling. Fire curve ZTV-ING is analysed employing only the THM model. The comparison of numerical results against experiment is performed in terms of temperature profiles, time of spalling initiation and failure mode, i.e. parameters measured in the experiment. All details regarding the experimental setup, testing and results are provided in Section 3 of this work.

8.3.1 Standard fire ISO 834 (ETK)

Material properties for the concrete at macro-scale and the three constituents at meso-scale correspond to those of the experimentally investigated material and are summarized in Table 8.1 and Table 8.2. Water content of the concrete at the time of testing was measured as 3 % mass content, which roughly corresponds to a relative humidity of 80 % for similar concrete mixture (Norling Mjörnell 1997). The relative humidity is assumed to be somewhat lower due to the poor workability of concrete which lead to generation of excessive voids.

The distribution of temperature along the depth is presented in Figure 8.6. The experimental data are taken from the specimen with addition of PP fibres, since the specimen without fibres experienced severe spalling and the temperature measurements are not comparable with the analysis, i.e. after the spalling started, the thermocouples were exposed to direct fire. As discussed in the experimental part of the work, it is found that the presence of the PP fibres does not influence the temperature distribution. In general, a reasonably good agreement between the experimental and numerical results at different depths can be observed.

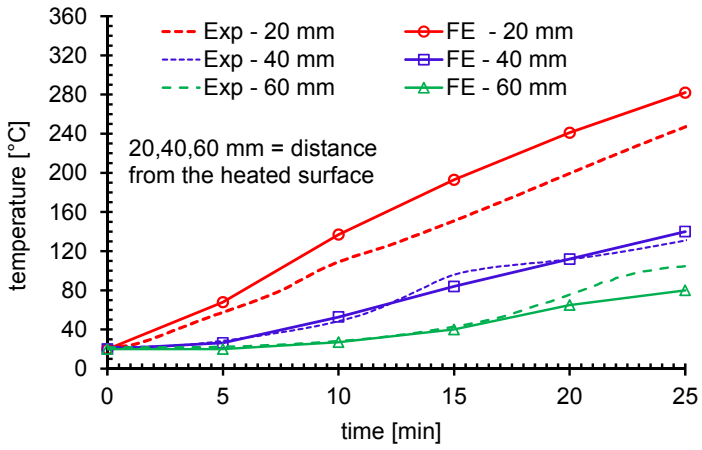

Figure 8.6. Temperature profiles: numerical and experimental results

8.3.1.1 ISO 834 fire analysed employing TM model

The most part of the numerical investigation is performed employing the thermo-hygro-mechanical model. However, for both macro- and meso-scale approach one analysis each is performed using only the thermo-mechanical model. In this case only the thermo-mechanical damage, i.e. the influences of material degradation and thermally induced stresses are taken into consideration and the influence of humidity and moisture transport is neglected.

Thermally induces stresses alone can also be experimentally investigated (on completely dry specimens), however, the distribution of the stresses across the specimen is very difficult to measure. On the other hand, the effect of pore pressure without the presence of thermally induced damage is not investigated, due to numerical instability of the THM model for this case. However, this is of little practical importance, since the generation of pore pressures is always associated with some sort of heating, in which case generation of thermally induced stresses is inevitable.

The macro-scale model, when accounting only for the thermally induced stresses, does not exhibit any damage of the explosive type. In this case only the expansion of the surface layer can be observed. Figure 8.7 shows the distribution of the principal tensile strains (damage) after 15 minutes of the ISO 834 fire. The damage is presented in terms of principal tensile strains, the red area representing the strain corresponding to the critical crack width for not reinforced concrete (w_c = 0.1 mm). This representation of damage is consistent for all the results presented within this work. The analysis is performed for the duration of 60 minutes, and no spalling could be observed, i.e. the damage occurs only at the surface of the specimen and its magnitude is approximately 10 times less than the critical damage.

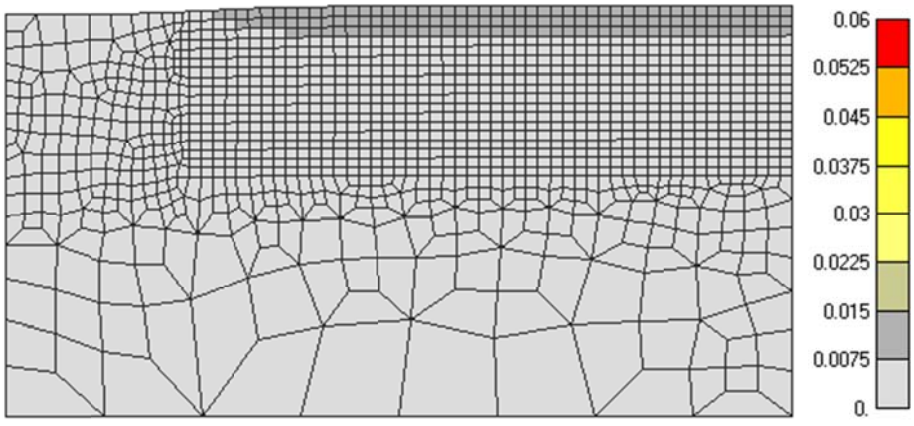

Figure 8.7. Principal tensile strains after 15 minutes of ISO 834 fire – macro-scale model (analysed using thermo-mechanical model)

The development of thermally induced stresses in the elements at different distances from the heated surface is shown in Figure 8.8. The thermal stresses parallel to the

surface rise from the thermal gradients present along the specimen depth. At the beginning of heating, the maximum stress is generated very close to the heated surface. As the specimen further heats, the location of the peak thermally induced stress shifts towards the inner parts of the specimen, whereas the part close to the surface undergoes relaxation. The damage observed is mechanical damage due to elevated temperature.

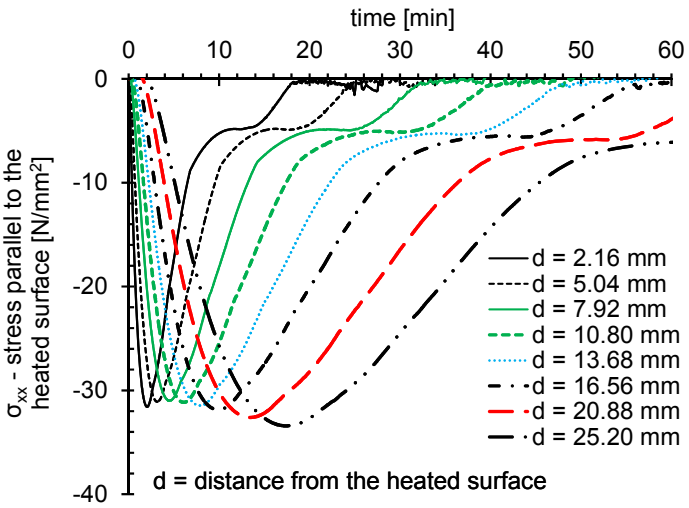

Figure 8.8. Stress parallel to the heated surface σ_{xx} at different distances from the surface – macro-scale model (analysed using thermo-mechanical model)

The meso-scale model shows somewhat different behaviour when analysing only the thermo-mechanical effects. Since concrete is considered as a three-phase material, the incompatibilities of the three phases inevitably lead to cracking. Principal tensile strains (damage) are shown in Figure 8.9. It can be observed that the specimen undergoes damage at the contact of aggregates and cement mortar, i.e. in the interfacial transition zone. However, the cracking occurs only after approximately 16.5 minutes of fire. Furthermore, the strain rate measured at the element where the damage first localizes is very low, significantly lower (approximately 30 times) than in the case when THM model is employed, as is demonstrated in the following section.

Explosive spalling is a very violent failure mode, whereas the present failure mode corresponds rather to thermal cracking and cannot be considered as explosive spalling. This type of thermal cracking could also be observed in the fire experiments where the whole concrete surface exhibited extensive cracking, see Section 3. The cracking of concrete surface in the case of concrete with PP fibres was observed after approximately 14 minutes of ISO 834 fire. It is very important to notice the difference between explosive spalling and non-explosive damage (thermally induced cracking). When thermally induced cracking occurs, the concrete cross section remains intact and the temperature distribution changes only slightly due to crack opening. In case of explosive spalling, the layers of concrete are removed from the specimen and the remaining concrete is exposed to very high temperatures.

The development of thermal stresses parallel to the heated surface is shown in Figure 8.10. The level of stresses is much higher than in the macro-scale model since there is no sudden relaxation of the stresses. The stresses tend to relax after a certain time, but at a much lower rate than in the case of the macro-model.

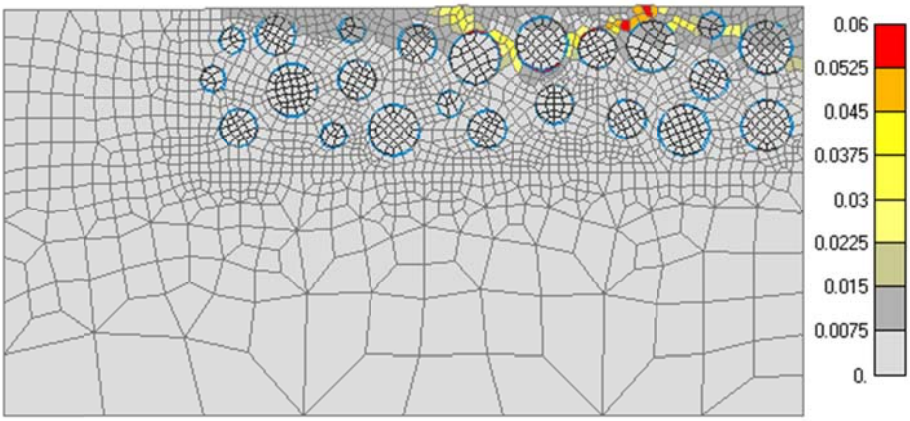

Figure 8.9. Principal tensile strains after 16 minutes of ISO 834 fire – meso-scale model (analysed using thermo-mechanical model)

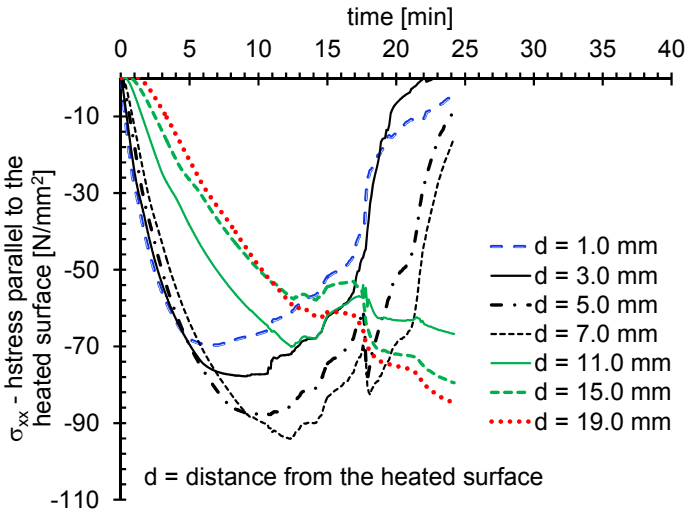

Figure 8.10. Thermally induced stresses σ_{xx} parallel to the heated surface – meso-scale model (analysed using thermo-mechanical model)

The explicit definition of load induced thermal strains in the macro-model is mainly responsible for this difference between the two models with respect to development of compressive stresses. Furthermore, the incompatibility of the three concrete constituents (at meso-scale) results in different distribution of compressive stresses than in the case of macro- scale model. such as explosive spalling, it is essential to model the concrete at meso-scale.

The two above examples demonstrated that the TM model cannot account for any aspect of explosive spalling observed in the experiments. This is due to the fact that

this approach completely neglects the effect of moisture on the behaviour of concrete under fire. This is consistent with the experimental data, which indicate that completely dry specimens do not experience explosive spalling (Connolly 1995).

8.3.1.2 ISO 834 fire analysed employing THM model

A typical failure in the case of macro-scale model is shown in Figure 8.11 (left). It should be noted here that the thermo-hygro-mechanical model is used only to evaluate the onset of spalling. It is not possible to simulate the successive failure of the specimen throughout the fire, since the analysis becomes unstable after the initial spalling. However, the principal goal of the investigation is to provide more insight into the mechanism behind explosive spalling, and for this purpose the prediction of onset of explosive spalling is considered to be sufficient.

It can be observed (Figure 8.11 left) that the damage is not localized, but rather the whole heated surface fails practically simultaneously. The front of pore pressures progresses parallel to the heated surface, and so does the thermally induced stress. Since the material properties are assumed to be same in every point of continuum, the failure occurs almost at the same time along the whole heated surface. Obviously, the macro-scale model is not able to reproduce the localization of failure as observed in the experiments.

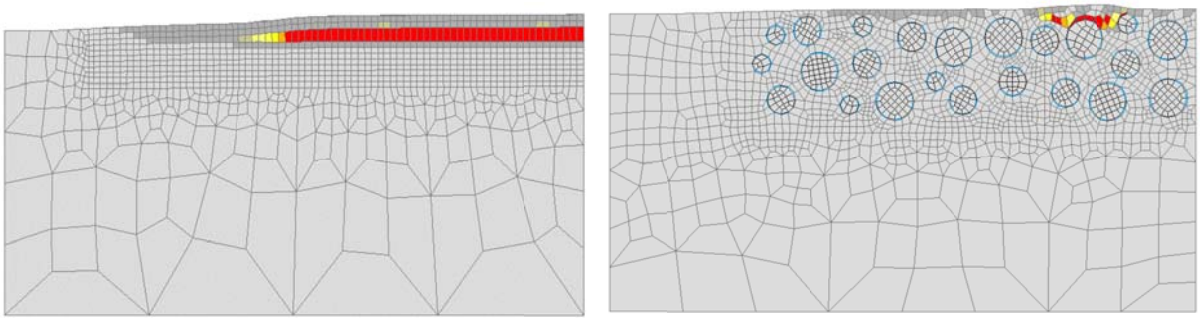

Figure 8.11. Typical failure mode of the macro-scale model (left) and meso-scale model (right) (analysed using thermo-hygro-mechanical model)

Figure 8.11 (right) shows the damage predicted by the meso-scale model at the onset of explosive spalling. A clear localization of the damage can be observed. The presence of the aggregates i.e. inhomogeneity allows for a more realistic crack pattern since it influences the distribution of both thermally induced stresses as well as moisture transport.

Damage on the tested specimens (at the end of the fire test) is shown in Figure 8.12. Experimentally observed explosive spalling is manifested by very violent failure of random parts of the concrete surface. Very pronounced scatter in terms of spalling time, location of damage and size (width and length) of the spalled concrete layer is observed. The depth of the initial spalling could not be measured in the experiment,

however, the layers of concrete that failed were observed to be rather thin. No pattern whatsoever could be observed as to preferred location of the initial explosive spalling (such as edge or mid part of the specimen).

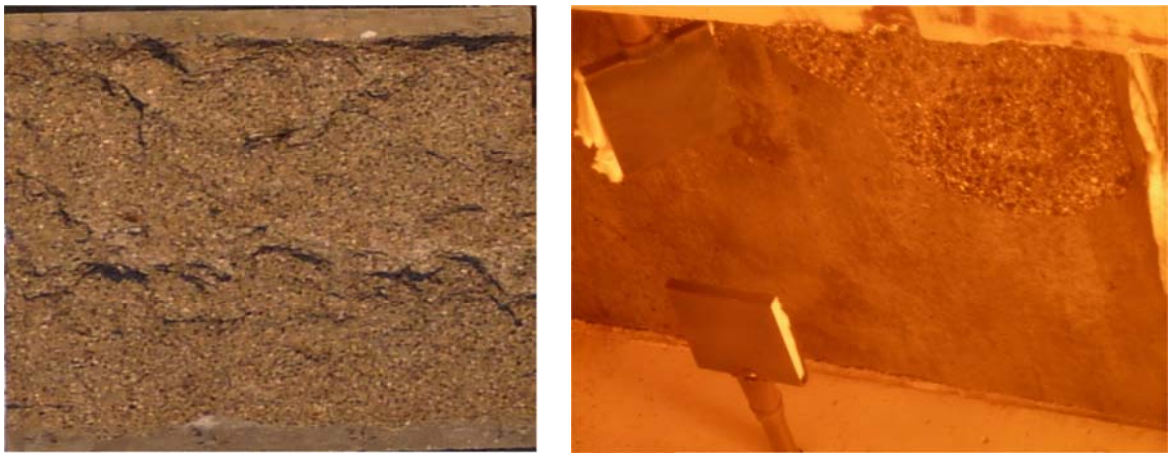

Figure 8.12. The specimen-without PP fibres-after fire (left) and during the fire (right)

The onset of spalling in the experiment is observed after 8 minutes of fire duration. However, these were isolated spalling events and not all specimens experienced explosive spalling immediately nor simultaneously. Successive explosive spalling of concrete layers at all three tested specimens occurred after approximately 9.5 minutes. Macro- and meso-scale models predict explosive spalling after 11.6 and 10.4 minutes, respectively. Even though the prediction of the meso-scale model lies somewhat closer to the experimental result, it can be stated that the both models can predict the onset of explosive spalling with reasonable accuracy.

The performance of the two modelling approaches is further evaluated by comparing the development of the relevant parameters in the element where the cracking initiated. Pore pressure and volumetric stress are shown in Figure 8.13 for macro- and meso-model. Volumetric stress is calculated as pore pressure multiplied by the porosity, following simplified engineering model suggested by Periskic (2009). Pore pressure and volumetric stress increase at a very low rate in the beginning of the analysis, up to approximately 2 minutes of fire, for both the models. As temperature rises, a saturated zone starts to create and a more rapid increase of volumetric stress precedes explosive spalling, demarcated by the red point in the diagram. Further increase in volumetric stress results from a reaction to mechanical damage (contribution of mechanical strain to the porosity). The relevant value of volumetric stress is the value immediately before the sudden rise of the same. Increase in porosity due to damage results in a sudden increase of volumetric stress, caused by numerical instability, and is not relevant for the evaluation.

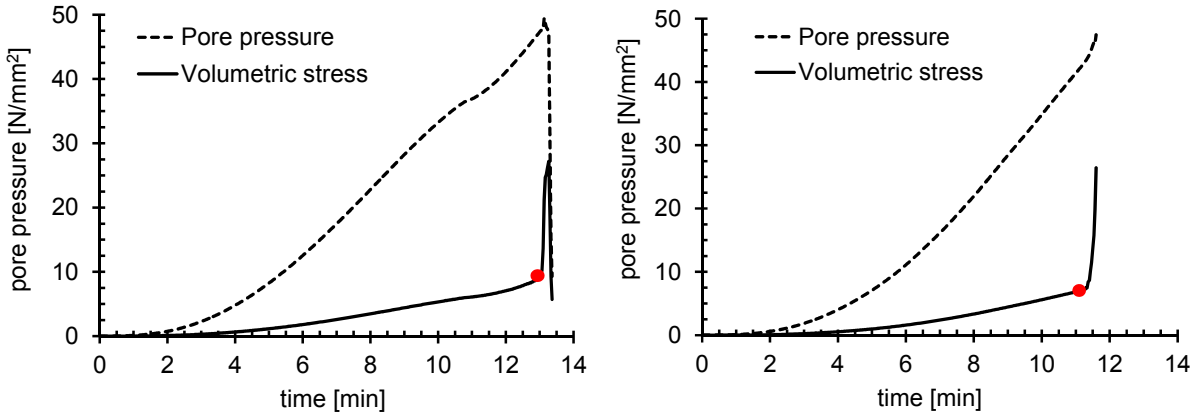

Figure 8.13. Development of pore pressure and volumetric stress at the location of cracking: macro- (left) and meso-model (right)

The porous system of concrete changes due to damage and increase in pore volume. This results in a drop of the both pore pressure and volumetric stress. The analysis becomes unstable at this time step. This is due to the fact that the crack opening (softening) is taking place, and, therefore, concrete cannot take up pore pressure which is load controlled. In the subsequent steps the pressure drops down and the analysis becomes stable. Similar drop of pore pressure at the location of spalling (or in the vicinity) observed by other researchers when measuring pore pressure in heated specimens which underwent spalling, (Phan 2007; Jui et al. 2008; Jansson & Boström 2010).

One of the important differences between the two modelling approaches is the pronounced difference in the absolute value of the pore pressure and volumetric stress at failure. Macro-scale model fails at a volumetric stress of 8.6 MPa, whereas the meso-scale model yields significantly lower value of 6.9 MPa.

The development of relative humidity and porosity is shown in Figure 8.14 for both macro and meso-scale model. The development of relative humidity in time differs for the two models, since in the case of meso-scale model the relative humidity distribution is influenced by the presence of very dense aggregates. Nevertheless, the general trend is similar. Comparing Figure 8.13 and Figure 8.14 it is evident that the increase in relative humidity leads to a more rapid rise of the pore pressure and consequently, volumetric stress. Porosity and permeability increase due to heating (size of pores and interconnectivity of the same increases) as well as due to damage cause by heating. In the first 10 minutes of heating porosity increases from initial value of 10 % to 15 % and 18 % for meso- and macro-scale model, respectively.

The temperature evolution of the cracked element is shown in Figure 8.15 for both models. It is evident that the two models predict a similar temperature increase in time, with meso-scale model exhibiting only slightly lower temperature. This can be expected, since the heterogeneity introduced in the meso-scale model does not in-

troduce any significant variation in the thermal properties. At the time of spalling, the temperature is approximately 380 °C. The air temperature at the same time is approximately 625 °C, which is consistent with the experimentally measured oven temperature at the onset of spalling (between 600° and 650 °C).

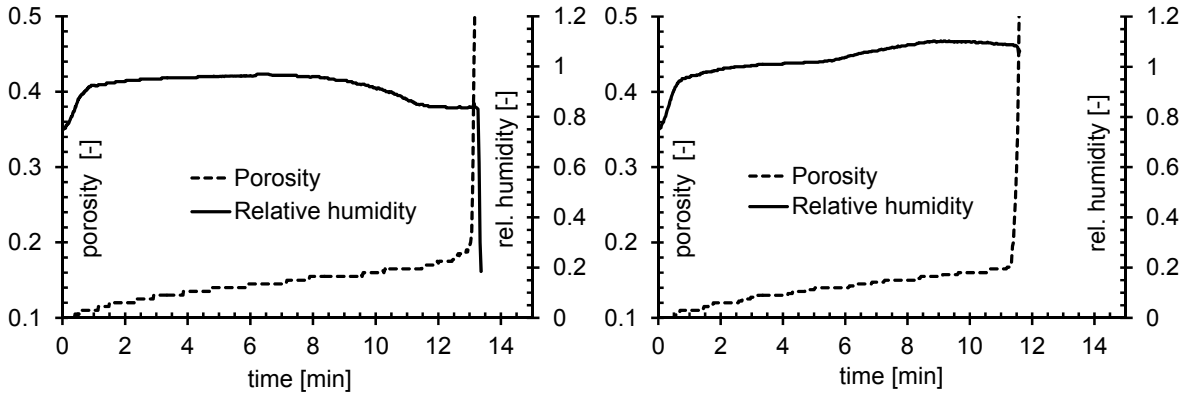

Figure 8.14. Development of relative humidity and porosity at the location of cracking: macro-scale model (left), meso-scale model (right)

It can be concluded that both models exhibit similar behaviour in terms of heat distribution in concrete, whereas the pore pressure and volumetric stress at the moment of failure differ significantly. This is mainly due to the fact that the macro-scale model considers concrete as a homogeneous material whereas meso-scale model accounts for the inhomogeneity, i.e. local variation of the material properties.

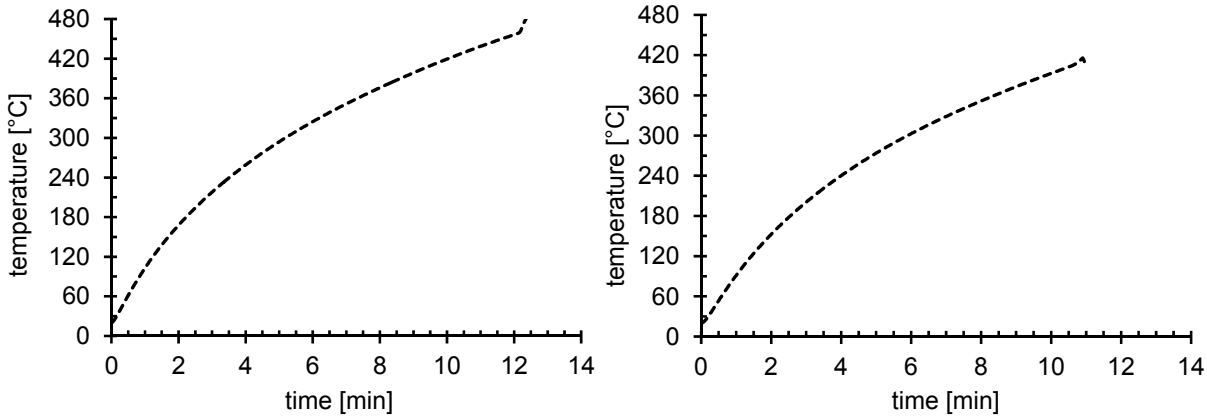

Figure 8.15. Development of temperature at the location of cracking: macro-scale model (left), meso-scale model (right)

The development of thermally induces stresses in two directions (σ_{xx} - parallel to the heated surface and σ_{zz} - perpendicular to the heated surface) is shown in Figure 8.16 and Figure 8.17 for the macro and meso-scale model, respectively. Macro-scale model predicts a strong relaxation of compressive stresses, such that the thermal compressive stresses (σ_{xx}) start to reduce at a very early stage of fire, approximately after 2 minutes. This relaxation is attributed to the predefined LITS, as discussed in

Section 6.7. These are incorporated in the macro-scale model and are only temperature dependent, but no time, i.e. heating rate dependency is accounted for. Consequently, the material undergoes relaxation when heated at higher load levels. At the moment of failure the compressive stresses parallel to the surface are approximately 10 N/mm^2. Since these are very low in comparison to compressive strength, the failure is mainly driven by the volumetric stress (pore pressure).

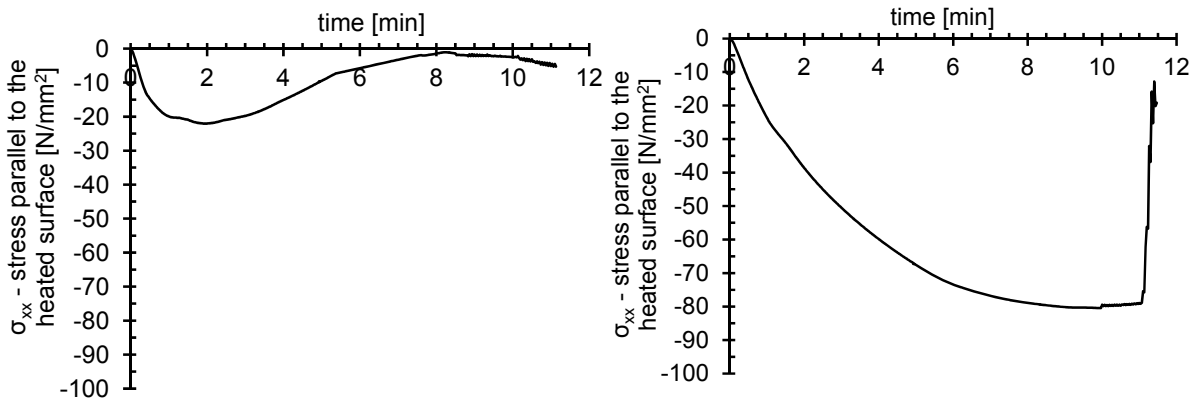

Figure 8.16. Thermally induces stresses σ_{xx} (stress parallel to the heated surface) at the location of cracking: macro-scale model (left) and meso-scale model (right)

On the other hand, meso-scale model (Figure 8.16 right) predicts much higher maximum value of horizontal stresses than the macro-scale model. These go up to approx. 80 % of the compressive strength of the material. As has been shown in Section 6.7, meso-scale model can predict the LITS without their predefinition.

The evolution of stress perpendicular to the heated surface (σ_{zz}) in the cracked element is plotted in Figure 8.17. The macro-scale model predicts almost no tensile stress in the direction perpendicular to heated surface up to the failure. In the case of meso-scale model, the tensile stresses in vertical direction are somewhat higher as a consequence of high compression in the horizontal x direction (parallel to the surface) and the local stress distribution between single aggregate pieces.

Both modelling approaches can reproduce the experimentally observed temperature distribution and the time of initial explosive spalling. However, the results show an important difference in the failure mechanism of the two modelling approaches. At macro-scale, the pore pressure (volumetric stress) seems to govern the failure. At meso-scale, a very high amount of potential energy is absorbed by the specimen due to thermally induced stresses. As volumetric stress (pore pressure) rises at relatively high rate, it acts as a trigger for the release of the accumulated potential energy and a very explosive failure takes place. The intensity of explosive spalling can be evaluated by considering the strain rate in the cracked element.

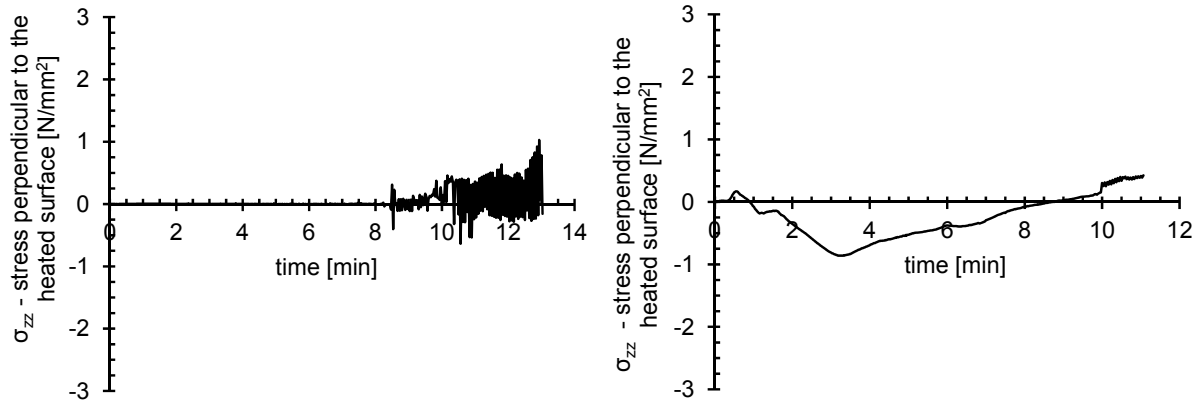

Figure 8.17. Thermally induces stresses σ_{zz} (vertical stress) at the location of cracking: macro-scale model (left) and meso-scale model (right)

Comparing the results obtained employing TM and THM model, it is obvious that the TM model cannot predict any aspect of explosive spalling for either of the two modelling approaches. This is attributed to the fact that the moisture transport plays a very important role in build-up of pore pressures and subsequent failure, whereas TM model does not account for the transport phenomena at all.

The development of thermally induced stresses is very similar for TM and THM model, but these stresses cannot result in explosive spalling without the presence of pore pressure. Therefore, the remaining part of the numerical study is performed employing THM model.

8.3.1.3 Tunnel fire curve (ZTV-ING) analysed employing THM model

Material properties for the concrete and its three constituents at meso-scale correspond to those of the experimentally investigated material and are summarized in Table 8.1 and Table 8.2. Water content of the concrete at the time of testing is measured as 2.5 % mass content, which approximately corresponds to a relative humidity of 65 % for similar concrete mixture (Baroghel-Bouny 2007).

The distribution of temperature for different depths in time is shown in Figure 8.18. A good agreement between the experimental and numerical results can be observed. As can be observed in the experimentally measured oven temperature (see Section 3), the initial part of the heating was at much higher rate than the target temperature of the ZTV-ING fire curve. This deviation is reflected in the temperature measurements at different depths. Same as for the ISO 834 fire curve, the temperature measurements are taken from the specimen with PP fibres, which did not experience spalling. In this case, the pore pressures could be relieved due to increased pore space created by the melted polypropylene, however, the amount of water and water vapour is substantial due to moisture transport. At the boiling temperature of water (100 °C), a part of the energy is used for the evaporation of water and the temperature cannot rise above 100 °C as fast as it would if no water would be present. The

process of evaporation is time dependent. The THM model can account for this effect only partially since all relevant quantities are only temperature dependent, but not time dependent. However, since the initial spalling occurs at a very low depth and at a very early stage of the fire, the numerical results can be considered to reproduce the experimental data with a reasonable accuracy.

The failure modes, both experimental and numerical, are very similar to those presented in the previous section (see Figure 8.11), and are, therefore, omitted. In the experiment, explosive spalling initiated after approximately 2.5 minutes, with successive spalling starting around 3.0 minutes after the onset of fire. Macro-scale model results in explosive spalling after 3.5 minutes, whereas meso-scale model undergoes spalling after 3.1 minutes of fire. Again, both models predict the spalling time with reasonable accuracy. Similar as in the case of ISO 834 curve, a very good agreement between the experimental and numerical data in terms of temperature profiles, failure mode and time of initial spalling can be observed.

The evolution of relevant parameters in the element where the cracking originated is shown in Figure 8.19 for macro- and meso-scale model. Similar differences between the two models as observed in the previous section can also be seen in the case of ZTV-ING fire. The level of pore pressure (and volumetric stress) is somewhat higher in the case of macro-scale model. Volumetric stress at failure is 6.0 N/mm^2 for the meso-scale model and 7.2 N/mm^2 for the macro-scale model.

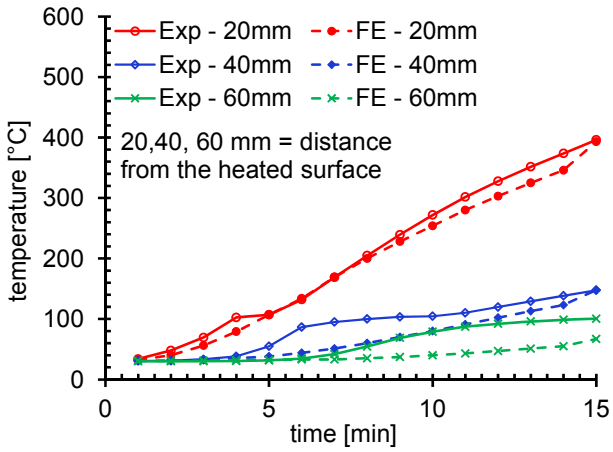

Figure 8.18. Temperature profiles: numerical and experimental results

Relative humidity and porosity in the cracked specimen are plotted in Figure 8.20. Both models predict an increase in porosity and relative humidity with increasing temperature, indicating the formation of a saturated zone. Even though the absolute values for the two models are not identical, the trend is very similar and it indicates that the zone with very high moisture content is created. After the relative humidity increases close to 100 % (approximately after 1 minute), the pore pressure and vol-

umetric stress start to develop at a much higher rate. The penetration of water vapour is inhibited by the “moisture clog”, hence pore pressures start to increase.
Porosity increases with heating as a consequence of change in the porous system. Furthermore, porosity increases with increasing crack width in concrete. At the moment of spalling cracks open abruptly causing porosity to increase accordingly.

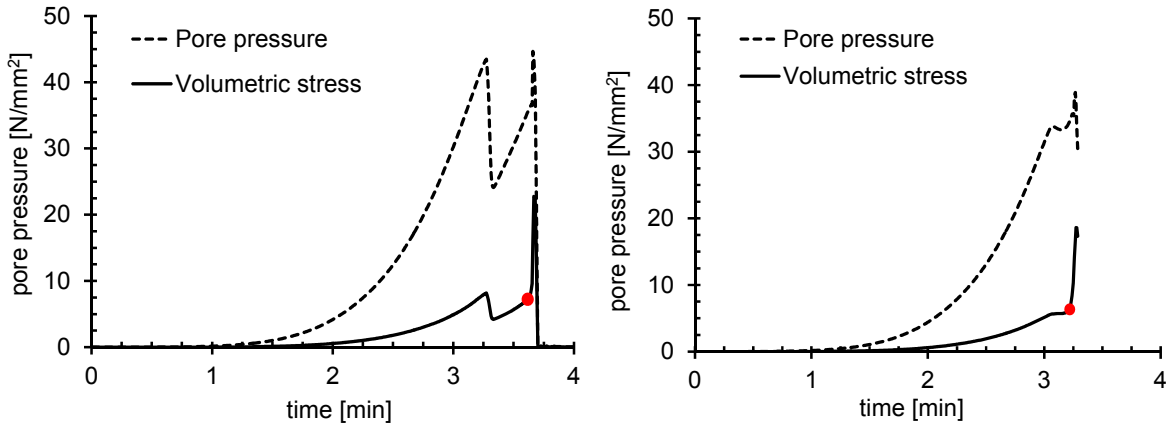

Figure 8.19. Development of pore pressure and volumetric stress at the location of cracking: macro- (left) and meso-model (right)

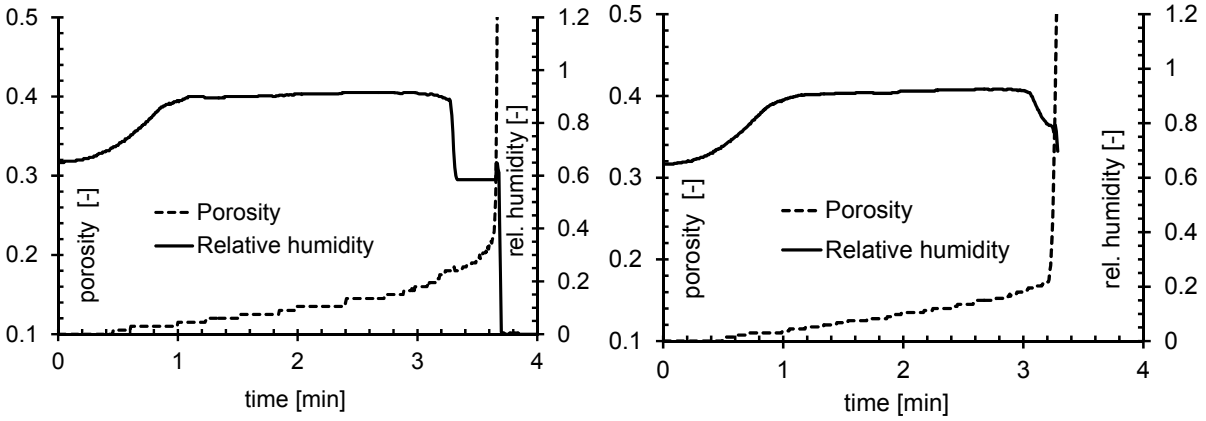

Figure 8.20. Development of relative humidity and porosity at the location of cracking: macro-scale model (left), meso-scale model (right)

The development of temperature in the cracked element is presented in Figure 8.21. Again, the behaviour of the two models is very similar. The temperature at the time when explosive spalling takes place is approximately 420 °C. The air temperature close to the concrete surface is 780 °C at the time of spalling at both macro- and meso-scale. This temperature value is very close to the experimentally observed oven temperature of approximately 750 °C (at the onset of spalling).

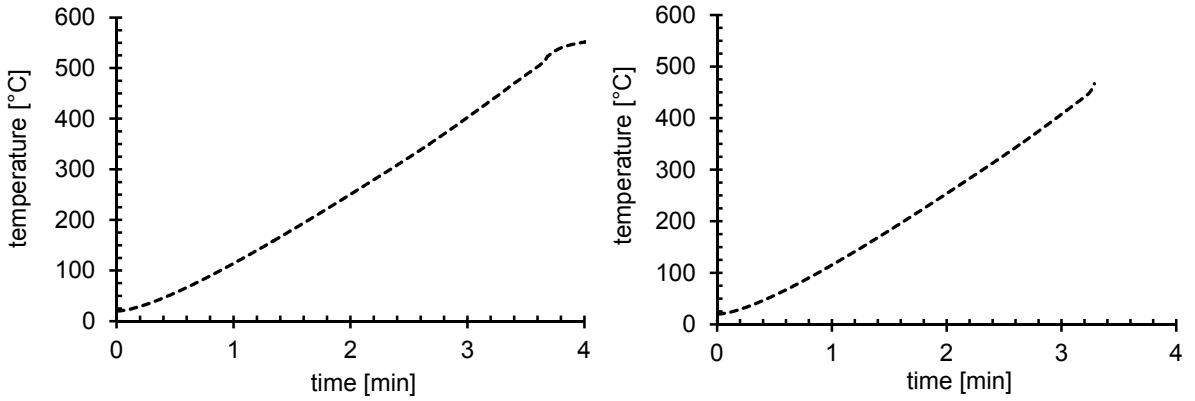

Figure 8.21. Development of temperature at the location of cracking: macro-scale model (left), meso-scale model (right)

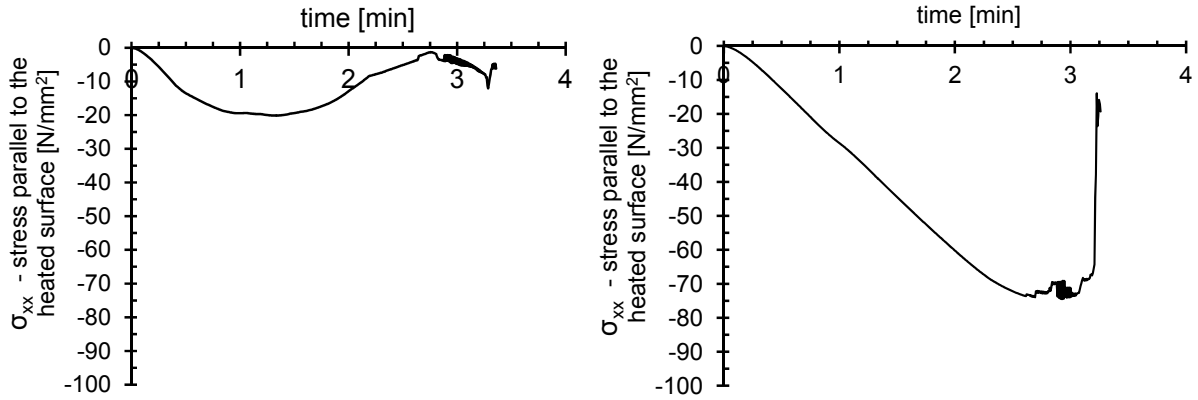

Figure 8.22. Thermally induces stresses σ_{xx} (stress parallel to the heated surface) at the location of cracking: macro-scale model (left), meso-scale model (right)

Thermally induced stresses parallel to the heated surface (σ_{xx}) are shown in Figure 8.22 for the two models. The main difference between the two modelling approaches is the contribution of thermally induced stresses to the mechanism of explosive spalling. Macro-scale model predicts very low levels of stresses due to heating, and these tend to relax at higher temperatures. As discussed in the case of ISO 834 fire curve, the main reason for this behaviour is the presence of LITS, which cause relaxation of stresses. Meso-scale approach gives thermal stresses up to 80 % of the compressive strength of concrete. It is interesting to observe that the level of compressive stress is more or less same as in the case of ISO 834 fire.

As discussed above, meso-scale model fails in explosive spalling under the combined action of the thermally induced stresses and volumetric stress, whereas the macro-scale model undergoes explosive spalling influenced mainly by the pore pressure/volumetric stress without significant influence of the thermally induced stresses. The level of the thermally induced stress is approximately 10 % of the initial compressive strength of concrete in case of the macro-scale model.

8.3.2 Conclusions

The thermo-hygro-mechanical model is employed in the simulation of the fire experiments on high strength concrete slabs exposed to two fire scenarios, standard fire ISO 834 and tunnel fire ZTV-ING. Two modelling approaches, macro- and meso-scale approach, are followed to access their suitability to predict the explosive spalling of concrete. Moreover, a comparison between TM and THM model is obtained based on response of both models to ISO 834 fire curve.

It is observed that TM model can capture only the thermo-mechanical degradation of material, but not explosive spalling. This is attributed to the fact that TM model completely neglects the effect of moisture transport. On the other hand, the results obtained employing THM model exhibit very good agreement with the experimental data.

In case of THM model, it is found that both modelling approaches (macro- and meso-scale) are able to reproduce the experimentally observed behaviour with respect to temperature profile across the specimen depth and the onset time of initial spalling. However, macro-scale model is unable to reproduce the local character of the failure, whereas meso-scale approach realistically captures the localization of damage.

Furthermore, the two approaches differ in the mechanism that leads to explosive spalling. At macro-scale the moisture transport governs the failure with relatively high pore pressure and volumetric stress, and the role of thermally induced stresses is only minor. On the other hand, the meso-scale model results in a failure driven by a combination of very high thermal stresses and pore pressure (volumetric stress), whereby pore pressure (volumetric stress) releases the potential energy absorbed due to thermally induced stresses. In order to fully understand the phenomena of explosive spalling, its mechanism as well as the main influencing parameters, in the subsequent section the results of extensive parametric study are presented and discussed.

8.4 Parametric study at macro- and meso-scale

A numerical study is performed in order to evaluate the suitability of macro- and meso-scale models to predict and capture the abrupt failure mode of concrete explosive spalling, as well as to explain the underlying mechanism. Furthermore, the influence of relevant parameters is studied. The investigated parameters include: geometrical nonlinearity, different heating curves, different (constant) heating rates, permeability of the cement mortar, relative humidity, compressive load, distribution of the aggregates, aggregate type and the load induced thermal strains (only in case of macro-scale model).

Table 8.3 provides an overview of all investigated parameters and the corresponding analyses. In the following sections the results of the parametric study at macro- and meso-scale are presented. All material properties used in the present study are summarized in Table 8.1 and Table 8.2. Geometry, boundary, loading conditions and finite element mesh are same as in the previous section.

In order to optimize computation time, analyses are performed on 2D models (1 row of elements) under assumption of plane strain conditions. However, these are compared to full 3D models, for both modelling approaches, to check the suitability of the 2D models. Large part of the investigation is performed for widely used ISO 834 fire scenario, however, analyses on meso-scale model are also performed for tunnel fire (ZTV-ING) curve as well as for a set of constant heating rates (ranging from 40 °C/min to 200 °C/min).

In the case of macro-scale model the LITS phenomenon is explicitly accounted for in the thermo-hygro-mechanical model. Moreover, a set of analysis is performed for the case where LITS is not accounted for in the thermo-hygro-mechanical model (only at macro-scale). The objective of these analyses is to evaluate the contribution of LITS to the behaviour of concrete at elevated temperatures. At meso-scale, LITS are not predefined, since the meso-scale model can automatically capture this phenomenon, as discussed in Section 6.7.2.

Table 8.3 Overview of the investigate parameters (2D analysis)

Parameters	Unit	Range of investigated values (ISO 834 fire)								scale	other parameters
thermal part	[-]	TM								macro meso	σ = 0 %
geometrical nonlinearity	[-]	GL								macro meso	$a_0 = 6x10^{-15}$, rH = 70 %, σ = 0 %
relative humidity rH	[%]	0	20	40	50	60	70	85	100	macro meso	$a_0 = 6x10^{-15}$, σ = 0 %
permeability a_0	[m/s]	$6x10^{-16}$	$2x10^{-15}$	$6x10^{-15}$	$2x10^{-14}$	$4x10^{-14}$	$8x10^{-14}$	$1x10^{-13}$	$2x10^{-13}$	macro meso	rH = 70 %, σ = 0 %
compressive load σ	[% f_c]	0	10	20	30	40	50			macro meso	$a_0 = 6x10^{-15}$, rH = 70 %
aggregate distribution	[-]	A	B	C						meso	$a_0 = 6x10^{-15}$, rH=40 %, rH = 70 %, rH = 100 %, σ = 0 %
aggregate type	[-]	quartz	granite	dolomite	limestone 1	limestone 2	limestone 3	basalt		macro meso	$a_0 = 4x10^{-14}$, $a_0 = 6x10^{-15}$, rH = 70 %, σ = 0 %

Parameters	Unit	Range of investigated values (macro-scale without LITS predefinition, ISO 834 fire)								scale	other parameters
thermal part	[-]	TM								macro meso	σ = 0 %
relative humidity rH	[%]	0	20	40	50	60	70	85	100	macro meso	$a_0 = 6x10^{-15}$, σ = 0 %
compressive load σ	[% f_c]	0	10	20	30	40	50			macro meso	$a_0 = 6x10^{-15}$, rH = 70 %

Table 8.4 Overview of the investigate parameters (2D analysis)

Parameters	**Unit**	**Range of investigated values (modified ZTV-ING fire)**								**scale**	**other parameters**
thermal part	[-]	TM								meso	σ = 0 %
geometrical nonlinearity	[-]	GL								meso	$a_0 = 6x10^{-14}$, rH = 70 %, σ = 0 %
relative humidity rH	[%]	0	20	40	50	60	70	85	100	meso	$a_0 = 6x10^{-14}$, σ = 0 %
permeability a_0	[m/s]	$6x10^{-16}$	$2x10^{-15}$	$6x10^{-15}$	$2x10^{-14}$	$4x10^{-14}$	$8x10^{-14}$	$1x10^{-13}$	$2x10^{-13}$	meso	rH = 70 %, σ = 0 %
compressive load σ	[% f_c]	0	10	20	30	40	50			meso	$a_0 = 6x10^{-14}$, rH = 70 %

Parameters	**Unit**	**Range of investigated values (constant heating rates)**								**scale**	**other parameters**
relative humidity rH	[%]	70								meso	$a_0 = 6x10^{-14}$, σ = 0 %
permeability a_0	[m/s]	$4x10^{-14}$								Meso	rH = 70 %, σ = 0 %
compressive load σ	[% f_c]	0								meso	$a_0 = 6x10^{-14}$, rH = 70 %
heating rate	[°C/min]	40	60	80	100	120	160	200		meso	$a_0 = 6x10^{-14}$, rH = 70 %

8.4.1 Comparison of 3D and 2D model

The major part of the parametric study is performed on 2D models under assumption of plane strain conditions. To verify the validity of 2D models, only one case is analysed using 3D FE (macro- and meso-scale) Model. The reason for the use of 2D models is the extremely high computation requirements of the 3D FE analysis.

The analysis is performed for relative humidity of 85 % and permeability of $4x10^{-15}$ m/s, under exposure to ISO 834 fire curve. The permeability input in the THM model corresponds to the relative permeability (permeability of a specimen at 100 % relative humidity and 25°C). The crack patterns obtained for both (macro- and meso-scale) models exhibit a very good agreement with the results obtained using the corresponding 2D models, as can be seen by comparing Figure 8.11 and Figure 8.23. Macro-scale model cannot fully capture the local failure, whereas meso-scale model undergoes a pronounced localization of damage.

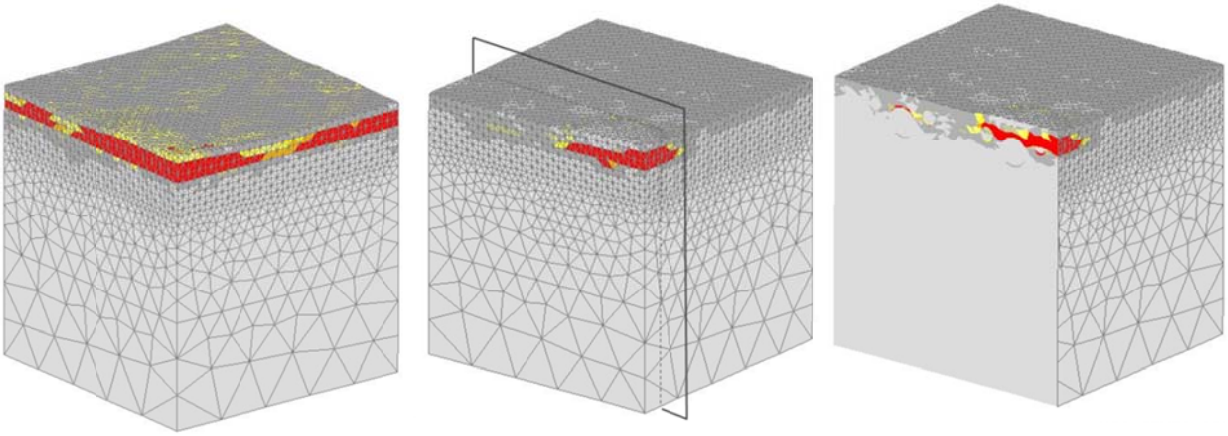

Figure 8.23. Failure mode of the macro- (left) meso-scale 3D model (right) in terms of principal tensile strain

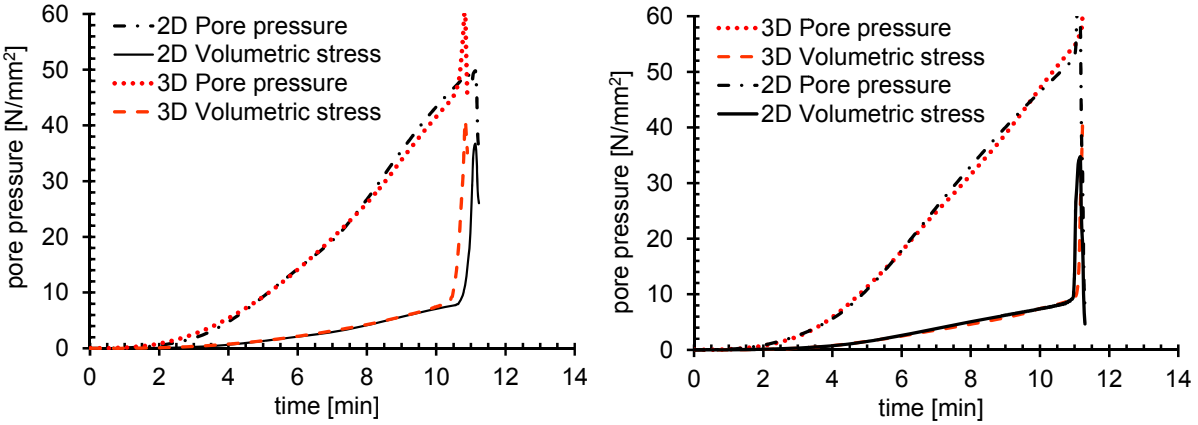

Figure 8.24. Comparison of pore pressure and volumetric for the 2D and 3D model: macro-scale (left) and meso-scale (right)

The time development of relevant parameters (pore pressure, volumetric stress, relative humidity, permeability and thermally induced stresses) is shown in Figure 8.25 and Figure 8.26. It can be observed that, with respect to the relevant parameters evaluated at the location of spalling, both 2D models exhibit a good agreement with the corresponding 3D models. It can be concluded that the use of 2D models for the analysis of concrete behaviour at high temperatures is acceptable. For this reason the remaining part of the parametric study is performed employing 2D models.

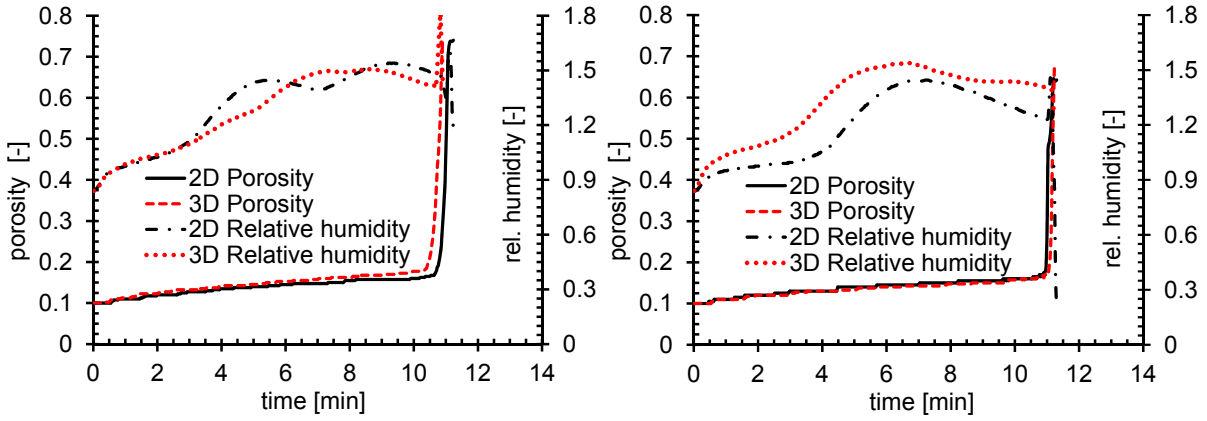

Figure 8.25. Comparison of relative humidity and porosity for the 2D and 3D model: macro-scale (left) and meso-scale (right)

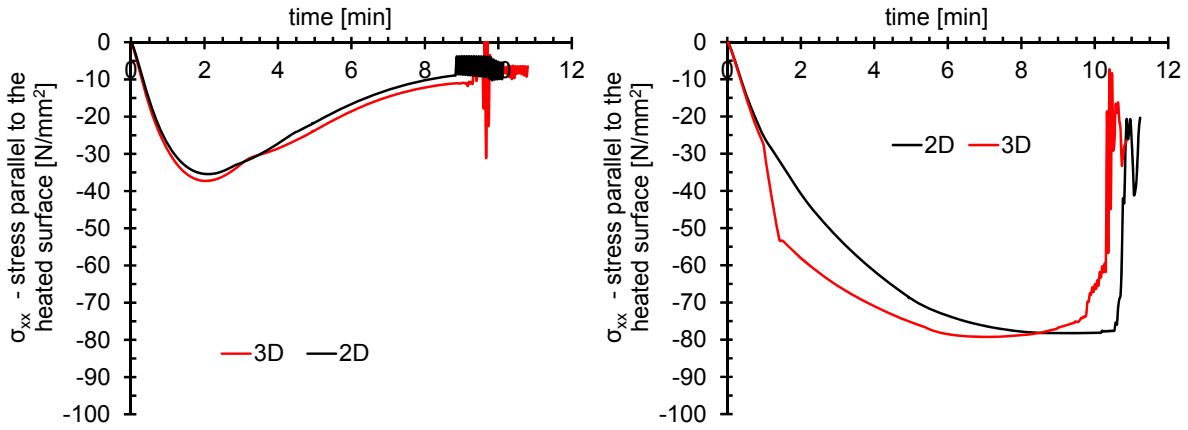

Figure 8.26. Comparison of thermally induced stresses σ_{xx} (parallel to the heated surface) for the 2D and 3D model: macro-scale (left) and meso-scale (right)

8.4.2 Heating rates and fire scenarios

One of the most important factors that influence explosive spalling is the severity of heating or fire. The gradient of the air temperature directly influences both parameters that are presumed to govern explosive spalling, namely thermally induced stresses and pore pressure within the specimen. Higher thermal gradients result in higher thermal stresses as well as in higher pore pressures.

In the present study two heating scenarios are investigated: ISO 834 fire (ETK or cellulosic curve) and ZTV-ING fire. The former defines a standard fire scenario and is widely accepted in codes worldwide (AS-1530.4 1979; DIN EN 1-2 2004; AS-1530.4 1979) to test the fire resistance of materials subjected to a category "A" fire (with the fire hazard rating based on the burning rate of general combustible building materials and building contents). The latter is a type of the standardized tunnel fire curve with extremely high temperature gradient of 250 °C/min in the first 5 minutes and subsequent constant temperature of 1200 °C in the following 25 minutes. This curve was developed in Germany as a result of experimental investigation (“Eureka” project) and is aimed at simulation of car fire in tunnels. Similar tunnel fire curves can be found in different codes and guidelines, all of them having very high initial temperature rise as well as the high maximum temperature.

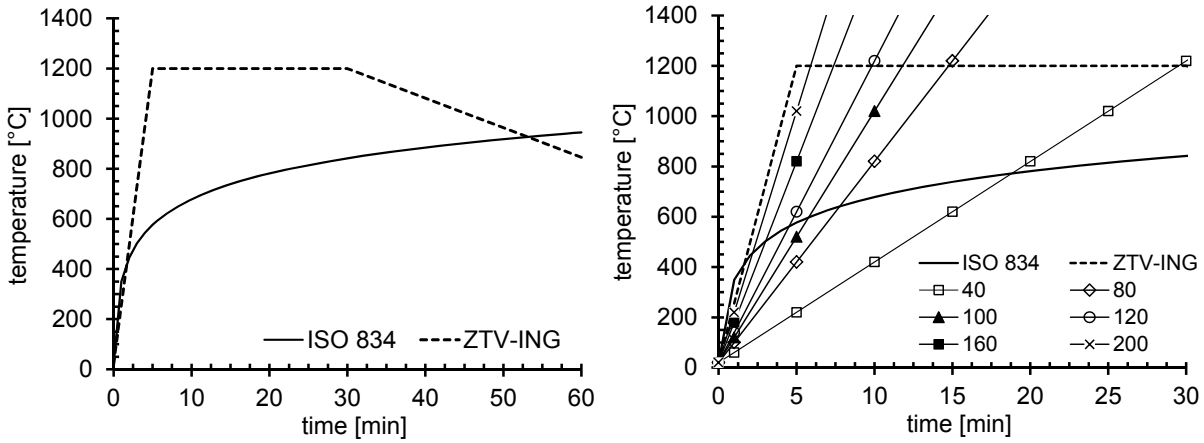

Figure 8.27. Overview of the investigated heating scenarios

The temperature development of the ISO 834 fire curve is described by the following expression:

$$T_{Air}(t) - T_{Air}(t_0) = 345 \log(8t - 1) \qquad (8.1)$$

where T_{Air} [°C] = air temperature and t [min] = time

The two fire curves are shown in Figure 8.27. In addition to these two standard fire curves, a number of different heating rates are also investigated to provide a better understanding of the influence of different heating rates on explosive spalling. The

heating rates employed in this study are: 40 °C/min, 60 °C/min, 80 °C/min, 100 °C/min, 120 °C/min, 160 °C/min and 200 °C/min. The same are plotted in Figure 8.27 (right) along with the two fire curves for better comparison.

The most part of the parametric study is performed under assumption of ISO 834 fire curve due to its wide application. Comparison of the two modelling approaches is, therefore, performed for ISO 834 fire only. Additionally, the performance of the meso-scale model is investigated for the ZTV-ING fire scenario, as well as for above listed heating rates.

8.4.3 ISO 834 fire

8.4.3.1 Geometric nonlinearity

When concrete is heated, very high compressive stresses can be generated in the region close to the concrete surface as a consequence of thermal gradients between the surface and the inner parts of concrete unaffected by the air temperature. These stresses together with pore pressure can result in a significant influence of geometric instability (buckling) on the behaviour of concrete under fire. In the numerical model, geometric nonlinearity is accounted for by using Green-Lagrange finite strain tensor and co-rotational Cauchy stress tensor for concrete.

In the present parametric study, geometric nonlinearity is accounted for in all the investigated cases. However, selected cases are analysed under assumption of geometric linearity in order to evaluate the effect of geometric instability on explosive spalling. Both macro- and meso- model are analysed for the heating scenario corresponding to ISO 834 fire curve with relative humidity of 70 % and permeability of $6x10^{-15}$ m/s.

The macro-scale model exhibits a moderate influence of geometric nonlinearity on explosive spalling. As can be seen from Figure 8.28, introduction of geometric nonlinearity results in somewhat earlier explosive spalling. The maximum values of all relevant parameters (pore pressure, volumetric stress, temperature, thermally induced stress) shown in Figure 8.28 remain almost the same as in case of geometric linearity, only the time of spalling shifts by approximately one minute, i.e. geometric instability due to high stresses results in an earlier failure of the concrete cover. It is also found that the inclusion of geometric nonlinearity does not change the failure mode of explosive spalling or the location where the spalling initiates.

Meso-scale model also exhibits similar sensitivity to geometric nonlinearity, as visible from Figure 8.29 and Figure 8.30. The maximum values of all relevant parameters again remain almost the same for the two investigated cases, with a delay of explosive spalling by approximately half a minute in the case of geometric linearity. Geometric nonlinearity introduces only a very moderate change of the behaviour of con-

crete with respect to explosive spalling. It contributes to an earlier failure of the concrete cover, whereby very similar behaviour of the macro- and meso-scale model is observed.

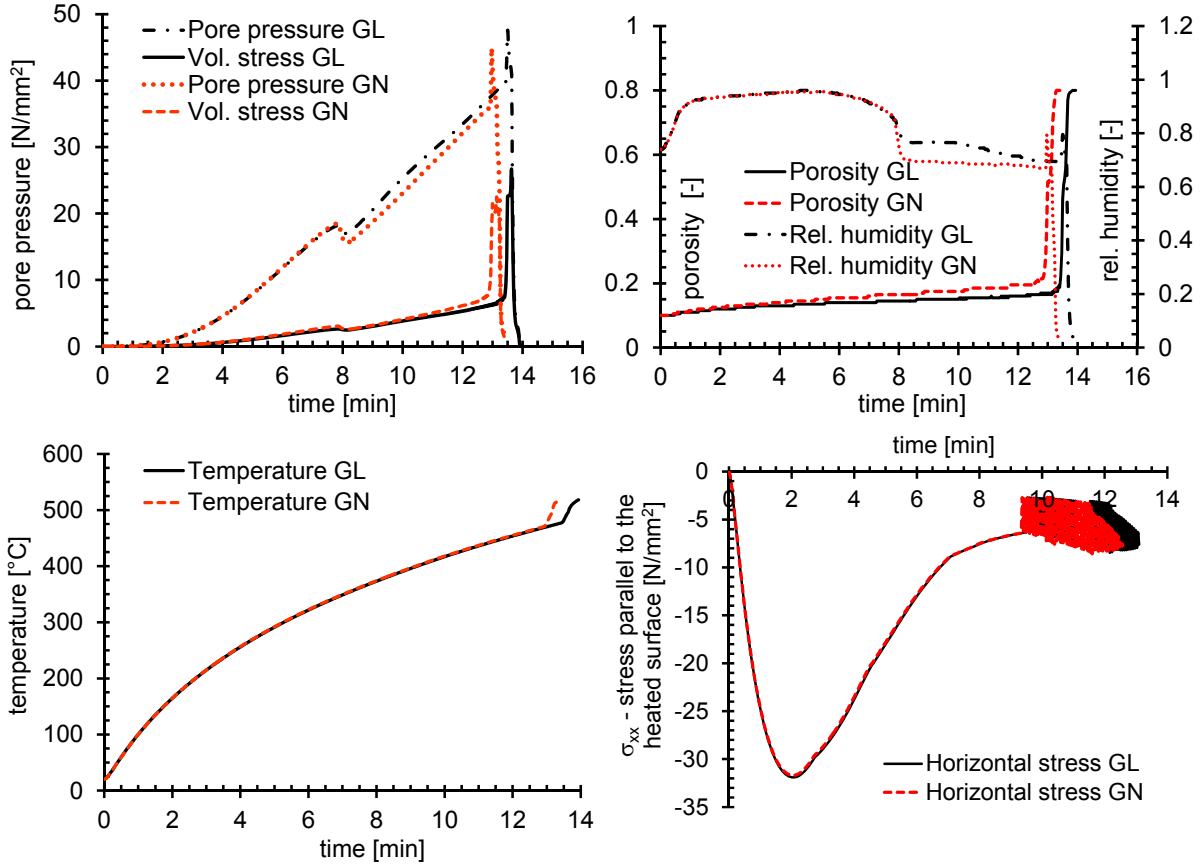

Figure 8.28. The development of relevant parameters in the element where cracking initiated – macro-scale model

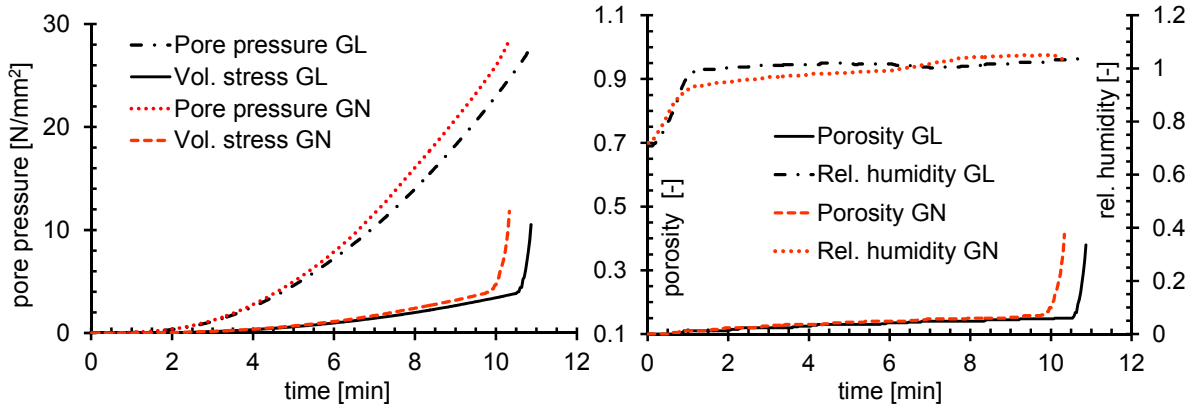

Figure 8.29. The development of relevant parameters in the element where cracking initiates – meso-scale model

Furthermore, the comparative analyses of the two models show that geometric instability alone cannot be considered to be the driving force behind explosive spalling.

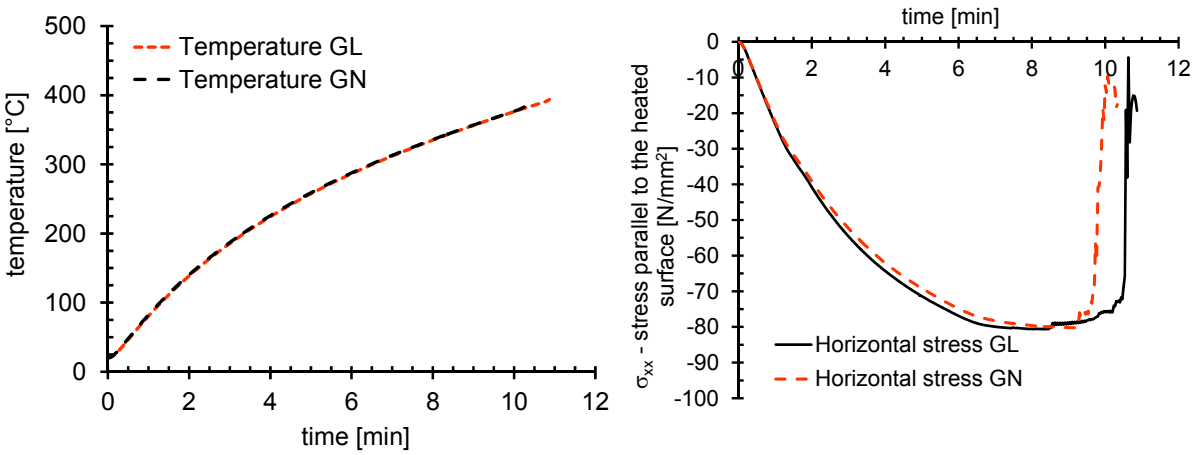

Figure 8.30. The development of relevant parameters in the element where cracking initiates – meso-scale model

8.4.3.2 Relative humidity

The water content in concrete (expressed also in terms of relative humidity) is one of the most important factors that control the sensitivity of concrete to explosive spalling. Higher amount of evaporable water facilitates the formation of the saturated zone inside the concrete specimen at elevated temperatures. Therefore, explosive spalling is likely to occur earlier in case of higher relative humidity. Numerous experimental studies confirmed the crucial role of relative humidity of concrete on explosive spalling. The importance of relative humidity is acknowledged by most of current codes and guidelines. Generally the maximum allowed water content in concrete is prescribed in order to avoid explosive spalling. DIN EN 1-2 (2004) recommends a maximum water content of 3 % (mass water content) as one of the measures to avoid explosive spalling of concrete.

In the present study the following values of relative humidity are investigated: 20 %, 40 %, 60 %, 70 %, 85 %, 92 % and 100 % and behaviour of both macro- and meso-scale model is analysed. Note that in the model relative humidity is expressed in terms of relative pore pressure, which is obtained by relative humidity from sorption curves. The analysis is performed for the ISO 834, for a permeability of $6x10^{-15}$ m/s for both models.

Figure 8.31 shows the time of spalling and failure strain for the macro-scale model. Failure strain rate is evaluated as the strain rate in time at the location where spalling initiates. Explosive spalling occurs only for relative humidity above 70 %. With increasing relative humidity the spalling takes place earlier.

The failure strain rate differs only by 20 % for the three investigated humidity values; the intensity of failure is only slightly dependent on relative humidity. The intensity of spalling is dependent on the magnitude and increase rate of the pore pressure and volumetric stress. As can be observed in Figure 8.32, the maximum difference in

pore pressure and volumetric stress for the investigated humidity values is approximately 20 %. Thermally induced stresses (parallel to heated surface) decrease to less than 10 % of compressive strength at the time of spalling. A typical development of the stresses parallel to heated surface is provided in Figure 8.32 (right). The stresses initially increase, but relax with rising temperature. The contribution of thermally induced stresses to spalling is therefore only minor. The parameter governing the failure mode at macro-scale is pore pressure (volumetric stress).

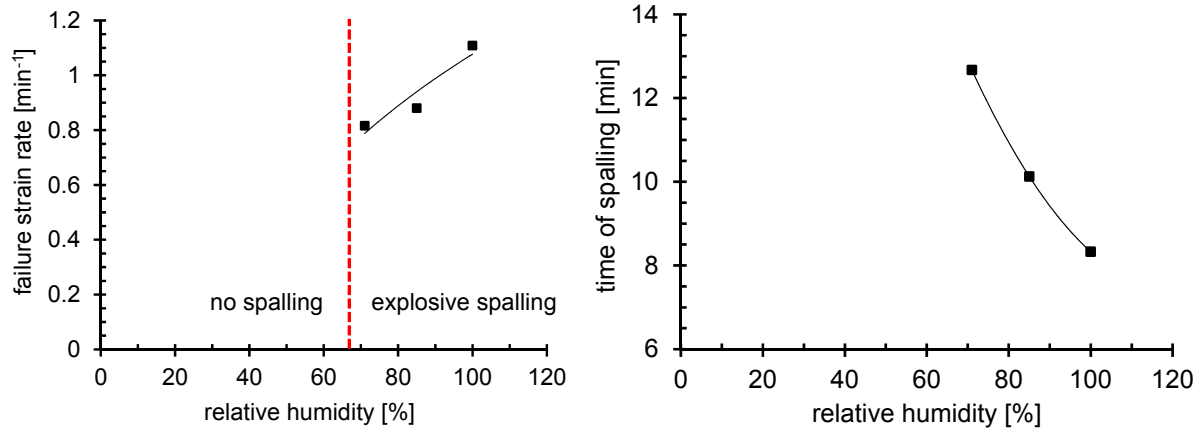

Figure 8.31. Failure strain rate (left) and time of spalling (right) – macro-scale model

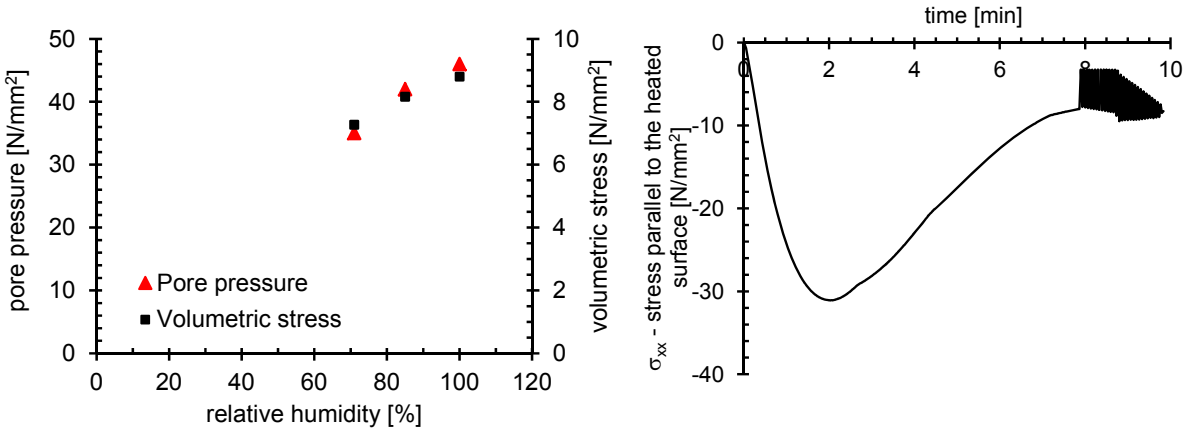

Figure 8.32. Pore pressures and volumetric stresses (left); a typical development of stresses parallel to the heated surface at the location of cracking– macro scale model

Figure 8.33 left depicts the failure strain rate for meso-scale model. For lower relative humidity (below ca. 50 %), the failure strain rate becomes very small and it is comparable with that of dry concrete. It is previously shown that dry concrete does not exhibit spalling, only thermally induced cracking occurs (see Section 8.3.1.1). With increasing relative humidity, the failure strain rate increases, i.e. the intensity of explosive spalling increases (higher energy release). Furthermore, it also initiates earlier since the higher humidity results in faster build-up of pore pressure, see Figure 8.33 (right).

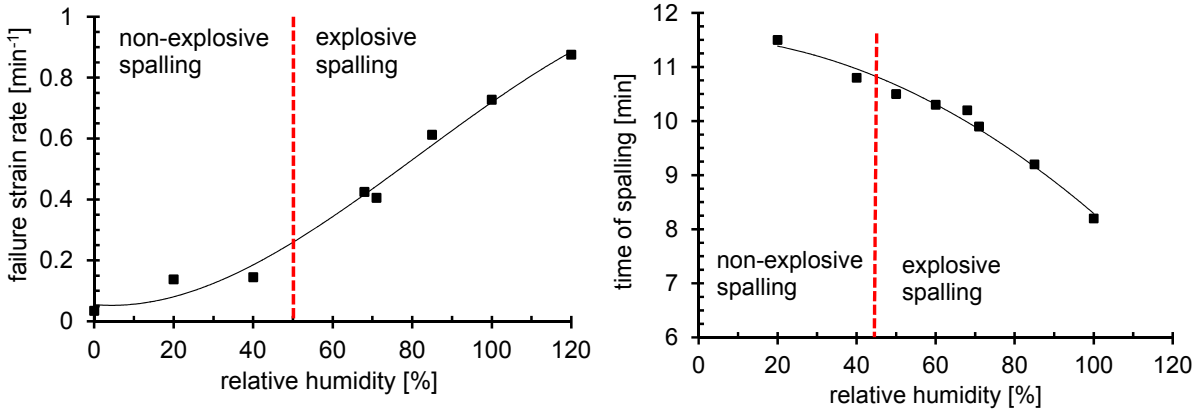

Figure 8.33. Failure strain rate (left) and time of spalling (right) – meso-scale model

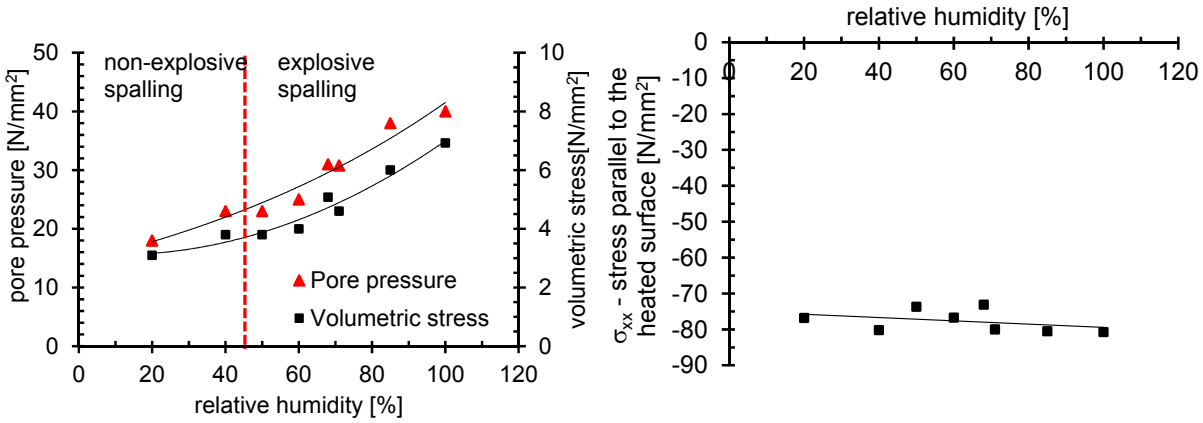

Figure 8.34. Pore pressures and volumetric stresses (left), compressive stress (right) – meso-scale model

Pore pressure and volumetric stress at failure (Figure 8.34 left) increase for higher humidity. These results correspond well to the available experimental data. Jui et al. (2008) observed that the pore pressure at spalling increases with higher relative humidity. It is also worth mentioning that the absolute values of pore pressure measured by the mentioned authors were 4.5 and 6 N/mm^2, which is comparable to the numerically obtained values for volumetric stress.

Compressive stress (parallel to the heated surface) remains almost constant and equal to approx. 80 % of the compressive strength for all the values of relative humidity. The results demonstrate the importance of compressive stress for the failure mode. High compressive stresses will inevitably lead to cracking, however, if pore pressures are formed at the same location, the combination of the two results in explosive spalling, intensity of which is governed by the level and increase rate of pore pressures.

For the same permeability of concrete, the two models exhibit quite different behaviour. Both models predict a significant influence of relative humidity on spalling. Macro-scale predicts spalling only for relatively high humidity level (above 70 %), where-

as meso-scale model results in explosive spalling for relative humidity above 50 %. The most important difference between the two approaches is mechanism that leads to failure. At macro-scale, the failure is driven by moisture transport and the parameter governing the behaviour is the volumetric stress. Meso-scale model results in a failure due to combination of thermally induced stresses and volumetric stress (pore pressure), which triggers explosive spalling.

8.4.3.3 Permeability

Permeability is considered as the most important material property that controls sensitivity of concrete to explosive spalling. If permeability increases, the connectivity of the porous network is higher and vapour pressure in the pores cannot increase at a fast rate. Many experimental studies (Kalifa et al. 2001; Zeiml et al. 2008) confirmed the role of permeability on explosive spalling, i.e. explosive spalling is more likely to occur if concrete exhibits low permeability. In this study the permeability of concrete specimens is varied from 1 x 10^{-16} to 2 x 10^{-13} m/s at a constant relative humidity of 70 %. It should be noted here that the permeability input in the THM model corresponds to the permeability of a specimen at 100 % relative humidity and 25°C.

Figure 8.35 gives an overview of the results for the macro-scale approach. For permeability higher than 1 x 10^{-14} m/s no explosive spalling is observed, whereas below this value explosive spalling occurs. At lower permeability values spalling occurs earlier due to a faster build-up of pore pressure. The failure strain rate decreases by 20 % as permeability increases by two orders of magnitude.

Similarly as shown in the previous section, there is only a slight change of pore pressure and volumetric stress at failure (approx. 20 %) with increasing permeability (see Figure 8.36), which again implies that the failure is mainly governed by the pore pressures. Low thermally induced stresses at failure (lower than 10 % f_c) for all investigated cases confirm this result.

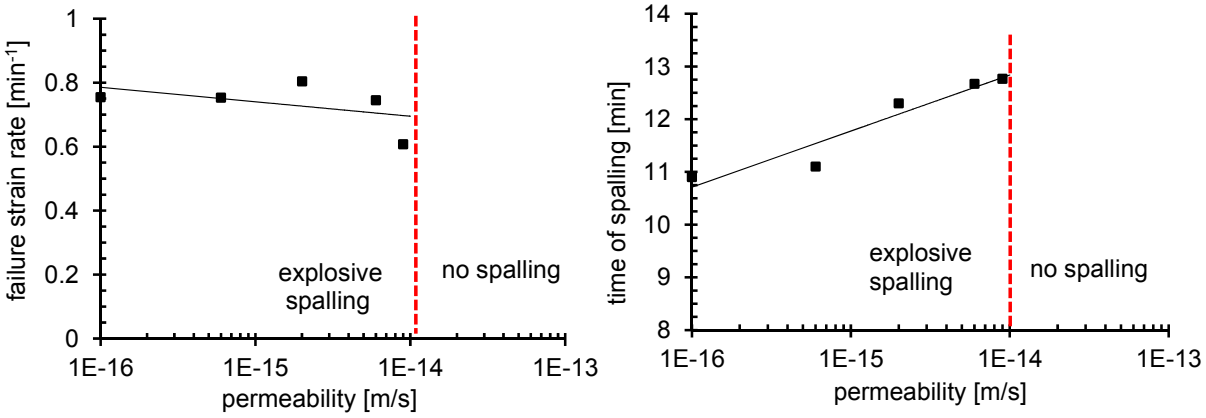

Figure 8.35. Failure strain rate (left) and time of spalling (right) – macro-scale model

The influence of permeability on failure strain rate and time of spalling at meso-scale is shown in Figure 8.37. For very low permeability values, spalling takes place at very high strain rate indicating its explosive nature. The failure takes place after only 10 minutes of fire. However, if permeability increases, spalling takes place later and at a lower strain rate. For permeability higher than 8 x 10^{-14} m/s the failure is slow and it can be considered to be non-explosive thermally induced cracking. Volumetric stress at failure (Figure 8.38) again exhibits the same trend as the strain rate. Explosive spalling takes place at relatively high stresses, whereas failure mode changes to thermally induced cracking if volumetric stress is very low.

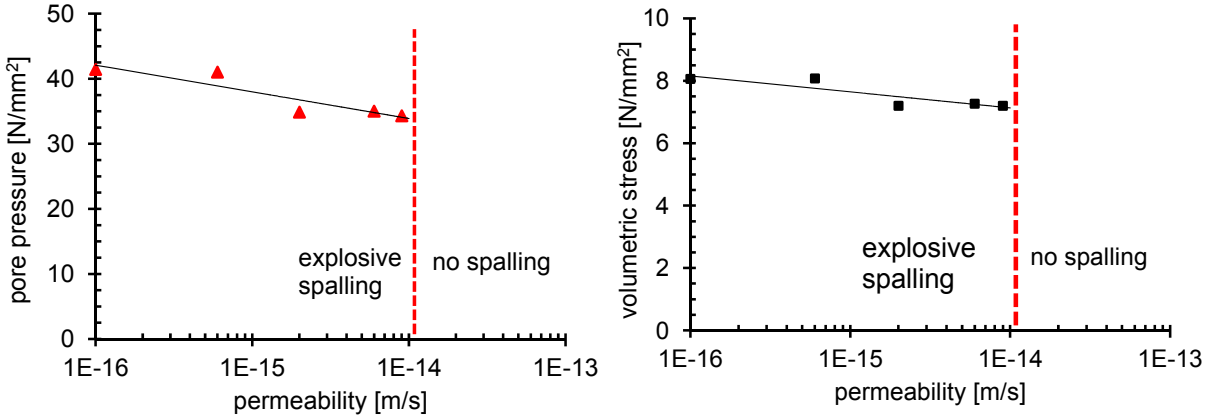

Figure 8.36. Pore pressure (left) and volumetric stress (right) at the onset of spalling– macro scale model

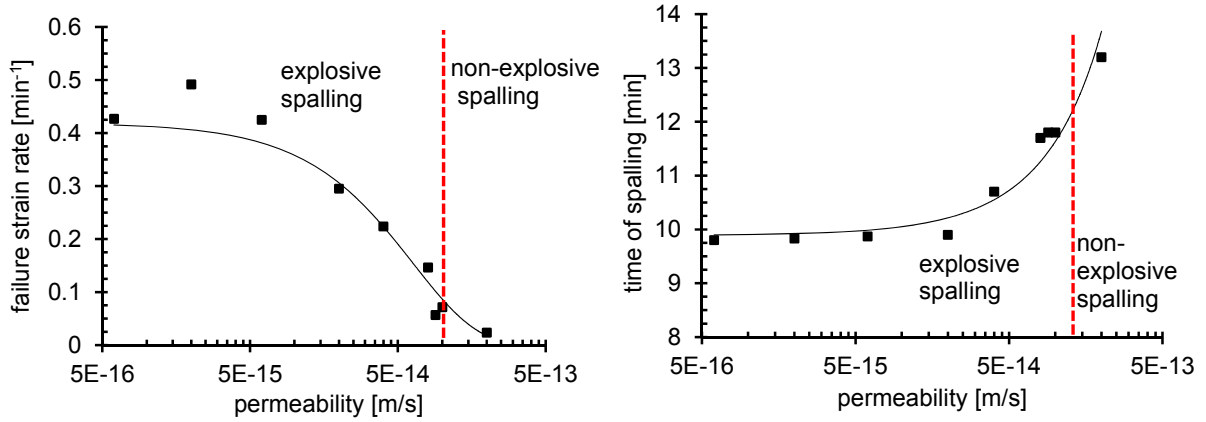

Figure 8.37. Failure strain rate (left) and time of spalling (right) – meso-scale model

Thermally induced stresses at failure are constant and independent of the failure mode. Very high level of thermally induced stresses is required for the specimen to spall, but it is the magnitude of pore pressure (volumetric stress) that governs the intensity of spalling.

Comparing the obtained results with the experimental data it is observed that both macro- and meso-model can predict the effect of permeability on explosive spalling. In the experiment is found that an increase in permeability of approximately two or-

ders of magnitude is sufficient to prevent explosive spalling. Here is assumed that the permeability of concrete with PP fibres is two orders of magnitude higher already at the room temperature. This assumption is reasonable considering the initial slow development of pore pressure observed in all investigated cases. In the experiment concrete without PP fibres (with permeability 1.5 x 10^{-15} m/s) exhibited explosive spalling, whereas concrete with PP fibres (with approx. two orders of magnitude higher permeability) experienced no spalling.

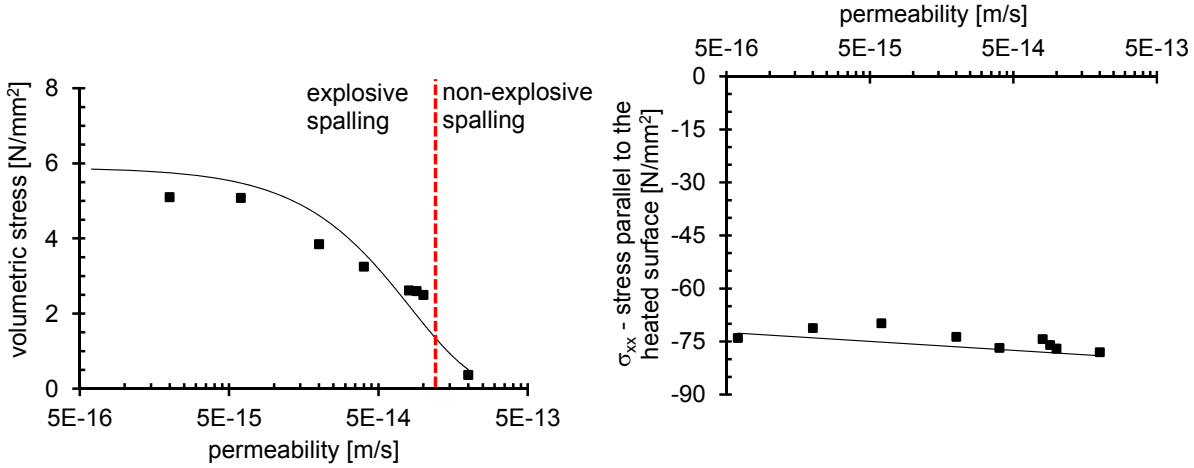

Figure 8.38. Pore pressures (left) and volumetric stresses (right) at the onset of spalling– meso scale model

8.4.3.4 Compressive load

A number of studies demonstrated that the concrete specimens loaded in compression before heating are more likely to experience explosive spalling (Meyer-Ottens 1972; Connolly 1995; Ali 2002; Zheng et al. 2010). If concrete is loaded in compression before heating, the compressive stresses are superimposed to the thermally induced stresses in concrete. It is, however, very demanding to experimentally investigate this scenario, especially if the compressive stresses are very high. In the present work, following load levels are investigated on macro- and meso-scale: 0 % f_c, 10 % f_c, 20 % f_c, 30 % f_c, 40 % f_c and 50 % f_c. Higher load levels are not considered for their low likelihood in standard concrete structures. After applying the load, the specimen is restrained in the horizontal direction, similar to the case without compressive load. Analyses are performed for permeability of 6 x 10^{-15} m/s and concrete relative humidity of 70 %.

Failure strain rate and time of spalling for the macro-scale model are shown in Figure 8.39. There is a slight increase in time of spalling with increasing compressive load, which indicates that the presence of additional compressive load has a beneficial effect on behaviour of concrete with respect to explosive spalling. Failure strain rate remains almost constant for all load levels. Similarly, pore pressure and volumetric stress (see Figure 8.40) exhibit almost no dependency on the level of compressive

load. Considering the fact that the failure at macro-scale is mainly governed by the moisture transport, it is understandable that the compressive loading does not significantly influence the behaviour of concrete with respect to explosive spalling.

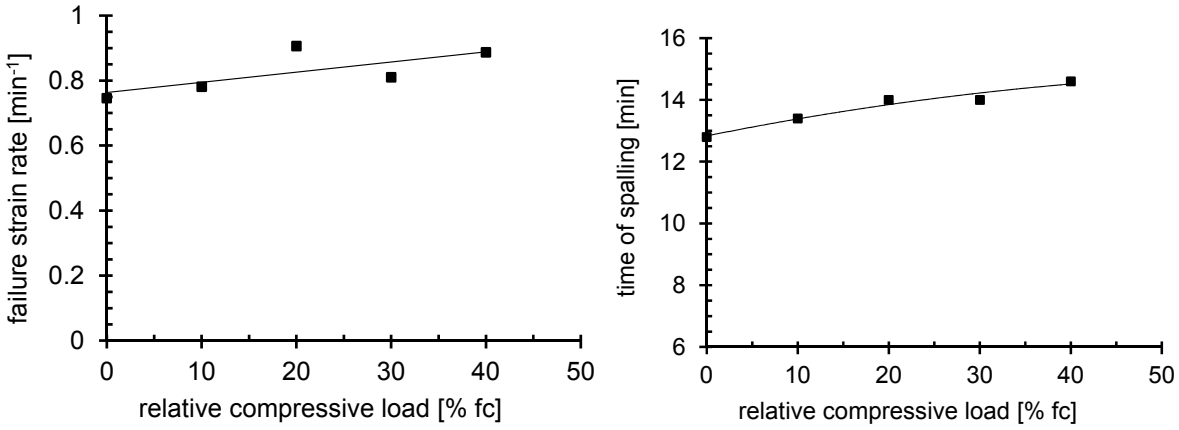

Figure 8.39. Failure strain rate at the onset of spalling (left) and time of spalling (right) – macro scale model

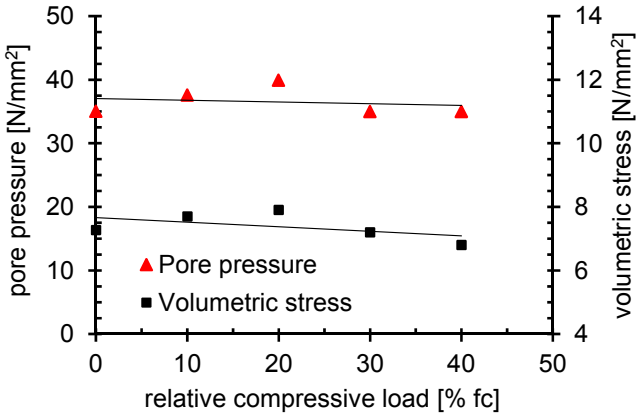

Figure 8.40. Pore pressures and volumetric stresses at the onset of spalling– macro scale model

Meso-scale model, on the other hand, predicts a very pronounced increase in risk of spalling with increasing compressive load, as can be observed in Figure 8.41. Time of spalling reduces significantly for higher load levels. It is shown earlier that the failure at meso-scale is governed by the combination of thermally induced stresses and volumetric stress (pore pressure). Compressive load applied prior to heating contributes to a more rapid increase in compressive stresses parallel to the heated surface.

Failure strain rate decreases with increasing load level, and for load levels above approximately 35 % of compressive strength the failure is more of the non-explosive sort, i.e. thermal cracking.

Figure 8.42 (left) shows the pore pressure and volumetric stress at the onset of spalling. For load levels above 35 % of compressive strength both the parameters de-

crease indicating the change of failure mode from explosive to non-explosive spalling. Stress parallel to the heated surface shown in Figure 8.42 (right) exhibits an increase for higher load levels. Thermally induced stresses are superimposed to the existing compressive stress, whereas the moisture transport remains approximately constant for all load levels. At higher loading levels failure is mainly governed by high stresses parallel to heated surface, whereas pore pressure and volumetric stress are quite low in magnitude.

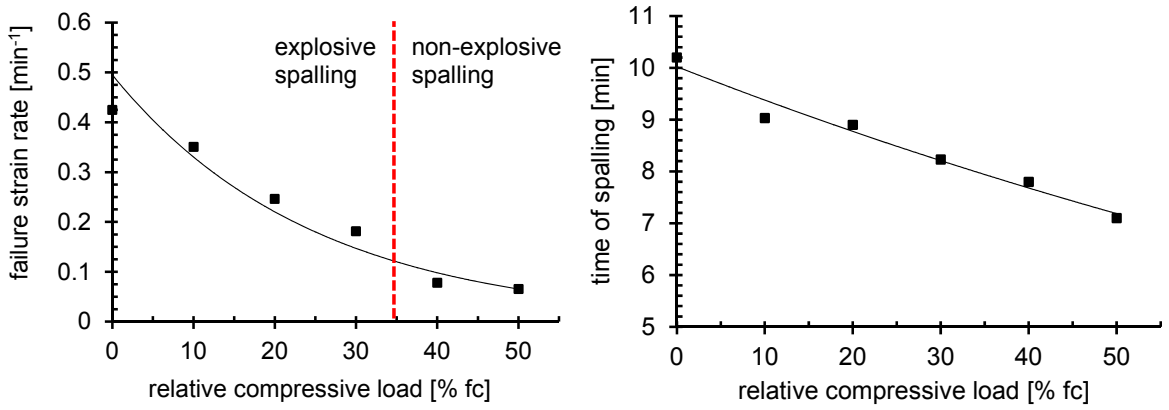

Figure 8.41. Pore pressures (left) and volumetric stresses (right) at the onset of spalling– meso scale model

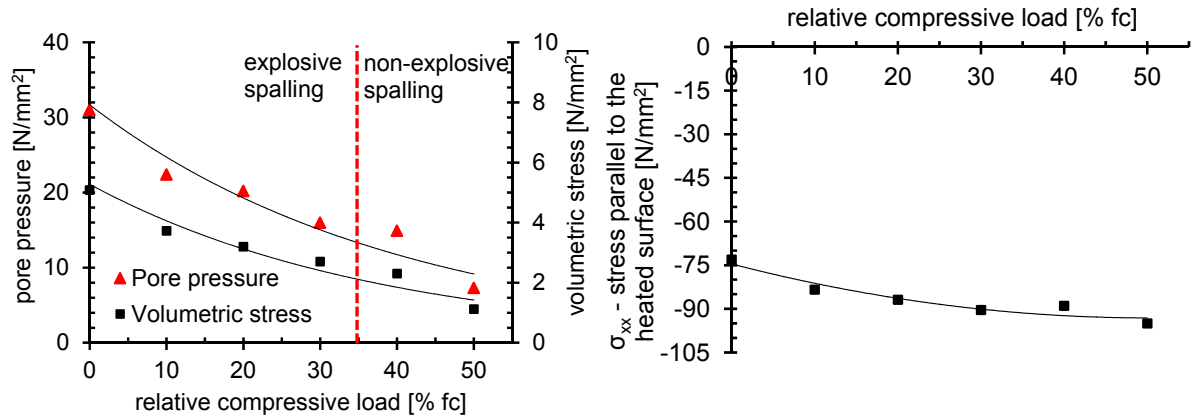

Figure 8.42. Pore pressures and volumetric stresses (left) and stress parallel to the heated surface (right) at the onset of spalling– meso scale model

The differences between the macro- and meso-scale modelling approaches become very evident when analysing the influence of compressive loading. Macro-scale model cannot predict any significant influence of compressive stress on explosive spalling. It is experimentally observed that the compressive loading has an adverse effect on explosive spalling, but this phenomenon cannot be captured by employing the macro-scale approach. Meso-scale model, however, can account for the effect of thermally induced stress. It can, therefore, also reproduce the experimentally observed behaviour.

It can be concluded that macro-scale model with explicit LITS definition only partially predicts the explosive spalling of concrete, its main drawbacks being the inability to realistically capture localization and the effect of compressive load. Homogeneity of concrete at macro-scale and presence of predefined LITS are considered to be the main reasons for the limited performance of this approach.

8.4.3.5 The role of load induced thermal strain

Multiple applications at macro-scale show that the implementation of LITS is important for the realistic response of structure to fire. The whole parametric study is performed following this approach. However, additional analyses are performed on macro-scale model, with aim of evaluating the influence of predefined LITS on explosive spalling of concrete. In this case, LITS are not predefined at macro-scale, same as is done for the meso-scale model. The results are then compared with those obtained with standard macro-scale model (with predefined LITS). The analyses are performed for ISO 834 fire scenario under variation of relative humidity and compressive load.

Figure 8.43 and Figure 8.44 show the development of relevant parameters in the element where explosive spalling initiates in case of rel. humidity of 70 % and without compressive loading. For comparison, the same parameters are plotted for the corresponding analysis with LITS. It can be observed that the stresses parallel to surface differ substantially for the two cases. When LITS is not taken into account, the maximum stress reached in a single element is more than 2 times higher than in the case where the relaxation through LITS is considered.

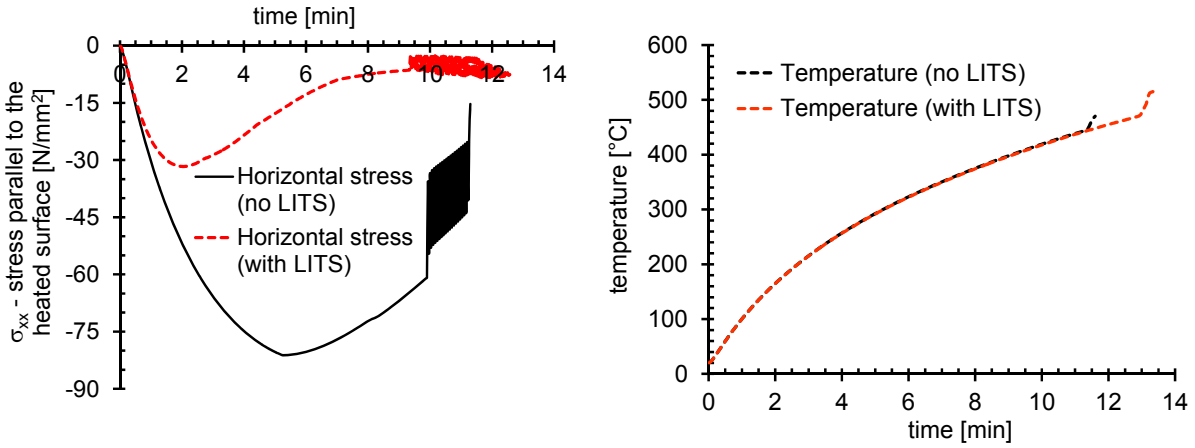

Figure 8.43. The development of relevant parameters in the element where cracking initiates – comparison of macro-scale model without and with LITS

After the peak at approximately 5 minutes of fire the stresses start to decrease. At the time where explosive spalling initiates, compressive stresses parallel to the surface are approximately 60 N/mm^2. The mechanism of the explosive spalling in this case is a combined action of thermal stresses and pore pressure (volumetric stress).

Similarly to the meso-scale analysis, the failure occurs when the volumetric stress triggers the potential energy accumulated due to relatively high thermally induced stresses. As can be expected, relative humidity and temperature show almost the same trend for both the analyses. In principle, pore pressure and volumetric stress exhibit the same trend in both cases; however, if LITS is not accounted for, a lower level of volumetric stress is sufficient for the abrupt failure of the model since the failure is not only driven by pore pressure, but by the combined action of compressive and volumetric stress.

Figure 8.45 and Figure 8.46 provides the evaluation of the results for different values of relative humidity ranging from 40 % to 100 %. Similar to all previous presented cases, failure strain rate increases with increasing humidity. When humidity increases, there is a higher amount of water in concrete. This leads to faster increase of pore pressures, which then lead to a more abrupt failure of concrete. As the pore pressures (volumetric stresses) develop faster, the explosive spalling itself occurs at an earlier time step. However, now the failure occurs at a higher pore pressure and volumetric stress for increased relative humidity.

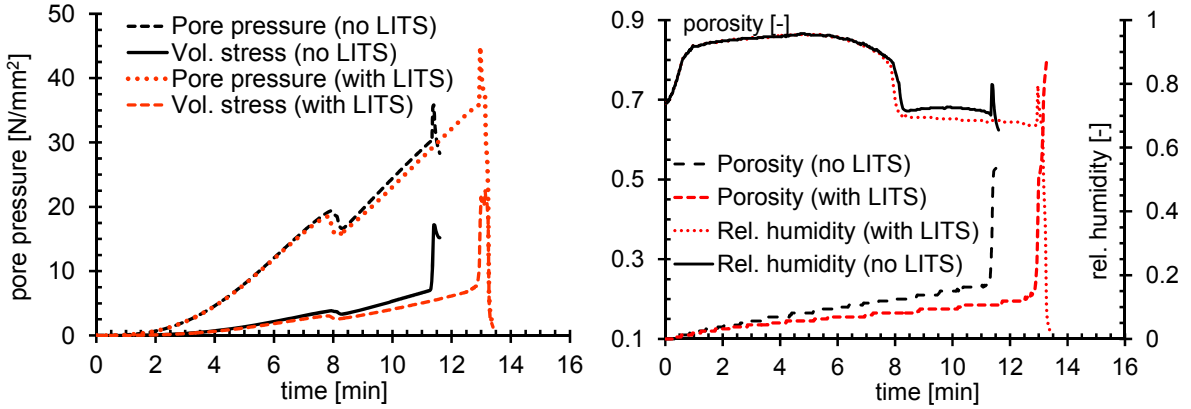

Figure 8.44. The development of relevant parameters in the element where cracking initiates – comparison of macro-scale model without and with LITS

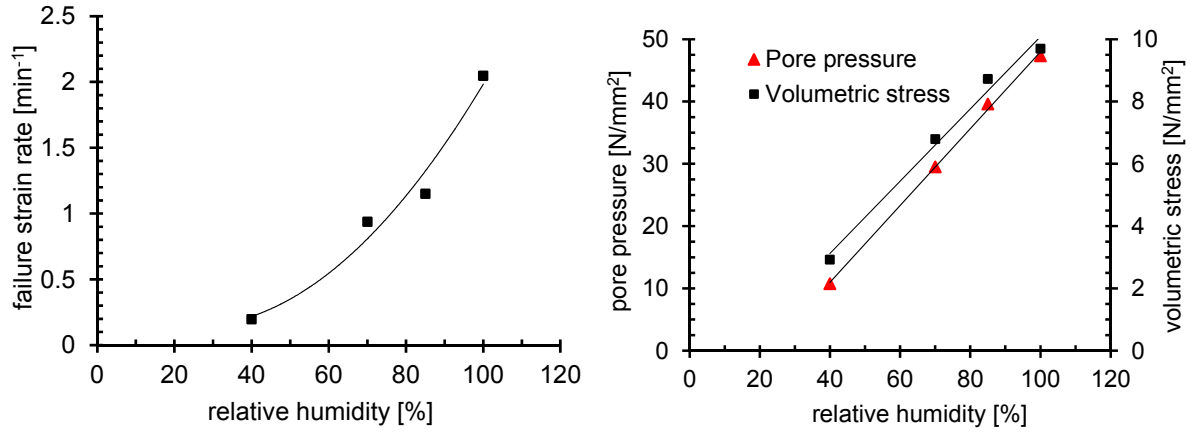

Figure 8.45. Influence of relative humidity – macro-scale model without LITS

Stresses parallel to the heated surface remain almost constant for the relative humidity of 70 % and higher. For the relative humidity of 40 % the failure occurs at a much lower compressive stress of ca. 25 N/mm^2. This implies that a relatively high level of compressive stress is required for the explosive spalling independent of the humidity. These results exhibit more resemblance to the meso-scale model than to the macro-scale model with LITS i.e. macro-scale model without LITS seems to capture the explosive behaviour of concrete somewhat better than the macro-scale model with LITS. However, it should be noted that the unrealistic failure of the whole heated surface as seen typically in macro-scale remains unchanged even if the LITS are not predefined.

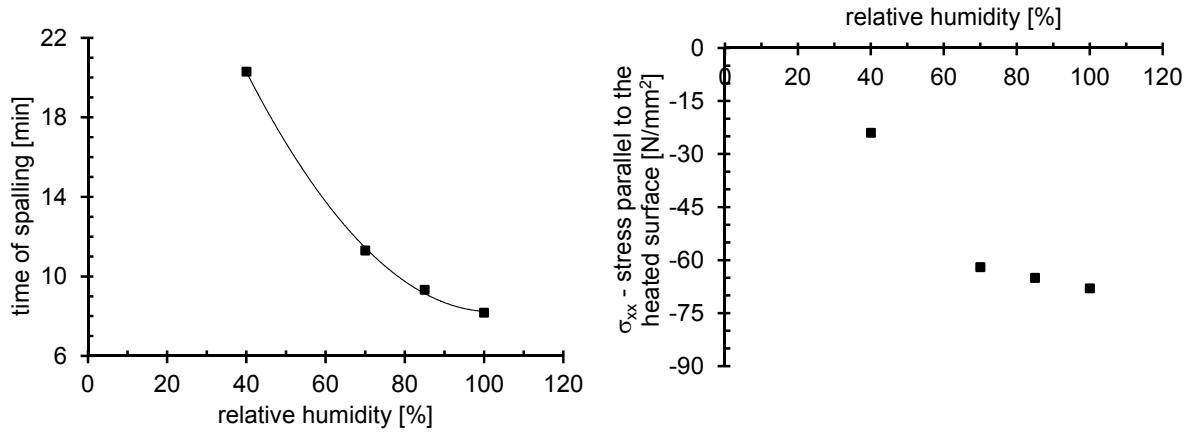

Figure 8.46. Influence of relative humidity – macro-scale model without LITS

One series of analyses is performed for different values of compressive loading (ranging from 10 % f_c to 50 % f_c) applied prior to heating. Figure 8.47 and Figure 8.48 depict the effect of compressive load on the macro-scale model without LITS. The results are very similar to those of the macro-scale model with LITS. No change in the time of spalling is observed as the level of compressive load applied prior to heating rises, i.e. the spalling occurs at the same time for all the investigated cases. The compressive stress at the moment of failure also remains constant. Accordingly, the level of the volumetric stress and pore pressure at failure remain constant for all the investigated cases. The macro-scale model without LITS predicts no effect of compressive stress on explosive spalling of concrete.

This is due to the inability of the macroscopic modelling approach to capture the incompatibility of the concrete phases and local distribution of stresses. The results presented in this section lead to a conclusion that the macroscopic approach without predefinition of LITS can give a more realistic mechanism of explosive spalling than the standard macro-scale model (with LITS), but cannot capture all of the aspects of this complex failure mode, such as failure mode and the effect of compressive stress.

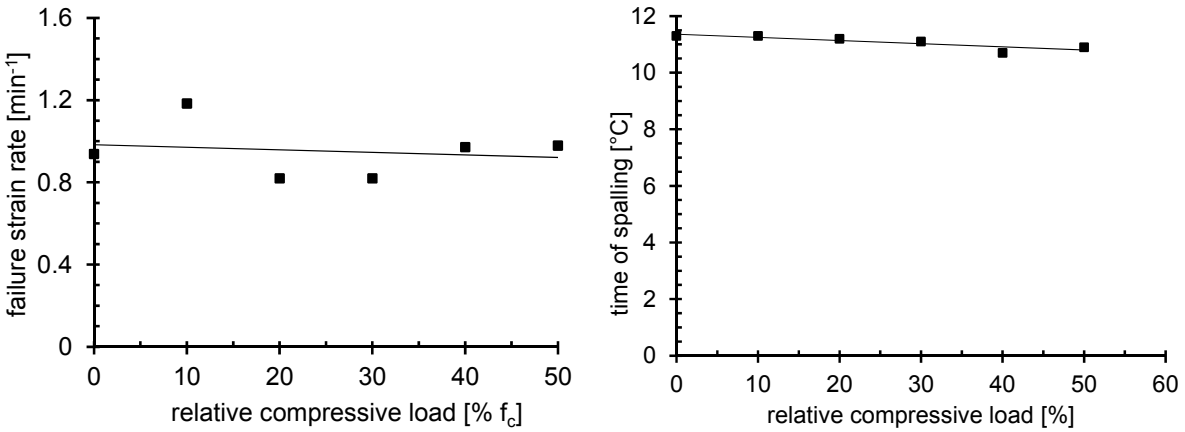

Figure 8.47. Influence of compressive load at macro-scale without predefined LITS

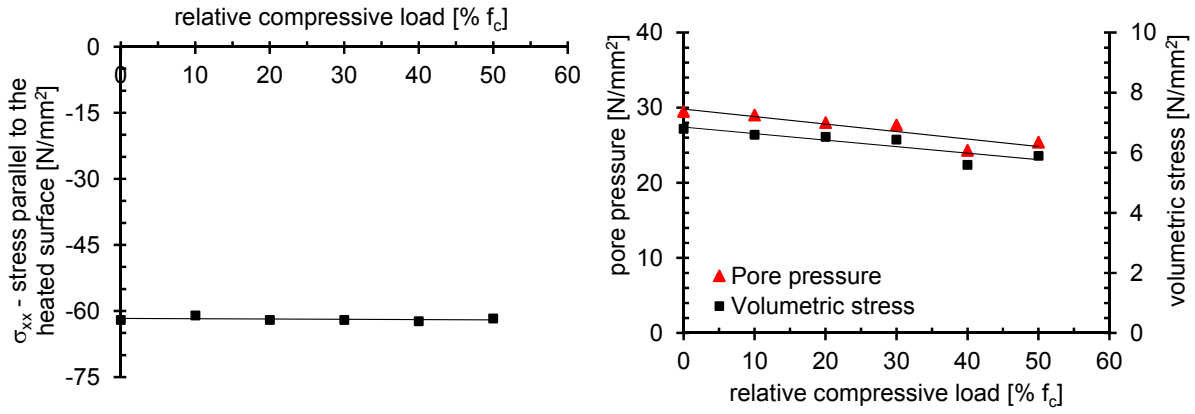

Figure 8.48. Influence of compressive load at macro-scale without predefined LITS

Even if this approach shows certain improvement as compared to the macro-scale with LITS, the exclusion of LITS from the model needs to be reasonably justified. As discussed in Section 6.7, LITS is found to originate partially from the changes that occur inside the cement place but the most part it is due to incompatibility of the three concrete phases. If concrete is assumed to be homogeneous, due attention should be given to the damage that is generated from this incompatibility within the thermo-mechanical model.

8.4.3.6 Aggregate type

Aggregate type, in particular coarse aggregate, is the main parameter that governs the thermal expansion of concrete as a composite. The employed thermo-hygro-mechanical model can account for different aggregates by means of mechanical and transport properties, as well as in terms of free thermal strains. The effect of aggregates on explosive spalling is not investigated experimentally in the framework of present work, however, the available experimental data indicate that certain types of aggregates make concrete more sensitive to explosive spalling. Thermally unstable aggregates (such as flint), as well as aggregates which exhibit high thermal dilatation

can enhance explosive spalling. This is attributed to the increased incompatibility of the concrete phases.

In this study, following aggregate types are investigated: basalt, granite, dolomite, two different quartz types and two different limestone types. The experimental data for the expansion of aggregates are taken from literature (Flynn 1999). Free thermal strains for the analysed aggregate types are presented in Figure 8.49 (left). In order to obtain free thermal strain for concrete at macro-scale, thermal dilatation of concrete is analysed using the meso-scale model, and incorporating the thermal strain for each component. In this way the total thermal strain (free thermal strain) for concrete at macro-scale is obtained. These results are presented in Figure 8.49 (right).

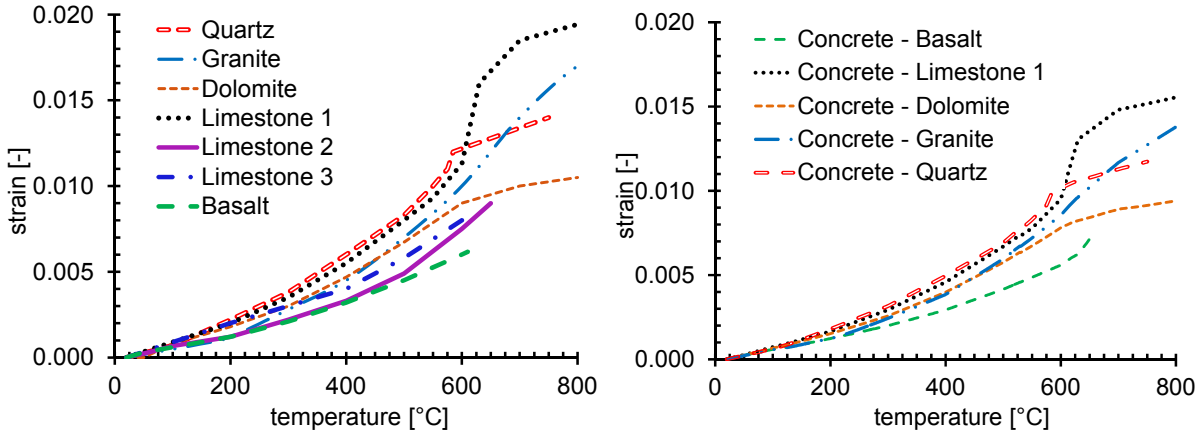

Figure 8.49. Free thermal strains of different aggregates (left) and corresponding concretes (right)

Permeability of the aggregates is assumed to be significantly lower than that of cement mortar (approximately one order of magnitude lower). Free thermal strain of the cement mortar is kept constant for all aggregate types. Furthermore, mechanical properties of all the aggregate types are assumed to be constant. Even though there are certain variations in mechanical properties of different aggregates, the variation within each material is very pronounced. Moreover, this study is mainly concentrated on investigating the difference in behaviour caused by the differences in free thermal strain. The analyses are performed for ISO 834 fire scenario and for concrete relative humidity 70 % at a permeability of 4×10^{-14} m/s at meso-scale and 6×10^{-15} m/s at macro-scale.

The time of spalling and volumetric stress for all aggregate types in case of macro-scale model are presented in Figure 8.50. Even though corresponding concrete types exhibit very different thermal dilatation, as visible in Figure 8.49 (right), the effect of the thermal dilatation exhibits almost no effect on the explosive spalling.

These results correspond well to the previous finding that the failure at macro-scale is mainly governed by pore pressure. In addition to lacking localization of failure and

inability to predict the effect of external compressive stress, macro-scale modelling approach is also inadequate to capture the effect of aggregate nature on the susceptibility of concrete to explosive spalling.

The time of spalling and failure strain rate for all aggregate types in case of meso-scale model are presented in Figure 8.51. Time to initial spalling increases for decreasing thermal dilatation of aggregates. Lower thermal dilatation of aggregates results in decreased incompatibility of the concrete phases, and consequently, slower development of thermally induced stresses. Therefore, the time of initial spalling reduces for aggregates with lower free thermal strain. However, the intensity of spalling as evaluated by strain rate at failure does not change significantly. The intensity of spalling is mainly governed by increase of heating and the pore pressures.

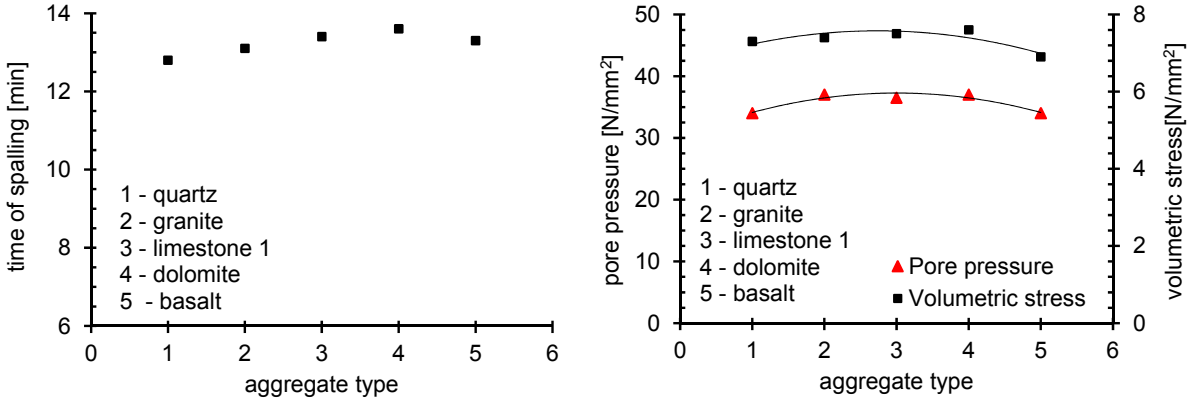

Figure 8.50. Time of spalling for concretes with different aggregates – macro-scale

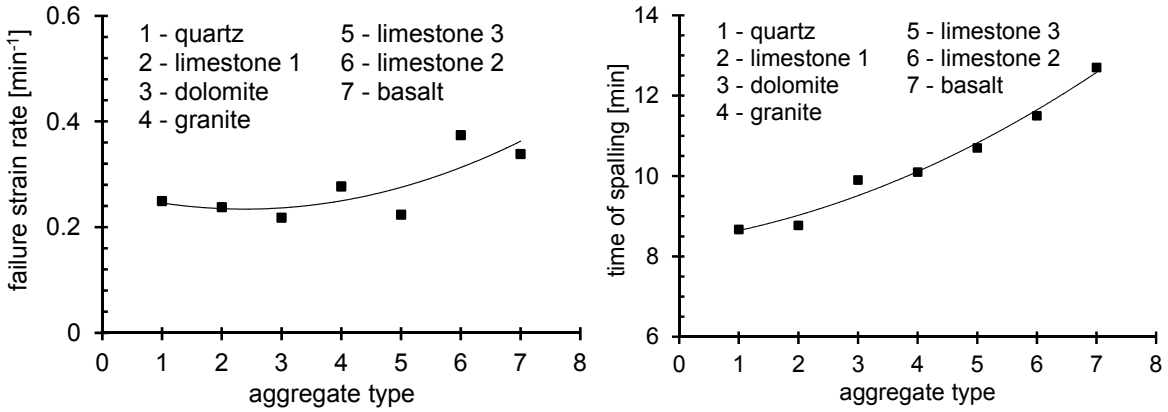

Figure 8.51. Failure strain rate and time of spalling for concretes with different aggregates – meso-scale

Since relative humidity and permeability are kept constant for all the aggregate types, pore pressure and volumetric stress at failure do not change significantly. This results in a slight change of failure strain rate, i.e. failure strain rate increases for aggregates with lower thermal dilatation. Pore pressure and volumetric stress at the onset of spalling are shown in Figure 8.52. Similar to all meso-scale models present-

ed previously, stresses parallel to the heated surface remain almost constant at about 80 % of the compressive strength.

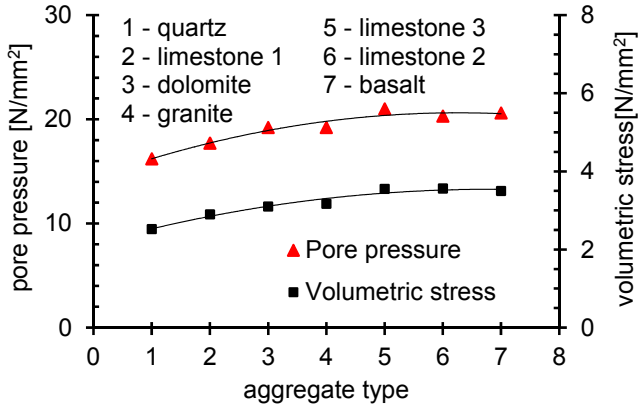

Figure 8.52. Volumetric stress and pore pressure for concretes with different aggregates – meso-scale

8.4.3.7 Aggregates distribution (meso-scale model)

The main motivation for the numerical analysis at meso-scale is the local character of explosive spalling. Keeping this in mind, it is required to assess the influence of different inhomogeneities in concrete. One of these is also the distribution of aggregate pieces within the concrete. Three different aggregate distributions are investigated. The three models (A, B and C) are shown in Figure 8.53. The analyses are performed for ISO 834 fire scenario, concrete relative humidity of 70 % and permeability of $6x10^{-15}$ m/s. Moreover, the influence of relative humidity is investigated for all three aggregates distributions. Change in the distribution of aggregates influences the local distribution of pore pressures and volumetric stresses, since dense aggregates impede the transport of water and water vapour towards the inner parts of concrete specimen.

Furthermore, thermally induced stresses also distribute differently. These changes of local parameters results in a change of location of explosive spalling, as can be observed in Figure 8.53. Not only the location of spalling changes, but there is also a change in time of initial spalling (Figure 8.54). This can also be explained by the influence of aggregates on distribution of pore pressure and thermally induced stresses. In the experiments and literature it is observed that the location of initial spalling is random even for the concrete specimens from the same batch. Numerical analysis shows that the distribution of aggregates plays an important role with respect to localization of damage. However, in real concrete specimens there are even more inhomogeneities than encompassed by this relatively simple model. For example, slight change in porosity of concrete mortar can result in a very pronounced change in permeability. However, such local changes of the cement matrix structure are not subject of this investigation. Figure 8.54 shows the effect of relative humidity on the behaviour of concrete with different distribution of aggregates. Even though the abso-

lute time to spalling differs for all three models, it can be observed that the general trend remains the same. Time of spalling increases and failure strain rate decreases with increasing relative humidity. Figure 8.55 depicts the influence of aggregates distribution on pore pressure and volumetric stress. Again, the results for the three distributions are very similar. The change of position of single aggregates influences only the distribution of pore pressures, but does not change the overall behaviour of concrete with respect to relevant parameters.

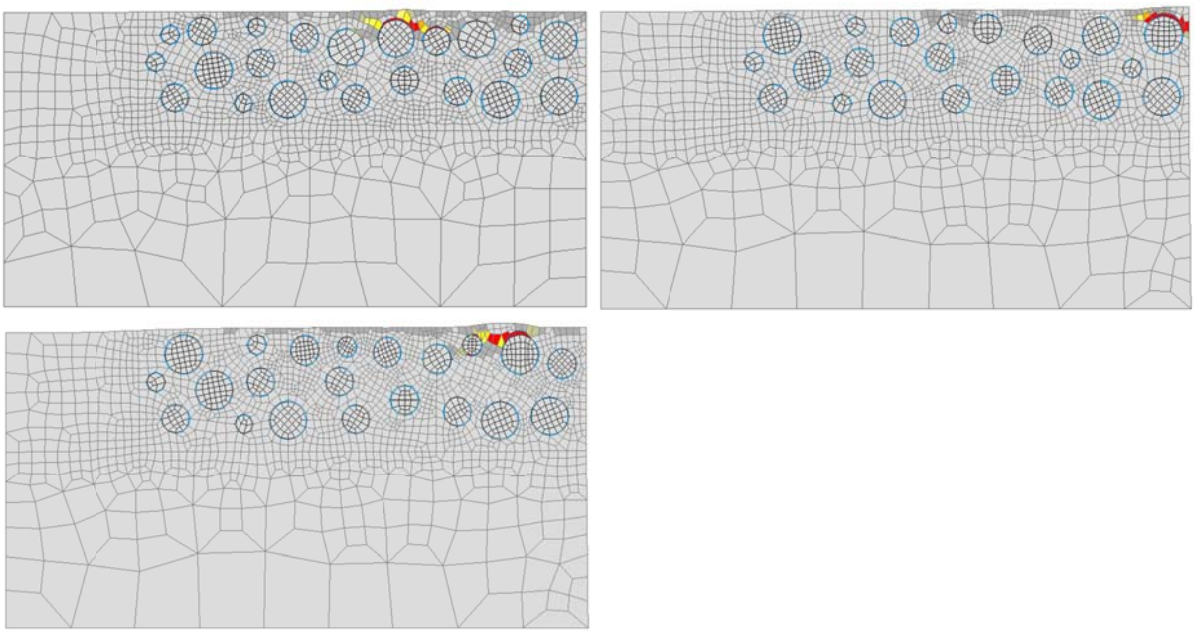

Figure 8.53. Three aggregate distributions (meso-scale model)

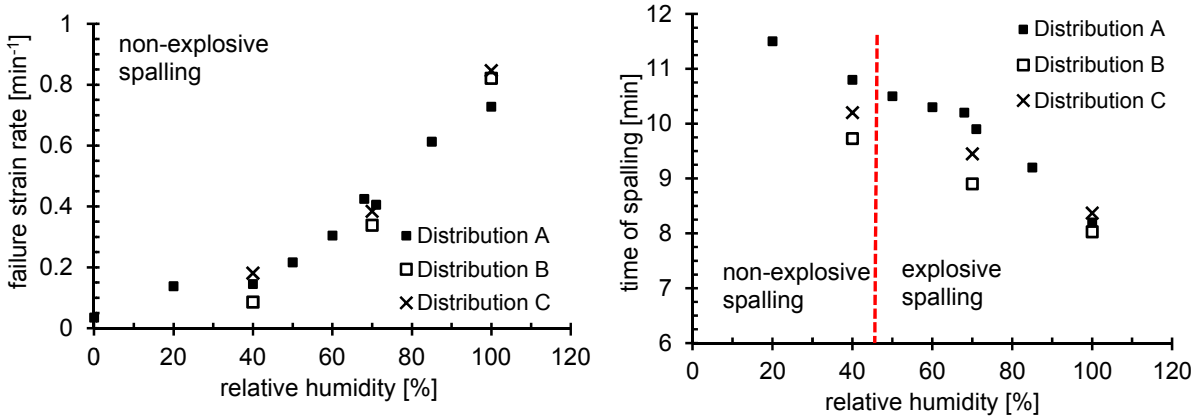

Figure 8.54. Failure strain rate and time of spalling for different aggregates distributions – meso-scale

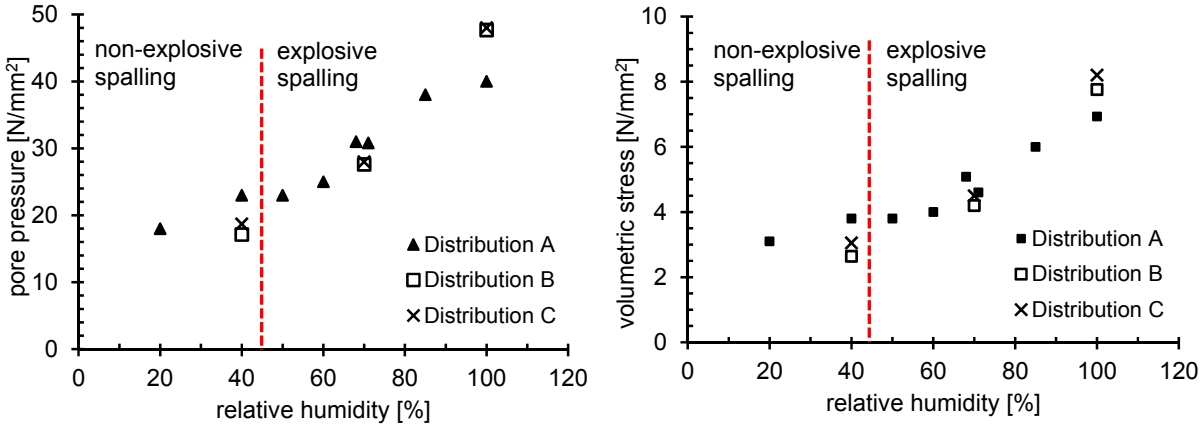

Figure 8.55. Pore pressure and volumetric stress for different aggregates distributions – meso-scale

8.4.4 ZTV-ING fire

It is previously shown that the macro-scale model can only partially capture the explosive spalling of concrete and that the meso-scale model is more suitable for analysis of localized damage caused by explosive spalling. Therefore, the analysis for the ZTV-ING fire curve is performed only at meso-scale. The analyses are carried out in order to investigate the effect of relative humidity, permeability and compressive load on explosive spalling.

8.4.4.1 Relative humidity

The analysis is performed for permeability of 6×10^{-14} m/s and following relative humidity values: 0 %, 20 %, 40 %, 70 %, 85 % and 100 %. Figure 8.56 gives an overview of the relevant parameters with respect to relative humidity.

In general, the overall trends are very similar to those observed for the ISO 834 fire, with decreasing probability of explosive spalling for lower relative humidity of concrete. However, the time of spalling does not differ much for the whole permeability range. This is due to the high thermal gradients, and consequently, high thermally induced stresses and pore pressures. Alone the thermally induced stresses lead to cracking (non-explosive spalling) after only 4 minutes of fire.
For all the investigated relative humidity values, the compressive stresses parallel to surface remain constant at around 80 % f_c. With increasing relative humidity, the moisture zone is created earlier and higher pore pressures and volumetric stresses are generated. In combination with high thermal stresses, these lead to very sudden bursting of concrete surface layers. For the analysed case, the change from explosive to non-explosive damage takes place at relative humidity of approx. 45 %.

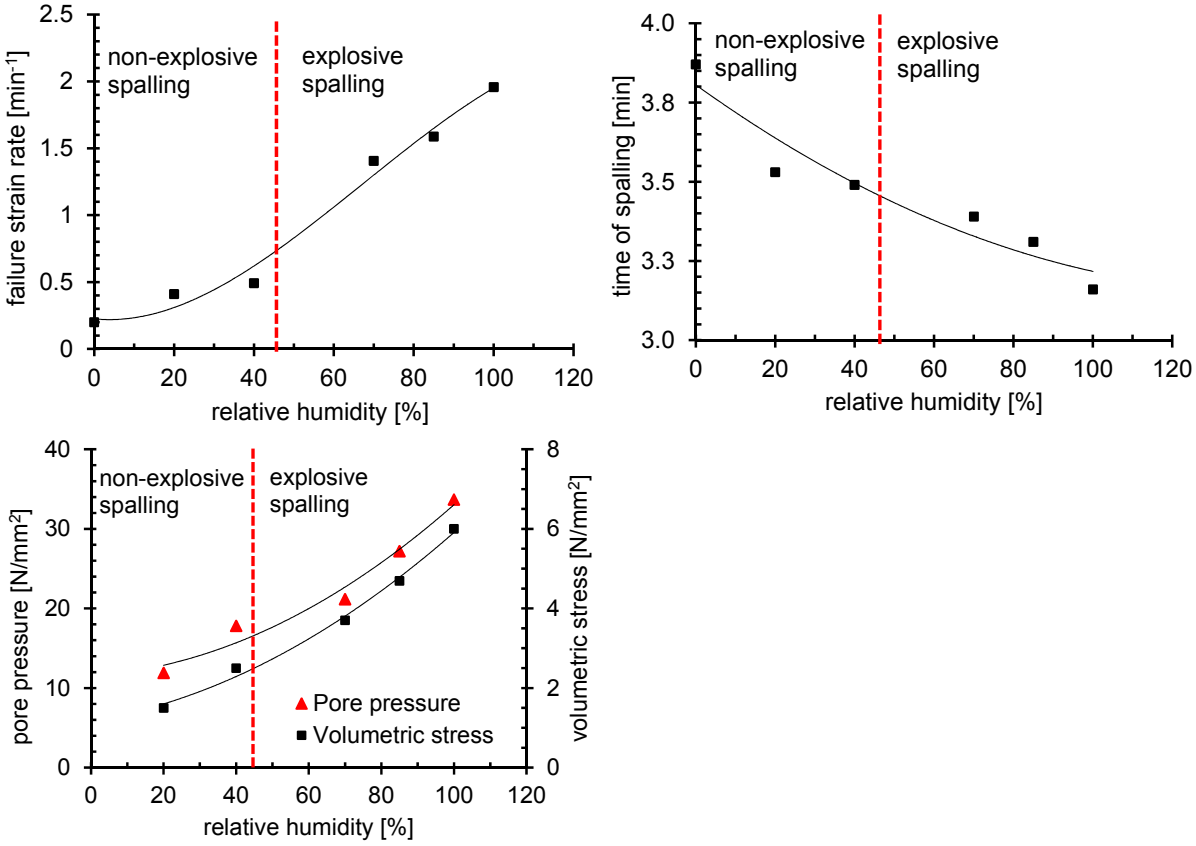

Figure 8.56. Influence of relative humidity on behaviour of HPC under ZTV-ING fire – meso-scale model

8.4.4.2 Permeability

The analysis is performed for relative humidity 70 % and following permeability values: $1x10^{-15}$ m/s, $6x10^{-15}$ m/s, $2x10^{-15}$ m/s, $4x10^{-14}$ m/s, $8x10^{-14}$, $2x10^{-13}$ m/s and $1x10^{-12}$ m/s.

As shown in Figure 8.57, lower permeability leads to an earlier spalling and a higher probability of explosive spalling. Due to the very high thermal gradients which inevitably lead to some sort of damage, the influence of permeability on time of spalling is very low. Nevertheless, for very high permeability values, the mode of failure changes from explosive to non-explosive spalling. This can be observed in the reduction of failure strain rate, as well as in the significant decrease of volumetric stress at the time of spalling.

Same as in all the previous analyses, the level of stresses parallel to the heated surface is almost constant at approx. 80 % f_c independent of the permeability value. It is worth mentioning that the level of thermally induced stresses at failure (meso-scale analysis) remains unchanged for both fire scenarios presented so far, thus confirming the importance of this parameter.

These results are consistent with the behaviour observed in the experimental part of the work. Plain concrete exhibited extensive explosive spalling, whereas concrete with PP fibres underwent severe thermally induced cracking. The permeability of the two concretes did not differ significantly at room temperature, however, the concrete with PP fibres exhibited an increase in permeability of 2 orders of magnitude when heated up to 200 °C. Comparing the performance of concrete at $3x10^{-15}$ m/s (plain concrete which experienced explosive spalling) and $3x10^{-13}$ m/s (concrete with PP fibres with did not spall) in Figure 8.57, it can be concluded that the model can realistically predict the behaviour of concrete in fire with respect to permeability.

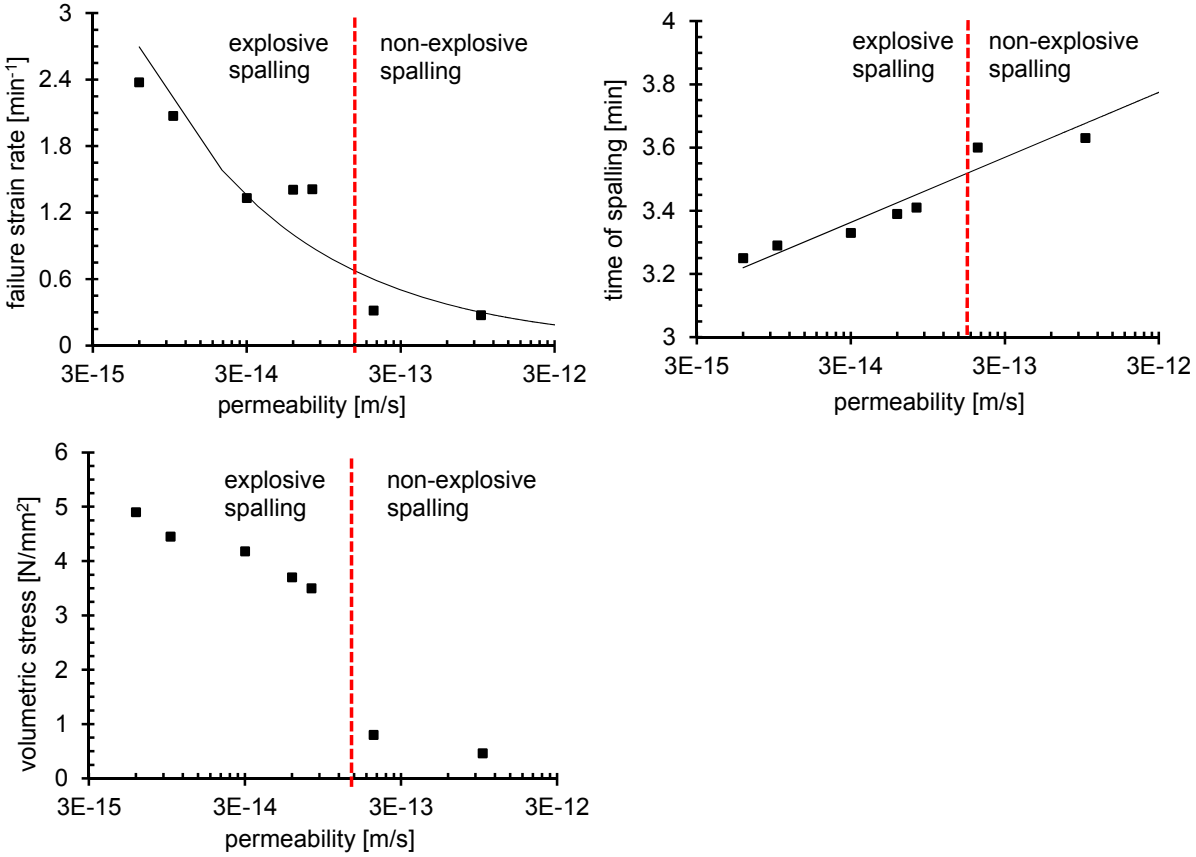

Figure 8.57. Influence of permeability on behaviour of HPC under ZTV-ING fire – meso-scale model

8.4.4.3 Compressive load

The analysis is performed for relative humidity 70 % and permeability of $6x10^{-14}$ m/s. Compressive load ranged from 0 % to 50 % of compressive strength.

An overview of relevant parameters at the location of spalling is provided in Figure 8.59 and Figure 8.59. Similar as in the case of ISO 834, compressive load applied before heating results in an earlier failure. However, the failure strain rate reduces with increasing load level thus indicating that the intensity of failure is reduced. At

very high load levels (40-50 % f_c) the failure tends to change from explosive spalling to thermally induced cracking. This trend is also indicated by very low levels of pore pressure and volumetric stress at high load levels. Stresses parallel to the heated surface slightly increase for higher load levels, also pointing towards the failure driven mainly by the compressive stress, i.e. non-explosive damage.

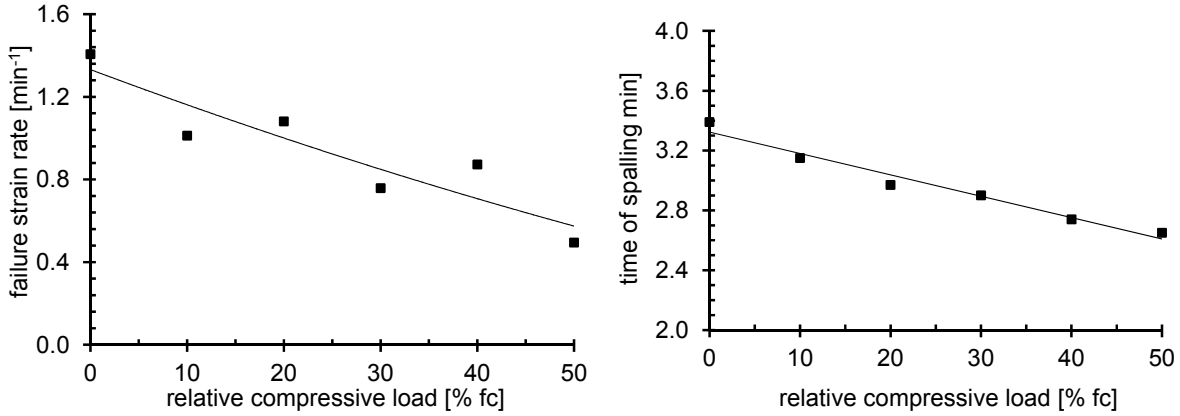

Figure 8.58. Influence of compressive load on behaviour of HPC under ZTV-ING fire – meso-scale model

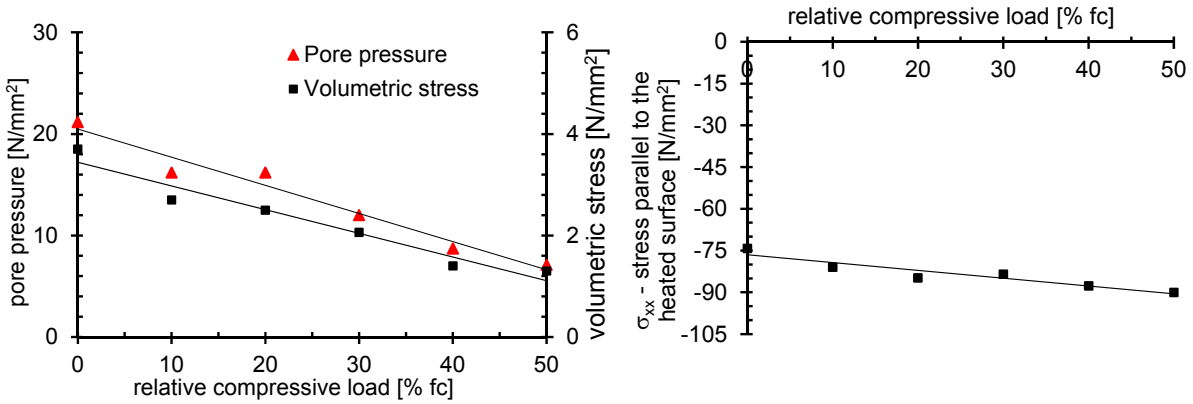

Figure 8.59. Influence of compressive load on behaviour of HPC under ZTV-ING fire – meso-scale model

8.4.5 Constant heating rate

Seven different heating rates are investigated, viz. 40 °C/min, 60 °C/min, 80 °C/min, 100 °C/min, 120 °C/min, 160 °C/min, and 200 °C/min. Concrete with relative humidity of 70 % and permeability of $6x10^{-14}$ m/s is used in all the analyses. The analysis is performed only for the meso-scale model.

The time of occurrence of explosive spalling for all the heating scenarios is plotted in Figure 8.60 (right). The crucial impact of the heating rate scenario on explosive spalling observed in the experiments is realistically captured by the numerical analyses. At high heating rates failure occurs approx. four times earlier than in case of relatively slow heating rate. The impact of heating rate on the spalling time is more pronounced

than any change in the material properties. Failure strain rate (Figure 8.60 left) indicates that the intensity of spalling increases with increasing heating rate.

Thermally induced stresses parallel to the heated surface at the time of failure are shown in Figure 8.61 (left) and it can be observed that these remain almost constant (around 80 % f_c) independent of the heating rate. Comparing these values with those obtained for ISO 834 and ZTV-ING fire it is evident that the level of compressive stresses at failure remains constant for all fire scenarios. With increased heating rate thermally induced stresses develop faster due to higher thermal gradient across the concrete section and explosive spalling can take place earlier. However, the failure is explosive only if a sufficient level of pore pressure and volumetric stress is reached.

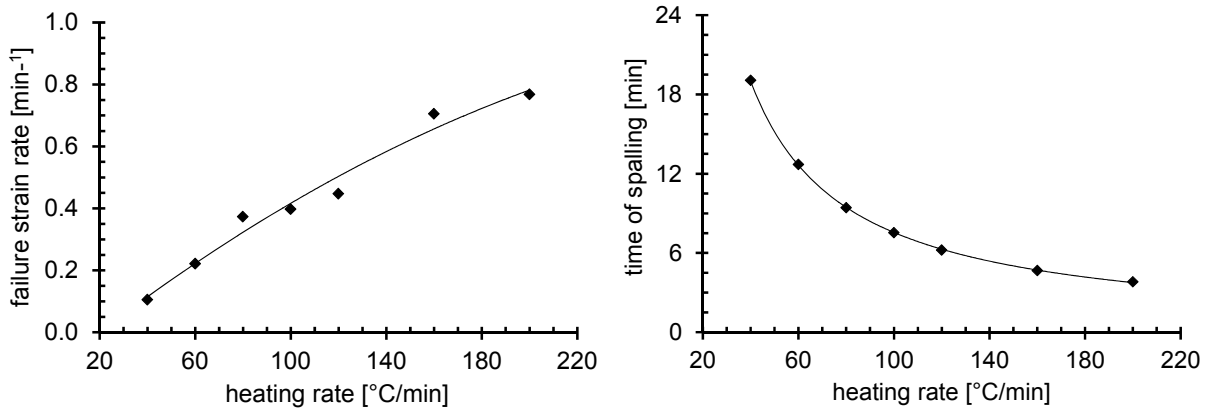

Figure 8.60. Failure strain rate at the location of cracking (left) and time of explosive spalling (right), for different heating scenarios

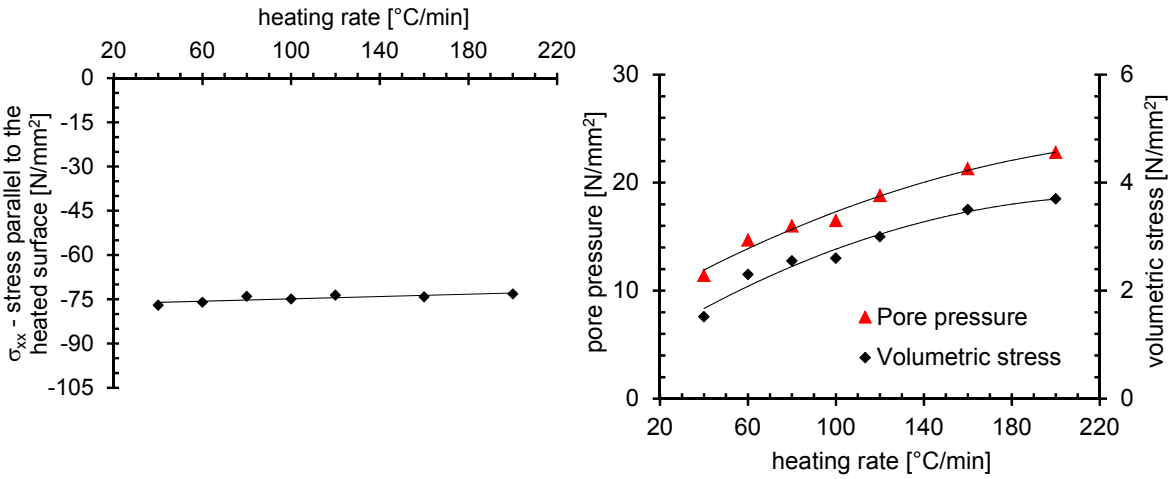

Figure 8.61. Development of relevant parameters at the location of cracking for different heating scenarios: stress parallel to the heated surface (left), volumetric stress and pore pressure (right)

Pore pressures follow the same trend as compressive stresses since increased thermal gradients result in an earlier creation of a saturated zone in concrete. The

initial development of relative humidity and pore pressure at the location of spalling for different heating rates is plotted in Figure 8.62. If relative humidity increases at a faster rate, the generation of pore pressure is facilitated. Therefore, the rate of increase in pore pressure and volumetric stress is much higher when concrete is heated faster. Since the pore pressure governs the intensity of failure, the same is higher for higher heating rates.

It can be concluded that the heating rate is the one of the most important parameters influencing explosive spalling. It is shown previously that explosive spalling occurs only for very high thermally induced stresses parallel to the heated surface. It can occur at different pore pressures, but thermally induced stresses are necessary for the failure to take place. Heating rate governs the rate at which both of these stresses evolve, and therefore governs the time at which concrete starts to spall explosively. Results obtained by numerical analysis realistically reproduce experimentally observed behaviour.

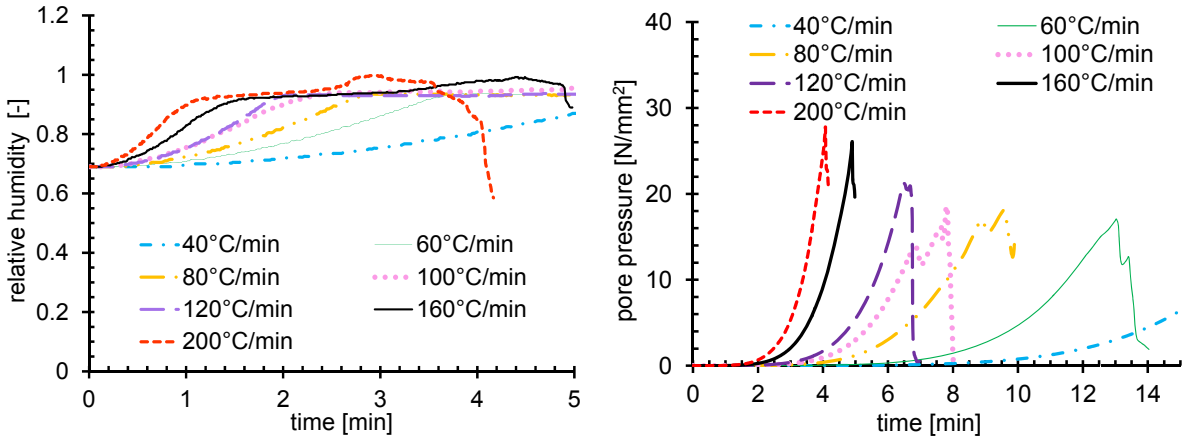

Figure 8.62. Development of relative humidity (left) and pore pressure (right) at the location of cracking for different heating rates

8.5 Conclusions

The mechanism of explosive spalling of concrete at high temperatures and the main influencing parameters are numerically investigated employing the thermo-hygro-mechanical model with temperature dependent microplane model. In most of engineering applications, classical macro-scale approach for concrete is widely accepted owing mainly to its simplicity and reliability, especially in case of mechanical loading. However, complex phenomena associated with severe spatial and temporal variations of stresses and strains in the material can render such simplified approach inadequate. Explosive spalling of concrete with its stochastic nature and local character is a typical example of such phenomenon. Local material properties seem to govern the behaviour, especially when considering the scatter of experimentally obtained data. Inhomogeneity of concrete as a composite of three phases can contribute sig-

nificantly to the mechanism and should, therefore, be accounted for. One of the aims of this study is to evaluate the performance of two modelling approaches, namely macro- and meso-scale, in case of high performance concrete exposed to elevated temperatures. At meso-scale, concrete is modelled as a three phase material comprising cement mortar, coarse aggregates and interfacial transition zone between the two. Specimen is exposed to one sided heating according to two widely used fire scenarios (ISO 834 and ZTV-ING) as well as to different constant heating rates.

First, the two modelling approaches are validated against experimental data. It is found that for the two isolated cases both models give reasonable results with respect temperature distribution and time of spalling, however, macro-scale approach is unable to capture the local failure. It is found for both models that thermally induced stresses alone (thermo-mechanical model) cannot cause explosive spalling i.e. that explosive spalling requires certain level of pore pressures. Moreover, it is found that geometric nonlinearity enhances explosive spalling in a way that it occurs somewhat earlier. However, instability caused by high thermally induced stresses is not one of the main driving forces behind explosive spalling.

Both modelling approaches can realistically reproduce the effect of relative humidity and permeability. As found in experiments, increased humidity of concrete promotes spalling, since it governs the amount of water (and water vapour) in concrete. At higher humidity, spalling is more likely to occur and it takes place earlier than at lower humidity. Macro-scale model predicts explosive spalling only in a very small range (from relative humidity ranging from 70 % to 100 %), for permeability of 6×10^{-15} m/s in case of ISO 834 fire. Meso-scale approach predicts spalling for a wider range of humidity (from rH 50 % to rH 100 %) for the same permeability.

The main difference between the two modelling approaches is the failure mechanism. Macro-scale model fails at almost same pore pressure, thus indicating that pore pressures govern the occurrence of spalling. Low thermal stresses at failure underline the importance of pore pressure. On the other hand, meso-scale model fails as a consequence of combined action of thermally induced compressive stresses and pore pressure, whereby pore pressure acts as a trigger to the energy accumulated due to high compressive stresses.

Permeability is one of the main material properties that govern explosive spalling, since it controls the ability of concrete to transport fluids. Both the models can capture the effect, whereby macro-scale model predicts only much smaller range of permeability at which concrete can spall than the meso-scale model. Macro-scale model fails at almost constant pore pressure over the whole range of permeability values, whereas meso-scale model experiences failure at lower pore pressures for higher permeability.

In case of imposed compressive stress, the two modelling approaches differ significantly. Macro-scale model predicts a slightly beneficial influence of load on susceptibility to explosive spalling. This is mainly due to the fact that macro-scale model fails when pore pressure exceeds certain critical value and the influence of thermally induced stresses is very small. Since all macro-scale analyses mentioned so far are performed with predefined LITS, one series of analyses is performed without LITS predefinition. It is found that macro-scale tends to fail over the whole heated surface even when LITS is not accounted for. Moreover, the effect of compressive stress and restraint also cannot be captured. Meso-scale model predicts the experimentally observed effect of load and restraint on explosive spalling, whereby explosive spalling occurs earlier if preloading is present. At very high load levels, the failure seems to change from explosive to non-explosive damage due to cracking caused by high compressive stresses.

The influence of aggregate nature is also investigated for both approaches. In case of macro-scale modelling approach, almost no effect of aggregate type is observed. Type of aggregate is found to have a significant influence on spalling in case of meso-scale approach. Aggregates with low thermal dilatation as well as thermally stable aggregates render concrete less susceptible to explosive spalling. This is associated with the degree of incompatibility between mortar and aggregates, and consequently with thermally induced stresses.

Meso-scale model is further analysed for different aggregate distributions. It is found that the local geometry of aggregates can influence the location of spalling. This partially explains the random behaviour observed in the experiments.

The effect of different heating rates is investigated at meso-scale. For slow heating rate explosive spalling occurs much later than for fast heating rates, and it is also associated with lower intensity and at a lower level of pore pressure. The rate of heating controls both thermally induced stresses and pore pressures; hence it has a very important influence the occurrence of spalling as well.

Overall, it can be concluded that explosive spalling is successfully modelled only at meso-scale. The main cause for explosive spalling is the release of potential energy accumulated due to high stresses. The trigger to this release is pore pressure and it is the governing parameter which defines whether the spalling will be of explosive or non-explosive type (thermally induced cracking).

9. CONCLUSIONS AND OUTLOOK

In the framework of the present work, explosive spalling of high performance concrete (HPC) is analysed employing experimental and numerical techniques. The response of concrete to two different heating scenarios is investigated on medium size slabs (700 x 700 x 350 mm) heated from one side only. As can be expected, concrete undergoes explosive spalling much earlier in case of fast tunnel fire scenario than in case of ISO 834 fire. Both concrete mixtures possessed lower moisture content at room temperature than the limit moisture provided in the current codes. These experiments point out the fact that some of the current code provisions are insufficient to mitigate explosive spalling. This is mostly due to the fact that these provisions are based on relatively old experimental data which were obtained for concrete without cement replacements, such as fly ash and silica fume. Moreover, the efficacy of polypropylene (PP) fibres is evaluated. Severe spalling is observed for both scenarios in case of plain HPC, whereas fibre addition almost completely alleviated spalling. It is well known that PP fibres mitigate spalling by increasing permeability of concrete.

In the second stage, an experimental setup for permeability measurements at room and elevated temperatures is developed and validated against widely used CEMBUREAU method. Permeability of concrete used in the fire experiments (without and with PP fibres) is measured at temperatures ranging from 20 °C to 300 °C. Concrete without PP fibres exhibits almost linear increase in permeability with rising temperature (in semi-log scale). These results are consistent with the findings of other researchers. However, the permeability of concrete with PP fibres increases already at temperature between 80 °C and 130 °C, thus indicating that the melting of fibres (at approx. 160 °C) is possibly not the only mechanism that contributes to the permeability increase. Concrete with fibres is further observed employing a scanning electron microscope at room temperature and after exposure to 200 °C. It is observed that the interface between concrete and fibre is initially very pronounced, with quite rough transition between the two phases. After exposure to 200 °C for various duration periods, it is observed that the melted fibres flow only into the micro-cracks generated around the fibre, but not in the cement matrix.

The interaction of compressive stresses and pore pressure is investigated on concrete cubes with side length of 150 mm. These are first heated to 230 °C to generate certain pore pressures within concrete and subsequently loaded in compression. It is found that concrete with short exposure to 230 °C fails in a typical compressive failure, whereas concrete heated for a longer period spalls very explosively. These very simple tests demonstrate the combined action of compressive stresses and pore pressure. Furthermore, it is shown that the same concrete cubes do not spall explosively if no additional compressive load is imposed (when cubes are taken out of the oven without subsequent loading in compression).

Further experimental study is necessary in order to understand the mechanism by which PP fibres contribute to permeability increase at temperatures below and around melting point. Scanning electron microscopy is shown to be a useful tool for such investigation and future research should be directed towards simultaneous measurement of permeability, porosity and investigation of microstructure especially at temperatures between 80 °C and 200 °C. Furthermore, experiments on specimens with different relative humidity and under compressive load applied prior to heating are required to fill the gaps in the existing data.

Numerical part of the study is performed employing the thermo-mechanical and thermo-hygro-mechanical model developed by Periskic (2009). Experimental measurements and existing experimental data point out some of the most important characteristics of explosive spalling, namely its stochastic nature and local character. In order to effectively simulate this phenomenon numerically, it is essential to account for the heterogeneity of concrete by employing meso-scale modelling approach. The transition from typically used macro-scale to meso-scale required certain adaptions of the thermo-hygro-mechanical model. Comparative study of behaviour of macro- and meso-scale model with respect to free thermal strain and load induced thermal strain is performed and it is found that the explicit definition of LITS is not required in case of the meso-scale model, as opposed to the macro-scale model.

One of the main objectives of the numerical study is to compare the performance of the two modelling approaches to capture the phenomenon of explosive spalling. Firstly, the two modelling approaches are used to simulate the experiments on slabs under one-sided heating. It is found that the thermo-mechanical model cannot predict any aspect of explosive spalling. When employing the thermo-hygro-mechanical model, both modelling approaches predicted explosive spalling with reasonable accuracy, however, macro-scale model could not capture the localization of failure observed in the experiments. Further, the two modelling approaches are employed to investigate the effect of main influencing parameters on spalling. Both resulted in increased likelihood of explosive spalling in case of high relative humidity, confirming the experimentally observed trends. Similarly, lower permeability is found to significantly increase the likelihood of spalling. Beyond certain permeability value, explosive spalling is completely avoided, which again corresponds well to the available experimental data. However, the detrimental effect of compressive stress cannot be captured using macro-scale model, whereas meso-scale model realistically reproduces experimentally observed tendency of increased likelihood of spalling at higher loads. Compressive stress contributes to total stress level and together with thermally induced stresses results in earlier occurrence of explosive spalling in concrete.

Furthermore, macro-scale model exhibited almost no sensitivity to different aggregate types (different thermal strain). However, at meso-scale it is found that aggregates with higher thermal dilatation promote spalling, as is observed in the experiments available in the literature. Hence, use of thermally stable aggregates can be

used as a passive measure to reduce explosive spalling. However, the use of PP fibres is the most effective measure and cannot be replaced solely by using more appropriate aggregates. The effect of aggregate distribution in concrete is studied on meso-scale model. The distribution of aggregates in concrete governs the location of the initial spalling event. These results are helpful for better understanding of the random nature of spalling in terms of spalling location.

Even though both modelling approaches exhibited relatively good agreement with trends observed in the experiments, it is found that the two models differ significantly in the mechanism that leads to explosive spalling. Spalling of macro-scale model is mainly driven by pore pressures, and the role of thermally induced stresses is insignificant. On the other hand, meso-scale model predicts spalling as a combination of thermally induced stresses and pore pressures, whereby pore pressure act as a trigger that relieves the potential energy accumulated due to high thermally induced compressive stresses. This type of combined action corresponds well to the behaviour of heated cubes presented in the experimental part of the study. Macro-scale model is found to be inadequate to predict explosive spalling since it cannot capture the local character of the failure nor the effect of compressive load on spalling, alongside with the fact that it almost completely neglects the effect of thermally induced stresses.

Numerical results presented in this thesis allow us to better understand the mechanism of explosive spalling as well as the main influencing parameters. However, further work is needed in order to clarify the effect of PP fibres. This can be performed by discrete modelling of fibres and corresponding implementation of the softening and melting processes of polypropylene in the FE code.

BIBLIOGRAPHY

Abbas, A., Carcasses, M. & Ollivier, J.-P., 1999. Gas permeability of concrete in relation to its degree of saturation. *Materials and structures*, 32(1), pp.3–8.

Aitcin, P.-C., 2011. *High performance concrete*, Taylor & Francis.

Albizzati, E. & Moore, E.P., 1996. *Polypropylene handbook: polymerization, characterization, properties, processing, applications*, Hanser.

Ali, F., 2002. Is high strength concrete more susceptible to explosive spalling than normal strength concrete in fire? *Fire and materials*, 26(3), pp.127–130.

Ali, F., Nadjai, A. & Abu-Tair, A., 2011. Explosive spalling of normal strength concrete slabs subjected to severe fire. *Materials and structures*, 44(5), pp.943–956.

Anderberg, Y. & Thelandersson, S., 1976. *Stress and deformation characteristics of concrete at high temperatures*, Lund Institute of Technology. Division of Structural Mechanics and Concrete Construction.

AS-1530.4, 1979. Fire test to Building Material. *Australian Standard*.

Austin, S., Robins, P. & Richards, M., 1992. Jetblast temperature-resistant concrete for Harrier aircraft pavements. *Structural engineer*, 70, pp.427–427.

Bamforth, P., 1987. The relationship between permeability coefficients for concrete obtained using liquid and gas. *Magazine of concrete research*, 39(138), pp.3–11.

Baroghel-Bouny, V., 2007. Water vapour sorption experiments on hardened cementitious materials: part I: essential tool for analysis of hygral behaviour and its relation to pore structure. *Cement and Concrete Research*, 37(3), pp.414–437.

Bazant, Z., Adley, M., Carol, I., Jirasek, M., Akers, S., Rohani, B., Cargile, J. & Caner, F., 2000. Large-strain generalization of microplane model for concrete and application. *Journal of engineering mechanics*, 126(9), pp.971–980.

Bazant, Z. & Kaplan, M., 1996. *Concrete at high temperatures: material properties and mathematical models*, American Society of Mechanical Engineers.

Bazant, Z. & Oh, B., 1983. Crack band theory for fracture of concrete. *Matériaux et construction*, 16(3), pp.155–177.

Bazant, Z. & Thonguthai, W., 1978. Pore pressure and drying of concrete at high temperature. *Journal of the Engineering Mechanics Division*, 104(5), pp.1059–1079.

Bazant, Z. & Thonguthai, W., 1979. Pore pressure in heated concrete walls: theoretical prediction. *Magazine of Concrete Research*, 31(107), pp.67–76.

Bentz, D.P., 2000. Fibers, percolation, and spalling of high-performance concrete. *ACI Materials Journal-American Concrete Institute*, 97(3), pp.351–359.

de Borst, R. & Peeters, P., 1989. Analysis of concrete structures under thermal loading. *Computer methods in applied mechanics and engineering*, 77(3), pp.293–310.

Boström, L., Wickström, U. & Adl-Zarrabi, B., 2007. Effect of specimen size and loading conditions on spalling of concrete. *Fire and materials*, 31(3), pp.173–186.

Canut, M. & Geiker, M., 2011. *Pore structure in blended cement pastes*.

CEB-FIP-bulletin-46, 2008. *Fire design of concrete structures – structural behaviour*, FIB-Fédération Internationale du Béton.

Chen, X., Rougelot, T., Davy, C., Chen, W., Agostini, F., Skoczylas, F & Bourbon, X., 2009. Experimental evidence of a moisture clog effect in cement-based materials under temperature. *Cement and Concrete Research*, 39(12), pp.1139–1148.

Choinska, M., Khelidj, A., Chatzigeorgiou, G. & Pijaudier-Cabot, G., 2007. Effects and interactions of temperature and stress-level related damage on permeability of concrete. *Cement and Concrete Research*, 37(1), pp.79–88.

Christiaanse, A., Langhorst, A. & Gerriste, A., 1972. *Discussion of fire resistance of lightweight concrete and spalling*, Dutch Society of Engineers (STUVO).

Connolly, R.J., 1995. The spalling of concrete in fires. *PhD Thesis*, Aston University.

Consolazio, G.R., McVay, M.C. & Rish III, J.W., 1998. Measurement and prediction of pore pressures in saturated cement mortar subjected to radiant heating. *ACI Materials Journal*, 95(5).

Copier, W., 1979. *The spalling of normalweight and lightweight concrete on exposure to fire*, Heron. PhD Thesis.

Cruz, C. & Gillen, M., 1980. Thermal expansion of Portland cement paste, mortar and concrete at high temperatures. *Fire and Materials*, 4(2), pp.66–70.

Dehn, F., Nause, P., Juknat, M., Orgass, M. & Koenig, A., 2010. *Brand-und Abplatzverhalten von Faserbeton in Straßentunneln*, Wirtschaftsverlag N. W.

Dougill, J., 1972. Modes of failure of concrete panels exposed to high temperatures. *Magazine of Concrete Research*, 24(79), pp.71–76.

Dwaikat, M. & Kodur, V., 2009. Hydrothermal model for predicting fire-induced spalling in concrete structural systems. *Fire safety journal*, 44(3), pp.425–434.

DIN EN 1-2, 2004. 1-2 Eurocode 2: Bemessung und Konstruktion von Stahlbeton- und Spannbetontragwerken-Teil 1-2: Allgemeine Regeln-Tragwerksbemessung für den Brandfall 1992. *Deutsche Fassung EN*, pp.1–1.

Felicetti, R., Gambarova, P., Sora, M. & Khoury, G., 2000. Mechanical behaviour of HPC and UHPC in direct tension at high temperature and after cooling. In Rossi, P, ed. *Fifth RILEM symposium on fibre-reinforced concretes (FRC)*. pp. 749–758.

Flynn, D.R., 1999. *Response of high performance concrete to fire conditions: review of thermal property data and measurement techniques*, National Institute of Standards and Technology.

Gallé, C. & Sercombe, J., 2001. Permeability and pore structure evolution of silico-calcareous and hematite high-strength concretes submitted to high temperatures. *Materials and Structures*, 34(10), pp.619–628.

Gary, M., 1916. *Brandproben an Eisenbetonbauten*, Ernst & Sohn.

Gawin, D., Pesavento, F. & Schrefler, B., 2003. Modelling of hygro-thermal behaviour of concrete at high temperature with thermo-chemical and mechanical material degradation. *Computer methods in applied mechanics and engineering*, 192(13), pp.1731–1771.

Gawin, D., Pesavento, F. & Schrefler, B., 2006. Towards prediction of the thermal spalling risk through a multi-phase porous media model of concrete. *Computer methods in applied mechanics and engineering*, 195(41), pp.5707–5729.

Grosse, C., Ozbolt, J., Richter, R. & Periskic, G., 2010. Acoustic emission analysis and thermo-hygro-mechanical model for concrete exposed to fire. *Journal of Acoustic Emission*, 28, pp.188–203.

Grosse, C., Richter, R. & Ozbolt, J., 2013. Combined acoustic emission and simulation approach to study fracture behavior of concrete under fire load. In Van Mier, JGM and Ruiz, G and Andrade, C and Yu, RC and others, ed. *8th International Conference on Fracture Mechanics of Concrete and Concrete Structures (FramCoS-8)*.

Hager, I., 2004. *Comportement à haute température des bétons à haute performance -évolution des principales propriétés mécaniques*, Ecole Polytechnique. PhD Thesis (in french).

Hager, I. & Pimienta, P, 2004a. Mechanical properties of HPC at high temperatures. In *Proc. Int. Workshop fib Task Group*. pp. 95–100.

Hager, I. & Pimienta, P, 2004b. The impact of the addition of polypropylene fibres on the mechanical properties of high performance concretes exposed to high temperatures. In Di Prisco, M and Felicetti, R and Plizzari, Giovanni A, ed. *PRO 39: 6th International RILEM Symposium on Fibre-Reinforced Concretes (FRC)-BEFIB 2004 (Volume 1)*. RILEM Publications.

Hager, I. & Tracz, T., 2010. The impact of the amount and length of fibrillated polypropylene fibres on the properties of HPC exposed to high temperature. *Archives of Civil Engineering*, 56(1), pp.57–68.

Hansen, K.K., 1986. *Sorption isotherms: a catalogue*, Technical University of Denmark, Department of Structural Engineering and Materials.

Harmathy, T. & Allen, L., 1973. Thermal properties of selected masonry unit concretes. In *ACI Journal Proceedings*.

van der Heijden, G., van Bijnen, R., Pel, L. & Huinink, H., 2007. Moisture transport in heated concrete, as studied by NMR, and its consequences for fire spalling. *Cement and concrete research*, 37(6), pp.894–901.

Hertz, K.D., 2003. Limits of spalling of fire-exposed concrete. *Fire Safety Journal*, 38(2), pp.103–116.

Hildenbrand, G. & Peehs, M., 1978. *Untersuchung der Wechselwirkung von Kernschmelze und Reaktorbeton*, Kraftwerk Union Erlangen / Reaktortechnik.

Hilsdorf, H. & Kropp, J., 1995. *Performance criteria for concrete durability*, Taylor & Francis.

Hoseini, M., Bindiganavile, V. & Banthia, N., 2009. The effect of mechanical stress on permeability of concrete: a review. *Cement and Concrete Composites*, 31(4), pp.213–220.

Ichikawa, Y. & England, G., 2004. Prediction of moisture migration and pore pressure build-up in concrete at high temperatures. *Nuclear engineering and design*, 228(1), pp.245–259.

IS456, 2000. Plain and reinforced concrete-code of practice. *Beaureau of Indian Standard, New Delhi, India*.

IS516, 1959. Methods of Test for Strength of Concrete. *Beaureau of Indian Standard, New Delhi, India*.

Jansson, R., 2008. *Material properties related to fire spalling of concrete*, Division of Building Materials, Lund Institute of Technology, Lund University.

Jansson, R. & Boström, L., 2010. The influence of pressure in the pore system on fire spalling of concrete. *Fire technology*, 46(1), pp.217–230.

Jui, C., Chuan, C. & Wen, C., 2008. Study of mechanical behavior of fiber reinforced concrete at elevated temperatures. In Nguyen, TD and Luong, DL and Ta, MH and Le, VH and Tran, TTH and Le, TH, ed. *3rd ACF international conference on Sustainable Concrete Technology and Structures* . pp. 578–585.

Jumppanen, U., 1989. Effect of Strength on Fire Behaviour of Concrete. Nordic Concrete Research. Publication No. 8 . *Publication of Nordic Concrete Federation*.

Kalifa, P., Chene, G. & Galle, C., 2001. High-temperature behaviour of HPC with polypropylene fibres: From spalling to microstructure. *Cement and concrete research*,

31(10), pp.1487–1499.

Kalifa, P., Tsimbrovska, M. & Baroghel-Bouny, V., 1998. High performance concrete at elevated temperatures - an extensive experimental investigation on thermal, hygral and microstructure properties. In Aitcin, PC and Delagrave, Y, ed. *Proceedings of the International Symposium on High-Performance and Reactive Powder Concretes*. pp. 259–279.

Karihaloo, B.L., 1995. *Fracture Mechanics & Structural Concrete*, Longman Pub Group.

Khoury, G., 2008. Polypropylene fibres in heated concrete. Part 2: Pressure relief mechanisms and modelling criteria. *Magazine of concrete research*, 60(3), pp.189–204.

Khoury, G., 1995. Strain components of nuclear-reactor-type concretes during first heat cycle. *Nuclear engineering and design*, 156(1), pp.313–321.

Khoury, G., 2006. Strain of heated concrete during two thermal cycles. Part 1: strain over two cycles, during first heating and at subsequent constant temperature. *Magazine of Concrete Research*, 58(6), pp.367–385.

Khoury, G. & Anderberg, Y., 2000. Concrete spalling review. *Fire Safety Design*.

Klinkenberg, L., 1941. The permeability of porous media to liquids and gases. *Drilling and production practice*.

Knack, I., 2011. The use of PP fibers in tunnel construction to avoid explosive spalling in case of fire. New test results for the clarification of the mode of action. In Koenders, EAB; Dehn, F, ed. *Concrete spalling due to fire exposure*. Delft University, pp. 297–307.

Kodur, V., Dwaikat, M. & Raut, N., 2009. Macroscopic FE model for tracing the fire response of reinforced concrete structures. *Engineering Structures*, 31(10), pp.2368–2379.

Kollek, J., 1989. The determination of the permeability of concrete to oxygen by the Cembureau method—a recommendation. *Materials and structures*, 22(3), pp.225–230.

Kordina, K. & Meyer-Ottens, C., 1999. *Beton Brandschutz-Handbuch*, Verlag Bau und Technik.

Kukla, K., 2010. *Concrete at high temperatures: hygro-thermo-mechanical degradation of concrete*, University of Glasgow. PhD Thesis.

Kumar, A. & Kumar, V., 2003. Behaviour of RCC beams after exposure to elevated temperatures. *Journal of the Institution of Engineers. India. Civil Engineering Division*, 84(nov), pp.165–170.

Lion, M., Skoczylas, Frédéric, Lafhaj, Z. & Sersar, M., 2005. Experimental study on a mortar. Temperature effects on porosity and permeability. Residual properties or direct measurements under temperature. *Cement and Concrete Research*, 35(10), pp.1937–1942.

Loosveldt, H., Lafhaj, Z. & Skoczylas, Frédéric, 2002. Experimental study of gas and liquid permeability of a mortar. *Cement and Concrete Research*, 32(9), pp.1357–1363.

Luccioni, B., Figueroa, M. & Danesi, R., 2003. Thermo-mechanic model for concrete exposed to elevated temperatures. *Engineering Structures*, 25(6), pp.729–742.

Malhotra, H.L., 1984. *Spalling of concrete in fires*, Construction Industry Research and Information Association, Technical Report No. 118.

Meyer-Ottens, C., 1974. *Abplatzversuche an Prüfkörpern aus Beton, Stahlbeton und Spannbeton bei verschiedenen Temperaturbeanspruchungen*, Beuth Verlag.

Meyer-Ottens, C., 1972. *Zur Frage der Abplatzungen an Betonbauteilen aus Normalbeton bei Brandbeanspruchung*, Technische Universität Braunschweig. PhD Thesis (In german).

Mindeguia, J.-C., Hager, I., Pimienta, P, Carré, H. & La Borderie, C., 2013. Parametrical study of transient thermal strain of ordinary and high performance concrete. *Cement and Concrete Research*, 48, pp.40–52.

Mindeguia, J.-C., Pimienta, Pierre, Noumowé, A. & Kanema, M., 2010. Temperature, pore pressure and mass variation of concrete subjected to high temperature—Experimental and numerical discussion on spalling risk. *Cement and concrete research*, 40(3), pp.477–487.

Mohr, O., 1900. Welche Umstände bedingen die Elastizitätsgrenze und den Bruch eines Materials. *Zeitschrift des Vereins deutscher Ingenieure*, 46, pp.1524–1530.

Neves, I.C., Rodrigues, J.P.C. & Loureiro, A. de P., 1996. Mechanical properties of reinforcing and prestressing steels after heating. *Journal of Materials in Civil Engineering*, 8(4), pp.189–194.

Nielsen, L., 2007. Moisture Sorption in Porous Materials: a best fit description from experimental data. *Moisture Sorption in Porous Materials*, 1, pp.36–01.

Norling Mjörnell, K., 1997. *Moisture Conditions in High Performance Concrete. Mathematical Modelling and Measurements*, Chalmers University of Technology, PhD Thesis.

Noumowe, A., Clastres, P., Debicki, G. & Costaz, J., 1996a. Thermal stresses and water vapor pressure of high performance concrete at high temperature. In Larrard, F and Lacrix, R, ed. *Proceedings, 4th International Symposium on Utilization of High-Strength/High-Performance Concrete*.

Noumowe, A., Clastres, P., Debicki, G. & Costaz, J., 1996b. Transient heating effect on high strength concrete. *Nuclear engineering and design*, 166(1), pp.99–108.

Ortiz, M., 1985. A constitutive theory for the inelastic behavior of concrete. *Mechanics of Materials*, 4(1), pp.67–93.

Ozbolt, J., Eligehausen, R. & Reinhardt, H., 1999. Size effect on the concrete cone pull-out load. In *Fracture Scaling*. Springer, pp. 391–404.

Ozbolt, J., Kozar, I., Eligehausen, R. & Periskic, G., 2005. Instationäres 3D Thermomechanisches Modell für Beton. *Beton-und Stahlbetonbau*, 100(1), pp.39–51.

Ozbolt, J., Li, Y. & Kozar, I., 2001. Microplane model for concrete with relaxed kinematic constraint. *International Journal of Solids and Structures*, 38(16), pp.2683–2711.

Ozbolt, J., Periskic, G., Reinhardt, H. & Eligehausen, R., 2008. Numerical analysis of spalling of concrete cover at high temperature. *Computers and Concrete*, 5(4), pp.279–293.

Pearce, C., Nielsen, C. & Bicanic, N., 2004. Gradient enhanced thermo-mechanical damage model for concrete at high temperatures including transient thermal creep. *International journal for numerical and analytical methods in geomechanics*, 28(7-8), pp.715–735.

Periskic, G., 2009. *Entwicklung eines 3D thermo-hygro-mechanischen Modells für Beton unter Brandbeanspruchung und Anwendung auf Befestigungen unter Zuglasten*, Universität Stuttgart. PhD Thesis (in german).

Phan, L., 2002. High-strength concrete at high temperature-An Overview. In König, G, ed. *International Symposium on Utilization of High-Strength, High-Performance Concrete, June*. pp. 16–20.

Phan, L., 2007. Spalling and mechanical properties of high strength concrete at high temperature. In Toutlemonde, F, ed. *Proceedings concrete under severe conditions,*. pp. 1595–1608.

Phan, L. & Carino, N., 2003. Code provisions for high strength concrete strength-temperature relationship at elevated temperatures. *Materials and Structures*, 36(2), pp.91–98.

Saito, H., 1965. Explosive spalling of prestressed concrete in fire, Occasonal report No. 22. *Building Research Institute, Japan,*.

Sanjayan, G. & Stocks, L., 1993. Spalling of high-strength silica fume concrete in fire. *ACI Materials Journal*, 90(2).

Schneider, U., 2010. Permeability of high perfromance concrete at elevated temperatures. In Kodur, V and Franssen, JM, ed. *Structures in Fire: Proceedings of the*

Sixth International Conference. pp. 809–816.

Schneider, U., 1982. *Verhalten von Beton bei hohen Temperaturen* Deutscher Ausschuss für Stahlbeton, ed., Ernst & Sohn.

Schneider, U., Herbst, H. & Diederichs, U., 1985. Permeability and Porosity of Concrete at Elevated Temperature. In Finzi, S, ed. *SMIRT8*. pp. 211–216.

Sertmehmetoglu, Y., 1977. *On a Mechanism of Spalling of Concrete Under Fire Conditions.*, King's College London (University of London). PhD Thesis.

Shah, S.P. & Ahmad, S.H., 1994. *High performance concrete. Properties and application*, McGraw-Hill .

Shirley, S.T., Burg, R.G. & Fiorato, A.E., 1988. Fire endurance of high-strength concrete slabs. *ACI Materials Journal*, 85(2).

Shorter, G. & Harmathy, T., 1965. Moisture clog spalling. *Proceedings of the Institution of Civil Engineers*, 20, pp.75–90.

Stabler, J.T., 2000. *Computational modelling of thermo-mechanical damage and plasticity in concrete*.

Suhaendi, S.L. & Horiguchi, T., 2006. Effect of short fibers on residual permeability and mechanical properties of hybrid fibre reinforced high strength concrete after heat exposition. *Cement and Concrete Research*, 36(9), pp.1672–1678.

Takeuchi, M., Hiramoto, M., Kumagai, N., Yamazaki, N., Kodaira, A. & Sugiyama, K., 1993. Material properties of concrete and steel bars at elevated temperatures. In Riera, JD, ed. *12th International Conference on Structural Mechanics in Reactor Technology*. pp. 13–138.

Taylor, G., 1938. Plastic strain in metals. *Journal of the Institute of Metals*, 62, pp.307–324.

Tenchev, R. & Purnell, P., 2005. An application of a damage constitutive model to concrete at high temperature and prediction of spalling. *International Journal of solids and structures*, 42(26), pp.6550–6565.

Wagner, W. & Kruse, A., 1998. The industrial standard IAPWS-IF97 for the thermodynamic properties and supplementary equations for other properties. *Properties of Water and Steam, Springer*.

Wang, K., Jansen, D.C., Shah, S.P. & Karr, A.F., 1997. Permeability study of cracked concrete. *Cement and Concrete Research*, 27(3), pp.381–393.

Yaragal, S.C. et al, 2010. *BRNS concrete at elevated temperature* , Technical Report.

Zeiml, M., Lackner, R., Leithner, D. & Eberhardsteiner, J., 2008. Identification of residual gas-transport properties of concrete subjected to high temperatures. *Cement and concrete research*, 38(5), pp.699–716.

Zhang, B. & Bicanic, N., 2002. Residual Fracture Toughness of Normal-and High-Strength Gravel Concrete after Heating to 600° C. *ACI Materials Journal*, 99(3).

Zhao, Jie, 2012. *Fire-Induced Spalling Modeling of High-Performance Concrete*, Technical University Delft. PhD Thesis.

Zhao, Jian, 2012. *Rock mechanics for civil engineering - Lecture notes*, Lausanne, Switzerland: Swiss Federal Institute of Technology.

Zheng, W., Hou, X., Shi, D. & Xu, M., 2010. Experimental study on concrete spalling in prestressed slabs subjected to fire. *Fire Safety Journal*, 45(5), pp.283–297.

Zhou, Y. & Mallick, P., 2002. Effects of temperature and strain rate on the tensile behavior of unfilled and talc-filled polypropylene. Part I: Experiments. *Polymer Engineering & Science*, 42(12), pp.2449–2460.

Zhukov, V., 1970. Explosive failure of concrete during a fire. *Translation No. DT*, 2124.

Zhukov, V., 1994. Forecast of a brittle failure of concrete by fire. *Scientific Research Institute for Concrete and Reinforced Concrete, Moscow*.

Zusätzliche technische Vertragsbedingungen und Richtlinien für Ingenieurbauten, 2003. ZTV-ING. *Bundesanstalt für Straßenwesen*.

Curriculum Vitae

Persönliche Daten

Josipa Bošnjak
geboren am 21. August 1982
in Mostar, Bosnien und Herzegowina
verheiratet

Schuldbildung und Beruf

05/2008 - heute	Wissenschaftliche Mitarbeiterin am Institut für Werkstoffe im Bauwesen der Universität Stuttgart
02/2006 - 02/2008	Mitarbeiterin im Projektbüro A3 d.o.o. Široki Brijeg, Bosnien und Herzegowina
09/2000 - 11/2005	Studium des Bauingenieurwesens an der Universität Mostar, Bosnien und Herzegowina
09/1994 - 06/2003	Gymnasium Frau Dominik Mandić, Široki Brijeg, Bosnien und Herzegowina, Allgemeine Hochschulreife